Département de Physique
Université de Fribourg (Suisse)

# Theoretical and experimental study of the Stark effect in the ground state of alkali atoms in helium crystals

## THESE

présentée à la Faculté des Sciences de l'Université de Fribourg (Suisse)
pour l'obtention du grade de
*Doctor rerum naturalium*

## Simone Ulzega

Italie

Acceptée par la Faculté des Sciences de l'Université de Fribourg (Suisse) sur la proposition de

Prof. Dr. Dionys Baeriswyl, Université de Fribourg (Président de Jury)
Prof. Dr. Antoine Weis, Université de Fribourg (Directeur de thèse)
Prof. Dr. Jean-Claude Dousse, Université de Fribourg (Corapporteur)
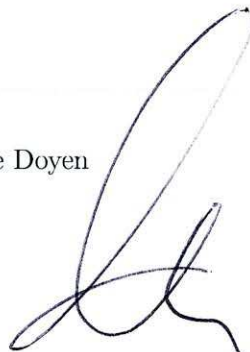Prof. Dr. Majed Chergui, EPFL, Lausanne (Corapporteur)

Fribourg, 17 Mars 2006

Le Directeur de thèse

Prof. Dr. Antoine Weis

Le Doyen

Prof. Dr. Marco Celio

# Abstract

This thesis work describes a detailed study of the Stark interaction in the ground state of cesium atoms trapped in a solid helium matrix. The motivation for the investigation of electric field effects on alkali species implanted in solid helium is related to the original main goal of our experimental activities, i.e., the measurement of a permanent atomic electric dipole moment (EDM). The existence of an atomic EDM simultaneously violates the discrete symmetries of time reversal (T) and parity (P). The search for an atomic EDM is thus of great scientific interest since it would prove the existence of new physics beyond the Standard Model and it would open the doors towards a better understanding of the fundamental interactions of elementary particles. At the beginning of the 1990s, the helium matrix doped with paramagnetic atoms was thought to be a specially well-suited system for an EDM experiment. The matrix-isolated cesium atoms, in the body centered cubic (bcc) phase of solid helium, reside in bubble-like cavities, which have a spherical shape when the atoms are in the radially symmetric $6S_{1/2}$ ground state. The helium crystal thus plays the role of a diamagnetic and perfectly isotropic trap where the atoms can be stored and studied for long times. A high degree of ground state spin polarization can be created by optical pumping and, owing to the absence of interaction with the crystal fields, the state of polarization can be maintained for an exceptionally long time ($\approx 1$ s). This slow spin relaxation rate allows high-resolution magnetic resonance spectroscopy to be performed on doped helium crystals. Moreover, the large electric breakdown voltage of superfluid and solid helium (in excess of 100 kV/cm) make the helium matrix an ideal environment for electric field experiments.

The experimental signature of a permanent EDM becomes visible when the atomic sample is exposed to an external electric field and provides a shift of the atomic energy levels *linear* in the applied field. The interaction of an atom with an external electric field, i.e., the Stark interaction, leads also to P– and T–conserving effects which are *quadratic* in the field strength. Although these quadratic effects are extremely small, they overwhelm any linear effect due to the EDM by several orders of magnitude and they thus appear in an EDM experiment as a systematic background which has to be characterized. The study of the quadratic effect has revealed several unexpected aspects that have renewed our motivations to pursue a detailed investigation of this research field.

The quadratic Stark effect in the ground state of alkali atoms, treated in the frame of a perturbation theory approach, can be parameterized in terms of a strongly suppressed tensor polarizability $\alpha_2$, which arises only as a third order effect when the hyperfine interaction is included in the perturbation. The forbidden third-order tensor effect is seven orders of magnitude smaller than the allowed second-order Stark interaction. The first theoretical model describing the Stark effect in the $nS_{1/2}$ ground state of alkali atoms was published in 1968 by Sandars. Since then, Sandars' work has been considered the main reference for the theory of the quadratic Stark effect in alkali ground states. The tensor polarizability of cesium was measured in a few experiments in the 1960s and about 40 years later in Fribourg by our group, by measuring the shift of the magnetic transitions between Zeeman sub-levels induced by an external electric field. Although all these experiments yielded compatible results, they showed a large discrepancy with respect to the theoretical value of the tensor polarizability derived from Sandars' model. It was shown that a similar discrepancy exists for all the alkalis.

The third order Stark interaction also leads to a shift of the hyperfine clock transition frequency ($\mid 6S_{1/2}F = 4, M = 0 > \leftrightarrow \mid 6S_{1/2}F = 3, M = 0 >$). This effect (static Stark

effect) is of special interest for the scientific community because of its close connection with the blackbody shift (dynamic Stark effect) of the clock transition frequency. A precise knowledge of this effect is of great importance for the definition of the second. At present, the atomic-clock community is involved in an important open debate due to the existence of contradicting values of the Stark shift of the hyperfine transition frequency. The first of these values is well represented by the experimental result of a group in Paris, while the second value is represented by the results (both theoretical and experimental) obtained by a group in Turin.

Therefore, the actual knowledge of the quadratic Stark effect is characterized by two major open questions. The first one concerns a long-standing discrepancy between experimental values and theoretical predictions of the tensor polarizability, while the second open question concerns the knowledge of the Stark shift of the clock transition, which is essential for the calibration of atomic clocks. This thesis work gives a relevant contribution to both the points mentioned above.

This work has been divided into two main parts:

- In Chapter 1 we give an introduction to this work. We present the main motivations for the experiment, we outline the main features of the doped helium matrix and we give a general overview of the role of the EDM in the framework of the search for new physics beyond the Standard Model. In Chapters 2 and 3 we present a novel theoretical investigation of the quadratic Stark effect. We apply perturbation theory up to third order, including the hyperfine interaction, and we show that we can reproduce the results of the "old" Sandars' theory. In a second step, we extend this theory in order to bridge the historical gap with experimental results. We show that the inclusion in the third order perturbation expansion of off-diagonal hyperfine matrix elements radically changes the value of the tensor polarizability thus leading to a full reconciliation of theory and experiment. Moreover, we highlight the existence of a sign error in Sandars' model. According to our theory the tensor polarizabilities of the hyperfine levels $F = 4$ and $F = 3$ have opposite signs, whereas in Sandars' theory $\alpha_2$ does not depend on $F$. It seems that this sign error has remained unnoticed in the literature for almost 40 years.

- Chapters 4, 5 and 6 are then dedicated to the experiment. We outline the main features of our apparatus used for high-resolution magnetic resonance experiments. The relevant technical improvements of the apparatus over the last two years led us to reach a sensitivity to resonance frequency shifts on the order of 1 Hz. We can apply fields up to about 50 kV/cm. We present the first measurement of the quadratic Stark effect in cesium atoms implanted in a solid helium matrix and we show that we obtain a result in very good agreement with previous measurements performed in more conventional environments. We also show results which prove unambiguously that the signs of the tensor polarizabilities predicted by our model are correct. In Chapter 7 we present our conclusions concerning the feasibility of an EDM experiment on paramagnetic atoms embedded in solid helium matrices, and we briefly sum up the main results of this work.

# Abstract

Questa tesi descrive lo studio dell'interazione Stark nello stato fondamentale di atomi di cesio intrappolati in una matrice di elio solido. La motivazione alla base del nostro interesse per gli effetti di un campo elettrico negli atomi alcalini impiantati in elio solido è connessa all'obiettivo originale delle nostre attività sperimentali, ovvero la misura di un momento di dipolo elettrico atomico permanente (EDM). L'esistenza di un EDM viola simultaneamente le simmetrie discrete di inversione temporale (T) e di parità (P). La ricerca di un EDM atomico é pertanto di notevole interesse scientifico in quanto proverebbe l'esistenza di un nuovo tipo di fisica oltre il Modello Standard ed aprirebbe le porte ad una migliore conoscenza delle interazioni fondamentali tra particelle elementari. All'inizio degli anni '90, venne suggerita l'idea che una matrice di elio drogata con atomi paramagnetici fosse un ambiente ideale per la misura di un EDM. Gli atomi di cesio isolati in una matrice di elio, nella fase isotropica detta *body centered cubic* (bcc), risiedono in cavità simili a bolle, che presentano una forma sferica quando gli atomi stessi si trovano in uno stato a simmetria sferica, quale lo stato fondamentale $6S_{1/2}$. Il cristallo di elio riveste quindi il ruolo di una struttura diamagnetica e perfettamente isotropica nella quale gli atomi possono essere intrappolati ed osservati per tempi molto lunghi. La tecnica nota come *optical pumping* permette di ottenere un elevato grado di polarizzazione degli spin atomici nello stato fondamentale. A causa dell'assenza di interazione con i campi elettrici e magnetici del cristallo di He, tale stato di polarizzazione puo' essere mantenuto per un tempo eccezionalmente lungo ($\approx 1$ s), garantendo un'alta risoluzione negli esperimenti di risonanza magnetica. Inoltre, il voltaggio di breakdown elettrico nell'elio superfluido e solido (maggiore di 100 kV/cm) rende la matrice di elio un ambiente ideale per esperimenti con campi elettrici.

Quando il campione atomico è esposto ad un campo elettrico esterno, l'esistenza di un EDM si manifesta come uno shift dei livelli energetici *lineare* nell'intensità del campo applicato. L'interazione di un atomo con un campo elettrico esterno, ovvero l'interazione Stark, produce anche effetti che non violano le simmetrie P e T, e che dipendono *quadraticamente* dall'intensità del campo. Sebbene questi effetti quadratici siano estremamente deboli, essi superano di diversi ordini di grandezza qualsiasi effetto lineare dovuto ad un EDM ed appaiono quindi come un background sistematico che necessita di una precisa caratterizzazione. Lo studio dell'effetto Stark quadratico ha pero' rivelato degli aspetti inattesi che ci hanno fornito un'ulteriore forte motivazione ad approfondire l'investigazione di questo campo di ricerca.

L'effetto Stark quadratico nello stato fondamentale degli atomi alcalini, trattato nel contesto della teoria delle perturbazioni, puo' essere caratterizzato tramite la polarizzabilità tensoriale $\alpha_2$, che appare solo come un debolissimo effetto di terzo ordine quando l'interazione iperfine viene inclusa nella perturbazione. Questo effetto tensoriale *proibito* è sette ordini di grandezza piu' debole dell'interazione Stark di secondo ordine. Il primo modello teorico dell'effetto Stark nello stato $nS_{1/2}$ degli atomi alcalini venne pubblicato nel 1968 da Sandars. Successivamente, il lavoro di Sandars è stato considerato il principale riferimento per la teoria dell'effetto Stark nello stato fondamentale degli alcalini. La polarizzabilità tensoriale del cesio è stata misurata negli anni '60 e, circa 40 anni piu' tardi, in un esperimento condotto dal nostro gruppo a Fribourg. Tutti questi esperimenti si basano sulla misura dello shift delle transizioni magnetiche tra livelli Zeeman, indotto da un campo elettrico esterno. Sebbene i risultati sperimentali siano in ottimo accordo tra loro, essi mostrano una notevole discrepanza rispetto al valore teorico dedotto dal modello di Sandars. E' stato inoltre dimostrato che tale disaccordo sussiste nel caso di tutti gli

atomi alcalini.

L'interazione Stark di terzo ordine produce anche uno shift della frequenza di transizione iperfine $| 6S_{1/2}F = 4, M = 0 > \leftrightarrow | 6S_{1/2}F = 3, M = 0 >$ (la frequenza di riferimento negli orologi atomici). Questo effetto (effetto Stark statico) è di particolare interesse per la comunità scientifica a causa della sua stretta connessione con il blackbody shift (effetto Stark dinamico) della cosiddetta clock transition frequency. Una precisa conoscenza di questo effetto è di grande importanza per la definizione dell'unità di tempo. Al momento, la comunità degli orologi atomici è impegnata in un vivissimo dibattito dovuto all'esistenza di valori contraddittori dello Stark shift della frequenza di transizione iperfine. Il primo di questi valori è rappresentato dal risultato sperimentale di un gruppo a Parigi, mentre il secondo valore è rappresentato dai risultati, teorico e sperimentale, ottenuti da un gruppo di Torino.

La conoscenza attuale dell'effetto Stark è quindi caratterizzata da due principali questioni aperte. La prima riguarda la discrepanza storica tra valori sperimentali e teorici della polarizzabilità tensoriale, mentre la seconda riguarda la conoscenza dello Stark shift della transizione iperfine, essenziale per una corretta calibrazione degli orologi atomici. Questa tesi fornisce un contributo rilevante ad entrambi i punti appena descritti.

Possiamo dividere questo lavoro in due parti principali:

- Il capitolo 1 è un'introduzione generale volta essenzialmente a chiarire le principali motivazioni alla base delle nostre attività sperimentali e teoriche. L'introduzione fornisce inoltre una descrizione delle piu' importanti caratteristiche della matrice di elio solido drogata con atomi alcalini, e una visione generale del ruolo dell'EDM nel contesto della ricerca di una nuova frontiera della fisica oltre il Modello Standard. Nei capitoli 2 e 3 presentiamo un nuovo modello teorico dell'effetto Stark quadratico. Applicando la teoria delle perturbazioni fino al terzo ordine ed includendo l'interazione iperfine, otteniamo i risultati della "vecchia" teoria di Sandars. In un secondo tempo estendiamo il nostro modello e dimostriamo che, includendo gli elementi di matrice non-diagonali dell'interazione iperfine nello sviluppo della perturbazione al terzo ordine, il valore della polarizzabilità tensoriale cambia radicalmente. Questo risultato comporta una completa riconciliazione tra teoria ed esperimenti. Inoltre, evidenziamo l'esistenza di un errore di segno nel modello di Sandars. Secondo il nostro modello le polarizzabilità tensoriali dei livelli iperfini F=4 e F=3 hanno segni opposti, mentre nel modello di Sandars $\alpha_2$ non dipende da F. Sembra che questo errore non sia mai stato rilevato in quasi 40 anni.

- I capitoli 4, 5 e 6 sono dedicati alle nostre attività sperimentali. Descriviamo innanzitutto le principali caratteristiche del nostro apparato per risonanza magnetica ad alta risoluzione. I progressi tecnici degli utlimi due anni ci hanno portato a raggiungere una sensitivity allo shift della frequenza di risonanza di circa 1 Hz, e ci hanno permesso di applicare campi elettrici fino a 50 kV/cm. Presentiamo quindi i nostri piu' importanti risultati: la prima misura dell'effetto Stark quadratico in atomi di cesio in una matrice di elio solido, in ottimo accordo con i risultati ottenuti in altri esperimenti condotti in ambienti piu' convenzionali, e una prova sperimentale che i segni delle polarizzabilità tensoriali predetti dal nostro modello sono corretti. Nel capitolo 7 concludiamo con alcune importanti osservazioni concernenti la realizzabilità di un esperimento per misurare un EDM in atomi paramagnetici intrappolati in matrici di elio solido, e riassumiamo brevemente i principali risultati conseguiti nel corso di questo lavoro di tesi.

# Contents

# Chapter 1

# Introduction

## 1.1 Historical overview and original motivation of the experiment

The CPT theorem is one of the most basic laws of modern physics. In simple words, it states that the "laws of physics", or more precisely a broad class of Lorentz invariant quantum field theories, are invariant with respect to the combined discrete symmetry operations $\mathbf{C}$ (charge conjugation), $\mathbf{P}$ (parity, i.e., mirror symmetry) and $\mathbf{T}$ (time reversal). On the other hand, there is no reason for these symmetries to be conserved individually and a violation of any one of them must be compensated by the violation of at least one of the others. This guarantees the validity of the CPT theorem.

Violations of parity were observed in 1957 in three independent experiments [1–3] in weak decays of $^{60}$Co nuclei, pions and muons. Today the violation of the discrete symmetry $\mathbf{P}$ is a very well understood phenomenon in the frame of the so-called Standard Model. Several atomic physics experiments in the 1980's have further provided experimental evidence for parity violation in atoms and have yielded quantitative results which are all fully compatible with the predictions of the Standard Model.

The question of the violation of $\mathbf{T}$, or equivalently the violation of the combined symmetry $\mathbf{CP}$, is much less well understood. In 1964 the violation of the combined symmetry $\mathbf{CP}$ was observed in the decay of the $K^0$-meson [4] and more recently also in the decay of the $B^0$-meson [5]. The only direct observation of a T-violating process was observed in the decay of neutral kaons in 1998 [6]. At present no other evidence for $\mathbf{CP/T}$ violation has been reported in literature despite an enormous experimental effort to unveil such effects in different systems ranging from elementary particles over atoms to molecules. Thus, the invariance of physical systems with respect to the reversal of the arrow of time remains a mysterious field which presents still nowadays a great challenge to experimentalists as well as theoreticians.

An extremely interesting way to search for $\mathbf{T}$-violating phenomena consists in searching for coexisting permanent magnetic and permanent electric dipole moments in elementary particles. If electrons had a permanent electric dipole moment (EDM) this would be transferred to atoms through an internal enhancement mechanism which turns out to be particularly strong in heavy paramagnetic species [7] [1]. The existence of a permanent electronic EDM

---

[1]Heavy polar molecules offer an even greater sensitivity to the electron EDM than heavy atoms and are thus very good candidates for EDM experiments. At present, Hudson et al. [8] are performing EDM

violates simultaneously the symmetry operations of parity and time reversal.

However the size of the electron EDM predicted by the Standard Model is extremely small and definitely beyond the sensitivity of feasible experiments. On the other hand it is generally admitted that, despite its enormous success in explaining many physical phenomena, the Standard Model is incomplete in some parts. Several alternative models (Multi-Higgs models, SUSY, Left-right symmetric models) predict a much larger electron EDM which does not seem to be so desperately far from present experimental sensitivities. The predictions of these novel models thus open new exciting doors towards a completely new and unexplored world. Today the search for a permanent EDM of the electron (in atoms or molecules) or a permanent EDM of the neutron is recognized as one of the most promising searches for new physics beyond the Standard Model.

In 1991 S.Kanorski and A.Weis proposed the use of matrix-isolated paramagnetic atoms in superfluid helium to perform a highly sensitive EDM experiment in which the He matrix plays the role of a trap in which atoms can be stored and studied for long time intervals. The main idea was that the diamagnetic character and the isotropy of the host matrix would guarantee long spin relaxation times of the implanted atoms and thus very narrow magnetic resonance lines. These properties together with a very large electric break-down voltage ($> 100 \, kV/cm$) were the main reasons why condensed helium was thought to be an ideal environment for a sensitive atomic EDM experiment [9–11].

In the following years the first optical spectroscopy experiments with Ba, Au and Cu atoms implanted in HeII were carried out by the group of A.Weis in collaboration with T.W.Hänsch at the Max Planck Institute for Quantum Optics (MPQ) in Garching, Germany [9] . The implantation of atoms was achieved by means of laser ablation and the detection by their laser-induced fluorescence. One of the main achievements of these first activities is related to the optical properties of Ba in superfluid helium which were quantitatively explained in the frame of the so-called *bubble model* [12]. Magnetic resonance experiments on alkali atoms in superfluid He were successfully performed by the Japanese group of T.Yabuzaki [13] but very broad resonance lines (linewidth on the order of $10^5$ Hz) were observed. In 1993 experiments were thus extended to solid $^4He$ by A.Weis and S.Kanorski. Solid He occupies a special position within the noble gas matrices since it is the only element in nature which does not solidify even at $T = 0 \, K$ unless a pressure in excess of 25 bar is applied. The reason for this unique behavior is twofold: the de Broglie wavelength of He is very large due to its low mass and the interatomic He-He interactions are very weak due to the small polarizability. The zero-point vibrations of He atoms are comparable to the interatomic separation and the atomic wavefunctions strongly overlap. Therefore pressurized He solidifies as a so-called *quantum crystal.*

Ba and Cs atoms were the first atomic species implanted in a solid He matrix by means of the same ablation technique [14, 15] applied in the liquid phase. In the following years the study of the optical properties of the implanted atoms allowed the extension of the bubble model to the solid matrix [16], optical pumping of Cs atoms in the bcc phase of solid $^4He$ was observed with very long longitudinal electronic spin relaxation times of $\approx 1 \, sec$ [17–19] and magnetic resonance lines of less than 20 Hz were obtained [20] in optical-r.f. magnetic resonance experiments. All those results were extremely encouraging steps on the way towards an EDM experiment. In view of that final goal the last 10 years were devoted

experiments on YbF molecules.

mainly to the study of the effects of the He crystal on the embedded atoms [19, 21–24] and to the optimization of the set-up for high resolution magnetic resonance experiments with large electric fields [24–26].

However, it was soon realized that beside the far-reaching goal of a possible EDM experiment, the helium matrix doped with foreign atoms is such a complex and unique system that it constitutes a research field for its own [2]. Among the most recent relevant results obtained during the investigation of the physical properties of He-matrix-isolated Cs atoms we mention the observation and theoretical study of multi-photon processes in the ground state of Cs [28, 29] and the investigation of the optical properties of the system, which recently led to the observation of exciplex molecules $Cs^*He_2$ and $Cs^*He_7$ [30, 31]. The importance of these latter results lies in the fact that while the former molecule had already been observed in other environments it was commonly believed that exciplexes $Cs^*He_n$ with $n > 2$ might not exist.

The present work is focused on the study of the interaction of solid He isolated alkali atoms with a static electric field. If atoms had a measurable permanent EDM it would appear in a double optical magnetic resonance experiment performed in a uniform external electric field as a very tiny shift of the magnetic resonance line *linear* in the applied field strength. On the other hand, the interaction of atoms with an external electric field, i.e., the Stark interaction, produces other effects beside the linear one due to the EDM (*if* there is a linear one). Although parity conservation implies that neither S nor P states can have a permanent electric dipole moment, the Stark interaction can mix their wavefunctions and the atom can acquire an *induced* electric dipole moment $< d_{ind} > \propto E$. In this case the energy of the atom in the external field is *quadratic* in the field strength. This contribution to the interaction atom-field, given by $H = -\mathbf{d}_{ind} \cdot \mathbf{E}$, conserves both P and T.

As we shall see in a later chapter, the quadratic Stark effect can be decomposed into an allowed scalar effect (proportional to the *scalar polarizability*) and a strongly suppressed tensor effect (proportional to the *tensor polarizability*) which is about *seven orders of magnitude* smaller than the former.

According to the present state of the art, the experimental upper limit on a permanent EDM in $^{133}$Cs is $d_{Cs} < 10^{-24} e \cdot cm$ [32]. This value leads to a linear P- and T-violating effect which is about *6 orders of magnitude* smaller than the P- and T-conserving quadratic one. The situation is summarized in Fig. 1.1.

In conclusion, the quadratic Stark effect would appear as a systematic background in a permanent atomic EDM measurement. As we shall see in more detail later, the basic idea of an EDM magnetic resonance experiment consists in measuring the shifts of the resonance line under the reversal of the orientation of the electric field ($\Delta\nu(\pm E)$). The linear effect would then appear as a tiny shift superposed to a large quadratic background. The characterization of this background is thus essential for an EDM experiment. This is the original basic motivation that has triggered the experimental and theoretical investigation reported here.

During the studies related to the EDM experiment, we realized important features of the quadratic Stark effect that go beyond its interest for a possible future EDM measurement:

---

[2]This field is closely related to experiments performed on doped He clusters, pursued in several laboratories worldwide. For more details one can read the review paper by Toennies et al. [27].

**Stark interaction:**      $H_{Stark} = -d \cdot E$

| ALLOWED SCALAR EFFECT | FORBIDDEN TENSOR EFFECT | EDM LINEAR EFFECT |
| $\propto \alpha_0(F) E^2$ | $\propto \alpha_2(F) E^2$ | $\propto d_0\, E$ |
| **1** | **$10^{-7}$** | **$< 10^{-13}$** |
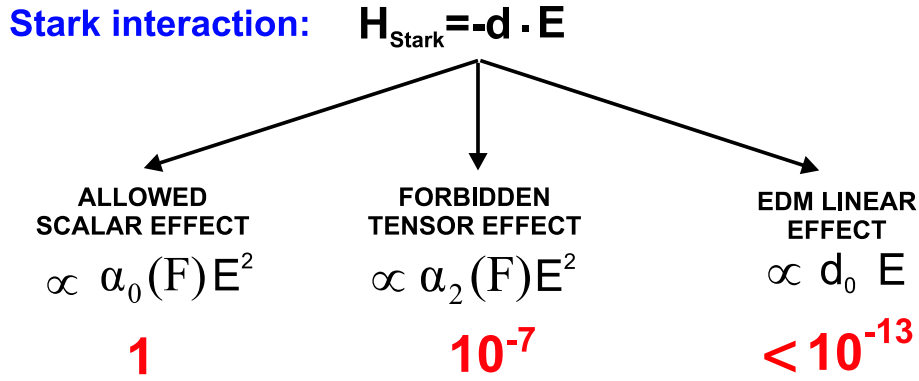
Figure 1.1: The energy associated with the interaction of an alkali atom with an external static electric field has three distinct contributions. The interaction mixes a small quantity of anti-symmetric P states into the symmetric S states thus inducing an electric dipole moment, responsible for an allowed scalar and a forbidden tensor effect (first two terms from the left). The parameters $\alpha_0$ and $\alpha_2$ are the so called scalar and tensor polarizabilities respectively and will be discussed in detail in a following chapter. We notice that both the effects of the induced dipole moment are quadratic in the applied field. On the other hand, if the atom has a permanent EDM then its interaction with the electric field will lead to an effect linear in the field itself (third term). In the bottom line of this sketch we report the relative orders of magnitude of the three contributions for a field of 10 kV/cm.

- the incompleteness of the theoretical models developed in the 1960's,

- a large gap between experimental measurements of the forbidden tensor polarizability and the theoretical predictions,

- the existence of an open debate concerning the quadratic Stark shift of the hyperfine clock transition in Cs with contradicting experimental results and an unsatisfactory theory.

In the present work we have produced significant novel contributions to the three points mentioned above.

In parallel to the theoretical efforts over the past 4 years we also deeply modified our experimental set-up with the main goal of measuring for the first time the quadratic Stark effect in the ground state of Cs atoms embedded in solid $^4He$. A few years ago at the University of Bonn and later in Fribourg some experiments aiming at measuring the Stark effect in solid He were carried out by our group without success [25]. Several technical improvements with respect to the original electric-field set-up were made. The pressure cell in which the He crystal is grown was modified to enable the application of much higher electric fields ($\approx 50$ kV/cm) and the general sensitivity of the apparatus was appreciably improved with respect to the first unsuccessful measurements. These efforts led to the first quantitative measurement of the quadratic Stark effect in the ground state of cesium atoms implanted in solid He.

This experimental result is of crucial importance in the frame of a comparison between the theoretical model that we present in this work and the historical model developed in the 1960's by Sandars [33]. According to this latter model the tensor polarizability of

the ground state does not depend on the quantum number F, whereas our novel model predicts a sign difference between the tensor polarizabilities of the levels F=4 and F=3. This disagreement can now be ruled out on the basis of our experimental results.

## 1.2 Cesium atoms in solid helium

In the most general sense, matrix isolation spectroscopy comprises a range of experimental techniques in which guest atoms, molecules or radicals are trapped in rigid host materials. The basic idea is that the embedded atomic species under investigation are spatially confined in the host matrix and thus prevented from diffusing and interacting/recombining with other particles. Of course this enables very long interaction times with applied static and/or dynamic fields, which is an essential prerequisite for high resolution spectroscopy experiments.

The idea of performing spectroscopy of atoms embedded in heavy rare gas matrices (Ne, Ar, Kr, Xe) goes back to Pimentel in 1954 [34]. Although the experimental advances described in this first paper were rather poor due to the relatively high temperature limit achievable in laboratories at that time [3], the idea was born and its power beyond some preliminary technical difficulties was immediately appreciated. Today rare-gas-matrix isolation is a well established technique which provides the advantage of trapping guest species in an inert environment [35, 36]. These features together with the transparency of noble gas matrices throughout the IR-visible-UV spectrum are the main reasons for the large success of rare-gas-matrix isolation in the framework of optical spectroscopy.

The use of matrix isolated atoms to search for EDMs was proposed only at the end of the eighties [37]. Unfortunately in heavy noble gas matrices the powerful optical methods of preparation (i.e., spin polarization of the atomic sample by optical pumping) and detection of magnetic resonance cannot be applied since the spin polarization of the implanted atoms is quickly destroyed by the strong interaction with crystal fields. For this reason in 1991 S.Kanorski, from the Lebedev Physical Institute of Moscow, and A.Weis from the Max Planck Institute for Quantum Optics in Garching, Germany, suggested the use of atoms immersed in superfluid $^4He$ and in 1993 the use of atoms embedded in a solid He matrix. Although helium has the disadvantages of being solid only if pressurized even at very low temperatures (our typical experimental conditions are T=1.5 K and P> 27 bars) and of having a very low heat of vaporization, condensed helium also has some unique properties that make the helium matrix an ideal environment to isolate foreign atomic species and perform high resolution magnetic resonance experiments. Helium is the only rare gas matrix in which spin polarization can be efficiently created by optical pumping and whose diamagnetic character enables very long spin relaxation times.

In the next sections we give a short overview of the main properties of condensed helium and we present our motivations for the use of such an exotic and unusual environment for our experiments. Although superfluid helium has been widely studied and is nowadays used in a number of different fields, our team at the University of Fribourg is, to our knowledge, the only one in the world involved in the investigation of doped solid $^4He$ crystals.

---

[3]In Pimentel's laboratory the lowest temperature was 66 K, which is cold enough to create Xe matrices, but too warm for solidifying Ne, Ar and Kr.

### 1.2.1 Solid $^4$He

The phase diagram of condensed $^4$He shown in Fig 1.2 can be divided into three distinct regions. At atmospheric pressure $^4$He becomes liquid at a temperature of $T = 4.21\,K$ and forms the so-called normal liquid (HeI-phase). If the temperature is further decreased $^4$He becomes superfluid (HeII-phase) at the critical temperature $T_c$. At saturated vapor pressure (svp) the fluid-superfluid phase transition takes place at $T_c = 2.177\,K$. The two fluid phases are separated by the so-called $\lambda-$line which shifts to lower temperatures with increasing pressures as shown in the phase-diagram.

Helium has the unique property to be the only natural substance which stays liquid down to the absolute zero under its vapor pressure. The solid region can be reached only by applying a pressure $P > 25$ bar. Under this condition, $^4$He crystallizes in three different structures depending on T and P [38]. The (uniaxial) hexagonal close-packed (hcp) structure is shown in Fig. 1.3.b while the (isotropic) body-centered cubic (bcc) structure is shown in Fig. 1.3.a. Above 1000 bar and 15 K $^4$He solidifies giving rise to a face-centered cubic (fcc) structure. It is well known that all other rare gas matrices condense only in close-packed structures (i.e., fcc) since those configurations enable the maximum number of atoms to be confined in a given volume. The bcc [4] structure that characterizes the helium phase diagram at low pressures is thus another extremely special property of helium among all solid rare matrices.

The exceptional behavior of helium in its superfluid and solid phases can be understood as a manifestation of macroscopic quantum properties. It is well known that the physical properties of liquid helium below the critical temperature $T_c$ can be understood only in the frame of a fully quantum mechanical model. It was predicted by Einstein in 1925 that an ideal gas of bosons, i.e., particles with integer spin (He has neither an electronic nor a nuclear angular momentum), would undergo a phase transition when the thermal de Broglie wavelength

$$\lambda_{dB} = \sqrt{\frac{h^2}{2\pi m k T}} \tag{1.1}$$

associated with the momentum distribution at the temperature T becomes larger than the mean distance between the particles. In this case the wavefunctions overlap and the particles condensate in the same lowest energy state. This process is well-known under the name of Bose-Einstein condensation (BEC) and it is the phenomenon that explains the superfluidity of helium.

The particular properties of solid helium can be understood on the basis of similar arguments. The interaction between neighboring He atoms is of the van der Waals type and can be described in first approximation by the combination of an attractive induced dipole-dipole part and a Pauli-type repulsive term. Due to the closed s-shell and the very small polarizability [5] characteristic of He atoms, the repulsive Pauli interaction dominates and the weak dipole-dipole interaction leads to an attractive potential well depth of only $\approx 7$ K at an internuclear separation of $\approx 2.96$ Å as shown in Fig. 1.4. We use the semi-empirical

---

[4]The bcc phase was only discovered in 1961 by observing a discontinuity in the velocity of sound at the phase boundary to the hcp region [41].

[5]The polarizability $\alpha_{He} = 1.34 a_0^3$, where $a_0$ is the Bohr radius, is the smallest known in nature.
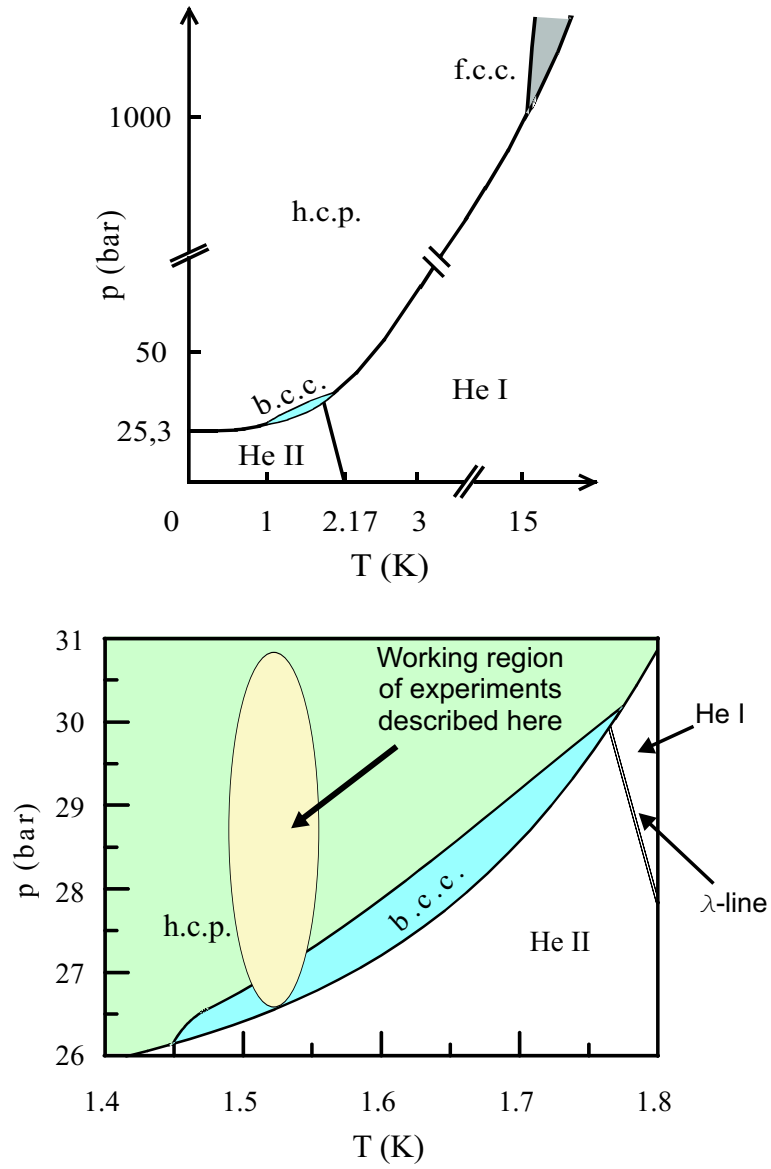
Figure 1.2: $^4$He phase diagram. The bottom diagram represents the p-T region relevant for our experiment.
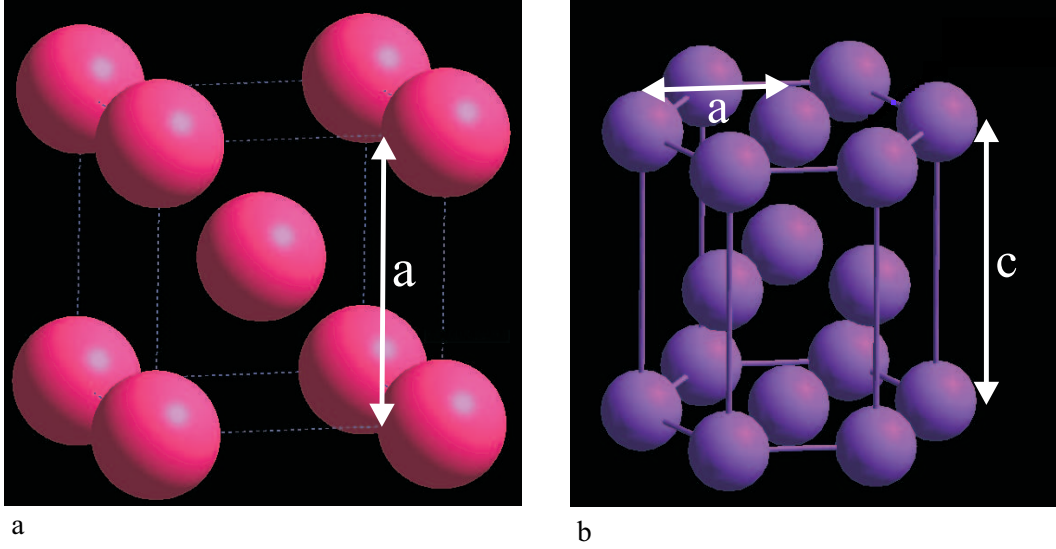
Figure 1.3: **a**) Primitive cell of the bcc structure. The lattice constant is a=4.12 Å at T=1.7 K and p=28.4 bar [39]. **b**) Primitive cell of the hcp structure. The lattice constants are a=3.67 Å and c=6.01 Å at T=1 K and p=26 bar [39, 40].

He-He pair potential given by Aziz [42] and Kilic [43].

The Heisenberg uncertainty principle $\Delta x \Delta p \sim \hbar$ leads to the following estimation of the zero-point kinetic energy

$$\Delta E_{kin} = \frac{\Delta p^2}{2M_r} \approx \frac{\hbar^2}{2M_r \Delta x^2} \,, \tag{1.2}$$

where $M_r$ is a reduced mass that we assume equal to two nucleon masses. The existence of a He-He bound state and thus of a solid phase requires the atoms to be localized in fixed positions in the lattice structure. It is not trivial to define to which extent this localization is required but for the sake of this discussion we can assume that the position of a given atom must be defined within 10% of the lattice spacing [44]. Now, from Fig. 1.4 we can infer an equilibrium interatomic distance of $\approx 3$ Å which means that the position of each atom must be defined to within 0.3 Å. Thus if we set $\Delta x = 0.3$ Å in Eq. 1.2 we obtain a zero-point kinetic energy $\Delta E_{kin}$ of 34 K. This energy is much larger than the attractive potential well. As a consequence helium stays liquid even at T=0 K at atmospheric pressure and the solid phase can be produced only under high pressure [6].

The large kinetic energy discussed above also explains the formation of a bcc instead of a fcc lattice structure. The zero-point vibrations of the atoms provide a source of internal pressure which forces the crystal to expand beyond the configuration that maximize the number of atoms in a given volume in order to minimize its total energy.

Due to their very low mass He atoms have a very large thermal de Broglie wavelength. From Eq. 1.1 at T=1.6 K we obtain $\lambda_{DB} \approx 7$ Å. Helium atoms are thus strongly delo-

---

[6]One should note that $H_2$ solidifies at T=14 K at atmospheric pressure despite its low molecular mass. This is a consequence of the large intermolecular potential which shows an attractive potential well of $\approx 100$ K.
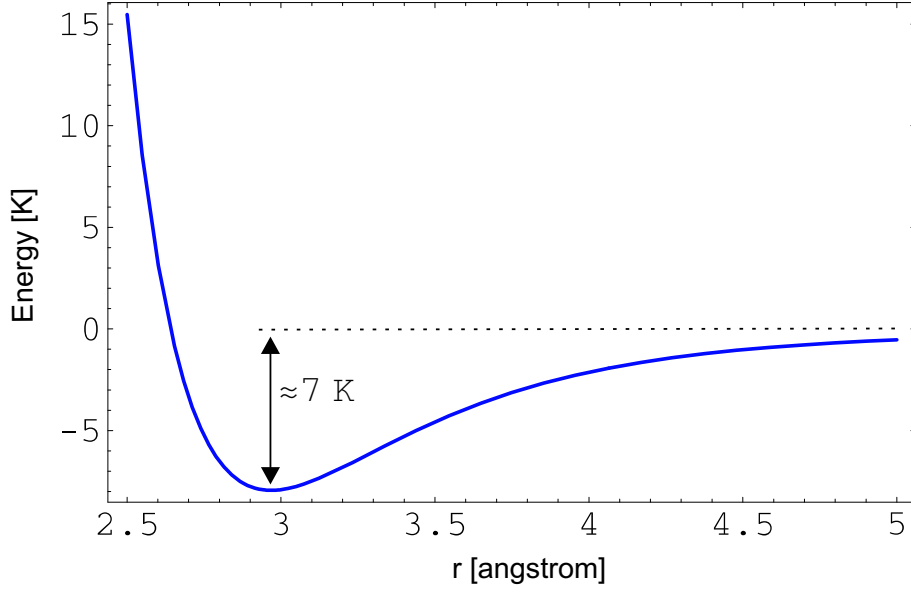
Figure 1.4: He-He pair potential given by Aziz [42] and Kilic [43]. The attractive potential well has a depth of $\approx 7$ K.

calized and when the solid is created under pressure the atomic wavefunctions exhibit a large mutual overlap giving the crystal a macroscopic quantum nature. Quantum solids are very soft and extremely compressible. These properties distinguish helium crystals from all other rare gas matrices and play an important role in the formation of the so-called *atomic bubbles*, discussed in Section 1.2.3.

### 1.2.2 Optical properties of solid $^4$He

Helium is transparent from the UV to the IR-region of the spectrum. The transition from the $1^1S_0$ ground state to the first excited state $2^1P_1$ of a free helium atom occurs in the VUV-region at $\lambda = 58.4nm$. This is of course an essential condition for the optical and magnetic resonance spectroscopy of embedded alkali-metal impurities.

The refraction index can be defined via the Clausius-Mosotti equation

$$n = \sqrt{\epsilon} = \sqrt{\frac{3 + 8\pi\alpha/V_m}{3 - 4\pi\alpha/V_m}}, \tag{1.3}$$

where $\alpha = 1.34a_0^3$ is the polarizability, $a_0$ is the Bohr radius and $V_m$ is the molar volume. For solid helium with a molar volume $V_m = 21$ cm$^3$ (corresponding to a density $\rho = 3 \cdot 10^{22}$ cm$^{-3}$) one has $n = 1.036$.

The fluid-solid phase transition is characterized by a density increase of 10% which corresponds to an increase of the index of refraction by 3%. Therefore the solidification process, as well as the hcp-bcc transition, can be easily observed by eye.

Although we performed all our measurements in the isotropic bcc phase, it is worth remarking that the anisotropy of the hcp phase produces optical birefringence. At $V_m = 21$ cm$^3$ the difference between the ordinary and extraordinary refractive indices is $\Delta n = 2.6 \cdot 10^{-6}$. Of course this should be kept into account when performing polarization-sensitive optical spectroscopy in the hcp phase.
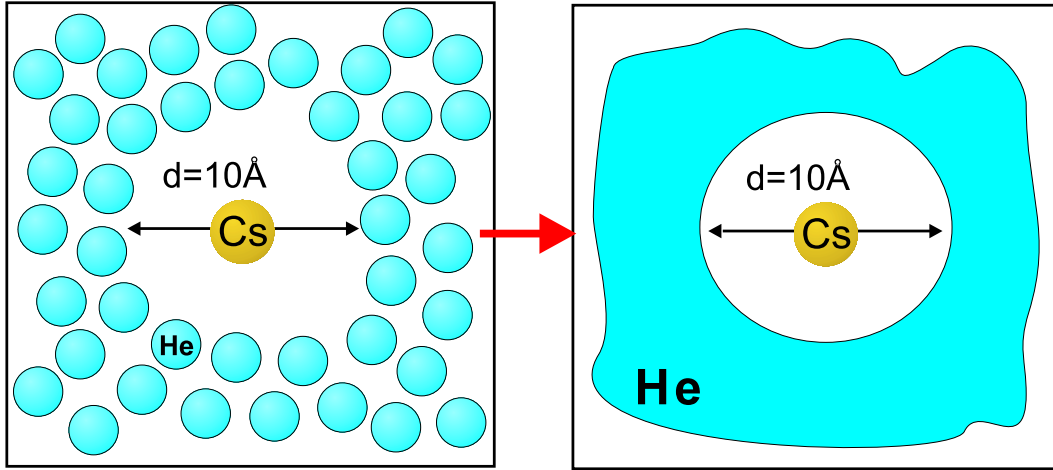
Figure 1.5: An illustration of an atomic bubble. **Left**: As explained in the text, the Pauli repulsive interaction between helium atoms and the alkali valence electron repels the He atoms from the location of the defect thus leading to the formation of a bubble shaped cavity. **Right**: The large zero-point oscillations of the He atoms produce a strong overlap of their wavefunctions and the matrix can be described as an isotropic continuous medium.

### 1.2.3 The bubble model

Rare gas matrix isolation has been used since the 1950's to trap atomic and molecular species in transparent and chemically neutral environments. In the traditional technique, using heavy rare gas matrices, guest atoms are condensed on a cold substrate simultaneously with the rare gas. Although this is a well-established and very efficient technique, it cannot be applied to helium, since the solid matrix cannot be formed via a simple cooling process. The use of a laser ablation technique to implant foreign atoms into a solid He matrix was first demonstrated with Ba and Cs in 1994 [14, 15] by Kanorski, Weis and collaborators at the Max-Planck-Institute for Quantum Optics.

The details of the implantation into solid helium will be addressed in a later chapter dedicated to our experimental set-up and techniques. Here we present a short overview of the so-called *atomic bubble model* that was first successfully applied to describe free electrons in superfluid helium [45–47] and which was later extended to atomic impurities in solid helium matrices. Of course we will focus our interest on alkali-metal impurities. A complete treatment of the bubble model can be found in [48].

The softness of the helium matrix, its high compressibility, the strong delocalization of helium atoms and the large overlap of their wavefunctions make the solid helium matrix qualitatively very similar to the environment encountered by foreign species in the superfluid phase. Therefore the modeling of the solid crystal as a continuous medium turns out to be extremely suitable for the description of the formation, the size and the symmetry of the trapping sites formed by the implanted atoms.

The impurity atom strongly perturbs the structure of the soft crystal in its near vicinity. The interaction of the valence electron of an implanted alkali atom with the closed S-shell electronic configuration of the surrounding helium atoms is characterized by a strong re-

(2) bubble relaxation

6P $_{1/2}$

Cs

He

$10^{-12}$ s

6P $_{1/2}$

life time: $10^{-8}$ s

(1) excitation: $10^{-13}$ s

(3) emission: $10^{-13}$ s

R $_0$

6S $_{1/2}$

$10^{-12}$ s

6S $_{1/2}$

(4) bubble relaxation
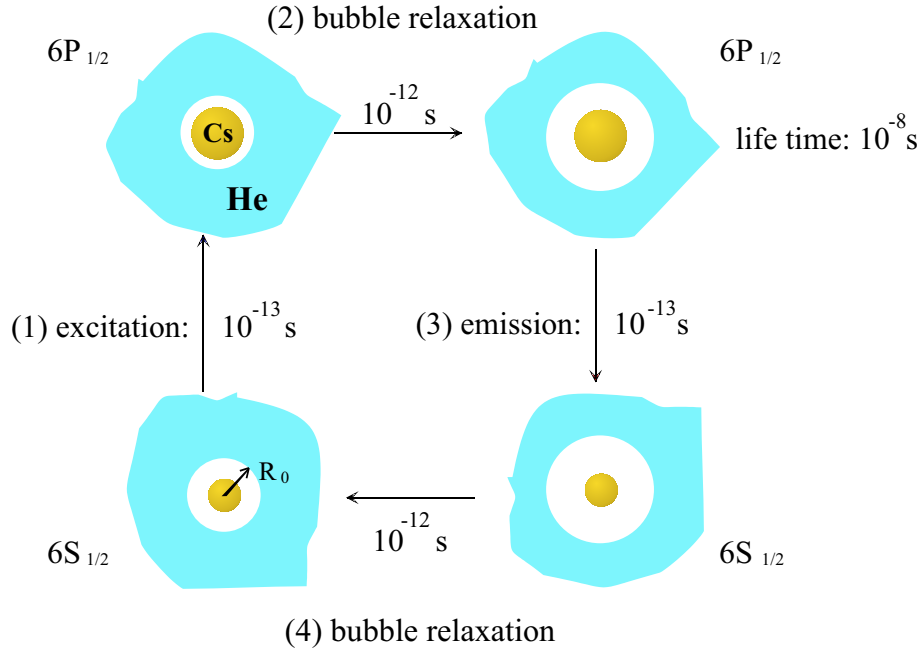
Figure 1.6: Schematic representation of the bubble evolution during the absorption-emission cycle.

pulsive potential due to the Pauli principle and a weak van der Waals attractive potential. The repulsion expels He atoms from the location of the atomic defect and leads to the formation of a bubble-shaped cavity with a radius of $\approx 5$ Å, as shown in Fig. 1.5.

The situation is radically different from all other heavy rare gas matrices which are not quantum solids. In this case the guest atom is mainly trapped in interstitial or substitutional sites produced by removing one or a few host atoms from their locations in the lattice structure. In the helium matrix the weak He-He binding energy is easily overcome by the repulsive perturbation due to the atomic impurity and the geometry of the trapping site is mainly determined by the alkali-He interaction. Therefore the shape of the bubble reflects the symmetry of the electronic wavefunction of the implanted atoms while the size of the bubble is determined by the balance between the Pauli repulsion on one side and the bubble surface tension and pressure-volume work required for the bubble creation on the other side.

In the isotropic bcc phase the shape of the bubble is determined only by the symmetry of the electronic wavefunction of the impurity. The $6S_{1/2}$ and $6P_{1/2}$ states of Cs atoms have a spherically symmetric electronic wavefunction because of their electronic angular momentum of J=1/2, and they are thus trapped in spherical bubbles. In hcp the situation is different because the anisotropy of the crystal compressibility tensor affects the shape of the trapping site by producing a small quadrupolar deformation (5 %) of the bubble [23].

The main properties of the optical spectra of Cs atoms implanted in solid helium can be qualitatively and quantitatively explained in the frame of the bubble model, at least for the D1 ($\mid 6S_{1/2} > \rightarrow \mid 6P_{1/2} >$) optical transition ($\lambda_{D1} = 894$ nm for free Cs atoms). For instance, in Fig. 1.6 one can follow the time evolution of the bubble during the absorption

and emission of resonance radiation.

(1) The atom is initially in its ground state $6S_{1/2}$, from where it is excited to $6P_{1/2}$. According to the Franck-Condon principle the shape of the cavity does not change during the excitation process although the $6P_{1/2}$ wavefunction occupies a larger volume than the ground state. This is the origin of the blue shift of the D1 excitation line ($\lambda_{D1} = 894$ nm for free Cs atoms) observed in solid helium ($\lambda_{D1}$=852 nm in solid helium). (2) The bubble size relaxes on a time scale of picoseconds. (3) The spontaneous emission takes place in a bubble that again does not change its shape during the transition process. The larger radius of the cavity leads to a much weaker disturbance of the atomic transition and thus the emission line turns out to be only slightly blue-shifted ($\lambda_{D1}$=888 nm). (4) Finally the bubble relaxes to its original shape.

All absorption and emission lines are broadened by the interaction with the surrounding environment and their positions and shapes depends of course on the pressure of the helium bulk.

The excitation and emission spectra of the D2 line are definitely more complicated since the state $6P_{3/2}$ does not have a spherical symmetry but an apple-like shape characterized by a nodal axis along which helium atoms can be attracted by the Cs core. This binding force leads to the formation of Cs*He$_n$ exciplexes. The formation process of these complexes is beyond the subject of this work and is fully described in [30, 31].

For more details about optical spectra, their interpretation in the frame of the bubble model and their pressure dependence we refer to [24, 49].

## 1.2.4 Spin physics in solid helium

Although the preparation of an optical or magneto-optical spectroscopy experiment in solid helium is not trivial because of the extreme experimental conditions of low temperature and high pressure, the choice of this unusual environment for an EDM experiment is based on some relevant advantages mainly related to the special quantum nature of helium crystals.

We summarize the most prominent features here:

- Solid rare gas matrices are transparent and chemically inert. Implanted atoms are isolated and trapped in a medium that strongly restricts their motion. This provides rather long interaction times with static, optical and radio-frequency fields.

- Solid helium is, unlike all other rare gas matrices, an extremely soft and thus highly compressible medium. Since the He-He interaction is much weaker than the interaction between helium atoms and the atomic impurity, implanted atoms create their own trapping sites by repelling the surrounding He atoms via the Pauli principle. The shape of the cavities where the atomic defects reside, i.e., the atomic bubbles, is almost entirely determined by the electronic configuration of the guest atom.

- $^4He$ is diamagnetic, i.e., it has neither electronic nor nuclear spin. This means that an atom with a spherical electronic charge distribution will reside in a spherical cavity in the center of which it will not experience any crystal field or field gradient. The

atomic spin is thus expected to be unperturbed in the bubble. As a consequence a high degree of spin polarization of the implanted atoms can be produced by optical pumping and the relaxation times of this spin polarization are exceptionally long. In 1995 Arndt and collaborators [18] measured the longitudinal and transverse spin relaxation times of Cs atoms in the bcc phase of solid helium with the results $T_1 \approx 1$ s and $T_2 \approx 250$ ms [7].

- Helium is characterized by a breakdown voltage in excess of 100 kV/cm. This property make solid helium specially suitable for experiments requiring large electric fields to be applied to the sample.

Helium is thus an ideal environment for high resolution spin physics and very sensitive magnetic resonance experiments.

## 1.3 An experiment searching for a permanent atomic electric dipole moment

The search for an atomic EDM is the original far-reaching goal of the experimental activities with helium-matrix-isolated alkali atoms that were started in the 1990's by A.Weis at the Max-Planck-Institute for Quantum Optics. The idea of an EDM experiment is also the basic motivation that triggered our theoretical and experimental investigation of the quadratic Stark effect, which is the subject of this work. Now, after more than ten years of efforts in the direction of an EDM experiment we have reached the conclusion that such an experiment will not be feasible. The search for an EDM in solid helium involves many challenging technological difficulties. Many of these were solved over the years, but, with increasing sensitivity, more, yet unsolved problems have emerged. Besides these technical problems our recent experimental results have also brought up some severe limitations of more fundamental nature. Nevertheless, since the idea of an EDM experiment has been over the past 10 years the main motivation behind all our research activities (and successes), we would like to dedicate this section to give a short and general review of the main theoretical and experimental concepts related to the electron EDM. We will discuss the reasons for which we abandon the road to the EDM experiment in a later chapter.

### 1.3.1 The P- and T-violating electric dipole moment

The orientation of a given quantum mechanical system such as a particle is entirely characterized by its total angular momentum $\vec{J}$. In the specific case of an isolated particle at rest, i.e., an electron for instance, the angular momentum $\vec{J}$ coincides with the spin $\vec{S}$. Any other vector property $\vec{V}$ associated with the particle must be either parallel or antiparallel to $\vec{S}$ [8].

The possibility of an independent orientation of $\vec{V}$ and $\vec{S}$ can be excluded on the basis of the Pauli principle as follows. If a particle had a vector property $\vec{V} \neq \vec{S}$ then a complete description of the quantum state of the particle would require, besides the specification of the projection $S_z$, an additional quantum number $V_z$ specifying the projection of $\vec{V}$ along the quantization axis. In other words, the S-independent vector property $\vec{V}$ would add an

---

[7] This is not the case in the anisotropic hcp phase where the spin relaxation can be three orders of magnitude faster than in the bcc phase.

[8] From a quantum mechanical point of view, here it is actually more correct to say that the matrix elements of the components $V_q$ must be proportional to the corresponding matrix elements of $S_q$.
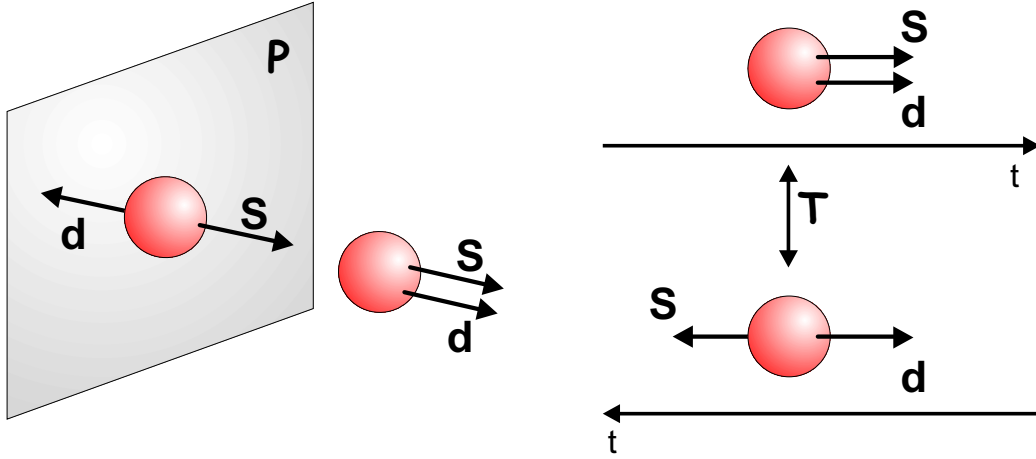
Figure 1.7: Coexistence of $\vec{d}$ and $\vec{S}$ and their behavior under the symmetry operations of mirror inversion P (left) and time reversal T (right).

additional degree of freedom to the particle thus allowing one to violate the Pauli principle. Alternatively, the (anti)parallelism of $\vec{V}$ and $\vec{S}$ can be seen in a more rigorous way as a consequence of the Wigner-Eckart theorem which implies the proportionality of the matrix elements of all the vector quantities associated with a given system.

The proportionality of the magnetic moment operator $\vec{\mu}$ and the angular momentum $\vec{S}$

$$\vec{\mu} = \frac{\mu}{\hbar}\vec{S},\tag{1.4}$$

where $\mu$ is the magnetic moment, is a well-known fact. If a particle has a permanent EDM $\vec{d}$, this would be also (anti)parallel to the angular momentum

$$\vec{d} = \frac{d}{\hbar}\vec{S}.\tag{1.5}$$

Let us consider now the behavior of $\vec{d}$ and $\vec{S}$ under the symmetry operations of mirror inversion (P) and time reversal (T), as sketched in Fig. 1.7. It is clear that the application of either P or T reverses the relative orientation of $\vec{d}$ and $\vec{S}$. This fact has important consequences. If we assume that P and T are good symmetries then the particle and its P- and T-symmetric counterpart have to occur with equal probabilities in nature, that is the EDM has to be both parallel and antiparallel to the angular momentum $\vec{S}$. Of course, this is possible only if $< \vec{d} >= 0$. If, on the other hand, $\vec{d}$ coexists with $\vec{\mu}$, or equivalently $\vec{d}$ with $\vec{S}$, this will be a manifestation of the violation of both the parity and the time reversal symmetry.

An alternative way to characterize the symmetry properties of the system consists in defining a rotationally invariant quantity (a scalar) such as $\xi = \vec{d}\cdot\vec{S}$ (or equivalently $\xi = \vec{d}\cdot\vec{\mu}$). It is easy to verify that $\xi$ is both a P- and T-pseudoscalar, i.e., that it changes sign under the considered symmetries: $P(\xi) = -\xi$ and $T(\xi) = -\xi$. The violation of P and T is thus equivalent to the existence of a non-vanishing pseudoscalar quantity $\xi$, i.e., a non-vanishing electric dipole moment $\vec{d}$, and vice-versa.

## 1.3.2 The electric dipole moment of the electron

The EDM of a finite sized particle, as the neutron, can be defined in a classical picture in the simple way

$$\vec{d} = \int \vec{r}\rho(\vec{r})d^3r \,, \tag{1.6}$$

where $\rho(\vec{r})$ is the charge density distribution of the particle. On the other hand, the EDM of a pointlike particle as the electron requires a definition which is not as straightforward as the one given above.

We will not go into the details of this definition since it goes beyond the main subject of this work. The EDM of the electron is discussed among others by Bernreuther and Suzuki in [50]. Following their approach, we just mention here that the electron EDM can be introduced by considering the relativistic coupling of the electron current

$$j_\mu = \bar{e}(p')\Gamma_\mu(q^2)e(p) \,, \tag{1.7}$$

where $q = p' - p$ and $\Gamma_\mu$ are Dirac matrices, to external electromagnetic fields described by the potential $A^\mu$ (Fig. 1.8).

The interaction given by

$$H = j_\mu A^\mu \,, \tag{1.8}$$

can be decomposed by considering the coupling of the electron 4-current to the 4-potential of the electromagnetic field and it can be expanded in terms of Lorentz invariant contributions with different rotational and P, T symmetries. The proportionality factors of these terms are called *form factors* $F_i(q^2)$. This expansion contains a term of the type $\vec{d}\cdot\vec{E}$ which describes the coupling of the electron to the external electric field. The proportionality factor of this electric term describes the EDM of the electron, which can be expressed in terms of the form factor $F_3$ as

$$d_e = \frac{F_3(0)}{2m} \,. \tag{1.9}$$

The Standard Model predicts the existence of a finite electron EDM but at the same time it puts the stringent limit

$$d_e < 10^{-37} \, e \cdot cm \,, \tag{1.10}$$

on the value of the EDM. This estimation is at least 10 orders of magnitude below the present best experimental sensitivity. Moreover, if one considers the evolution of the sensitivity of the experimental EDM search over the last 25 years one reaches the conclusion that there is little hope to measure such a small quantity in the coming decades.

On the other hand, the detection of an electron EDM in a near future will be an unambiguous signature of the existence of some new physics beyond the Standard Model. There are indeed some alternative models (without going into details we just mention Multi-Higgs models, supersymmetry (SUSY), left-right symmetric models), which may explain the baryon asymmetry of the universe [51]. These models predict an electron EDM much
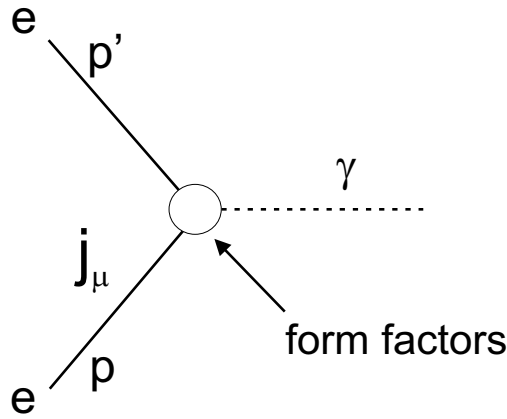
Figure 1.8: Coupling of electron to external electromagnetic fields.

closer to the present experimental sensitivity. The most optimistic predictions lie in the range

$$10^{-28} < d_e < 10^{-25}\, e \cdot cm\,. \tag{1.11}$$

Although these theoretical values have to be considered just as coarse estimations based on the assumption of some reasonable parameter values, they definitely present a new and extremely exciting perspective. For more details about the various alternative models and the electron EDM one can refer to the exhaustive reviews [50, 52, 53].

At present, the best experimental upper limit on the electron EDM is due to the experiment performed on $^{205}Tl$ in Berkeley by Regan et al [54]

$$d_e(exp) < 1.6 \times 10^{-27}\, e \cdot cm\,. \tag{1.12}$$

### 1.3.3 The electric dipole moment of atoms

The Schiff theorem [55] states that a neutral system of electrostatically bound particles with electric dipole moments cannot have a permanent EDM. This obviously implies that an eventual electronic dipole moment can not be transferred to the atom. However this statement is true only if one assumes that the constituent particles are:

- non-relativistic,

- point-like objects,

- without magnetic interactions.

These assumptions are not fulfilled in real atoms and in particular they turn out to be strongly violated in heavy (high Z) atoms. Therefore, as first pointed out by Sandars in 1965 [7], atoms can possess a permanent EDM which can be *several orders of magnitude* larger than the electronic EDM.

The transfer of the dipole moment of the electron to the atom arises as a consequence of the second order relativistic coupling of the electron spin to the electrostatic field of the

nucleus.

An easy and instructive way to describe such a mechanism is the following. The coupling of states with the same parity by the electronic dipole operator $\hat{d} = e\hat{r}$ is forbidden by the selection rule $\Delta L \neq 0$ [9]. Therefore atoms in a state of given parity should not have a permanent electric dipole moment

$$< d_{atom} > = < \psi \mid d \mid \psi > = 0 \,. \tag{1.13}$$

However, if states with different parity, S and P for instance, are coupled by the P-, T-violating mixing perturbation $V_{mix} = -d \cdot E_N$, where $E_N$ is the nuclear electric field, one can write the perturbed S-state as

$$\widetilde{\mid s >} = \mid s > + \frac{< p \mid V_{mix} \mid s >}{\Delta E_{sp}} \mid p > \,, \tag{1.14}$$

where $\Delta E_{sp}$ is the energy difference between the mixed states. The atom can thus acquire an electric dipole moment

$$< d_{atom} > = \widetilde{< s \mid} d \widetilde{\mid s >} = 2 \frac{< s \mid V_{mix} \mid p > < p \mid d \mid s >}{\Delta E_{sp}} \,, \tag{1.15}$$

where we have assumed that all the matrix elements are real. It is important to observe here that the interaction of the P- and T-violating atomic EDM with an external electric field

$$H = -d_{atom} \cdot E_{ext} \propto E_{ext} \,,$$

leads to an effect *linear* in the field $E_{ext}$.

The atomic EDM has to be distinguished from the atomic dipole moment *induced* by the mixing perturbation $V_{mix} = V_{Stark} = -d \cdot E_{ext}$ due to an *applied external* electric field $E_{ext}$. In this case the interaction energy H defined above is obviously *quadratic* in the electric field $E_{ext}$

$$H = -d_{ind} \cdot E_{ext} \propto E_{ext}^2 \,.$$

The transferring mechanism of the electron EDM to the atom leads to an *enhancement factor*

$$R = \frac{d_{atom}}{d_e} \propto \alpha^2 Z^3 \,, \tag{1.16}$$

where $\alpha$ is the fine structure constant and Z is the atomic number. Such a mechanism is particularly strong in heavy (i.e., high Z) paramagnetic (i.e., with unpaired spins) atoms [10]. This explains the choice of Cs for our experiment. The theoretical prediction for the enhancement factor in Cs is [32]

$$R_{Cs} = 120 \pm 20 \,. \tag{1.17}$$

---

[9]This selection rule is related to the odd symmetry of the electric dipole operator. Its origin will be cleared up in the next chapter.

[10]In diamagnetic atoms the enhancement factor from the second order contribution vanishes since the electronic spins are coupled. An enhancement factor arises only as a third order effect and it is thus smaller than in paramagnetic atoms.

For the sake of completeness we have to mention that besides the coupling of the electronic EDM to the nuclear field there are other possible mixing interactions $V_{mix}$ that can give rise to a net atomic EDM:

- P- and T-violating contributions to electron-nucleons interactions,

- coupling of EDMs of the nucleons to external fields,

- P- and T-violating nucleon-nucleon interactions.

However, since in heavy paramagnetic atoms these effects play a minor role if compared to the electron EDM contribution, we will not enter a detailed discussion.

We will rather conclude this section dedicated to the atomic EDM by briefly reviewing the basic principle of an experiment searching for it.

### 1.3.4 The basic idea of an EDM experiment

In general, as we already explained in a previous section, a P- and T-violating particle can be characterized by a pseudoscalar property related to the coexistence of magnetic and electric dipole moments, $\xi_{system} = \vec{\mu} \cdot \vec{d}$.

An apparatus to measure such a system property must be characterized by a corresponding P- and T-odd property, i.e., by a pseudoscalar apparatus helicity $\xi_{app}$ that changes sign both under P and T.

The pseudoscalar property of the measuring apparatus can be easily defined by considering the combination of magnetic and electric fields as $\xi_{app} = \vec{B} \cdot \vec{E}$. It is straightforward to verify that in fact this quantity changes sign under both the symmetry operations of interest. The inversion of the relative orientation of $\vec{B}$ and $\vec{E}$ corresponds to a simultaneous mirror and time reversal operation.

This is the basic principle on which most EDM experiments are based.

In our specific case, the interaction energy of an alkali atom in a state $\mid F, M_F >$ with an external magnetic field $\vec{B}$ and an electric field $\vec{E}$, that we assume both parallel to the quantization axis, is given by

$$\frac{E_{F,M_F}}{\hbar} = -\frac{1}{\hbar} < F, M_F \mid \vec{\mu} \cdot \vec{B} + \vec{d} \cdot \vec{E} \mid F, M_F >=$$
$$= \omega_L M_F + \mid d \mid E_z M_F + \alpha_{scal} E_z^2 + \alpha_{tens} E_z^2 \left[ 3M_F^2 - F(F+1) \right] , \quad (1.18)$$

where $\omega_L = \frac{g_F \mu_b}{\hbar} B_z$ is the Larmor frequency, $\alpha_{scal}$ and $\alpha_{tens}$ are proportional to the scalar and tensor polarizabilities respectively and we have used the important fact that the atomic EDM is parallel to the total angular momentum F, i.e., $\vec{d} = \mid d \mid \vec{F}$.

The first term in this last equation is obviously related to the interaction of the magnetic moment of the atom with the external magnetic field parameterized by the Larmor frequency $\omega_L$. The second term, *linear in the electric field* and proportional to the amplitude $\mid d \mid$, is due to the coupling of the permanent atomic EDM with the external field, while the last two terms, *quadratic in the electric field*, are associated with the effect of the induced atomic dipole moment.
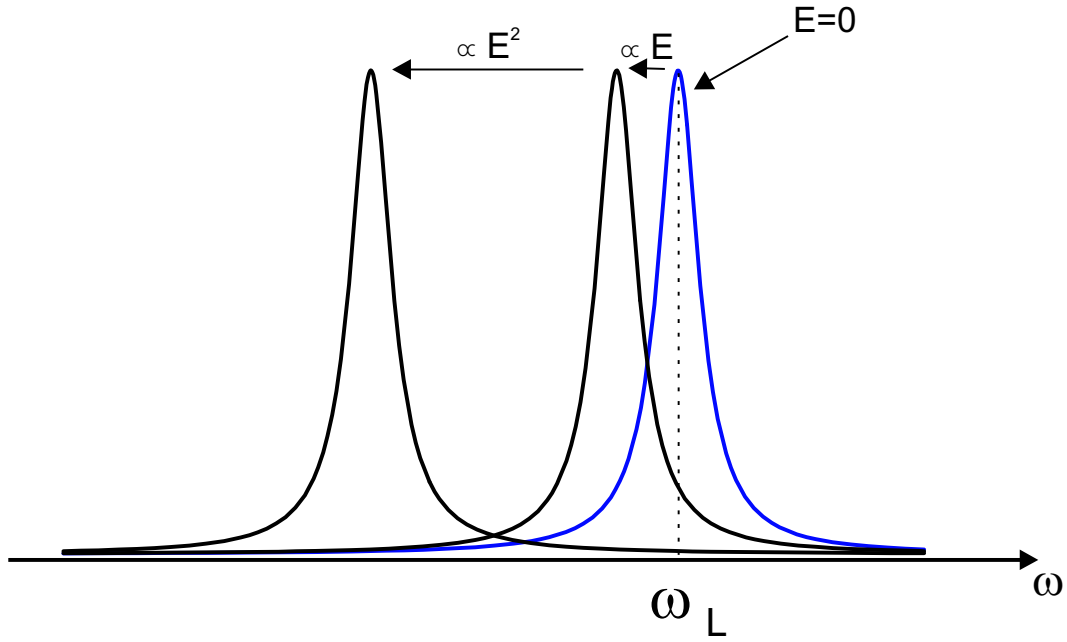
Figure 1.9: Magnetic resonance lines with and without electric field. When E=0 the resonance is centered at $\omega = \omega_L$. When E≠0, the resonance experiences two shifts: a linear one due to the atomic EDM and a quadratic one due to an induced electric dipole moment. Note that the shifts are not drawn to scale. The linear shift is expected to be 6 orders of magnitude smaller than the quadratic one in a field of 10 kV/cm.

Therefore in an optical-rf magnetic resonance experiment [11] in the ground state of Cs, the resonance line, centered at the Larmor frequency $\omega_L$ in absence of electric fields, will experience both linear and quadratic shifts when the external electric field is turned on, as shown schematically in Fig. 1.9. Therefore an experiment based on the relative change of the applied electric and magnetic field orientations would in principle enable these two effects to be separated from each other. The detection of a linear effect would be then the experimental signature of the atomic EDM.

As already mentioned in previous sections, the goal of an EDM experiment led us to start the theoretical and experimental study of the *quadratic* part of this interaction.

As we shall see in the next chapters, the investigation of the quadratic Stark effect turned out to be much more interesting and exciting than the simple characterization of a background.

---

[11] As described in detail in Chapter 4, the rf field oscillating at frequency $\omega_{rf}$ induces transitions between adjacent Zeeman levels $\mid F, M_F >$ and $\mid F, M_F \pm 1 >$.

# Chapter 2

# The tensor polarizability

## 2.1 Introduction

The shift and splitting of atomic energy levels due to the interaction of the atom with an external electric field is known as the Stark effect. The phenomenon was discovered in 1913 by the physicist Johannes Stark who was awarded the Nobel prize in 1919 for his discovery. Then in the following years the interest in the Zeeman effect greatly exceeded the interest in the Stark effect for several reasons. Experimentally, the generation of large electric fields presents more technical difficulties than the generation of magnetic fields. Furthermore, many interesting atomic states have a total electronic angular momentum $J = 1/2$ (the ground state of alkali atoms for instance) and will hence, as explained below, not exhibit a conventional Stark effect. The splitting of alkali ground-state levels occurs only as a strongly suppressed higher order effect, whose study suffers, in comparison to the Zeeman effect, of its extreme weakness. Theoretically, the study of the Stark effect requires non-trivial spectroscopic methods which make its investigation much more complex than the study of the Zeeman effect.

It was only 30 years after its discovery that the Stark interaction received a renewed attention. The quadratic Stark shift of the hyperfine transition in the ground state of $^{133}$Cs was measured by Haun and Zacharias in 1957 [56], while the splitting of Zeeman sub-levels was observed in 1964 by Lipworth and Sandars [57]. A few years later, in 1967 and 1968, Angel and Sandars published two theoretical papers which gave a detailed analysis of the quadratic Stark effect [33, 58] which is still considered the main reference point for the theory of the Stark interaction. In the following years, up to today, a part of the scientific community showed a deep interest in electric field effects on the ground-state hyperfine transition $\mid F = 4, M_F = 0 > \leftrightarrow \mid F = 3, M_F = 0 >$ because of its important role in the definition of the second by atomic-clocks [59–61]. On the other hand, the analytical and technical difficulties associated with electric field phenomena discouraged further efforts in the direction of a deeper understanding of the Stark effect on the magnetic sub-structure of the ground state of alkali atoms. After a few experimental results obtained in the 60s [62, 63], the only attempt to measure the quadratic Stark effect in the ground state of Cs was carried out in 2002 by the Fribourg Atomic Physics group in an atomic beam level crossing experiment [64] and more recently in a magnetic resonance experiment performed on Cs atoms embedded in a solid He matrix (addressed in this work). The lack of a deeper theoretical study of the Stark interaction in alkali ground states has left us with the heritage of a large discrepancy between theoretical predictions and experimental results.

In this chapter we will present a novel detailed theoretical investigation of the quadratic

Stark effect in the ground state of alkali atoms based on a perturbative approach, and we will show that we may now have a final answer to the problem of the large gap between theory and experiments.

### 2.1.1 The Stark interaction

The interaction of an atom with an external electric field $\mathbf{E}$ is described by the Stark hamiltonian

$$H_{Stark} = -\mathbf{d} \cdot \mathbf{E} \,, \tag{2.1}$$

where

$$\mathbf{d} = - \mid e \mid \cdot \mathbf{r} \,, \tag{2.2}$$

is the atomic electric dipole operator, $\mid e \mid$ the elementary charge and $\mathbf{r}$ the electronic position operator [1].

The basic properties of the hamiltonian (2.1) are determined by the symmetry of the position operator $\mathbf{r}$. An inversion of the spatial coordinates changes sign of the position operator: $\mathbf{r}(x,y,z) = -\mathbf{r}(-x,-y,-z)$. An operator with this symmetry property is said to have an *odd parity*.

Two generic atomic states described by the wave functions $\Psi_1$ and $\Psi_2$ can be coupled by the electric dipole operator $\mathbf{d}$ only if the matrix element taken between those two states is non-zero

$$\int_V \Psi_1^* e\mathbf{r}\Psi_2 dv \neq 0 \,. \tag{2.3}$$

Due to the odd parity of the operator $\mathbf{r}$, the condition expressed by Eq. 2.3 can be fulfilled only if the combined parity of the wave functions $\Psi_1$ and $\Psi_2$ is odd, i.e. if the two wave functions have opposite parity. Since the parity of a wave function $\Psi$ is defined by the orbital angular momentum quantum number $L$ according to

$$\Psi(x,y,z) = (-1)^L \Psi(-x,-y,-z) \,, \tag{2.4}$$

it follows that electric dipole interactions are governed by the selection rules [2]

$$\Delta L = \pm 1, \tag{2.5}$$
$$\Delta L \neq 0 \,.$$

Thus the Stark interaction cannot couple states with the same parity. This means that the interaction with an external electric field does not lead, in first order, to any change of the energy of atomic states [3]

---

[1] In this work we treat the particular case of alkali atoms. Therefore the operator $\mathbf{r}$ has to be understood as the position operator associated with the valence electron of the atom, which occupies a ground state $n^2S_{1/2}$.

[2] Actually the parity conservation condition expressed by Eq. 2.3 is satisfied by the more general requirement that $\Delta L$ is odd. The restriction $\Delta L = \pm 1$ is due to the vector character of the dipole interaction which requires $\Delta L = 0, \pm 1$.

[3] This statement is not true in the case of atomic hydrogen. The special nature of hydrogen is due to the special nature of the Coulomb potential, which does not remove the degeneracy of states with different parity, i.e. the degeneracy with respect to L. In hydrogen, states with different parity can have the same energy $E_n$, so that a state can be written as a linear combination: $\mid \Psi >= \sum_{L,M_L} \mid nLM_L >$. Therefore the matrix element (2.6) is non-zero and hydrogen levels exhibit a first order Stark shift linear in the electric field.

$$\Delta E_{Stark}^{(1)} = < \Psi \mid H_{Stark} \mid \Psi > = 0 \,. \tag{2.6}$$

The effects of the Stark interaction on the structure of atomic energy levels appear only as higher order contributions and are quadratic in the applied field. The perturbation of the energy of an atomic level $\mid nL_J, F, M_F >$ induced by a static electric field of amplitude $\mathbb{E}$ can then be parameterized as

$$\Delta E_{Stark} = -\frac{1}{2}\alpha(nL_J, F, M_F)\mathbb{E}^2 \,, \tag{2.7}$$

where $\alpha$ is called *the electric polarizability*.

We will show that the *second order* term of the perturbation expansion leads to different effects depending on the value of the total electronic angular momentum J of the perturbed state [33, 58]. In the case of alkali atoms the interaction with an external electric field leads to an overall shift of the ground state (J=1/2) but does not affect its hyperfine and magnetic sub-structure. The second order effect can thus be parameterized in terms of the *scalar polarizability* $\alpha_0^{(2)}$ as follows [4]

$$\Delta E_{Stark}^{(2)} = -\frac{1}{2}\alpha_0^{(2)}\mathbb{E}^2 \,. \tag{2.8}$$

In *third order*, the joint effect of the hyperfine and the Stark interactions leads to a very tiny splitting of the ground-state magnetic sub-levels together with a shift of the hyperfine transition. The electric polarizability has then two contributions and the third order perturbation can be written in the form

$$\Delta E_{Stark}^{(3)}(F, M_F) = -\frac{1}{2}\alpha_0^{(3)}(F)\mathbb{E}^2 - \frac{1}{2}\alpha_2^{(3)}(F)\frac{3M_F^2 - F(F+1)}{I(2I+1)}\mathbb{E}^2 \,. \tag{2.9}$$

In this last equation

- the first term is parameterized by $\alpha_0^{(3)}(F)$ which is an $F-$dependent third order contribution to the scalar polarizability. This term gives the main contribution to the Stark shift of the ground state hyperfine splitting.

- The second term is parameterized by the *forbidden tensor polarizability* $\alpha_2^{(3)}(F)$. Due to its dependence on the magnetic quantum number $M_F$, this term is responsible for the splitting of Zeeman sub-levels.

We will come back to this parametrization of the electric polarizability in greater detail later in this chapter. Here we just present an estimation of the orders of magnitude of the parameters involved in the interaction to give an idea of the smallness of the effect we are dealing with:

$$\frac{\alpha_0^{(3)}(F)}{\alpha_0^{(2)}} \approx 10^{-5} \quad \text{and} \quad \frac{\alpha_2^{(3)}(F)}{\alpha_0^{(2)}} \approx 10^{-7} \,. \tag{2.10}$$

The theoretical investigation of the quadratic Stark interaction will be developed in detail in the next sections of this chapter.

---

[4]The superscript (2) refers to the order of the perturbation while the subscript 0 refers to the rotational symmetry, scalar in this case.

### 2.1.2 The Stark hamiltonian in terms of irreducible tensor components

For the calculations that follow it is more convenient to write the operator $\mathbf{d}$ in terms of its spherical components

$$
d_\pm = \mp \frac{1}{\sqrt{2}} (d_x \pm i d_y) ,
$$
$$
d_0 = d_z , \tag{2.11}
$$

where $d_{i=x,y,z}$ are the usual cartesian components. The spherical components $d_q$ defined in Eq. 2.11 are proportional to the spherical harmonics $Y_{1,q}$ or equivalently to the renormalized spherical harmonics $C_q^k = \sqrt{\frac{4\pi}{2k+1}} Y_{k,q}$ with $k = 1, q = \pm 1, 0$, as shown in Appendix A. Therefore the operator $\mathbf{d}$ can be written in the form of an *irreducible spherical tensor* operator of rank 1 as

$$
\mathbf{d}^1 = \mid d \mid \cdot \mathbf{C}^1 , \tag{2.12}
$$

where the quantity $\mid d \mid$ *does not* depend on the angular variables of the system.

The advantage of the irreducible tensor formalism is that we can easily benefit from the intrinsic rotational symmetries of the problem. By applying the Wigner-Eckart theorem to the tensor operator $\mathbf{d}^1$ we can expand the matrix elements of its spherical components $d_q$ as follows

$$
< n_1 L_1 J_1 F_1 M_1 \mid d_q \mid n_2 L_2 J_2 F_2 M_2 > = (-1)^{F_1 - M_1} \begin{pmatrix} F_1 & 1 & F_2 \\ -M_1 & q & M_2 \end{pmatrix} < F_1 \parallel d \parallel F_2 > .
$$
$$
\tag{2.13}
$$

The *reduced matrix element* $< F_1 \parallel d \parallel F_2 >$ describes the purely dynamical part of the interaction and *does not* depend on the orientation dependent quantum numbers $M_1$, $M_2$ and q, while the geometrical properties of the system are fully described by the 3j-symbol. This property of the Wigner-Eckart theorem, i.e., the factorization of matrix elements into geometrical and dynamical factors, will be widely exploited in the present chapter.

More details about the irreducible tensor algebra are given in Appendix A. Here we just recall that reduced matrix elements can be simplified by decoupling the total angular momentum $\mathbf{F}$ into the electron and nuclear angular momenta, $\mathbf{J}$ and $\mathbf{I}$ respectively. Since the operator $\mathbf{d}$ acts only in the space of the electron variables, we can re-write Eq. 2.13 in terms of reduced matrix elements in the electron sub - space as follows

$$
< J_1 I F_1 M_1 \mid d_q \mid J_2 I F_2 M_2 > = (-1)^{F_1 + F_2 + J_1 + I + 1 - M_1} \sqrt{(2F_1 + 1)(2F_2 + 1)}
$$
$$
\times \begin{pmatrix} F_1 & 1 & F_2 \\ -M_1 & q & M_2 \end{pmatrix} \begin{Bmatrix} J_1 & I & F_1 \\ F_2 & 1 & J_2 \end{Bmatrix} < J_1 \parallel d \parallel J_2 > . \tag{2.14}
$$

The reduced matrix element in Eq. 2.14 can be further simplified by decoupling the total electronic angular momentum $\mathbf{J}$ into the orbital angular momentum and spin, $\mathbf{L}$ and $\mathbf{S}$

respectively. Eq. 2.13 can thus be written in its final form [5]

$$
\begin{aligned}
< n_1 L_1 J_1 F_1 M_1 \mid d_q \mid n_2 L_2 J_2 F_2 M_2 > = & (-1)^{F_1 + F_2 + J_1 + J_2 + L_{max} - M_1} \\
& \times \sqrt{(2F_1 + 1)(2F_2 + 1)} \sqrt{(2J_1 + 1)(2J_2 + 1)} \sqrt{L_{max}} \begin{pmatrix} F_1 & 1 & F_2 \\ -M_1 & q & M_2 \end{pmatrix} \\
& \begin{Bmatrix} J_1 & F_1 & I \\ F_2 & J_2 & 1 \end{Bmatrix} \begin{Bmatrix} L_1 & J_1 & S \\ J_2 & L_2 & 1 \end{Bmatrix} R_{n_1 L_1, n_2 L_2} \,, \quad (2.15)
\end{aligned}
$$

where $R_{n_1 L_1, n_2 L_2}$ is the *radial integral* between the states $\mid n_1 L_1 >$ and $\mid n_2 L_2 >$. More details are given in Appendices A and B.

A crucial point in our calculations is the detailed knowledge of the reduced dipole matrix elements $< J_1 \parallel er \parallel J_2 >$, or equivalently of the radial integrals $R_{n_1 L_1, n_2 L_2}$. In the literature there are both experimental and theoretical results [65–75] concerning the determination of these matrix elements. However, in our search for reliable values we found several inconsistencies concerning their signs. In our calculations we have to deal with matrix elements that are not squared and thus the knowledge of the phase of each element has a crucial importance. In order to overcome this problem we use a statistical Thomas-Fermi potential with corrections to include the spin-orbit interaction and core dipole and quadrupolar polarization to solve the Schrödinger equation and calculate analytical wave functions for the states $nS_{1/2}$, $nP_{1/2,3/2}$ and $nD_{3/2,5/2}$ of cesium with $n = 6$–18. These wave functions are then used to calculate all the relevant radial integrals. The signs of the matrix elements are then easily determined by evaluating numerically the 3j- and 6j-symbols that appear in Eq. 2.15. Our wave functions have been tested by reproducing a number of well-known atomic parameters (hyperfine and spin-orbit coupling constants, lifetimes) with very satisfactory results. At present we can make estimations of reduced dipole matrix elements which are in good agreement with the absolute values of the matrix elements reported in the literature and, more importantly, we can determine their signs. We will come back to this point later in this chapter.

The calculations of the Cs wave functions were mainly carried out by another Phd student of our group, A.Hofer, who will discuss his thesis in 2007. His work will contain all the details concerning our calculations of cesium wave functions. Here we just give an introduction in Appendix C.

The other important part of the Stark interaction is of course the applied electric field. A uniform field can be written in terms of cartesian coordinates in the laboratory frame as

$$
\mathbf{E} = \begin{pmatrix} E_x \\ E_y \\ E_z \end{pmatrix} = \mathbb{E} \begin{pmatrix} \sin\theta \cos\phi \\ \sin\theta \sin\phi \\ \cos\theta \end{pmatrix} \,, \quad (2.16)
$$

where $\mathbb{E}$ is the amplitude of the field and where we have introduced the polar and azimuthal angles, $\theta$ and $\phi$ respectively (see Fig. 2.1).

Throughout all this work we will assume that the amplitude $\mathbb{E}$ of the electric field is uniform over the small volume of the experiment and we will therefore consider $\mathbb{E}$ as a parameter that does not depend on spatial coordinates.

---

[5] The most general case requires and additional phase factor $(-1)^{I+S}$. For Cs, we have $(-1)^{I+S} = (-1)^{7/2+1/2} = 1$.
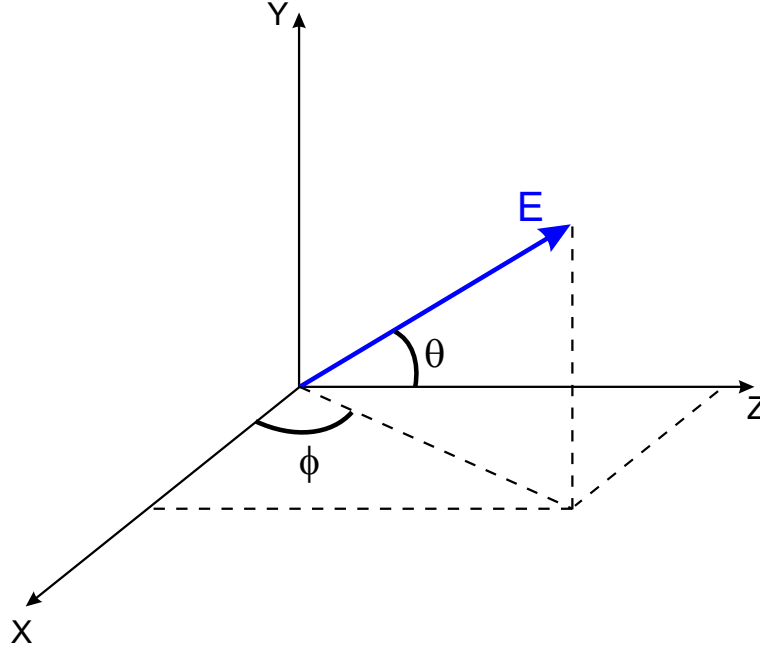
Figure 2.1: The polar and azimuthal angles $\theta$ and $\phi$

It is straightforward to introduce the spherical components of the field

$$E_\pm = \mp \frac{1}{\sqrt{2}}(E_x \pm iE_y)\,,$$
$$E_0 = E_z\,, \tag{2.17}$$

and to show that

$$E_\pm = \mp \frac{\mathbb{E}}{\sqrt{2}} \sin(\theta)e^{\pm i\phi}\,,$$
$$E_0 = \mathbb{E}\cos(\theta)\,. \tag{2.18}$$

The components of the electric field $\mathbf{E}$ written in the form (2.18) are again proportional to the three spherical harmonics $Y_{1,q}$ (or equivalently to the renormalized spherical harmonics $C_q^1$) and the vector $\mathbf{E}$ is thus written in the form of an *irreducible spherical tensor* of rank 1.

The Stark hamiltonian given by Eq. 2.1 can be written in terms of spherical components as

$$H_{Stark} = -\mathbf{d} \cdot \mathbf{E} = -\sum_{q=-1}^{1}(-1)^q d_q E_{-q} = e\sum_{q=-1}^{1}(-1)^q r_q E_{-q}\,. \tag{2.19}$$

With the hamiltonian expressed in terms of irreducible tensor operators it is straightforward to apply the Wigner-Eckart theorem and the angular momenta decoupling rules defined in Appendices A and B to calculate matrix elements of the Stark interaction. This will be done to a large extent in the frame of the perturbation theory that we will introduce in the next section.

## 2.2 The perturbation theory

In this section we give a short overview of the perturbation theory. We will consider stationary perturbations described by a hamiltonian that does not depend on time, and we will apply the method to the specific case of non-degenerate states. We recall the basic concepts of non-degenerate perturbation theory up to third order in its general form and briefly describe its application to the Stark interaction.

### 2.2.1 The method

Let us assume that the hamiltonian H of a physical system can be put in the form

$$H = H_0 + W \,, \tag{2.20}$$

where the eigenvalues and eigenvectors of $H_0$ (the *unperturbed hamiltonian*) are known

$$H_0 \mid \varphi_i >= E_i^0 \mid \varphi_i > \,, \tag{2.21}$$

and where $W \ll H_0$ (actually this inequality must hold for the matrix elements of the two operators). This last condition enables us to write $W = \epsilon \widetilde{W}$ where $\epsilon \ll 1$ is a dimensionless parameter. In Eq. 2.21 we have assumed that the eigenvalues $E_i^0$ are all non-degenerate.

One then calculates the solutions to the eigenvalue equation for the total hamiltonian

$$H \mid \Psi >= E \mid \Psi > \,. \tag{2.22}$$

We assume that the eigenvalues and eigenvectors of Eq. 2.22 can be expanded in power series in the following way

$$E = E_0 + \epsilon \widetilde{E}_1 + \epsilon^2 \widetilde{E}_2 + ... + \epsilon^q \widetilde{E}_q + ... = E_0 + E_1 + E_2 + ... + E_q + ... \,, \tag{2.23}$$

$$\mid \Psi >= \mid \Psi_0 > + \epsilon \mid \widetilde{\Psi}_1 > + ... + \epsilon^q \mid \widetilde{\Psi}_q > + ... = \mid \Psi_0 > + \mid \Psi_1 > + ... + \mid \Psi_q > + ... \,. \tag{2.24}$$

Now, if we substitute the expansions (2.23) and (2.24) into Eq. 2.22, with the definition (2.20), and we require this equation to be satisfied for any arbitrary small $\epsilon$ we obtain a system of equations, each corresponding to a given power of $\epsilon$. For the generic $q^{th}-$order term we obtain

$$(H_0 - E_0) \mid \widetilde{\Psi}_q > + (\widetilde{W} - \widetilde{E}_1) \mid \widetilde{\Psi}_{q-1} > - \widetilde{E}_2 \mid \widetilde{\Psi}_{q-2} > ... - \widetilde{E}_q \mid \widetilde{\Psi}_0 >= 0 \,, \tag{2.25}$$

with $q \geq 1$.

Let us consider now a given unperturbed eigenvalue $E_n^0$ and its corresponding eigenvector $\mid \varphi_n >$. We want to determine how they are perturbed by the interaction W.

A reasonable assumption is that the perturbed eigenvalue and eigenvector ($E$ and $\mid \Psi >$ respectively) coincide with the unperturbed ones ($E_n^0$ and $\mid \varphi_n >$) when the perturbation approaches zero (i.e., when $\epsilon \to 0$). Therefore in the definitions (2.23) and (2.24) we set $E_0 = E_n^0$ and $\mid \Psi_0 >= \mid \varphi_n >$ [6].

---

[6]This equality is not entirely true. Actually $\mid \Psi_0 >$ is proportional to $\mid \varphi_n >$ through a phase factor $e^{i\phi}$. For the sake of simplicity we assume here $\phi = 0$.

We will not go into more details since these calculations can be found in any text book on quantum mechanics (see for example [76]). Here it will be enough to recall that by projecting Eq. 2.25, with q=1, onto the unperturbed basis states $\{\mid \varphi_i >\}_{i=1,..,n,..}$ it is straightforward to calculate the *first order* correction to the energy

$$E_1 = <\varphi_n \mid W \mid \varphi_n>, \tag{2.26}$$

and to the eigenvector [7]

$$\mid \Psi_1 >= \sum_{p \neq n} \frac{<\varphi_p \mid W \mid \varphi_n>}{E_n^0 - E_p^0} \mid \varphi_p > . \tag{2.27}$$

By applying to Eq. 2.25 the same procedure (i.e., projections onto unperturbed basis states) with q=2,3 one can calculate the corrections to the energy to *second order*

$$E_2 = \sum_{p \neq n} \frac{\mid<\varphi_p \mid W \mid \varphi_n>\mid^2}{E_n^0 - E_p^0} , \tag{2.28}$$

and to *third order*

$$E_3 = \sum_{p_1 \neq n, p_2 \neq n} \frac{<\varphi_n \mid W \mid \varphi_{p_1}><\varphi_{p_1} \mid W \mid \varphi_{p_2}><\varphi_{p_2} \mid W \mid \varphi_n>}{(E_n^0 - E_{p_1}^0)(E_n^0 - E_{p_2}^0)} -$$
$$- \sum_{p \neq n} \frac{\mid<\varphi_p \mid W \mid \varphi_n>\mid^2 <\varphi_n \mid W \mid \varphi_n>}{(E_n^0 - E_p^0)^2} . \tag{2.29}$$

## 2.2.2 The perturbation theory approach to the Stark interaction

The crucial point for the investigation of the Stark effect is now the choice of the perturbing hamiltonian.

In the spherically symmetric ground state $\mid nS_{1/2} >$ of alkali atoms the Stark hamiltonian of the interaction with an external electric field does not affect the hyperfine and Zeeman sub-structures. Nevertheless, under the effect of electric fields a tiny splitting of the magnetic sub-levels of the ground state of $^{133}$Cs has unambiguously been measured in several experiments [57, 62–64], as well as a shift of the hyperfine transition frequency [56, 59–61]. As Lipworth and Sandars already pointed out in 1964 [57], the reason for this F and $M_F$ dependent shift is a strongly suppressed *forbidden tensor polarizability* that arises in third order when one includes the hyperfine interaction in the perturbation.

The hyperfine interaction operator $H_{hf}$ has three contributions.

- $H_{Fermi}$: the Fermi contact interaction for $nS_{1/2}$ states.

- $H_{d-d}$: the dipole-dipole interaction for the excited states $nL_j$ with $L > 0$.

- $H_Q$: the electric quadrupole interaction only for the excited states $nL_j$ with $L, j \geq 0$.

---

[7]In principle, this and the following sums have also to be extended over the continuum states. However, in the case of Cs, this contribution turns out to be negligible (see Section 2.3.3).
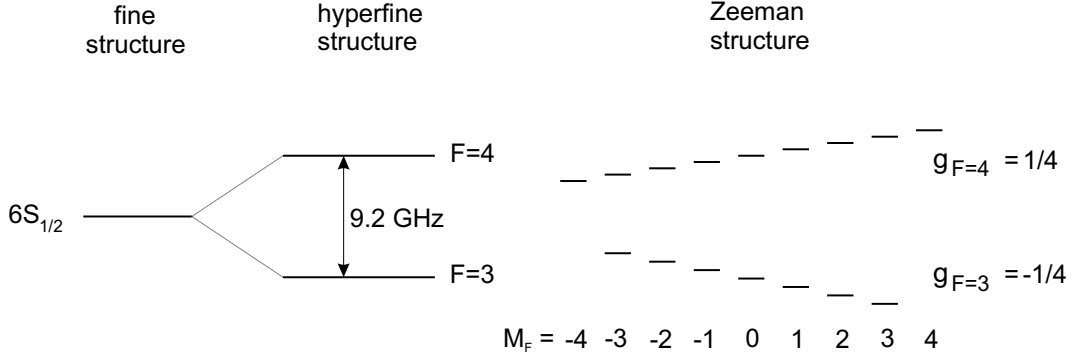
Figure 2.2: Energy scheme of the ground state of $^{133}$Cs with hyperfine structure (not to scale) and linear Zeeman effect in a small magnetic field (not to scale). Due to the different signs of the g-factors $g_{F=3}$ and $g_{F=4}$ the energy shifts of the Zeeman levels in the two hyperfine multiplets also have opposite signs. The gyromagnetic ratio in the ground state is approximately $g_F = g_{I \pm J} \approx \pm 3.50 \, kHz/\mu T$.

The Fermi contact interaction is governed by the selection rule $\Delta L = 0$, while the dipole-dipole and the quadrupole parts of the hyperfine interaction have selection rules $\Delta L = 0, \pm 2$. These selection rules will play a central role in the identification of off-diagonal hyperfine contributions to the third order Stark interaction (see Section 2.5).

In the presence of an external magnetic field (typically $\sim 5\mu T$ in our experiment) we have to include in the perturbation also the Zeeman interaction $H_Z = -\vec{\mu} \cdot \vec{B}$, where $\vec{\mu}$ is the magnetic moment operator of the atom. We assume a static magnetic field $\hat{B} = \hat{z}$.

Therefore we write the perturbation in presence of static magnetic and electric fields in the general form

$$W = H_{hf} + H_Z + H_{Stark} \,. \tag{2.30}$$

The unperturbed hamiltonian $H_0$ is the hamiltonian of the free atom with spin-orbit coupling.

## 2.3 The first and second order effects

We discuss here the first and second order contributions to atomic energy levels due to the perturbation defined by Eq. 2.30. Because of parity conservation, as explained in Section 2.1.1, alkali atoms do not exhibit a first order linear Stark effect. In second order the Stark interaction leads to a shift of the ground state quadratic in the electric field and to the definition of the scalar polarizability $\alpha_0^{(2)}$. We will describe this effect in the irreducible tensor formalism and we will make a numerical estimation of $\alpha_0^{(2)}$.

### 2.3.1 First order perturbation

The first order energy shift of a ground state level $\mid 6S_{1/2}, F, M_F >$ is given by

$$\Delta E_{F,M_F}^{(1)} = <6S_{1/2}, F, M_F \mid (H_{hf} + H_Z + H_{Stark}) \mid 6S_{1/2}, F, M_F >=$$

$$= \frac{1}{2} A_{6S_{1/2}}[F(F+1) - J(J+1) - I(I+1)] + \hbar\omega_L(F)M_F, \quad (2.31)$$

where $A_{6S_{1/2}}$ is the ground state hyperfine constant and $\omega_L = \frac{g_F \mu_B}{\hbar} B_z$ is the Larmor frequency. Since we are taking the matrix element between two states with the same parity (i.e., the same orbital angular momentum L), there is no contribution from $H_{Stark}$ because of the selection rule defined in Eq. 2.5.

The energy shift given by Eq. 2.31 is the usual solution to the Breit-Rabi problem in the low-(magnetic)-field limit (Zeeman regime), linear in the magnetic quantum number $M_F$. The ground state is split by the hyperfine interaction into the two hyperfine components $F = 3$ and $F = 4$ and the degeneracy of the magnetic sub-levels is removed by the magnetic field, as shown in Fig. 2.2.

### 2.3.2 Second order perturbation: the scalar polarizability in the irreducible spherical tensor formalism

The second order correction to the energy of ground state levels is given by Eq. 2.28. In this case the contributions to $\Delta E_{Stark}^{(2)}$ of the hyperfine and the Zeeman hamiltonians vanish and the second order perturbation turns out to be due entirely to the Stark interaction. We can thus write

$$\Delta E_{Stark}^{(2)}(F, M_F) = \sum_n \sum_{J=1/2}^{3/2} \sum_{f=|I-J|}^{I+J} \sum_{m=-f}^{f} \frac{|<nP_J, f, m_f \mid H_{Stark} \mid 6S_{1/2}, F, M_F >|^2}{\Delta E(6S_{1/2}, nP_J)},$$

$$(2.32)$$

where the sums are taken over all possible excited P-states and where $\Delta E(6S_{1/2}, nP_J)$ is the energy difference $E(6S_{1/2}) - E(nP_J)$ [8].

In principle Eq. 2.32 can be evaluated only by knowing the exact wave functions of both ground and excited P states and while this is rather straightforward in the case of the hydrogen atom it is obviously much more complicated in the case of a complex atom such as Cs. Nevertheless, by using the irreducible spherical tensor formalism extremely important information about the character of the interaction can be obtained without entering analytical calculations. Therefore we follow here the approach suggested by Angel and Sandars [58].

We define an *effective Stark operator* in the following way

$$H_{Stark}^{eff} = \mathbf{d} \cdot \mathbf{E} \cdot \lambda^{(2)} \cdot \mathbf{d} \cdot \mathbf{E}, \quad (2.33)$$

where the projection operator $\lambda^{(2)}$ is defined as

$$\lambda^{(2)} = \sum_{n,j,f,m_f} \frac{\mid nP_j, f, m_f ><nP_j, f, m_f \mid}{\Delta E(6S_{1/2}, nP_j)}. \quad (2.34)$$

With this notation the second order effect on a given state can be simply seen as the expectation value of the operator $H_{Stark}^{eff}$ in that state.

---

[8] It can be interesting to note here that the sign of this energy difference is always negative. This reflects the fact that the coupling of the ground state to excited P-states leads to a repulsive effect.

The next step consists in separating the part of $H_{Stark}^{eff}$ that depends on the electric field from the one which depends on the atom *and* the part that depends only on the amplitude of the field from the one which depends on its orientation. This can be done in the frame of the irreducible tensor formalism in two steps as follows.

- We define the components $\{\}_Q^K$ of two tensor operators of rank K in terms of Clebsch-Gordan coefficients in the following way

$$\{\mathbf{d}^1 \lambda^{(2)} \mathbf{d}^1\}_Q^K = \sum_{q,q'} < 11qq' \mid KQ > \mathbf{d}_q^1 \lambda^{(2)} \mathbf{d}_{q'}^1 \,, \tag{2.35}$$

$$\{\mathbf{EE}\}_Q^K = \sum_{q,q'} < 11qq' \mid KQ > \mathbf{E}_q^1 \mathbf{E}_{q'}^1 \,. \tag{2.36}$$

- We introduce the *rank-K multipole components* of the effective Stark operator

$$H_{Stark}^{(K)} = \{\mathbf{d}^1 \lambda^{(2)} \mathbf{d}^1\}^K \cdot \{\mathbf{EE}\}^K \,, \tag{2.37}$$

where the dot product between two tensors of rank K is defined by

$$T^K \cdot U^K = \sum_{Q=-K}^{K} (-1)^Q T_Q^K U_{-Q}^K \,, \tag{2.38}$$

and we expand the effective Stark interaction as the sum of a scalar and a tensor operator

$$H_{Stark}^{eff} = \sum_K (-1)^K H_{Stark}^{(K)} = H_{Stark}^{(0)} + H_{Stark}^{(2)} \,. \tag{2.39}$$

The vector component $H_{Stark}^{(1)}$ vanishes since $\{\mathbf{EE}\}_Q^1 = 0$ for any $Q = 0, \pm 1$.

The equivalence of Eq. 2.33 and Eq. 2.39 can be proved by expanding explicitly the calculations [9]. It is also straightforward to verify from Eq. 2.36 and Eq. 2.37 that the scalar Stark operator $H_{Stark}^{(0)}$ depends only on the modulus of the field because

$$\{\mathbf{EE}\}_0^0 \propto \mathbb{E}^2 \,, \tag{2.40}$$

while the tensor operator $H_{Stark}^{(2)}$ depends on its orientation because

$$\{\mathbf{EE}\}_0^2 \propto (3E_z^2 - \mathbb{E}^2) \,. \tag{2.41}$$

The second order Stark effect defined in Eq. 2.32 can be rewritten in the simple form

$$\Delta E_{Stark}^{(2)}(F, M_F) = < 6S_{1/2}, F, M_F \mid H_{Stark}^{(0)} + H_{Stark}^{(2)} \mid 6S_{1/2}, F, M > \,. \tag{2.42}$$

---

[9]Equivalently one could also consider the following instructive argument. In the simple case $\mathbf{E} \parallel \hat{z}$, one can write $H_{Stark}^{eff} \propto d_z^2 = \frac{1}{3} \left[ d^2 - \left( d^2 - 3d_z^2 \right) \right]$. The first term, $d^2$, has the rotational symmetry of a scalar operator ($T_0^{(0)}$), while the second term, $d^2 - 3d_z^2$, has the rotational symmetry of a tensor of rank 2 ($T_0^{(2)}$).

This matrix element can be reduced by applying the Wigner-Eckart theorem and, since the effective Stark operators act only in the space of the electron, one can also decouple the nuclear and electronic angular momenta, $\mathbf{I}$ and $\mathbf{J}$ respectively. For the tensor part of the interaction one finds

$$< 6S_{1/2}, F, M_F \mid H_{Stark}^{(2)} \mid 6S_{1/2}, F, M_F > \propto < J = 1/2 \parallel \{\mathbf{d}^1 \lambda^{(2)} \mathbf{d}^1\}^2 \parallel J = 1/2 >= 0 \,. \tag{2.43}$$

This is a general result: a tensor operator of rank 2 cannot couple two states with J=1/2, therefore states characterized by total electronic angular momentum J=1/2 *do not* exhibit a tensor Stark effect in second order.

Thus in the ground state of Cs (or equivalently of any alkali metal atom) the second order energy correction is entirely due to the scalar part of the interaction which depends only on the magnitude of the electric field and which can be parameterized as

$$\Delta E_{Stark}^{(2)} = -\frac{1}{2} \cdot \alpha_0^{(2)} \cdot \mathbb{E}^2 \,, \tag{2.44}$$

where $\alpha_0^{(2)}$ is the second order *scalar polarizability*. The energy shift given by Eq.2.44 does not depend on the quantum numbers F and $M_F$ and therefore it turns out to be only an overall shift of the ground state, while the hyperfine and the Zeeman sub-structures stay unchanged.

### 2.3.3 Second order perturbation: an estimation of the scalar polarizability

We can evaluate the scalar polarizability $\alpha_0^{(2)}$ by applying the Wigner-Eckart theorem to Eq. 2.32 and by decoupling $F$ into $J$ and $I$. We obtain

$$\Delta E_{Stark}^{(2)} = \sum_{n,j,f,m} \frac{|< nP_j, f, m \mid \sum_{q=0,\pm 1} d_q E_{-q} \mid 6S_{1/2}, F, M_F >|^2}{\Delta E(6S_{1/2}, nP_j)} =$$

$$= \sum_{n,j,f,m} \sum_q \mid E_{-q} \mid^2 \begin{pmatrix} f & 1 & F \\ -m & q & M_F \end{pmatrix}^2 \frac{|< nP_j, f \parallel er \parallel 6S_{1/2}, F >|^2}{\Delta E(6S_{1/2}, nP_j)} =$$

$$= \sum_{n,j,f,m} \sum_q \mid E_{-q} \mid^2 (2f+1)(2F+1) \begin{pmatrix} f & 1 & F \\ -m & q & M_F \end{pmatrix}^2 \begin{Bmatrix} j & I & f \\ F & 1 & 1/2 \end{Bmatrix}^2 \frac{|< nP_j \parallel er \parallel 6S_{1/2} >|^2}{\Delta E(6S_{1/2}, nP_j)} =$$

$$= \sum_n \frac{e^2}{6} \left( \frac{|< nP_{1/2} \parallel r \parallel 6S_{1/2} >|^2}{\Delta E(6S_{1/2}, nP_{1/2})} + \frac{|< nP_{3/2} \parallel r \parallel 6S_{1/2} >|^2}{\Delta E(6S_{1/2}, nP_{3/2})} \right) \mathbb{E}^2 \,. \tag{2.45}$$

As expected from the considerations based on the irreducible tensor analysis, the expression in Eq. 2.45 does not depend on the orientation of the electric field $\theta$ originally contained in $E_q$ nor on the quantum numbers $F$ and $M_F$ and represents thus only a scalar shift of the ground state. The scalar polarizability can be estimated now by comparing Eq. 2.45 to Eq. 2.44.

As pointed out by Zhou and Norcross [77] one has to add to this polarizability of the valence electron the dipole polarizability of the $Cs^+-$core, which is given by these authors as [10]

---

[10]In the literature the scalar polarizability is often expressed in atomic units $a_0^3$ as well as in $cm^3$.
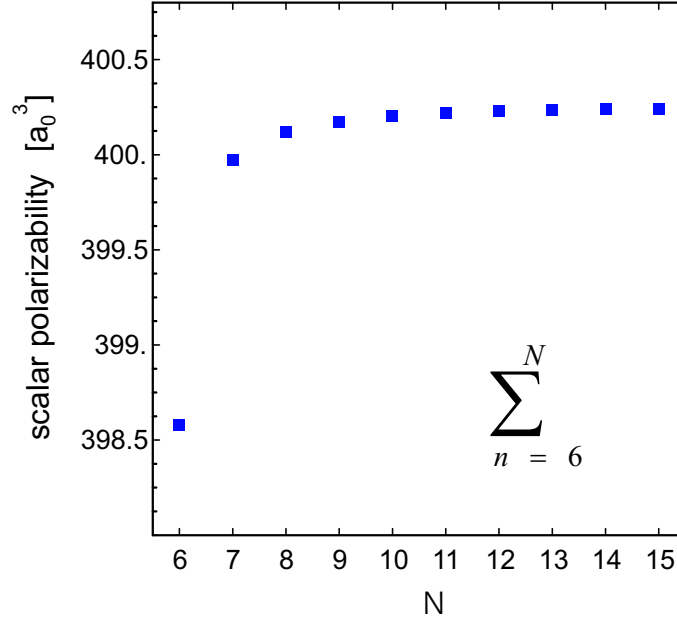
Figure 2.3: The second order scalar polarizability $\alpha_0^{(2)}$ in dependence of the number of excited nP states included in the perturbation sum. The effect of the $Cs^+$ core calculated in [77] is already included. The relative contribution of the $6P_{1/2,3/2}$ states amounts to about 96%, in very good agreement with the result of Derevianko et al. [80], while the contribution of $7P_{1/2,3/2}$ states is about 0.3%. The $nP_{1/2,3/2}$ states with $n = 8$–15 contribute only to 0.07%.

$$\alpha_{core} = 0.00389 \, \frac{Hz}{(V/cm)^2} = 15.6 \, a_0^3 \,, \tag{2.46}$$

with an uncertainty of less than 0.1%.

In Fig. 2.3 we report the contributions to the scalar polarizability of $nP_j$ states with n=6,...,15. In this calculation we have used the experimental values of the reduced electric dipole matrix elements between the ground state and the excited 6P and 7P states reported in [74] and [73] respectively (see Table 2.8). All the other reduced matrix elements are given by Fabry as oscillator-strengths in [78]. We will discuss reduced matrix elements in details later in this chapter. The energies of atomic states are taken from Moore [79]. By neglecting contributions [11] from states with $n > 15$ our numerical result for the second order scalar polarizability is

$$\alpha_0^{(2)} = 0.09961 \, \frac{Hz}{(V/cm)^2} = 400.3 \, a_0^3 \,. \tag{2.47}$$

The relative ground state Stark shift is plotted as a function of the applied electric field in Fig. 2.4. The scalar polarizability was calculated by Zhou and Norcross [77] in the frame

---

The conversion factors to "laboratory units" $\frac{Hz}{(V/cm)^2}$ are: $\alpha_0 \left[ \frac{Hz}{(V/cm)^2} \right] = 2.4883 \cdot 10^{-4} \cdot \alpha_0 \left[ a_0^3 \right] = 1.6792 \cdot 10^{21} \cdot \alpha_0 \left[ cm^3 \right]$.

[11] This approximation, which neglects the effect of the continuum states, can also be justified by the calculations of Derevianko et al. [80]. According to these authors the nP states with $n = 7,...,\infty$ and the continuum states give a contribution to the scalar polarizability which is only 0.5%.
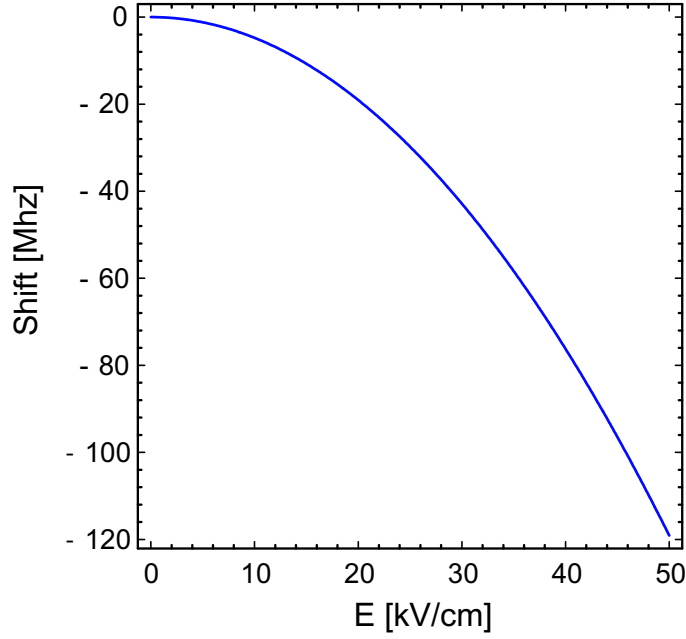
Figure 2.4: Frequency shift of the ground state due to second-order Stark interaction.

of a much more sophisticated and complex model based on the solution of the relativistic Dirac equation for a semi-empirical Thomas-Fermi potential including core perturbations by the valence electron. Their calculation yields the result

$$\alpha_0^{(2)} = 400.6 \; a_0^3 \, , \tag{2.48}$$

which is very close to what we obtain in our simple perturbation theory approach. A more recent theoretical result was reported by Derevianko and Porsev [80]

$$\alpha_0^{(2)} = 400.49(81) \; a_0^3 \, , \tag{2.49}$$

while the most recent experimental result is due to Amini and Gould [81]

$$\alpha_0^{(2)} = 401.0(6) \; a_0^3 \, . \tag{2.50}$$

We thus observe a very good global agreement between the result of our calculation of $\alpha_0^{(2)}$ and the theoretical and experimental values reported in the literature. However, the scalar second order polarizability of the alkali ground state is well understood at a level of $10^{-3}$ and therefore it is not of primary relevance for this work [12]. In the next sections of this chapter we will rather present novel calculations of third order effects which are $10^5$ and $10^7$ times smaller than the scalar Stark shift.

---

[12]The scalar polarizability $\alpha_0^{(2)}$ is actually relevant in our work only in the sense that under some simplifying assumptions the third order effect can be expressed in terms of the second order polarizability. This point will be addressed in detail later in this chapter.

## 2.4 Third order Stark effect

We discuss now the third order effect due to the perturbation $H_{hf} + H_Z + H_{Stark}$. This perturbation can be simplified by observing that with typical experimental magnetic fields of $\sim 5\mu T$ one obtains for the energy $\Delta E$ involved in the interaction

$$\Delta E_{Zeeman} \ll \Delta E_{hf} \,. \tag{2.51}$$

Since the matrix elements of $H_Z$ always appear as an additive contribution to the other terms, the Zeeman interaction will be omitted in all the following calculations.

We will introduce the third order scalar polarizability $\alpha_0^{(3)}$ and the tensor polarizability $\alpha_2^{(3)}$, and we will give a numerical estimation for both of these parameters. We will show the existence of a relevant gap between the theory and experimental results and we will also remark the existence of an important sign-difference between our theory and the result given by Sandars in 1967 [33].

### 2.4.1 General considerations based on the irreducible tensor formalism approach

In the frame of the irreducible tensor formalism we can obtain several important information about the main features of the third order effect without developing analytical calculations.

The third order perturbation of a ground state level $(F, M_F)$ is given by Eq. 2.29 which we rewrite here for convenience

$$\Delta E^{(3)} = \sum_{p_1 \neq n, p_2 \neq n} \frac{< \varphi_n \mid W \mid \varphi_{p_1} >< \varphi_{p_1} \mid W \mid \varphi_{p_2} >< \varphi_{p_2} \mid W \mid \varphi_n >}{(E_n^0 - E_{p_1}^0)(E_n^0 - E_{p_2}^0)} -$$
$$- \sum_{p \neq n} \frac{\mid < \varphi_p \mid W \mid \varphi_n >\mid^2 < \varphi_n \mid W \mid \varphi_n >}{(E_n^0 - E_p^0)^2} \,, \tag{2.52}$$

where

$$\mid \varphi_n > \rightarrow \mid 6S_{1/2}, F, M_F > \,,$$
$$W \rightarrow (H_{hf} + H_{Stark}) \,. \tag{2.53}$$

The perturbation $\Delta E^{(3)}$ is thus given by the sum of two terms. The second one is proportional to the (Fermi contact) hyperfine interaction in the ground state while the first one is proportional to the (magnetic dipole and electric quadrupole) hyperfine interaction in the excited P-states. In the following we will consider them separately.

#### 2.4.1.1 Second term of Eq 2.52

If we keep into account the selection rules associated with the two perturbing interactions, and we follow the same procedure described in Section 2.3.2 for the second order polarizability, we can write

$$- \sum_p \frac{|<\varphi_p \mid H_{Stark} \mid \varphi_n>|^2}{(E_n^0 - E_p^0)^2} <\varphi_n \mid H_{hf} \mid \varphi_n> =$$

$$- E_{hf}(F) \sum_p \frac{|<\varphi_p \mid H_{Stark} \mid \varphi_n>|^2}{(E_n^0 - E_p^0)^2} = -E_{hf}(F) <\varphi_n \mid H_{pert}^{eff} \mid \varphi_n>, \quad (2.54)$$

where the sum is taken over all excited $\mid nP_j, f, m >$ states. The *effective perturbation operator* is defined as

$$H_{pert}^{eff} = \mathbf{d} \cdot \mathbf{E} \cdot \lambda^{(3)} \cdot \mathbf{d} \cdot \mathbf{E}, \quad (2.55)$$

where

$$\lambda^{(3)} = \sum_p \frac{\mid \varphi_p ><\varphi_p \mid}{(E_n^0 - E_p^0)^2}. \quad (2.56)$$

It is important to observe that for any given unperturbed state $\mid \varphi_n >=\mid 6S_{1/2}, F, M_F >$ the matrix element $<\varphi_n \mid H_{hf} \mid \varphi_n>$ in Eq. 2.54 is just a (F-dependent) scalar corresponding to the hyperfine interaction energy $E_{hf}(S_{1/2}, F)$ and therefore it can be factored out of the sum. Moreover, the expectation value of the effective operator that appears at the end of Eq. 2.54 is similar to the expression of the second order perturbation, treated in Section 2.3.2, except for the squared energy denominator in the definition of $\lambda^{(3)}$. Therefore, by referring to Eq. 2.35, Eq. 2.36 and Eq. 2.37, with $\lambda^{(2)}$ replaced by $\lambda^{(3)}$, one can show that the effective perturbation operator $H_{pert}^{eff}$ can be expanded as the sum of a scalar operator, $H_{pert}^{(0)}$, and a tensor operator of rank 2, $H_{pert}^{(2)}$, and the perturbation of the level $\mid 6S_{1/2}, F, M_F >$ can be written as

$$< 6S_{1/2}, F, M_F \mid H_{pert}^{eff} \mid 6S_{1/2}, F, M_F > =$$

$$=< 6S_{1/2}, F, M_F \mid (H_{pert}^{(0)} + H_{pert}^{(2)}) \mid 6S_{1/2}, F, M_F > =$$

$$=< 6S_{1/2}, F, M_F \mid H_{pert}^{(0)} \mid 6S_{1/2}, F, M_F > . \quad (2.57)$$

Because of the reasons explained in Section 2.3.2, the tensor part of the perturbation vanishes and the only contribution to the energy of the system is the scalar term. But unlike the second order contribution, this third order scalar term *does now depend* on the quantum number F because of the factor $E_{hf}(S_{1/2}, F)$. Thus the effect of the perturbation can be parameterized in terms of an F-dependent third order scalar contribution $\alpha_0^{(3)}(F)$ to the polarizability as

$$\Delta E_0^{(3)}(F) = -\frac{1}{2} \cdot \alpha_0^{(3)}(F) \cdot \mathbb{E}^2. \quad (2.58)$$

The subscript 0 in $\Delta E_0^{(3)}$ reflects the scalar nature of this effect. Because of its dependence on the quantum number F, this scalar part of the third order contribution leads to a *shift of the hyperfine transition frequency*. But since it does not depend on the magnetic quantum number $M_F$ it does not affect the structure of Zeeman sub-levels.

### 2.4.1.2 First term of Eq 2.52

In this case also very important information can be inferred from the irreducible tensor formalism without developing explicit calculations. We just recall the main steps of the usual procedure.

We introduce an effective perturbation operator

$$H_{pert}^{eff} = \mathbf{d} \cdot \mathbf{E} \cdot \lambda^{(3)} \cdot \mathbf{d} \cdot \mathbf{E} \,, \tag{2.59}$$

where the projector $\lambda^{(3)}$ must be redefined as

$$\lambda^{(3)} = \sum_{p_1,p_2} \frac{\mid \varphi_{p_1} ><\varphi_{p_1} \mid H_{hf} \mid \varphi_{p_2} ><\varphi_{p_2} \mid}{(E_n^0 - E_{p_1}^0)(E_n^0 - E_{p_2}^0)} \,, \tag{2.60}$$

and where the sum is taken over all excited $\mid nP_j >$ states. We note that in this case the matrix elements $<\varphi_{p_1} \mid H_{hf} \mid \varphi_{p_2} >$ does not behave as a scalar and it cannot be factored out of the sum. The operator $\lambda^{(3)}$ thus exhibits an explicit dependence on the hyperfine interaction $H_{hf}$. This remark is of extreme importance for the final conclusions of this discussion.

The next step consists in decomposing the effective perturbation operator into the sum of a scalar operator and a tensor operator of rank-2

$$H_{pert}^{eff} = H_{pert}^{(0)} + H_{pert}^{(2)} \,, \tag{2.61}$$

where $H_{pert}^{(0)}$ and $H_{pert}^{(2)}$ are defined as in Eq. 2.35 and Eq. 2.36 respectively, with $\lambda^{(2)}$ replaced by $\lambda^{(3)}$. As explained in Section 2.3.2 we have now separated the field from the atom, and the part of the interaction that depends only on the amplitude of the field (scalar term) from the part that depends on its orientation (tensor term).

The scalar part of the perturbation gives yet another additional small (F-dependent) contribution to the scalar polarizability and leads to a correction of $\alpha_0^{(3)}$ of approximately 1%, while the tensor part can be written by applying the Wigner-Eckart theorem and by using the definitions of Eq. 2.35, Eq. 2.36 and Eq. 2.37 as

$$< 6S_{1/2}, F, M_F \mid H_{Pert}^{(2)} \mid 6S_{1/2}, F, M_F > \propto$$

$$\propto \begin{pmatrix} F & 2 & F \\ -M_F & 0 & M_F \end{pmatrix} < F \parallel \{\mathbf{d}^1 \lambda^{(3)} \mathbf{d}^1\}^2 \parallel F > \{\mathbf{EE}\}_0^2 \propto$$

$$\propto (3M_F^2 - F(F+1)) < F \parallel \{\mathbf{d}^1 \lambda^{(3)} \mathbf{d}^1\}^2 \parallel F > (3E_z^2 - \mathbb{E}^2) \,. \tag{2.62}$$

The $2^{nd}-$rank tensor operator $\{\mathbf{d}^1 \lambda^{(3)} \mathbf{d}^1\}^2$ *does not* act in the space of the electronic variables only, but $\lambda^{(3)}$ contains the hyperfine interaction term $\mathbf{J} \cdot \mathbf{I}$ and thus depends explicitly on the relative orientations of the electronic and nuclear angular momenta in the excited P-states. Since $\{\mathbf{d}^1 \lambda^{(3)} \mathbf{d}^1\}^2$ acts explicitly in both the space of the electron and of the nucleus we *cannot* decouple F into J and I in Eq. 2.62 and since a tensor of rank 2 has non-vanishing expectation values for states with F=3 and F=4 we can state in general that

$$< 6S_{1/2}, F, M_F \mid H_{Pert}^{(2)} \mid 6S_{1/2}, F, M_F > \propto < F \parallel \{\mathbf{d}^1 \lambda^{(3)} \mathbf{d}^1\}^2 \parallel F > \neq 0 \,. \tag{2.63}$$

Equivalently, one could observe that the magnetic dipole-dipole and the electric quadrupole parts of the hyperfine interaction in the excited P-states have the rotational symmetries of $k = 0, 2$ and $k = 2$ tensors, respectively. Together with the scalar Stark interaction, the first term of Eq 2.52 thus has a scalar and a tensor part.

Therefore, in third order perturbation theory the tensor part of the interaction does not vanish and gives a contribution to the perturbed atomic energy level which depends on

- the orientation of the electric field and on its modulus through the factor $(3E_z^2 - \mathbb{E}^2) \propto (3\cos^2\theta - 1)\mathbb{E}^2$.

- the magnetic quantum number $M_F^2$. This term of the perturbation is therefore responsible for the lifting of the Zeeman degeneracy in the hyperfine levels of the ground state.

Following Sandars [33], we can parameterize the tensor part of the third order effect in terms of the *tensor polarizability* $\alpha_2^{(3)}(F)$ as [13]:

$$\Delta E_2^{(3)}(F, M_F) = -\frac{1}{2} \cdot \alpha_2^{(3)}(F) \cdot \frac{3M_F^2 - F(F+1)}{I(2I+1)} \cdot \frac{3\cos^2(\theta) - 1}{2} \cdot \mathbb{E}^2 \,. \tag{2.64}$$

Here we use the subscript 2 in the notation $\Delta E_2^{(3)}$ to stress the tensor character of this component of the third order effect.

### 2.4.1.3 Summary

In summary, we have shown that the third order contribution to the energy of a ground state level $\mid 6S_{1/2}, F, M_F >$ perturbed by an external static electric field can be written in terms of the scalar and tensor polarizabilities as

$$\Delta E^{(3)}(F, M_F) = -\frac{1}{2}\alpha^{(3)}(F, M_F)\mathbb{E}^2 =$$
$$= -\frac{1}{2}\alpha_0^{(3)}(F)\mathbb{E}^2 - \frac{1}{2}\alpha_2^{(3)}(F)\frac{3M_F^2 - F(F+1)}{I(2I+1)}\frac{3\cos^2(\theta) - 1}{2}\mathbb{E}^2 \,. \tag{2.65}$$

### 2.4.2 Third order polarizabilities: symbolic calculations

We present a first estimation of the third order polarizabilities $\alpha_0^{(3)}(F)$ and $\alpha_2^{(3)}(F)$ by considering *only the diagonal matrix elements* of the hyperfine hamiltonian

$$< L_1, J_1, F_1, M_1 \mid H_{hf} \mid L_2, J_2, F_2, M_2 > \propto \delta_{L_1 L_2}\delta_{J_1 J_2}\delta_{F_1 F_2}\delta_{M_1 M_2} \,. \tag{2.66}$$

Under this assumption we can write the third order effect given by Eq. 2.29 in the form

$$\Delta E_{Stark}^{(3)}(F, M_F) = \sum_n \sum_{j=1/2}^{3/2} \sum_{f=|I-j|}^{I+j} \sum_{m=-f}^{f} \frac{|< nP_J, f, m \mid H_{Stark} \mid 6S_{1/2}, F, M >|^2}{\Delta E(6S_{1/2}, nP_j)^2}$$
$$\times \Delta E_{hf}(nP_Jfm, 6S_{1/2}FM) \,, \tag{2.67}$$

where

---

[13]For the time being we include in $\alpha_2^{(3)}(F)$ the contribution of both the magnetic dipole-dipole interaction and the electric quadrupole interaction. We will consider them separately in the next sections.

$$\Delta E_{hf}(nP_J fm, 6S_{1/2}FM) =$$
$$= <nP_J, f, m \mid H_{hf} \mid nP_J, f, m> - <6S_{1/2}, F, M \mid H_{hf} \mid 6S_{1/2}, F, M> . \quad (2.68)$$

We write the hyperfine hamiltonian as $H_{hf} = H_{Fermi} + H_{d-d} + H_Q$ and use the parametrization of Arimondo et al. [82]

$$<6S_{1/2}, F, M \mid H_{Fermi} \mid 6S_{1/2}, F, M> = \frac{1}{2} K A_{6S_{1/2}} ,$$

$$<nP_J, F, M \mid H_{d-d} \mid nP_J, F, M> = \frac{1}{2} K A_{nP_J} , \quad (2.69)$$

$$<nP_{3/2}, F, M \mid H_Q \mid nP_{3/2}, F, M> = \frac{(K+1) - 2I(I+1)J(J+1)}{2I(2I-1)2J(2J-1)} B_{nP_{3/2}} ,$$

where $K = F(F+1) - J(J+1) - I(I+1)$. We also introduce the notation

$$\frac{e^2 \mid <6S_{1/2} \parallel r \parallel nP_j> \mid^2}{\Delta E(6S_{1/2}, nP_j)^2} = \mathcal{C}_{nP_j} . \quad (2.70)$$

The sum in Eq. 2.67 can be evaluated by applying the Wigner-Eckart theorem and the standard angular momentum decoupling rules. After some algebraic manipulation one can show that the third order perturbation takes the form

$$\Delta E_{Stark}^{(3)}(F, M_F) = a_0(F)\mathbb{E}^2 + a_2(F) \left[3M_F^2 - F(F+1)\right] \mathbb{E}^2 . \quad (2.71)$$

By comparing Eq. 2.71 with Eq. 2.65 one obtains the scalar polarizabilities in the case of cesium

$$\alpha_0^{(3)}(F=4) = \frac{7}{36} \sum_n \left[(3A_{6S_{1/2}} + A_{nP_{1/2}})\mathcal{C}_{nP_{1/2}} + (3A_{6S_{1/2}} - 5A_{nP_{3/2}})\mathcal{C}_{nP_{3/2}}\right] , \quad (2.72)$$

and

$$7\alpha_0^{(3)}(F=3) = -9\alpha_0^{(3)}(F=4) . \quad (2.73)$$

We note *en passant* that the ratio $\frac{9}{7}$ in Eq. 2.73 corresponds to the ratio of the hyperfine energies of the levels F=4 and F=3, given by their statistical weights 2F+1 [14]. The Fermi-contact interaction, proportional to $A_{6S_{1/2}}$, provides the dominant contribution to $\alpha_0^{(3)}$, although it also has a small contribution ($\approx 1\%$) from the scalar part of the magnetic dipole-dipole interaction (proportional to $A_{nP_j}$).

In the same way one obtains for the tensor polarizabilities

$$\alpha_2^{(3)}(F=4) =$$
$$= -\frac{7}{18} \sum_n \left[2A_{nP_{1/2}}\mathcal{C}_{nP_{1/2}} - A_{nP_{3/2}}\mathcal{C}_{nP_{3/2}}\right] + \frac{1}{12} \sum_n \left[B_{nP_{3/2}}\mathcal{C}_{nP_{3/2}}\right] , \quad (2.74)$$

---

[14]Since $H_{hf} \propto \vec{J} \cdot \vec{I}$ does not produce work, the condition $\sum_F (2F+1)E_{hf}(F) = 0$ has to be always fulfilled. In the ground state of cesium (J=1/2, I=7/2) this condition leads to $9E_{hf}(4) + 7E_{hf}(3) = 0$.

and

$$\alpha_2^{(3)}(F = 3) =$$
$$= \frac{7}{18} \sum_n \left[ 2A_{nP_{1/2}} \mathcal{C}_{nP_{1/2}} - A_{nP_{3/2}} \mathcal{C}_{nP_{3/2}} \right] + \frac{5}{36} \sum_n \left[ B_{nP_{3/2}} \mathcal{C}_{nP_{3/2}} \right] . \quad (2.75)$$

In Eqs. 2.74 and 2.75 the terms proportional to $A_{nP_j}$ represent the contribution of the tensor part of the magnetic dipole-dipole interaction, while the terms proportional to $B_{nP_{3/2}}$ represent a small contribution ($\approx 0.1\%$) due to the electric quadrupole hyperfine interaction.

### 2.4.3 Comparison with Sandars' parametrization

We want to compare now the expressions derived in the previous section with the standard parametrization of the third order polarizabilities given by Sandars in [33] for an electric field $E \parallel z$

$$\Delta E_{Stark}^{(3)}(F, M_F) = -\frac{1}{2} \alpha^{(3)} \mathbb{E}^2 , \quad (2.76)$$

where the third order polarizability $\alpha^{(3)}$ is given by three contributions which correspond to the hyperfine contact interaction ($\alpha_{10}$), the hyperfine dipole-dipole interaction ($\alpha_{12}$) and the electric quadrupole interaction ($\alpha_{02}$). The explicit expressions given by Sandars are

$$\alpha^{(3)}(F = 4) = \alpha_{10} + (\alpha_{12} + \alpha_{02}) \frac{3M_F^2 - F(F+1)}{I(2I+1)} =$$
$$= \alpha_{10} + (\alpha_{12} + \alpha_{02}) \frac{3M_F^2 - F(F+1)}{28} , \quad (2.77)$$

and

$$\alpha^{(3)}(F = 3) = -\frac{I+1}{I} \alpha_{10} + (\alpha_{12} + \frac{2I+3}{2I-1} \alpha_{02}) \frac{3M_F^2 - F(F+1)}{I(2I+1)} =$$
$$= -\frac{9}{7} \alpha_{10} + (\alpha_{12} + \frac{5}{3} \alpha_{02}) \frac{3M_F^2 - F(F+1)}{28} . \quad (2.78)$$

The comparison of these latter equations to our results of Section 2.4.2 leads to the following important remarks.

- The scalar term $\alpha_{10}$ is dominated by the contribution of the Fermi-contact interaction, but it also has a small contribution from the magnetic dipole-dipole interaction (see Eq. 2.72) which seems to be neglected by Sandars.

- The relative contributions of the scalar and electric quadrupole terms, $\alpha_{10}$ and $\alpha_{02}$ respectively, for F=3 and F=4 are consistent in our and in Sandars' expressions.

- The relative contributions of the dipole-dipole term $\alpha_{12}$ for F=3 and F=4 appear with opposite signs in our expressions, while in Sandars' treatment the sign does not depend on F. According to our calculations, $\alpha_{12}$ in Sandars' expression 2.78 should

read "$-\alpha_{12}$". It seems that this sign error has remained unnoticed in the literature for almost 40 years. In Chapter 6 of this work we will present experimental evidence that the relative signs of the $\alpha_{12}$ terms for F=4 and F=3 should indeed be opposite as derived in our calculations. In the next Section we will discuss the consequences of this sign difference in the ground state of cesium.

### 2.4.4 The third order shift of Zeeman transitions

The frequency shift of a generic ground state level $\mid F, M_F >$ exposed to a combination of electric ($E_z$) and magnetic ($B_z$) fields can be written in the form

$$\Delta\nu_{(F,M_F)} \equiv \frac{\Delta E^{(3)}(F, M_F)}{h} = \nu_L(F)M_F - \alpha_2^{(3)}(F)\frac{3M_F^2 - F(F+1)}{56}\mathbb{E}^2 \,, \qquad (2.79)$$

where $\nu_L = \frac{g_F\mu_b}{h}B_z$ is the Larmor frequency associated with the magnetic field and we have assumed for simplicity $\theta = 0$. The situation is represented graphically in Fig. 2.5. The transitions

$$\mid 4, 4 > \rightarrow \mid 4, 3 >$$
$$\mid 3, 3 > \rightarrow \mid 3, 2 >$$

are the most relevant ones in magnetic resonance experiments on optically pumped atoms in which the states $\mid 4, 4 >$ and $\mid 3, 3 >$ are the most populated. This condition is fulfilled in the isotropic bcc phase of solid He where the dominant optical pumping mechanism is the so-called *repopulation pumping* as was first demonstrated by Lang et al. [19] (this point will be addressed in more details in Chapter 4). The frequency shifts of these two relevant transitions are given by

$$\Delta\nu_{(4,4),(4,3)} = \mid \nu_L(4) - \frac{3}{8}\alpha_2^{(3)}(4)\mathbb{E}^2 \mid = \mid \nu_L(4) \mid \left(1 - \frac{3}{8}\frac{\alpha_2^{(3)}(4)}{\mid \nu_L(4) \mid}\mathbb{E}^2\right) \,, \qquad (2.80)$$

$$\Delta\nu_{(3,3),(3,2)} = \mid \nu_L(3) - \frac{15}{56}\alpha_2^{(3)}(3)\mathbb{E}^2 \mid = \mid \nu_L(3) \mid \left(1 + \frac{15}{56}\frac{\alpha_2^{(3)}(3)}{\mid \nu_L(3) \mid}\mathbb{E}^2\right) \,, \qquad (2.81)$$

where in the last equality of the two equations above we have used the property of the g-factors $g_3/g_4 \approx -1$. The sign of the tensor polarizability $\alpha_2^{(3)}(F)$ plays then the crucial role. In our model, neglecting the small contribution ($\approx 10^{-3}$) of the electric quadrupole interaction, we have

$$\frac{\alpha_2^{(3)}(4)}{\alpha_2^{(3)}(3)} = -1 \,, \qquad (2.82)$$

and the resonance frequencies $\Delta\nu_{(4,4),(4,3)}$ and $\Delta\nu_{(3,3),(3,2)}$ are thus shifted by the interaction with the electric field *in the same direction*. The situation is reversed in Sandars' model where

$$\frac{\alpha_2^{(3)}(4)}{\alpha_2^{(3)}(3)} = 1 \,, \qquad (2.83)$$

and the two resonances are shifted in opposite directions (the situation according to Sandars' theory is sketched in Fig. 2.6). The experimental investigation of the relative shift of
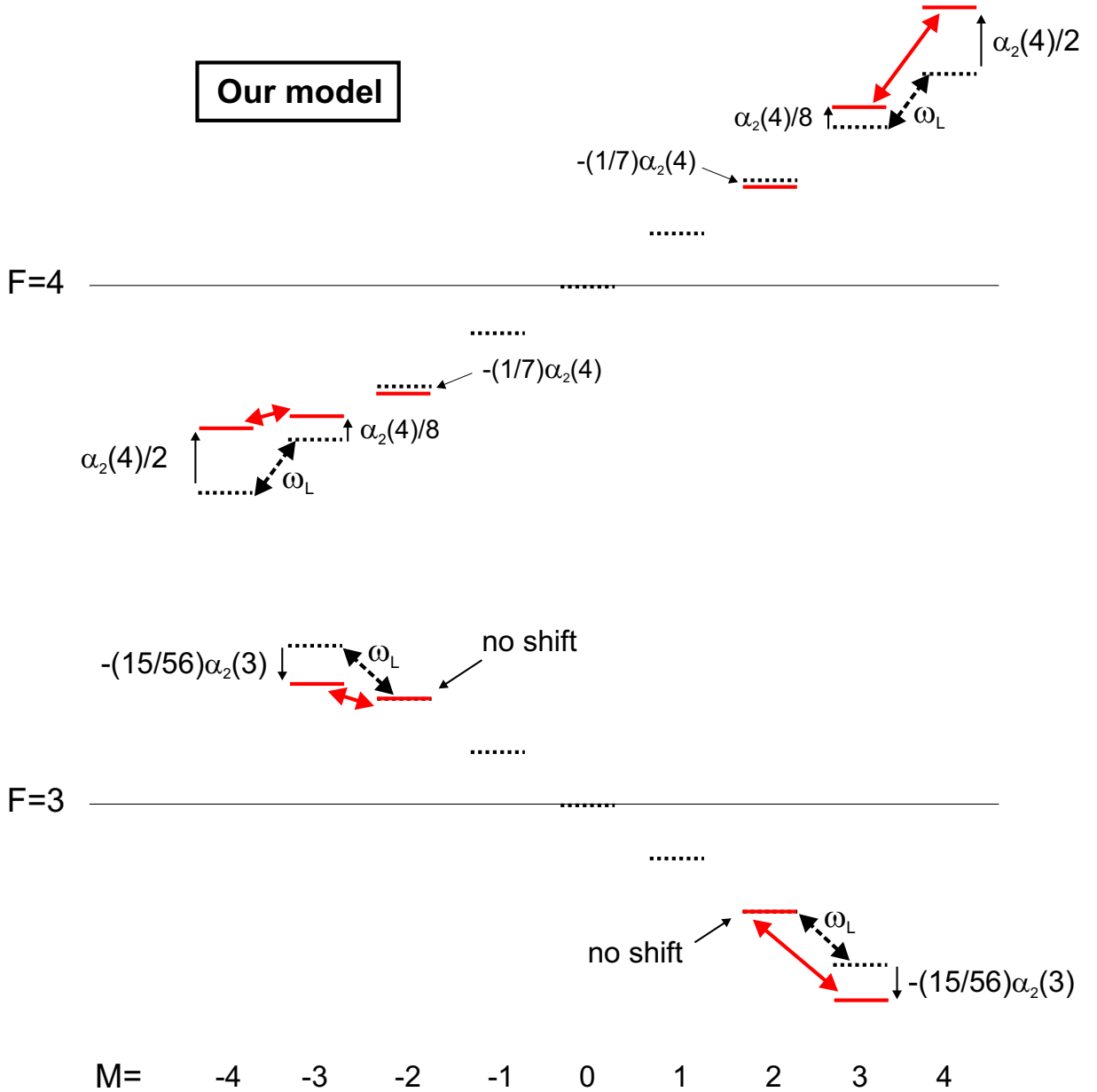
Figure 2.5: The ground state of Cs under the effect of electric and magnetic fields (not drawn to scale). The black dotted lines represent the Zeeman levels under the effect of a magnetic field. In a magnetic resonance experiment without electric fields one measures the Larmor frequency $\omega_L$. The red solid lines represent the Zeeman levels under the effect of static parallel magnetic and electric fields (for the sake of simplicity we show only the effect on the levels $M = \pm4, \pm3, \pm2$). The Stark shift of the atomic levels is proportional to $\mathbb{E}^2$ and in the figure we give the proportionality constants in terms of the absolute values of the tensor polarizabilities $\mid \alpha_2^{(3)}(F) \mid$. In a magnetic resonance experiment driving the transitions $\mid 4,4 > \rightarrow \mid 4,3 >$ and $\mid 3,3 > \rightarrow \mid 3,2 >$ the two resonance frequencies are both shifted to higher frequencies (we have implicitly assumed that $\alpha_2^{(3)}(4) < 0$). One can observe that if the atoms are pumped by $\sigma^- -$polarized light into the levels $\mid 4, -4 >$ and $\mid 3, -3 >$, the corresponding resonances are both shifted by the Stark interaction towards lower frequencies.
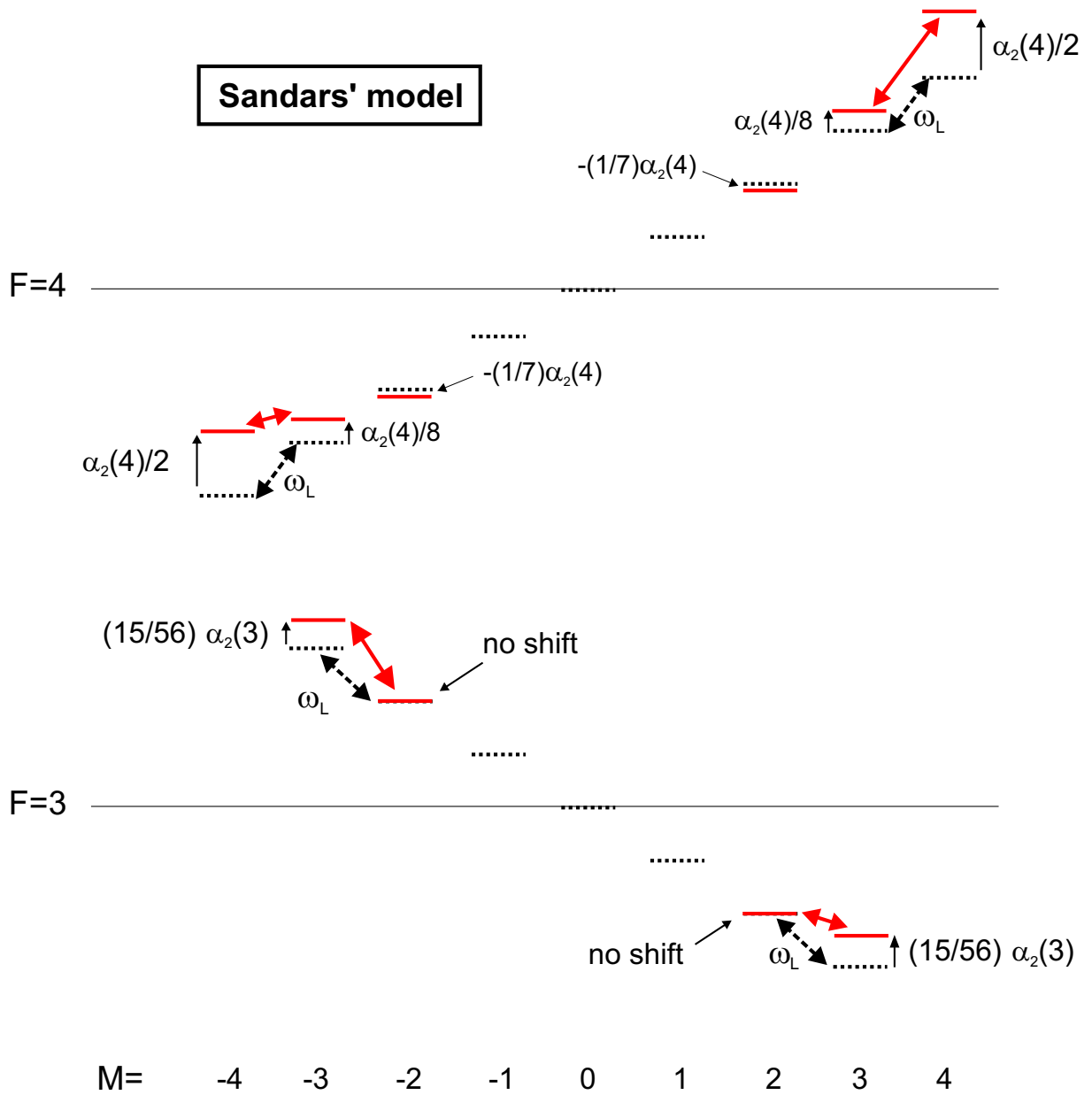
Figure 2.6: The ground state of Cs under the effect of electric and magnetic fields **according to Sandars' model** (not drawn to scale). The black dotted lines represent the Zeeman levels under the effect of a magnetic field. In a magnetic resonance experiment without electric fields one measures the Larmor frequency $\omega_L$. The red solid lines represent the Zeeman levels under the effect of static parallel magnetic and electric fields (for the sake of simplicity we show only the effect on the levels $M = \pm 4, \pm 3, \pm 2$). The Stark shift of the atomic levels is proportional to $\mathbb{E}^2$ and in the figure we give the proportionality constants in terms of the absolute values of the tensor polarizabilities $\mid \alpha_2^{(3)}(F) \mid$. In a magnetic resonance experiment driving the transitions $\mid 4, 4 > \rightarrow \mid 4, 3 >$ and $\mid 3, 3 > \rightarrow \mid 3, 2 >$, the former resonance frequency is shifted to higher frequencies while the latter is shifted towards lower frequencies.

the two resonances will thus represent a definitive test of the two models.

We give here also a general expression for the frequency shift of the generic magnetic transition $\mid F, M_F > \rightarrow \mid F, M_F - 1 >$ under the effect of an external electric field

$$\Delta\nu_{(F,M_F),(F,M_F-1)} = -\frac{3}{56}\alpha_2^{(3)}(F)(2M_F - 1)\mathbb{E}^2 \,. \tag{2.84}$$

It is then straightforward to verify that the splitting of adjacent magnetic resonances induced by the electric field within a given hyperfine level does not depend on F nor on M

$$\Delta\nu_{(F,M_F),(F,M_F-1)} - \Delta\nu_{(F,M_F-1),(F,M_F-2)} = -\frac{3}{28}\alpha_2^{(3)}(F)\mathbb{E}^2 \,. \tag{2.85}$$

The interaction with the external electric field thus produces in a magnetic resonance experiment a set of equally spaced peaks.

### 2.4.5 The third order shift of the hyperfine clock transition

The third order scalar term $\alpha_0^{(3)}$ is responsible for the shift of the clock transition

$$\Delta\nu_{00} = \mid 6S_{1/2}, F = 4, M = 0 > \leftrightarrow \mid 6S_{1/2}, F = 3, M = 0 > \,.$$

Also the term proportional to $\alpha_2^{(3)}$ gives a small contribution ($\approx 1\%$) to that shift due to its dependence on F. The (static) Stark shift of the clock transition frequency will be addressed in detail in Chapter 3. Here we just observe that from Eq. 2.65 one can derive the following important expression

$$\Delta\nu_{00} = \frac{1}{h}\left[\Delta E^{(3)}(F = 4, M_F = 0) - \Delta E^{(3)}(F = 3, M_F = 0)\right] =$$
$$= -\frac{1}{2}\left[\frac{16}{7}\alpha_0^{(3)}(4) - \frac{8}{7}\alpha_2^{(3)}(4)\frac{3\cos^2(\theta) - 1}{2}\right]\mathbb{E}^2 \,. \tag{2.86}$$

The expression above is slightly different in Sandars' model, which predicts $\alpha_2^{(3)}(4) = \alpha_2^{(3)}(3)$. In this case it is straightforward to show that the coefficient 8/7 of the tensor contribution is replaced by 2/7.

### 2.4.6 Graphical representation of the perturbation with only diagonal contributions

In Fig. 2.7 we give a graphical representation of both the second order and the third order effect when we include in the perturbation only diagonal hyperfine matrix elements.

### 2.4.7 The tensor polarizability: a first numerical estimation

We can make a first numerical estimation of the tensor polarizability $\alpha_2^{(3)}$ under the following assumptions:

- we retain only the first term (n=6) in the perturbation series given by Eq 2.74 and Eq. 2.75,
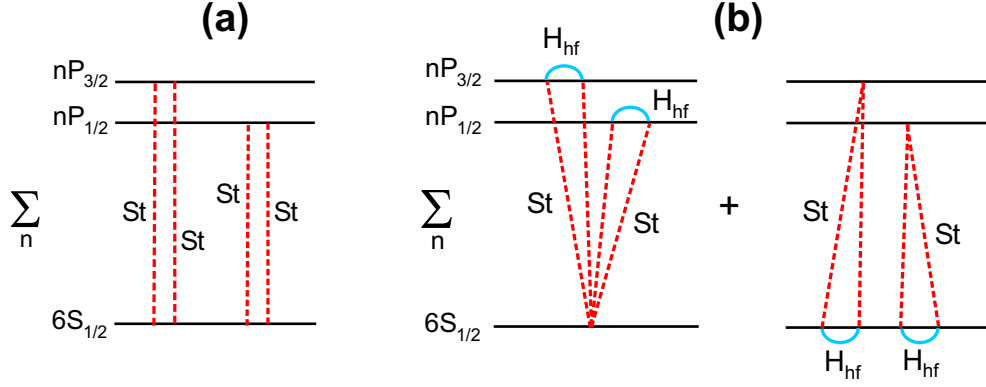
Figure 2.7: Second and third order perturbation with diagonal hyperfine interaction. The dotted red lines represent the Stark interaction while the blue solid lines represent the diagonal hyperfine matrix elements. **(a)** In second order the Stark interaction couples the ground state to the excited P states and then the P states back to the ground state. This contribution is proportional to the scalar polarizability $\alpha_0^{(2)}$ (see Section 2.3.2). **(b)** In third order the hyperfine interaction in the ground state leads to an F-dependent scalar contribution proportional to the third order scalar polarizability $\alpha_0^{(3)}$, while the hyperfine interaction in the nP states leads to a F- and M-dependent tensor contribution proportional to the tensor polarizability $\alpha_2^{(3)}$.

- we neglect the contribution of the electric quadrupole interaction because $B_{6P_{3/2}} \ll A_{6P_j}$. According to [83, 84] the hyperfine constants in 6P states are $A_{6P_{1/2}} = 291.920\,MHz$, $A_{6P_{3/2}} = 50.275\,MHz$ and $B_{6P_{3/2}} = -0.53\,MHz$,

- we use the experimental values of the reduced dipole matrix elements given in [74]:

$$< 6S_{1/2} \parallel er \parallel 6P_{1/2} >= 4.4978(61)\,a_0 e\,, \tag{2.87}$$

$$< 6S_{1/2} \parallel er \parallel 6P_{3/2} >= 6.3311(72)\,a_0 e\,. \tag{2.88}$$

The theoretical (absolute) values of these matrix elements reported in the literature [67, 69, 70, 72] are in good agreement with the experimental results given above at a level of 1–2%. Nevertheless, we found several inconsistencies concerning their signs. Although in the calculations involving only diagonal hyperfine matrix elements the reduced dipole matrix elements are all squared, we need to make the remark that the signs of $< 6S_{1/2} \parallel er \parallel 6P_j >$ will become of crucial importance later when we include in the perturbation expansion off-diagonal hyperfine matrix elements.

Using the numerical values given above and the coupling scheme of Fig. 2.7.b we obtain

$$\alpha_2^{(3)}(F = 4) \approx -5.46 \times 10^{-2}\,\frac{Hz}{(kV/cm)^2}\,, \tag{2.89}$$

and

$$\alpha_2^{(3)}(F = 3) = -\alpha_2^{(3)}(F = 4) \approx 5.46 \times 10^{-2}\,\frac{Hz}{(kV/cm)^2}\,. \tag{2.90}$$

This result is represented by point (f') in Fig. 2.8. The tensor polarizability of the ground state of Cs atoms was measured in an atomic beam experiment using a Ramsey-resonance technique by Carrico and collaborators in 1968 [62] with the result

$$\alpha_2^{(3)}(F=4) = -3.39(53) \times 10^{-2} \frac{Hz}{(kV/cm)^2}, \tag{2.91}$$

and in 1969 by Gould and collaborators [63] who obtained

$$\alpha_2^{(3)}(F=4) = -3.66(21) \times 10^{-2} \frac{Hz}{(kV/cm)^2}. \tag{2.92}$$

More recently, the tensor polarizability has been measured in another atomic beam experiment using a purely optical technique by the Fribourg Atomic Physics group [64] with the result

$$\alpha_2^{(3)}(F=4) = -3.34(20) \times 10^{-2} \frac{Hz}{(kV/cm)^2}. \tag{2.93}$$

Although all the measurements are characterized by a good global agreement (see Fig. 2.8), they all disagree with the simple theoretical estimation given above (Eq. 2.89). This discrepancy between theory and experiments is confirmed by the theoretical prediction of Gould and collaborators [63] [point (f) in Fig. 2.8]

$$\alpha_2^{(3)}(F=4) = -4.133 \times 10^{-2} \frac{Hz}{(kV/cm)^2}. \tag{2.94}$$

This estimation is based on even more restrictive approximations than our simple estimation:

1. the authors assume that the tensor polarizability is entirely due to an admixture of the 6P states only into S states and they consider only diagonal hyperfine matrix elements. This is similar to our approximation.

2. They further assume that the hyperfine coupling constants $A_{nP_j}$ are connected by the well defined relationship

$$A_{nL_J} \propto \frac{L(L+1)}{J(J+1)} \langle \frac{1}{r^3} \rangle, \tag{2.95}$$

which yields

$$A_{nP_{1/2}} = 5A_{nP_{3/2}}. \tag{2.96}$$

This relationship holds for one-electron atoms but it turns out to be a quite coarse assumption in Cs, where the corresponding ratio of experimental values, used in our calculations, is

$$A_{nP_{1/2}} = 5.8A_{nP_{3/2}}, \tag{2.97}$$

3. the spin-orbit splitting of 6P states is neglected by setting

$$\Delta E(6S_{1/2}, 6P_{1/2}) = \Delta E(6S_{1/2}, 6P_{3/2}) \equiv \Delta E_{6S-6P}. \tag{2.98}$$

This is again a very coarse approximation in Cs where the spin-orbit splitting of 6P states is $\approx 17\,THz$, which amounts to 5% of the average energy $\Delta E_{6S-6P}$.

If we also use the approximations 2 (Eq. 2.96) and 3 (Eq. 2.98) in our calculations and if we assume that

$$< 6S_{1/2} \parallel er \parallel nP_{3/2} > = \sqrt{2} < 6S_{1/2} \parallel er \parallel nP_{1/2} >, \tag{2.99}$$

we can write

$$\alpha_2^{(3)}(F=4) \approx -\frac{28}{9} \frac{|< 6S_{1/2} \parallel er \parallel 6P_{1/2} >|^2}{\Delta E_{6S-6P}^2} A_{nP_{3/2}}. \tag{2.100}$$

Using Eq. 2.98 and Eq. 2.99 the second order scalar polarizability $\alpha_0^{(2)}$ (see Eq. 2.45) then takes the form

$$\alpha_0^{(2)} \approx \frac{|< 6S_{1/2} \parallel er \parallel 6P_{1/2} >|^2}{\mid \Delta E_{6S-6P} \mid}, \tag{2.101}$$

and the tensor polarizability $\alpha_2^{(3)}$ can be expressed in terms of the scalar polarizability $\alpha_0^{(2)}$ as

$$\alpha_2^{(3)}(F=4) \approx -\frac{28}{9} \alpha_0^{(2)} \frac{A_{6P_{3/2}}}{\mid \Delta E_{6S-6P} \mid} \approx -4.48 \times 10^{-2} \frac{Hz}{(kV/cm)^2}. \tag{2.102}$$

where we have used our calculated value for the scalar polarizability $\alpha_0^{(2)}$. This result is represented by point (f") in Fig. 2.8. We thus observe an agreement at a level of 6% with the result of Gould et al. [63] given in Eq. 2.94 and obtained under the same assumptions. We consider this agreement satisfactory for the sake of this discussion.

The approximate estimation given by Eq. 2.102 is definitely closer to experimental results than Eq. 2.89 but cannot resolve the discrepancy between experiments and theory. To our knowledge, in the literature over the 40 years that have passed after the publication of Sandars' theoretical model, there were no other attempts to find a solution to this discrepancy. The situation before this work is summarized in Fig. 2.8.

Moreover, a similar and in some cases even more pronounced disagreement between theory and experiments was also found for the other alkalis Na, K, [85]Rb and [87]Rb [63]. The theoretical prediction turns out to be always larger (in modulus) then the measured value. In Table 2.1 we report the tensor polarizabilities that were calculated and measured by Gould and his collaborators. Note that the theoretical predictions are based on the same approximations that we already discussed in the case of Cs.

Of course we can still consider the following contributions in Eq 2.74 and Eq. 2.75.

- The electric quadrupole interaction in states $nP_{3/2}$. It is straightforward to verify that the inclusion of the electric quadrupole constant $B_{6P_{3/2}}$ changes the tensor polarizability by only $\approx 0.05\%$.

| Element | Theory $[\times 10^{-2} \frac{Hz}{(kV/cm)^2}]$ | Experiment $[\times 10^{-2} \frac{Hz}{(kV/cm)^2}]$ | Deviation |
|---------|-----------------------------------------------|--------------------------------------------------|-----------|
| $^{133}$Cs | -4.133 | $-3.659 \pm 0.211$ | 2.3 |
| $^{87}$Rb | -2.000 | $-1.392 \pm 0.089$ | 6.8 |
| $^{85}$Rb | -0.780 | $-0.456 \pm 0.024$ | 13.5 |
| $^{39}$K | -0.093 | $-0.064 \pm 0.004$ | 7.2 |
| $^{23}$Na | -0.173 | $-0.149 \pm 0.013$ | 1.8 |

Table 2.1: Calculated and measured tensor polarizabilities $\alpha_2^{(3)}$ for the alkalis. The deviation is expressed in units of the corresponding experimental error. Data are taken from Gould et al. [63].

- The inclusion of nP states with $n > 6$ in the perturbation expansion. The contribution from the 7P states can be calculated by using the experimental values of the reduced dipole matrix elements given by Vasilyev et al. [73]

$$< 6S_{1/2} \parallel er \parallel 7P_{1/2} >= 0.2757(20)a_0 e \,, \qquad (2.103)$$

$$< 6S_{1/2} \parallel er \parallel 7P_{3/2} >= 0.5856(50)a_0 e \,. \qquad (2.104)$$

The contribution of the 7P states to the tensor polarizability is only $\approx 0.03\%$.

Therefore we have to find another way to fix the problem of the large long-standing gap between theoretical predictions and experimental values. The approach that we present in this work is essentially based on the idea that the reconciliation of theory and experiments can be achieved by searching for *missing terms* in the third order perturbation expansion. Since the first term of Eq. 2.52 is actually not restricted to diagonal matrix elements of the hyperfine interaction, such a search for new perturbing terms has led us to investigate the effects of *off-diagonal hyperfine matrix elements*. As we will show in the next section these matrix elements give a contribution to the tensor polarizability $\alpha_2^{(3)}$ which is large enough to change in a radical way our first estimation given in Eq. 2.89. These contributions allow us to bridge the old discrepancy between theory and experiments.
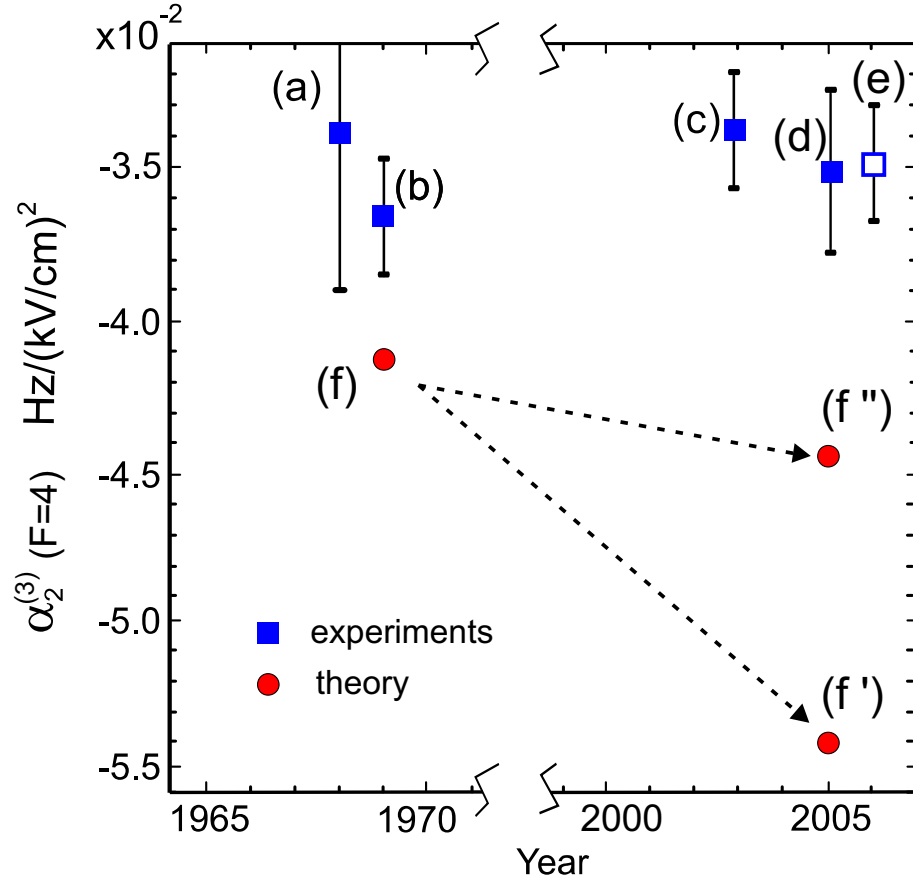
Figure 2.8: The third order tensor polarizability of the F=4 Cs ground state before this work. The filled squares represent experimental values of (a) from Carrico et al.[62], (b) from Gould et al.[63], (c) from Ospelkaus et al. [64] and (d) from this work [85] (see Chapter 6). The empty square (e) represents a weighted average of (a), (b), (c) and (d). The dots represent (f) the theoretical value from [63] given in Eq. 2.94 and (f',f") our re-evaluations (Eqs. 2.89,2.102) of the latter value as discussed in the text.

$$6S_{1/2} \xrightarrow{\ H_{Stark}\ } n_1 P_{J1} \xrightarrow{\ H_{Hf}\ } n_2 P_{J2} \xrightarrow{\ H_{Stark}\ } 6S_{1/2}$$

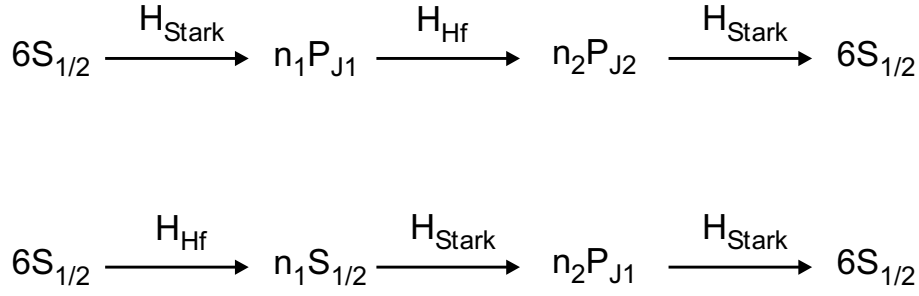$$6S_{1/2} \xrightarrow{\ H_{Hf}\ } n_1 S_{1/2} \xrightarrow{\ H_{Stark}\ } n_2 P_{J1} \xrightarrow{\ H_{Stark}\ } 6S_{1/2}$$

Figure 2.9: The contributions of the Stark interaction and of the off-diagonal hyperfine interaction to the third order perturbation.

## 2.5 Off-diagonal hyperfine matrix elements

In this section we show that the inclusion of off-diagonal hyperfine matrix elements

$$< n_1, L_1, J_1, F_1, M_1 \mid H_{hf} \mid n_2, L_2, J_2, F_2, M_2 >$$

yields additional contributions which can bridge the large gap between theory and experiments. The Stark and the hyperfine interactions are combined in the third order perturbation according to the possible schemes represented graphically in Fig. 2.9. In each term of the third order perturbation expansion there are two matrix elements of the Stark interaction and one off-diagonal matrix element of the hyperfine interaction. The Stark interaction couples S and P states ($\Delta L = \pm 1$) while the hyperfine interaction mixes states according to the selection rules $\Delta L = 0$ (Fermi contact interaction) and $\Delta L = 0, \pm 2$ (dipole-dipole and quadrupole interaction).

We investigate *three different coupling schemes.*

1. the mixing of levels belonging to the same fine-structure multiplet (i.e., states identified by the same set of quantum numbers except for J),

2. the mixing of levels with the same set of angular momentum quantum numbers (i.e., same L and J) but different principal quantum number n,

3. the mixing of levels with different n and different J.

The hyperfine interaction is always diagonal in F and M, that is

$$< \gamma_1, F_1, M_1 \mid H_{hf} \mid \gamma_2, F_2, M_2 > \propto \delta_{F_1,F_2} \delta_{M_1,M_2} . \qquad (2.105)$$

We will first describe the general method used to calculate all the matrix elements, then we will treat separately the three coupling schemes mentioned above and we will show how each of those families of off-diagonal elements contributes to the quadratic Stark effect.

For a detailed investigation of the hyperfine interaction we refer to the comprehensive review by Arimondo et al. [82].

### 2.5.1 Off-diagonal hyperfine matrix elements: general approach

The first order term of $H_{hf}$, i.e., the magnetic dipole part of the hyperfine interaction [15] can be written [82] in spherical tensor form as

$$H_{hf} = \{a_{l,j} \left[ \mathbf{L} - (\mathbf{S} - 3(\mathbf{S} \cdot \mathbf{n})\mathbf{n}) \right] + a_s \mathbf{S}\} \cdot \mathbf{I} =$$
$$= \left\{ a_{l,j} \left[ \mathbf{L} - \sqrt{10} \left( \mathbf{C}^{(2)} \times \mathbf{S} \right)^{(1)} \right] + a_s \mathbf{S} \right\} \cdot \mathbf{I}, \quad (2.106)$$

where $\mathbf{L}$, $\mathbf{S}$ and $\mathbf{I}$ are the electronic orbital angular momentum, the electronic spin and the nuclear momentum tensor operators, respectively, $a_{l,j}$ and $a_s$ are the hyperfine coupling constants, $\mathbf{C}^{(2)}$ is the second rank normalized spherical harmonic operator and $\mathbf{n}$ is a unit vector directed along the position vector of the valence electron. The first and the second term in Eq. (2.106), both proportional to $a_{l,j}$, describe the orbital and the spin dipolar interactions, respectively, while the third term, proportional to $a_s$, is the Fermi contact interaction. The latter term has non-zero matrix elements only between S-states ($L = 0$) while the first two terms require $L > 0$. In the following we consider the magnetic dipole-dipole and the Fermi-contact interactions separately.

#### 2.5.1.1 The magnetic dipole-dipole hyperfine interaction

The first term in Eq. 2.106, due to the orbital motion of the electron, can be rewritten in the following way

$$< J_1, I, F, M \mid \mathbf{L} \cdot \mathbf{I} \mid J_2, I, F, M >=$$

$$= (-1)^{J_2+I+F} < J_1 \parallel L \parallel J_2 >< I \parallel I \parallel I > \begin{Bmatrix} J_1 & I & F \\ I & J_2 & 1 \end{Bmatrix} =$$

$$= (-1)^{F+2J_2+I+S+L_1+1} \sqrt{(2J_1+1)(2J_2+1)} \times$$

$$\times \begin{Bmatrix} J_1 & I & F \\ I & J_2 & 1 \end{Bmatrix} \begin{Bmatrix} L_1 & J_1 & S \\ J_2 & L_2 & 1 \end{Bmatrix} < L_1 \parallel L \parallel L_2 >< I \parallel I \parallel I >, \quad (2.107)$$

where the matrix element $< J_1 \parallel L \parallel J_2 >$ has been further reduced by decoupling J into S and L. The interaction described by the expression above is *diagonal* in L and it is thus governed by the selection rule $\Delta L = 0$.

The second term of Eq. 2.106 depends on the intrinsic angular momentum S of the electron and can be rewritten as follows

---

[15]In the discussion that follows we neglect the second order contribution of the electric quadrupole term $H_Q$.

$$- \sqrt{10} < J_1, I, F, M \mid \sum_q (-1)^q \left[ C^2 \times S^1 \right]_q^1 I_{-q} \mid J_2, I, F, M >=$$

$$= (-1)^{J_2+I+F+1} \sqrt{10} < J_1 \parallel \left[ C^2 \times S^1 \right]^1 \parallel J_2 > < I \parallel I \parallel I > \begin{Bmatrix} J_1 & I & F \\ I & J_2 & 1 \end{Bmatrix} , \quad (2.108)$$

where $< J_1 \parallel \left[ C^2 \times S^1 \right]^1 \parallel J_2 >$ can be expressed in terms of a 9j-symbol by decoupling J into S and L as prescribed in [86]:

$$< J_1 \parallel \left[ C^2 \times S^1 \right]^1 \parallel J_2 >=$$

$$= \sqrt{3} \sqrt{(2J_1+1)(2J_2+1)} \begin{Bmatrix} L_1 & L_2 & 2 \\ S & S & 1 \\ J_1 & J_2 & 1 \end{Bmatrix} < L_1 \parallel C^2 \parallel L_2 > < S \parallel S \parallel S > . \quad (2.109)$$

Moreover, the reduced matrix element $< L_1 \parallel C^2 \parallel L_2 >$ can be rewritten (see Appendix B) as

$$< L_1 \parallel C^2 \parallel L_2 >= (-1)^{L_1} \sqrt{(2L_1+1)(2L_2+1)} \begin{pmatrix} L_1 & 2 & L_2 \\ 0 & 0 & 0 \end{pmatrix} . \quad (2.110)$$

The selection rule that can be derived from the expression above is $\Delta L = 0, \pm 2$. The spin dipolar part of the dipole-dipole interaction can therefore couple P-states of different principal quantum numbers ($\Delta L = 0$) but also the ground state (S-state) to excited D-states ($\Delta L = \pm 2$).

From Eq. 2.107, Eq. 2.108 and Eq. 2.109, by setting $S = 1/2$ and $I = 7/2$, we obtain the following general formula

$$< n_1 J_1, F, M \mid H_{d-d} \mid n_2 J_2, F, M >=$$

$$= (-1)^{F+J_2+L_1+1} < a_{l,j} > 3\sqrt{7} \sqrt{(2J_1+1)(2J_2+1)} \begin{Bmatrix} J_1 & 7/2 & F \\ 7/2 & J_2 & 1 \end{Bmatrix} \left[ H_{hf}^{(\text{orbital})} + H_{hf}^{(\text{spin})} \right] ,$$
$$(2.111)$$

where we have explicitly separated the contribution of the magnetic dipole orbital interaction

$$H_{hf}^{(\text{orbital})} = (-1)^{J_2} 2\sqrt{3} \begin{Bmatrix} L_1 & J_1 & 1/2 \\ J_2 & L_2 & 1 \end{Bmatrix} \delta_{L_1, L_2} , \quad (2.112)$$

from that of the spin dipolar interaction

$$
H_{hf}^{(\mathrm{spin})} = (-1)^{7/2} 3\sqrt{10}\sqrt{(2L_1+1)(2L_2+1)} \begin{pmatrix} L_1 & 2 & L_2 \\ 0 & 0 & 0 \end{pmatrix} \begin{Bmatrix} L_1 & L_2 & 2 \\ 1/2 & 1/2 & 1 \\ J_1 & J_2 & 1 \end{Bmatrix} \cdot
$$
(2.113)

The expectation value of the constant $a_{l,j}$ in a state $(L, J)$ is related to the hyperfine constant $A_{nL_J}$ by the relation

$$
< a_{l,j} > = A_{nL_J} \frac{J(J+1)}{L(L+1)} \,,
$$
(2.114)

and in the one-electron atom approximation does not depend on J. It is important to observe here that this last equation leads to the approximation $A_{nP_{1/2}} = 5A_{nP_{3/2}}$ used in Section 2.4.7. As we already remarked this does not hold in a strict sense in the case of Cs where the ratio of the hyperfine constants $A_{nP_J}$ is about 5.8 and $a_{l,j}$ does depend also on the total electronic angular momentum J. Following the parametrization of Arimondo et al. [82], the expectation value of the coupling constant $< a_{l,j} >$ between two generic states $| n_1L_1, J_1 >$ and $| n_2L_2, J_2 >$ is given by

$$
< a_{l,j} > = \frac{2g_I}{h} \cdot \frac{\mu_0}{4\pi} \cdot \mu_b^2 \cdot < r^{-3} > = \frac{2g_I}{h} \frac{\mu_0}{4\pi} \mu_b^2 \int_0^\infty \Psi_{n_1L_1,j_1}^* \cdot \frac{1}{r^3} \cdot \Psi_{n_2L_2,j_2} r^2 dr \,,
$$
(2.115)

where $g_I \approx 0.39885 \cdot 10^{-3}$ is the nuclear g-factor and $\mu_b$ is the Bohr magneton.

As a test for our model wave functions (described in Appendix C) we have first calculated the well-known diagonal hyperfine constants $A_{nP_{1/2,3/2}}$ for n=6,7,8,9 and we have observed a satisfactory agreement, at a level of 4–8%, with the experimental values given in the literature, as shown in Table 2.2. Numerical estimations of some of the off-diagonal expectation values $< a_{l,j} >$ used in this work are shown in Tables 2.3 and 2.4 [16].

We finally note that if we set $J_1 = J_2$ in Eq. 2.111 and $a_{l,j} = A_{nP_J} \frac{J(J+1)}{2}$ we obtain the well-known hyperfine splitting of the $P_J$ multiplets. For $J_1 = J_2 = 1/2$,

$$
< H_{hf} >_{F=4} = \frac{7}{4} A_{6P_{1/2}}
$$
$$
< H_{hf} >_{F=3} = -\frac{9}{4} A_{6P_{1/2}} \,,
$$
(2.116)

and for $J_1 = J_2 = 3/2$,

$$
< H_{hf} >_{F=5} = \frac{21}{4} A_{6P_{3/2}}
$$
$$
< H_{hf} >_{F=4} = \frac{1}{4} A_{6P_{3/2}}
$$
$$
< H_{hf} >_{F=3} = -\frac{15}{4} A_{6P_{3/2}}
$$
$$
< H_{hf} >_{F=2} = -\frac{27}{4} A_{6P_{3/2}} \,.
$$
(2.117)

---

[16]In the calculations presented in this work we use for the hyperfine coupling constants the more precise experimental values rather than our calculated values whenever they are available in the literature.

| Diagonal hf constants | Our calculated value | From the literature | Deviation |
|:---:|:---:|:---:|:---:|
| $A_{6P_{1/2}}$ | 317.9 | $291.920(19)^{(a)}$ | 8% |
| $A_{6P_{3/2}}$ | 48.3 | $50.275(3)^{(b)}$ | 4% |
| $A_{7P_{1/2}}$ | 99.9 | $94.35(4)^{(c)}$ | 6% |
| $A_{7P_{3/2}}$ | 15.4 | $16.605(6)^{(c)}$ | 7% |
| $A_{8P_{1/2}}$ | 45.0 | $42.97(10)^{(c)}$ | 5% |
| $A_{8P_{3/2}}$ | 7.0 | $7.58(1)^{(c)}$ | 7% |

Table 2.2: Hyperfine coupling constants for P-states calculated by using our wave functions based on a semiempirical Thomas-Fermi potential model, compared to the experimental values given by (a) Rafac et al. [83], (b) Tanner et al. [84], (c) Arimondo et al. [82]. The values are given in MHz.

| Off-diagonal hyperfine (d-d interaction) coupling constants | Value [$MHz$] |
|:---:|:---:|
| $\langle 6P_{1/2} \mid a_{l,j} \mid 6P_{3/2} \rangle$ | 187.8 |
| $\langle 6P_{1/2} \mid a_{l,j} \mid 7P_{1/2} \rangle$ | 785.3 |
| $\langle 6P_{1/2} \mid a_{l,j} \mid 7P_{3/2} \rangle$ | 106.1 |
| $\langle 6P_{1/2} \mid a_{l,j} \mid 8P_{1/2} \rangle$ | 527.1 |
| $\langle 6P_{1/2} \mid a_{l,j} \mid 8P_{3/2} \rangle$ | 71.5 |
| $\langle 6P_{3/2} \mid a_{l,j} \mid 7P_{1/2} \rangle$ | 105.2 |
| $\langle 6P_{3/2} \mid a_{l,j} \mid 7P_{3/2} \rangle$ | 143.1 |
| $\langle 6P_{3/2} \mid a_{l,j} \mid 8P_{1/2} \rangle$ | 70.63 |
| $\langle 6P_{3/2} \mid a_{l,j} \mid 8P_{3/2} \rangle$ | 9.64 |
| $\langle 7P_{1/2} \mid a_{l,j} \mid 7P_{3/2} \rangle$ | 85.0 |
| $\langle 7P_{1/2} \mid a_{l,j} \mid 8P_{1/2} \rangle$ | 422.2 |
| $\langle 7P_{1/2} \mid a_{l,j} \mid 8P_{3/2} \rangle$ | 57.3 |
| $\langle 7P_{3/2} \mid a_{l,j} \mid 8P_{1/2} \rangle$ | 57.1 |
| $\langle 7P_{3/2} \mid a_{l,j} \mid 8P_{3/2} \rangle$ | 7.8 |

Table 2.3: Expectation values of the hyperfine coupling constant $a_{l,j}$ between states $n_1 P_{j_1}$ and $n_2 P_{j_2}$. These values were obtained by evaluating Eq. 2.115 with the wave functions that we calculate by means of the Schrödinger/Thomas-Fermi potential approach.

| Off-diagonal hyperfine (d-d interaction) coupling constants | Value [$MHz$] |
|---|---|
| $\langle 6S_{1/2} \mid a_{l,j} \mid 5D_{3/2} \rangle$ | 74.3 |
| $\langle 6S_{1/2} \mid a_{l,j} \mid 6D_{3/2} \rangle$ | 42.9 |
| $\langle 6S_{1/2} \mid a_{l,j} \mid 7D_{3/2} \rangle$ | 28.4 |
| $\langle 6S_{1/2} \mid a_{l,j} \mid 8D_{3/2} \rangle$ | 21.2 |

Table 2.4: Expectation values of the hyperfine coupling constant $a_{l,j}$ between the ground state $6S_{1/2}$ and states $nD_{3/2}$. The coupling to states $nD_{5/2}$ is forbidden by the selection rule $\Delta J = 0, \pm 1$. These values were obtained by evaluating Eq. 2.115 with the wave functions that we calculate by means of the Schrödinger/Thomas-Fermi potential approach.

### 2.5.1.2 The Fermi-contact interaction

In the alkali ground state (L=0) the hyperfine interaction is given by the Fermi-contact term $H_{Fermi}$. In this special case the interaction is

$$H_{Fermi} = a_s \mathbf{S} \cdot \mathbf{I}. \tag{2.118}$$

By applying the usual angular momentum decoupling rules and by setting $S = 1/2$ and $I = 7/2$ we can write

$$< n_1 S_{1/2}, F, M \mid H_{Fermi} \mid n_2 S_{1/2}, F, M >=$$

$$= (-1)^F < a_s > 6\sqrt{21} \left\{ \begin{matrix} 1/2 & 7/2 & F \\ 7/2 & 1/2 & 1 \end{matrix} \right\} \left\{ \begin{matrix} 1/2 & 1/2 & 0 \\ 1/2 & 1/2 & 1 \end{matrix} \right\} =$$

$$= (-1)^F < a_s > 3\sqrt{21} \left\{ \begin{matrix} 1/2 & 7/2 & F \\ 7/2 & 1/2 & 1 \end{matrix} \right\}, \quad (2.119)$$

where

$$< a_s >= \frac{g_I}{h} \frac{16\pi}{3} \frac{\mu_0}{4\pi} \mu_b^2 \Psi_{n_1 S_{1/2}}^*(0) \Psi_{n_2 S_{1/2}}(0). \tag{2.120}$$

In the equation above $\Psi_{n S_{1/2}}(0)$ is the value of the electronic wave function at the nucleus position. We notice that by setting $n_1 = n_2 \equiv n$ the definition above leads to the traditional expression of the hyperfine constant $A_{n S_{1/2}} \propto \mid \Psi_{n S_{1/2}}(0) \mid^2$.

The diagonal hyperfine constants calculated with our wave functions are compared to the experimental ones given in the literature in Table 2.5.

The expectation values of the coupling constants $a_s$, involving the ground state and S states with n=7,8,9, calculated with our model wave functions are listed in Table 2.6.

| Diagonal hf constants | Our calculated value | From the literature | Deviation |
|:---:|:---:|:---:|:---:|
| $A_{6S_{1/2}}$ | 2412.9 | $2298.158^{(a)}$ | 5% |
| $A_{7S_{1/2}}$ | 576.4 | $545.90(9)^{(b)}$ | 5% |
| $A_{8S_{1/2}}$ | 230.9 | $219.3(2)^{(c)}$ | 5% |
| $A_{9S_{1/2}}$ | 115.5 | $110.1(5)^{(a)}$ | 5% |

Table 2.5: Hyperfine coupling constants for S-states calculated by using our wave functions based on a semiempirical potential model, compared to the experimental values given by (a) Arimondo et al. [82], (b) Gilbert et al. [87], (c) Herrmann et al. [88]. The values are given in MHz.

| Off-diagonal hyperfine (Fermi interaction) coupling constants | Value $[MHz]$ |
|:---:|:---:|
| $\langle 6S_{1/2} \mid a_s \mid 7S_{1/2} \rangle$ | 1186.6 |
| $\langle 6S_{1/2} \mid a_s \mid 8S_{1/2} \rangle$ | 751.1 |
| $\langle 6S_{1/2} \mid a_s \mid 9S_{1/2} \rangle$ | 531.1 |

Table 2.6: Expectation values of the hyperfine coupling constant $a_s$ between states $6S_{1/2}$ and $nS_{1/2}$. These values are obtained by evaluating Eq. 2.120 with the wave functions that we calculate by means of a Thomas-Fermi potential approach.
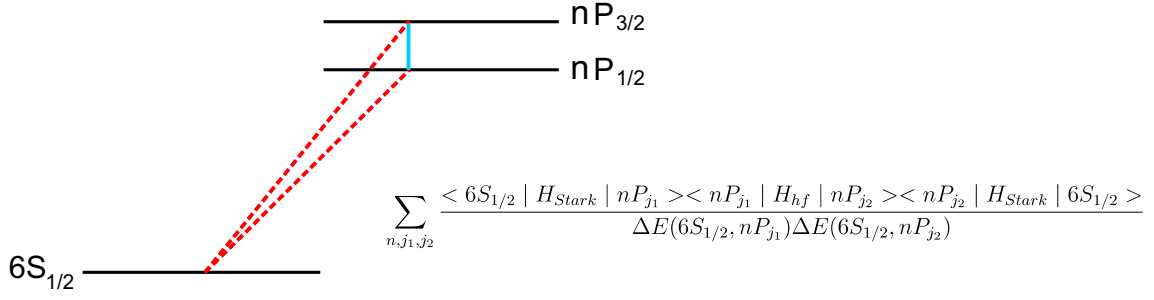
$$\sum_{n,j_1,j_2} \frac{< 6S_{1/2} \mid H_{Stark} \mid nP_{j_1} >< nP_{j_1} \mid H_{hf} \mid nP_{j_2} >< nP_{j_2} \mid H_{Stark} \mid 6S_{1/2} >}{\Delta E(6S_{1/2}, nP_{j_1})\Delta E(6S_{1/2}, nP_{j_2})}$$

Figure 2.10: The hyperfine interaction (blue solid line) can mix the wave functions of $nP_J$ states that belong to the same fine-structure multiplet but with different electronic angular momenta J. The Stark interaction (dotted red lines) then connects the ground state to the excited P states as shown in the figure.

### 2.5.2 Off-diagonal hyperfine matrix elements $< nP_{j_1} \mid H_{hf} \mid nP_{j_2} >$

We consider the mixing of levels belonging to the same fine-structure multiplet, that is we calculate matrix elements of the form

$$< nP_{j_1}, F, M \mid H_{d-d} \mid nP_{j_2}, F, M >,$$

with $j_1 \neq j_2$. We observe that in Eq. 2.111

- the electronic angular momenta $J_i$ can assume only the values 1/2 and 3/2,

- the 6j-symbols *do not* change under the exchange of $J_1$ and $J_2$,

- the 9j-symbol changes sign under an exchange of $J_1$ and $J_2$,

and we obtain after some calculations the compact result

$$< nJ_1, F, M \mid H_{d-d} \mid nJ_2, F, M >=$$
$$= -\frac{\sqrt{(5 - F)(F - 2)(F + 3)(F + 6)}}{12} \cdot < a_{l,j} >_{nP_{1/2}, nP_{3/2}} . \quad (2.121)$$

In Fig. 2.10 we represent schematically the contribution of these matrix elements and the role that they play in the third order Stark interaction.
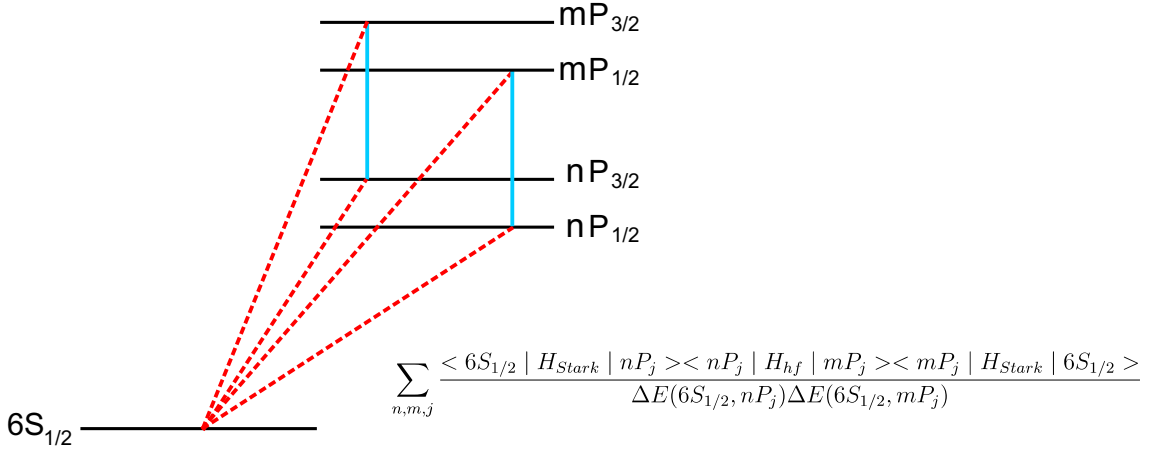
$$\sum_{n,m,j} \frac{<6S_{1/2}\mid H_{Stark}\mid nP_j><nP_j\mid H_{hf}\mid mP_j><mP_j\mid H_{Stark}\mid 6S_{1/2}>}{\Delta E(6S_{1/2},nP_j)\Delta E(6S_{1/2},mP_j)}$$

Figure 2.11: The hyperfine interaction (blue solid line) can mix the wave functions of $nP_J$ states with different principal quantum number n. The interaction is in this case diagonal in all the other quantum numbers: $L$, $J$, $F$ and $M_F$. The Stark interaction (dotted red lines) connects first the ground state to the state $nP_j$, then the state $mP_j$ back to the ground state, or viceversa.

### 2.5.3 Off-diagonal hyperfine matrix elements $<n_1P_J\mid H_{hf}\mid n_2P_J>$

We next consider the mixing of levels defined by the same set of quantum numbers except for the principal quantum number n, that is we calculate matrix elements of the form

$$<n_1,L,J,F,M\mid H_{d-d}\mid n_2,L,J,F,M>,$$

with $n_1\neq n_2$. This coupling scheme and its contribution to the third order Stark interaction is represented graphically in Fig. 2.11. From Eq. 2.111 we obtain the compact expressions

$$<n_1,J=1/2,F,M\mid H_{d-d}\mid n_2,J=1/2,F,M>$$
$$=(-1)^F\frac{336}{(F+4)(F+5)}<a_{l,j}>_{n_1P_{1/2},n_2P_{1/2}}, \quad (2.122)$$

and

$$<n_1,J=3/2,F,M\mid H_{d-d}\mid n_2,J=3/2,F,M>$$
$$=\frac{2}{15}[2F(F+1)-39]<a_{l,j}>_{n_1P_{3/2},n_2P_{3/2}} \ . \quad (2.123)$$

$$\sum_{n,m,j_{1,2}} \frac{<6S_{1/2}\mid H_{Stark}\mid nP_{j_1}><nP_{j_1}\mid H_{hf}\mid mP_{j_2}><mP_{j_2}\mid H_{Stark}\mid 6S_{1/2}>}{\Delta E(6S_{1/2},nP_{j_1})\Delta E(6S_{1/2},mP_{j_2})}$$
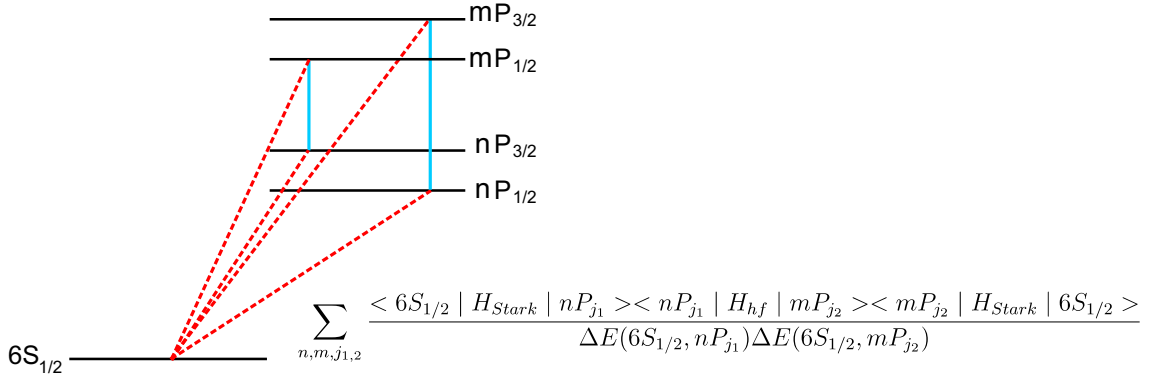
Figure 2.12: The hyperfine interaction (blue solid line) mixes the wave functions of states with different principal quantum number n and different total electronic angular momentum J. The Stark interaction (dotted red lines) then mixes the excited P states into the ground state.

### 2.5.4 Off-diagonal hyperfine matrix elements: $<n_1P_{J_1}\mid H_{hf}\mid n_2P_{J_2}>$

The most general case concerns the coupling of levels with different n and different J

$$<n_1,L,J_1,F,M\mid H_{d-d}\mid n_2,L,J_2,F,M>,$$

with $n_1\neq n_2$ and $J_1\neq J_2$. This mixing scheme is sketched in Fig. 2.12. The compact form of Eq. 2.121 can be easily generalized to this case just by replacing the hyperfine constants as follows

$$<a_{l,j}>_{nP_{1/2},nP_{3/2}}\longrightarrow<a_{l,j}>_{n_1P_{1/2},n_2P_{3/2}}\ .$$

### 2.5.5 Off-diagonal hyperfine matrix elements $<6S_{1/2}\mid H_{hf}\mid nD_{3/2}>$

We consider now the mixing of the ground state to excited D-states, i.e., we calculate matrix elements of the form

$$<6S_{1/2},F,M\mid H_{d-d}\mid nD_{3/2},F,M>\ .$$

These matrix elements are allowed because of the term $H_{hf}^{(\mathrm{spin})}$ in Eq. 2.111. The inspection of this term also shows that the ground state cannot be coupled to states $nD_{5/2}$ because of the selection rule $\Delta J=0,\pm1$. After some calculations we obtain the compact form

$$\begin{aligned}<6S_{1/2},F,M\mid & H_{d-d}\mid nD_{3/2},F,M>\\ &=\frac{\sqrt{(5-F)(F-2)(F+3)(F+6)}}{4}<a_{l,j}>_{6S_{1/2},nD_{3/2}}\ .\quad(2.124)\end{aligned}$$

In Fig. 2.13 we represent schematically the contribution of these matrix elements.

$$2 \sum_{n,m,j} \frac{< 6S_{1/2} \mid H_{Stark} \mid nP_j >< nP_j \mid H_{Stark} \mid mD_{3/2} >< mD_{3/2} \mid H_{hf} \mid 6S_{1/2} >}{\Delta E(6S_{1/2}, nP_j)\Delta E(6S_{1/2}, mD_{3/2})}$$
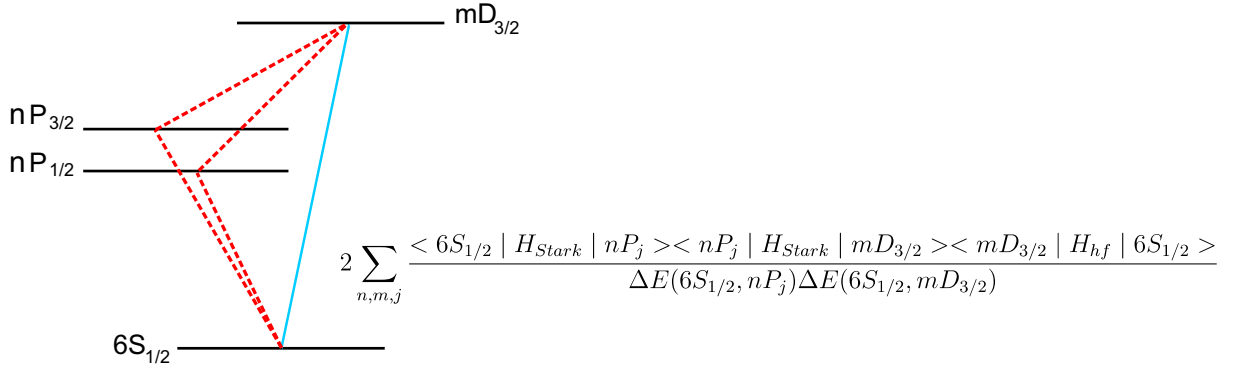
Figure 2.13: The hyperfine interaction (blue solid line) can mix the wave functions of $mD_{3/2}$ states into the ground state. The Stark interaction (dotted red lines) then connects S, P and D-states as shown in the figure. We observe essentially two equivalent paths to come back to the ground state via excited P and S states: $6S \to n_P P \to n_D D \to 6S$ and $6S \to n_D D \to n_P P \to 6S$. In both cases one has to apply twice the Stark operator and once the hyperfine operator. Note that these two paths are equivalent. This explains the factor 2 in front of the sum.



$$2 \sum_{n,m,j} \frac{< 6S_{1/2} \mid H_{Stark} \mid nP_j >< nP_j \mid H_{Stark} \mid mS_{1/2} >< mS_{1/2} \mid H_{hf} \mid 6S_{1/2} >}{\Delta E(6S_{1/2}, nP_j)\Delta E(6S_{1/2}, mS_{1/2})}$$
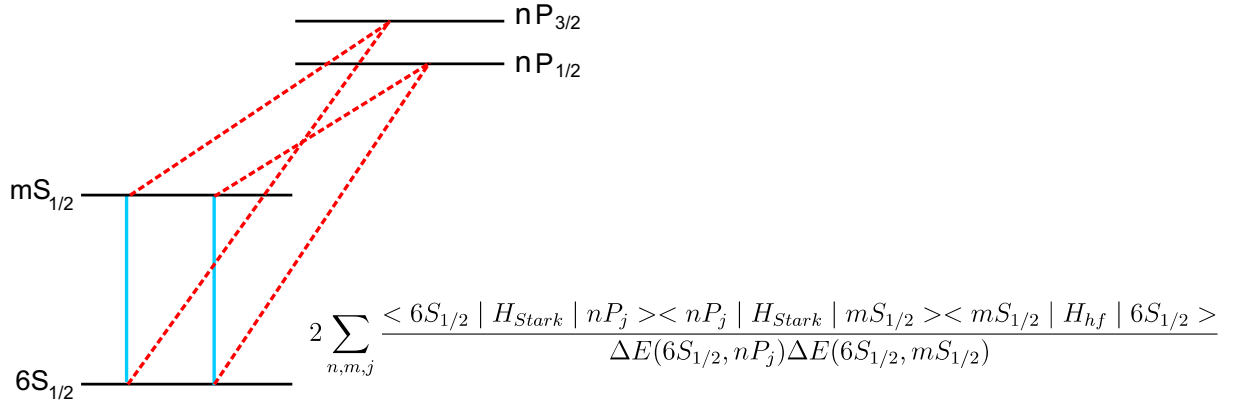
Figure 2.14: The hyperfine interaction (blue solid line) mixes the wave functions of excited S states into the ground state and the Stark interaction (dotted red lines) couples S and P states. We observe essentially two equivalent paths to come back to the ground state via excited P and S states: $6S \to n_P P \to n_S S \to 6S$ and $6S \to n_S S \to n_P P \to 6S$. In both cases one has to apply twice the Stark operator and once the hyperfine operator. Note that these two paths are equivalent. This explains the factor 2 in front of the sum.

### 2.5.6 Off-diagonal hyperfine matrix elements $< n_1 S_{1/2} \mid H_{hf} \mid n_2 S_{1/2} >$

The ground state $6S_{1/2}$ can be coupled to an excited $nS$ state by the Fermi-contact hyperfine interaction as shown by Eq. 2.119. This coupling scheme contributes to the third order quadratic Stark effect in the way sketched in Fig. 2.14. From Eq. 2.119 one obtains

$$< n_1 S_{1/2}, F, M \mid H_{Fermi} \mid n_2 S_{1/2}, F, M >$$
$$= (-1)^F \frac{126}{(F+4)(F+5)} < a_s >_{n_1 S_{1/2}, n_2 S_{1/2}} . \quad (2.125)$$

### 2.5.7 Comparison to off-diagonal matrix elements calculated by other authors

Off diagonal hyperfine matrix elements of the form

$$< n_1, L, J, F, M \mid H_{hf} \mid n_2, L, J, F, M >,$$

were calculated by Feichtner et al. [65] using hydrogenic wave functions. These authors define the following coupling coefficients

$$\frac{< 6S_{1/2}, F \mid H_{hf} \mid nS_{1/2}, F >}{\Delta E(6S_{1/2}, nS_{1/2})} = \mathbb{A}_{n \frac{1}{2} F} \qquad \text{n=7,8,9} , \qquad (2.126)$$

$$\frac{< 6P_J, F \mid H_{hf} \mid nP_J, F >}{\Delta E(6P_J, nP_J)} = \mathbb{B}_{nJF} \qquad \text{n=7,8,9} , \qquad (2.127)$$

and

$$\frac{< 7P_J, F \mid H_{hf} \mid nP_J, F >}{\Delta E(7P_J, nP_J)} = \mathbb{C}_{nJF} \qquad \text{n=8,9} . \qquad (2.128)$$

Numerical values for all the coefficients $\mathbb{A}_{n \frac{1}{2} F}$, $\mathbb{B}_{nJF}$ and $\mathbb{C}_{nJF}$ defined above are given in [65]. We can thus compare the hyperfine matrix elements calculated with our wave functions to the ones obtained by Feichtner et al. with hydrogenic wave functions. This comparison is shown in Table 2.7. Our calculated matrix elements show a disagreement with the ones from [65] in the range of $5\% - 1000\%$. The origin of these large discrepancies is not yet clear. Nevertheless we stress again the fact that at present, with our wave functions, we are able to calculate well-known diagonal hyperfine constants with an error that is never larger than a few percent. These results make us feel confident in the reliability of our wave functions. On the other hand, the hydrogenic approximations used by Feichtner and collaborators are not completely clear in some steps of their calculations. Basically these authors parameterize the off-diagonal hyperfine matrix elements in terms of the S-state hydrogenic wave functions at r=0 according to the so-called Fermi-Segré (FS) formula

$$\mid \Psi_{nS}^{FS}(0) \mid^2 = \frac{1}{\pi} \frac{Z_a^2 Z}{n_*^3 a_0^3} (1 + \frac{\partial \Delta}{\partial n}) , \qquad (2.129)$$

where the correction factors $Z_a$, $n_*^3$ and $1 + \frac{\partial \Delta}{\partial n}$ are given for instance in [86]. The off-diagonal matrix elements involving P-states are then expressed as

$$< nP_J \mid H_{hf} \mid n'P_J > \propto \frac{\Psi_{nS}(0)\Psi_{n'S}(0)}{\mid \Psi_{6S}(0) \mid^2} . \qquad (2.130)$$

This approximation and the choice of the correction parameters given above could be possible sources for the observed discrepancies. Another very important difference between our model and Feichtner's model is that in the latter the spin-orbit interaction is neglected whereas it is explicitly included in the calculation of our model wave functions (see Appendix C). This feature of Feichtner's model seems to be a very coarse approximation.

The matrix elements involving S-states can also be estimated by applying the factorization rule [17]

$$< n_1 S \mid H_{hf} \mid n_2 S > = \sqrt{< n_1 S \mid H_{hf} \mid n_1 S >< n_2 S \mid H_{hf} \mid n_2 S >} . \tag{2.131}$$

The calculated and experimental diagonal hyperfine constants are given in Table 2.5. By using our calculated values the factorization rule yields

$$\langle 6S_{1/2}F = 3 \mid H_{hf} \mid 7S_{1/2}F = 3 \rangle = 2653.5 \quad MHz \,,$$
$$\langle 6S_{1/2}F = 4 \mid H_{hf} \mid 7S_{1/2}F = 4 \rangle = 2063.8 \quad MHz \,,$$
$$\langle 6S_{1/2}F = 3 \mid H_{hf} \mid 8S_{1/2}F = 3 \rangle = 1679.4 \quad MHz \,,$$
$$\langle 6S_{1/2}F = 4 \mid H_{hf} \mid 8S_{1/2}F = 4 \rangle = 1306.2 \quad MHz \,, \tag{2.132}$$

and by using the experimental values of Table 2.5

$$\langle 6S_{1/2}F = 3 \mid H_{hf} \mid 7S_{1/2}F = 3 \rangle = 2520.2 \quad MHz \,,$$
$$\langle 6S_{1/2}F = 4 \mid H_{hf} \mid 7S_{1/2}F = 4 \rangle = 1960.1 \quad MHz \,,$$
$$\langle 6S_{1/2}F = 3 \mid H_{hf} \mid 8S_{1/2}F = 3 \rangle = 1597.3 \quad MHz \,,$$
$$\langle 6S_{1/2}F = 4 \mid H_{hf} \mid 8S_{1/2}F = 4 \rangle = 1242.4 \quad MHz \,, \tag{2.133}$$

We observe a global satisfactory agreement, at the level of 5%, between the results reported above. Moreover, if we compare the off-diagonal matrix elements given in Eqs. 2.132, obtained by applying the "geometrical average rule" (Eq. 2.131), to the calculated ones given in Table 2.7, we notice that the factorization rule is very well fulfilled (to better than 1%) in the frame of our model. This is of course another point in favor of the reliability of our model wave functions.

Furthermore, the following matrix elements

$$\langle 6P_{1/2}F = 4 \mid H_{hf} \mid 6P_{3/2}F = 4 \rangle \approx 91.2 \quad MHz \,,$$
$$\langle 6P_{1/2}F = 3 \mid H_{hf} \mid 6P_{3/2}F = 3 \rangle \approx 80.1 \quad MHz \,,$$

were derived in [91] from a lowest-order Dirac-Hartree-Fock calculation. These values have to be compared to our results: 185.1 $MHz$ and 162.6 $MHz$ respectively. In this case the discrepancy amounts to about a factor two.

---

[17]The validity of this rule for s-states was recently demonstrated to hold at a level of $10^{-3}$ by Dzuba and Flambaum [89] in the frame of a relativistic many-body calculation. On the other hand this formula is not believed to be applicable to P-states [90].

| Hyperfine matrix elements | Our value | From [65] | Deviation[%] |
|---|---|---|---|
| $\langle 6S_{1/2}F = 3 \mid H_{hf} \mid 7S_{1/2}F = 3\rangle$ | -2669.8 | -2407.5 | 10 |
| $\langle 6S_{1/2}F = 4 \mid H_{hf} \mid 7S_{1/2}F = 4\rangle$ | 2076.5 | 1873.7 | 10 |
| $\langle 6S_{1/2}F = 3 \mid H_{hf} \mid 8S_{1/2}F = 3\rangle$ | -1690.0 | -1517.4 | 10 |
| $\langle 6S_{1/2}F = 4 \mid H_{hf} \mid 8S_{1/2}F = 4\rangle$ | 1314.5 | 1189.1 | 10 |
| $\langle 6P_{1/2}F = 3 \mid H_{hf} \mid 7P_{1/2}F = 3\rangle$ | -4711.8 | -804.2 | 486 |
| $\langle 6P_{1/2}F = 4 \mid H_{hf} \mid 7P_{1/2}F = 4\rangle$ | 3664.7 | 625.2 | 486 |
| $\langle 6P_{3/2}F = 2 \mid H_{hf} \mid 7P_{3/2}F = 2\rangle$ | -515.2 | -484.5 | 6 |
| $\langle 6P_{3/2}F = 3 \mid H_{hf} \mid 7P_{3/2}F = 3\rangle$ | -286.2 | -269.2 | 6 |
| $\langle 6P_{3/2}F = 4 \mid H_{hf} \mid 7P_{3/2}F = 4\rangle$ | 19.1 | 17.9 | 7 |
| $\langle 6P_{3/2}F = 5 \mid H_{hf} \mid 7P_{3/2}F = 5\rangle$ | 400.7 | 376.7 | 6 |
| $\langle 6P_{1/2}F = 3 \mid H_{hf} \mid 8P_{1/2}F = 3\rangle$ | -3162.6 | -505.8 | 525 |
| $\langle 6P_{1/2}F = 4 \mid H_{hf} \mid 8P_{1/2}F = 4\rangle$ | 2459.8 | 394.1 | 524 |
| $\langle 6P_{3/2}F = 2 \mid H_{hf} \mid 8P_{3/2}F = 2\rangle$ | -34.6 | -304.6 | 89 |
| $\langle 6P_{3/2}F = 3 \mid H_{hf} \mid 8P_{3/2}F = 3\rangle$ | -19.2 | -169.0 | 89 |
| $\langle 6P_{3/2}F = 4 \mid H_{hf} \mid 8P_{3/2}F = 4\rangle$ | 1.28 | 11.0 | 88 |
| $\langle 6P_{3/2}F = 5 \mid H_{hf} \mid 8P_{3/2}F = 5\rangle$ | 26.9 | 236.6 | 89 |
| $\langle 7P_{1/2}F = 3 \mid H_{hf} \mid 8P_{1/2}F = 3\rangle$ | -2533.2 | -233.6 | 984 |
| $\langle 7P_{1/2}F = 4 \mid H_{hf} \mid 8P_{1/2}F = 4\rangle$ | 1970.3 | 181.6 | 985 |
| $\langle 7P_{3/2}F = 2 \mid H_{hf} \mid 8P_{3/2}F = 2\rangle$ | -28.1 | -14.1 | 99 |
| $\langle 7P_{3/2}F = 3 \mid H_{hf} \mid 8P_{3/2}F = 3\rangle$ | -15.6 | -78.3 | 80 |
| $\langle 7P_{3/2}F = 4 \mid H_{hf} \mid 8P_{3/2}F = 4\rangle$ | 1.04 | 5.2 | 80 |
| $\langle 7P_{3/2}F = 5 \mid H_{hf} \mid 8P_{3/2}F = 5\rangle$ | 21.9 | 109.6 | 80 |

Table 2.7: Hyperfine matrix elements calculated by following the procedure described in the text with our wave functions obtained from the Schrödinger equation for a Thomas-Fermi potential, compared to the same matrix elements calculated by Feichtner et al. [65] with hydrogenic wave functions. The values are given in MHz.

To our knowledge, in the literature there are no theoretical nor experimental results concerning off-diagonal hyperfine matrix elements between S and D-states and between P-states with different principal quantum number n and different angular momentum J.


## 2.6 Reduced electric dipole matrix elements

Beside the hyperfine matrix elements, a precise knowledge of reduced electric dipole matrix elements is essential for evaluating the Stark matrix elements. Some of the numerical values of the reduced matrix elements used in this work are listed in Table 2.8.

We recall here that in the literature there are several experimental and theoretical papers [65–75] which give numerical values for reduced electric dipole matrix elements. Unfortunately these works show severe disagreements concerning the signs of the matrix elements. This is of course a problem for our calculations, in which the phases of the matrix elements appear explicitly. With our atomic wave functions, we can reproduce the absolute theoretical and experimental values of all the matrix elements involving states with $n = 6$–$8$ reported in the literature, with a discrepancy that varies from a few percent to about 10% in the worst case, as shown in Table 2.8. Our phases comply with the conventions described in Appendices A and B and in Section 2.1.2. We attribute the sign differences between our calculated reduced matrix elements and the ones given in the literature to the conventions discussed in the appendices.

The situation is well summed up in Table 2.8 where we show a comparison between some of our numerical values and the corresponding reduced matrix elements reported in [65, 69, 72–74].

Very precise experimental values (with uncertainties on the order of $10^{-3}$) for the dipole matrix elements involving nS and mP states with n,m=6,7 can be found in the literature [72–74]. The discrepancies with respect to our calculated values are in these cases in the range 2–8% as shown in Table 2.8.

In the numerical calculations that follow, in this and in the next Chapter, we will use experimental values for hyperfine coupling constants and reduced dipole matrix elements whenever they are available in the literature. We will therefore use the experimental values for the matrix elements $< nS_{1/2} \parallel d \parallel mP_{1/2,3/2} >$ with n,m=6,7 from [72–74] and the experimental values given in Table 2.5 for the diagonal hyperfine constants $A_{nS_{1/2}}$. The off-diagonal hyperfine matrix elements $< 6S_{1/2} \mid H_{hf} \mid nS_{1/2} >$ are then evaluated by applying the factorization rule given in Eq. 2.131. All the other parameters used in the calculations presented in this work are derived from our Cs wave functions.


## 2.7 Third order Stark effect with hyperfine off-diagonal terms

We have calculated the electronic wave functions for $nS_J$, $nP_J$, and $nD_J$ states up to $n = 18$ and we have included in the third order perturbation expansion all the off-diagonal matrix elements treated in Section 2.5.

| Reduced matrix elements | Our value $[a_0e]$ | from the literature | Deviation[%] |
|---|---|---|---|
| $\langle 6S_{1/2}\|er\|6P_{1/2}\rangle$ | 4.43 | -4.4978(61) [a] | 2 |
| $\langle 6S_{1/2}\|er\|6P_{3/2}\rangle$ | 6.13 | -6.3311(72) [a] | 3 |
| $\langle 6S_{1/2}\|er\|7P_{1/2}\rangle$ | 0.26 | 0.2757(20) [b] | 6 |
| $\langle 6S_{1/2}\|er\|7P_{3/2}\rangle$ | 0.54 | 0.5856(50) [b] | 8 |
| $\langle 6S_{1/2}\|er\|8P_{1/2}\rangle$ | 0.073 | 0.079 [c] | 8 |
| $\langle 6S_{1/2}\|er\|8P_{3/2}\rangle$ | 0.19 | 0.214 [c] | 11 |
| $\langle 7S_{1/2}\|er\|6P_{1/2}\rangle$ | -4.28 | -4.233(22) [d] | 1 |
| $\langle 7S_{1/2}\|er\|6P_{3/2}\rangle$ | -6.58 | -6.479(31) [d] | 2 |
| $\langle 7S_{1/2}\|er\|7P_{1/2}\rangle$ | 10.76 | 10.308(15) [d] | 4 |
| $\langle 7S_{1/2}\|er\|7P_{3/2}\rangle$ | 14.71 | 14.320(20) [d] | 3 |
| $\langle 7S_{1/2}\|er\|8P_{1/2}\rangle$ | 1.02 | -0.917 [c] | 11 |
| $\langle 7S_{1/2}\|er\|8P_{3/2}\rangle$ | 1.80 | -1.624 [c] | 10 |
| $\langle 8S_{1/2}\|er\|6P_{1/2}\rangle$ | 0.99 | 1.004 [e] | 1 |
| $\langle 8S_{1/2}\|er\|6P_{3/2}\rangle$ | 1.46 | -1.46 [e] | < 1 |
| $\langle 8S_{1/2}\|er\|7P_{1/2}\rangle$ | 9.09 | -8.75 [e] | 4 |
| $\langle 8S_{1/2}\|er\|7P_{3/2}\rangle$ | 13.78 | 13.59 [e] | 1 |
| $\langle 8S_{1/2}\|er\|8P_{1/2}\rangle$ | -17.7 | - | - |
| $\langle 8S_{1/2}\|er\|8P_{3/2}\rangle$ | -24.5 | - | - |

Table 2.8: Numerical values of the reduced matrix elements of the electric dipole operator. In the third column we report the matrix elements given in the literature. (a) experimental values from Rafac et al. [74]; (b) experimental values from Vasilyev et al. [73]; (c) theoretical values from Blundell et al. [69]; (d) experimental values from Safronova et al. [72] and (e) theoretical values from Feichtner et al. [65].

### 2.7.1 General considerations on the perturbation expansion

The hyperfine off-diagonal terms can be grouped in three distinct families.

- The hyperfine mixing of P-states leads to:

$$\sum_{n_1,n_2} \sum_{j_1,j_2} \sum_{f,m} \frac{<n_2 P_{j_2}, f, m \mid H_{hf} \mid n_1 P_{j_1}, f, m>}{\Delta E(6S_{1/2}, n_1 P_{j_1}) \Delta E(6S_{1/2}, n_2 P_{j_2})} \times$$
$$\times <6S_{1/2}, F, M_F \mid H_{Stark} \mid n_2 P_{j_2}, f, m><n_1 P_{j_1}, f, m \mid H_{Stark} \mid 6S_{1/2}, F, M_F> .$$
$$(2.134)$$

- The hyperfine mixing of S- and D-states leads to:

$$2 \sum_{n_1,n_2} \sum_{j} \sum_{f,m} \frac{<6S_{1/2}, F, M_F \mid H_{hf} \mid n_2 D_{3/2}, F, M_F>}{\Delta E(6S_{1/2}, n_2 D_{3/2}) \Delta E(6S_{1/2}, n_1 P_j)} \times$$
$$\times <n_2 D_{3/2}, F, M_F \mid H_{Stark} \mid n_1 P_j, f, m><n_1 P_j, f, m \mid H_{Stark} \mid 6S_{1/2}, F, M_F> .$$
$$(2.135)$$

- The mixing of S states leads to:

$$2 \sum_{n_1} \sum_{n_2 \neq 6} \sum_{j} \sum_{f,m} \frac{<6S_{1/2}, F, M_F \mid H_{hf} \mid n_2 S_{1/2}, F, M_F>}{\Delta E(6S_{1/2}, n_2 S_{1/2}) \Delta E(6S_{1/2}, n_1 P_j)} \times$$
$$\times <n_2 S_{1/2}, F, M_F \mid H_{Stark} \mid n_1 P_j, f, m><n_1 P_j, f, m \mid H_{Stark} \mid 6S_{1/2}, F, M_F> .$$
$$(2.136)$$

The term in Eq. 2.136 is proportional to the hyperfine mixing of S-states only and yields a contribution which *does not* depend on the magnetic quantum number $M_F$. This term produces only a scalar effect which affects the shift of the clock transition frequency but not the tensor polarizability $\alpha_2^{(3)}$. On the other hand, Eqs. 2.134 and 2.135 depend on the hyperfine mixing of P-states and on the hyperfine mixing of S- and D-states, respectively, and thus lead to an $M_F$−dependent contribution which affects the value of $\alpha_2^{(3)}$. We thus conclude that all the terms represented by Eqs. 2.134, 2.135 and 2.136 contribute to the Stark shift of the clock transition frequency $\Delta\nu_{00}$, while only Eqs. 2.134 and 2.135 contribute to the tensor polarizability.

As we already did in the part dedicated to the diagonal terms, we apply the Wigner-Eckart theorem and the usual decoupling rules for angular momenta to Eqs. 2.134, 2.135 and 2.136. Then we isolate the terms proportional to $3M_F^2 - F(F + 1)$ and we write the perturbation in the form given by Eq. 2.71, from which it is straightforward to calculate the corrections to the parameters $\alpha_2^{(3)}$ and $\alpha_0^{(3)}$, which are responsible for the splitting of magnetic sub-levels and for the hyperfine-transition shift, respectively.

We observed that the relative importance with which the diagonal and off-diagonal matrix elements contribute to the two effects of interest, i.e., $\alpha_2^{(3)}$ and $\Delta\nu_{00}$, is quite different, as clearly shown in table 2.9. These different weights will play a central role in the estimation of the uncertainty of the clock frequency shift. This very important point will be addressed in Chapter 3.

| Matrix elements | Contributions [%] to | |
| :---: | :---: | :---: |
| | $\alpha_2^{(3)}$ | $\Delta\nu_{00}$ |
| $< 6S_{1/2} \mid H_{hf} \mid 6S_{1/2} >$ | — | 58.1 |
| $< nP_j \mid H_{hf} \mid nP_j >$ | 146.9 | −1.2 |
| $< 6S_{1/2} \mid H_{hf} \mid nS_{1/2} >$ | — | 40.9 |
| $< n_1P_j \mid H_{hf} \mid n_2P_j >$ | 90.9 | < 0.01 |
| $< nP_{j_1} \mid H_{hf} \mid nP_{j_2} >$ | −35.0 | 1.6 |
| $< n_1P_{j_1} \mid H_{hf} \mid n_2P_{j_2} >$ | −1.7 | 0.1 |
| $< 6S_{1/2} \mid H_{hf} \mid nD_{3/2} >$ | −101.1 | 0.5 |

Table 2.9: Relative contributions of diagonal and off-diagonal matrix elements to the tensor polarizability $\alpha_2^{(3)}$ and to the hyperfine clock transition Stark shift $\Delta\nu_{00}$. The first two lines refer to the diagonal hyperfine matrix elements, while the other 5 lines describe the contributions of the different types of off-diagonal matrix elements.

## 2.7.2 The tensor polarizability

The numerical evaluation of Eq. 2.67 together with Eqs. 2.134, 2.135 and 2.136 yields

$$\alpha_2^{(3)}(F = I \pm J) = \mp 3.72(25) \times 10^{-2} \frac{Hz}{(kV/cm)^2} . \qquad (2.137)$$

In Fig. 2.8 we have shown the existence of a large discrepancy between theory and experiments. In Fig. 2.15 we include the result given above and we claim that the present calculation of $\alpha_2^{(3)}$ finally yields, after 40 years, a good agreement with all the experimental data.

The precision of our result strongly depends on the uncertainty of the hyperfine and electric dipole matrix elements calculated by using our Schrödinger wave functions. In order to make an estimation of this uncertainty we have used the wave functions to evaluate well-known atomic parameters, such as diagonal hyperfine constants and reduced electric dipole matrix elements of low-lying states and we have compared them to the corresponding experimental values [18]. We have thus found discrepancies in the range 2–8%, as shown in Tables 2.2, 2.5 and 2.8. We have then assumed an average error of 5% for the reduced matrix elements and for the off-diagonal hyperfine constants used in the calculations and we have estimated a final uncertainty for $\alpha_2^{(3)}$ of about 7%.

---

[18]For the estimation of the uncertainty we have considered only reduced dipole matrix elements involving states with n=6,7 and hyperfine constants for nS- and nP-states with n=6,7,8, because precise experimental values for these parameters are available in the literature, as one can see in Tables 2.2, 2.5 and 2.8.
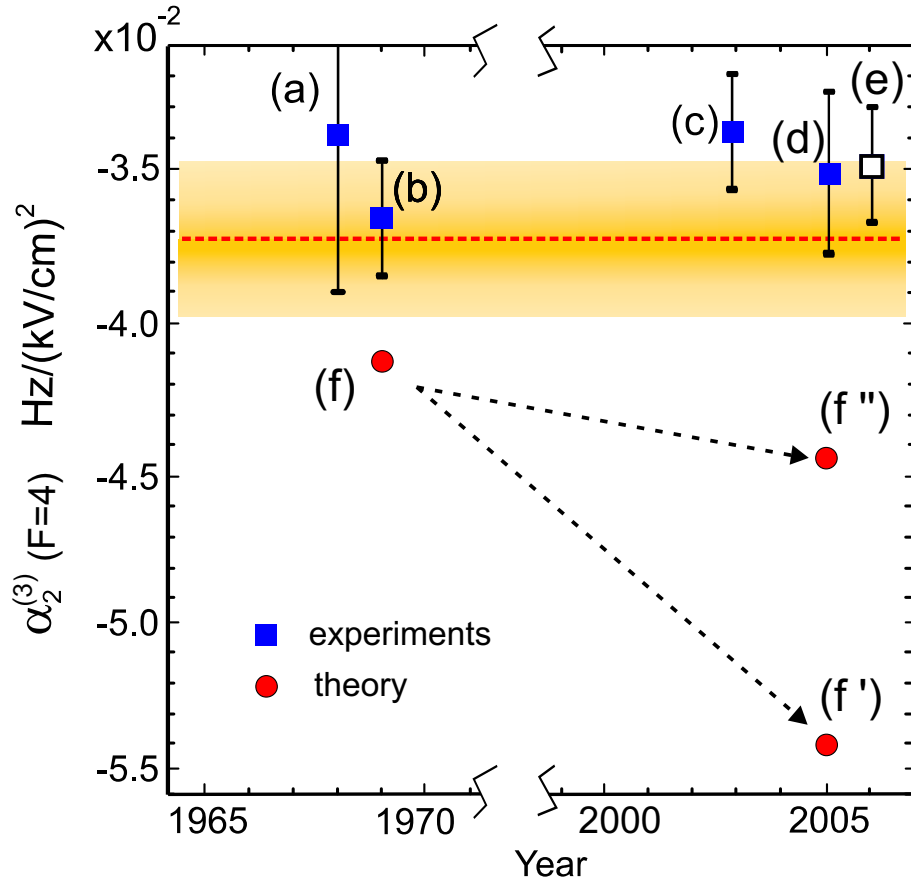
Figure 2.15: The third order tensor polarizability of the F=4 Cs ground state. The filled squares represent experimental values of (a) from Carrico et al.[62], (b) from Gould et al.[63], (c) from Ospelkaus et al. [64] and (d) from this work [85]. The empty square (e) represents a weighted average of (a), (b), (c) and (d). The dots represent (f) the theoretical value from [63] given in Eq. 2.94 and (f',f") our re-evaluations (Eqs. 2.89,2.102) of the latter value as discussed in Section 2.4.7. The dotted horizontal line is the result of the present work with its uncertainty (shaded band).

# Chapter 3

# The quadratic Stark effect in the ground state of cesium

We recall that the Stark shift of a generic level $\mid F, M_F >$ of the ground state of cesium can be parameterized in terms of the third order scalar polarizability $\alpha_0^{(3)}$ and of the tensor polarizability $\alpha_2^{(3)}$ as

$$\Delta E^{(3)}(F, M_F) = -\frac{1}{2} \cdot \alpha_0^{(3)}(F) \cdot \mathbb{E}^2 - \frac{1}{2} \cdot \alpha_2^{(3)}(F) \cdot \frac{3M_F^2 - F(F+1)}{28} \cdot \frac{3\cos^2(\theta) - 1}{2} \cdot \mathbb{E}^2 \ , \ (3.1)$$

where $\theta$ defines the orientation of the electric field with respect to a given quantization axis [1].

The expression 3.1 has been introduced in the previous chapter in the frame of a detailed third order perturbation analysis of the interaction between an atom and an external electric field. Here we show the effect of this interaction on the Zeeman and hyperfine structures of the ground state of cesium.

## 3.1 The quadratic Stark shift of the Zeeman levels

In Fig. 3.1 and Fig 3.2 we plot the shift of the magnetic sub-levels of the hyperfine components F=4 and F=3 in the ground state of Cs as a function of the electric field for two orthogonal orientations of the field, $\theta = 0$ and $\theta = \pi/2$, and for the forbidden tensor polarizability given by Eq. 2.137. One can notice that the effect of the Stark interaction in the configuration $\theta = \pi/2$ is reduced by a factor of 2 with respect to the configuration $\theta = 0$ due to the factor $(3\cos^2(\theta) - 1)/2$. One can also note that the level (F=3,M=2) is not shifted by the electric field because of the factor $3M^2 - F(F+1)$.

The dependence of the splitting of the magnetic sub-levels on the orientation of the electric field can be appreciated in Fig. 3.3 where their shift is plotted as a function of the angle $\theta$ for an electric field of $50 \, kV/cm$. The principal feature appearing from this figure is the existence of a *magic angle* $\theta_m$ at which the Stark effect vanishes and the magnetic levels are not shifted by the electric field. The origin of the angle $\theta_m$ can be easily understood by looking at Eq. 3.1: the effect of the applied electric field vanishes when

---

[1] In our magnetic resonance experiments the direction of the static magnetic field $\vec{B}_0$, which defines the z-axis of our laboratory reference system, is often the most convenient choice for the quantization axis.
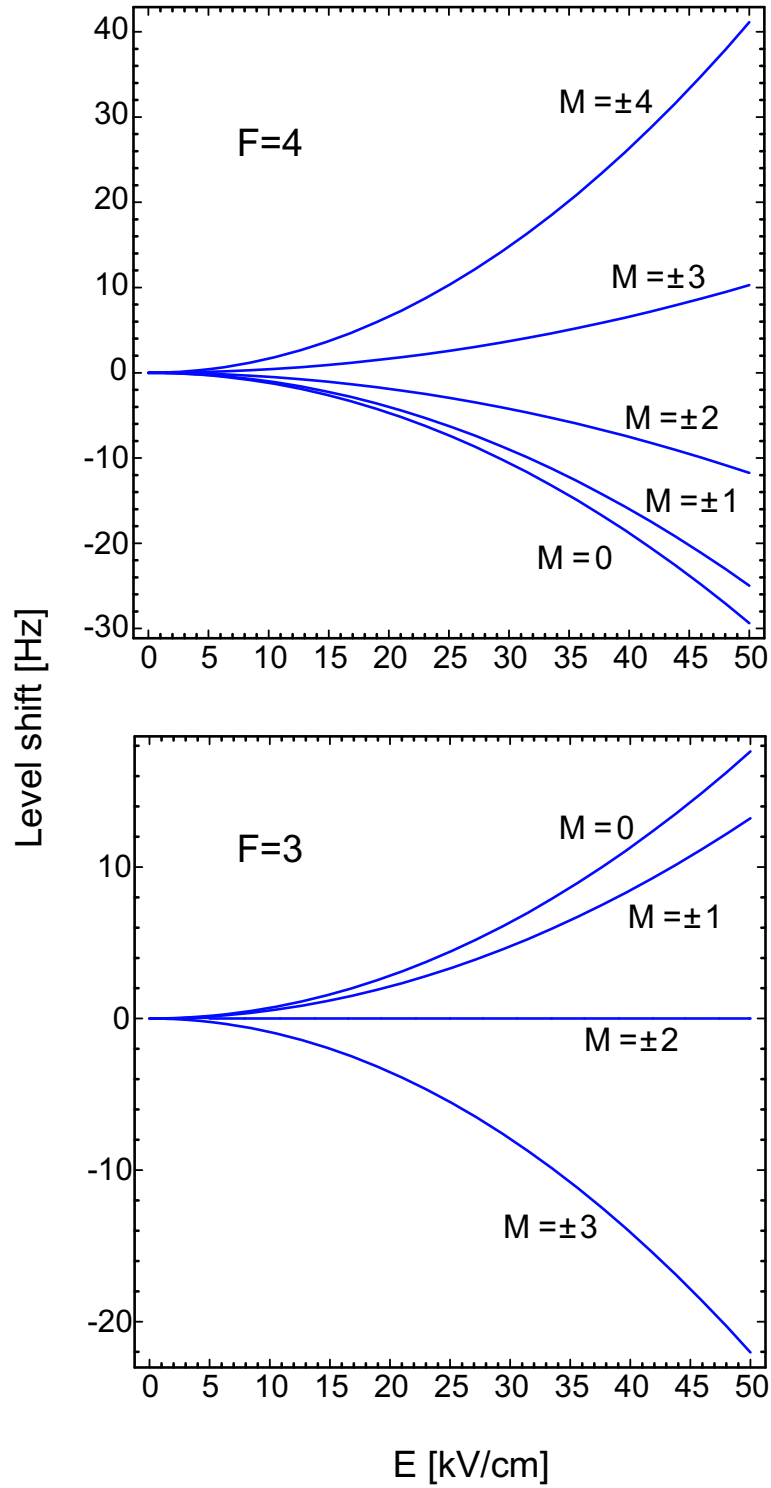
Figure 3.1: Quadratic Stark shift of the magnetic sub-levels of the ground state of Cs as a function of the applied electric field oriented along the quantization axis ($\theta = 0$).
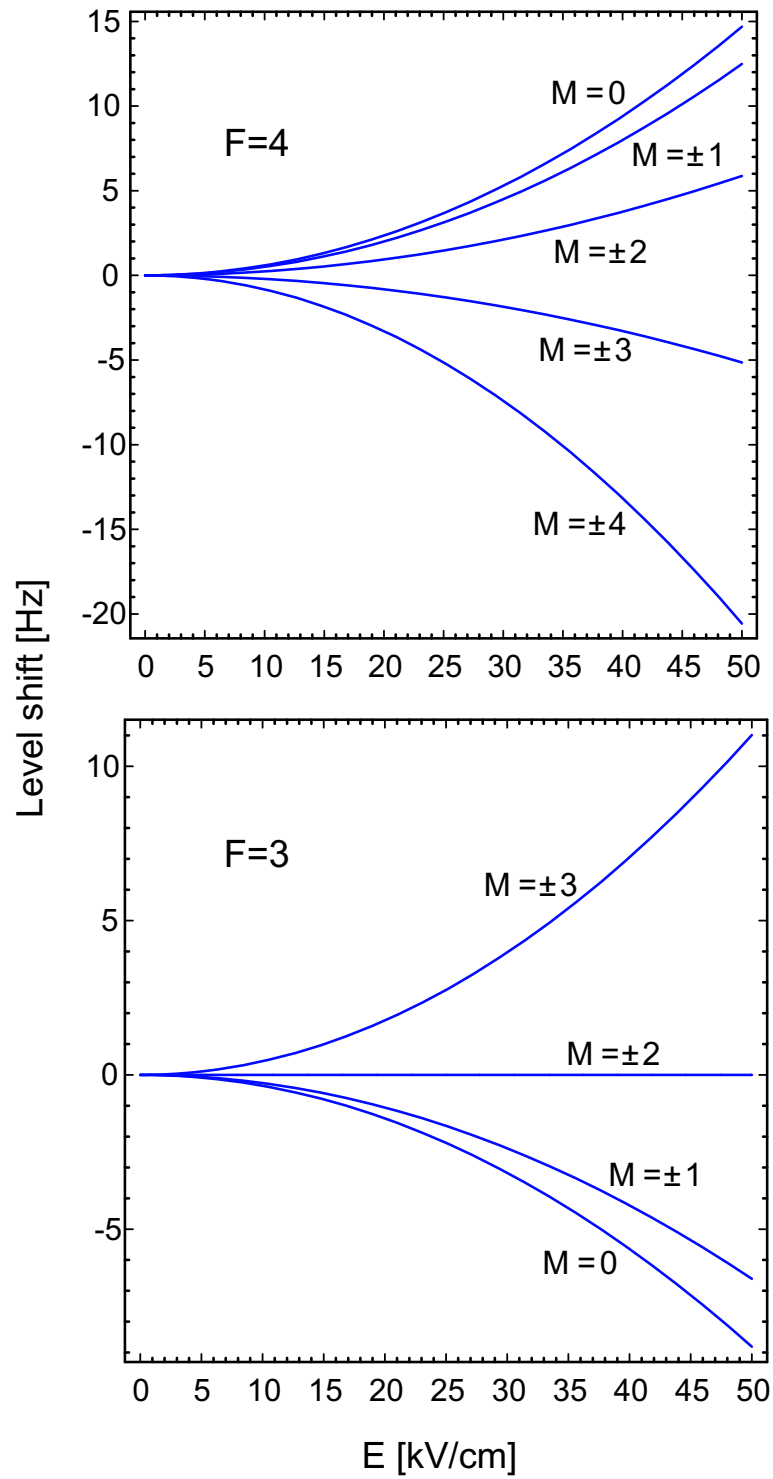
Figure 3.2: Quadratic Stark shift of the magnetic sub-levels of the ground state of Cs as a function of the applied electric field perpendicular to the quantization axis $(\theta = \pi/2)$.

$$\cos\theta_m = \frac{1}{\sqrt{3}}\,, \tag{3.2}$$

which is satisfied when $\theta_m \approx 54.7°$. In other words, the existence of the magic angle is just a consequence of the tensor character of the interaction.

In Fig. 3.4 we plot the shift of the frequencies corresponding to the magnetic transitions

$$\Delta\nu_{(4,4)\to(4,3)} = -\frac{3}{8}\alpha_2^{(3)}(4)\frac{3\cos^2\theta - 1}{2}\mathbb{E}^2\,, \tag{3.3}$$

and

$$\Delta\nu_{(3,3)\to(3,2)} = -\frac{15}{56}\alpha_2^{(3)}(3)\frac{3\cos^2\theta - 1}{2}\mathbb{E}^2\,, \tag{3.4}$$

as a function of the electric field in the two relevant configurations $\theta = 0$ (i.e., the configuration where the Stark effect is maximized) and $\theta = \pi/2$.

Although the tensor polarizabilities $\alpha_2^{(3)}(4)$ and $\alpha_2^{(3)}(3)$ have opposite signs, in presence of an external magnetic field, i.e., in a magnetic resonance experiment, the resonances corresponding to F=4 and F=3 are shifted in the same direction as discussed in 2.4.4. The situation is reversed in Sandars' model [33] where the shifts of the two resonances, i.e. F=4 and F=3, have opposite signs. From 3.3, 3.4 and by taking into account that $\nu_{(4,4)\to(4,3)} < \nu_{(3,3)\to(3,2)}$, one can infer the differential shift of the magnetic resonances corresponding to F=4 and F=3. According to our calculations we expect

$$\Delta\nu_{(3,3)\to(3,2)} - \Delta\nu_{(4,4)\to(4,3)} = -\frac{3}{28}\mid\alpha_2^{(3)}(4)\mid\frac{3\cos^2\theta - 1}{2}\mathbb{E}^2\,, \tag{3.5}$$

while Sandars' calculations predict a differential shift which is 6 times larger

$$\Delta\nu_{(3,3)\to(3,2)} - \Delta\nu_{(4,4)\to(4,3)} = -\frac{9}{14}\mid\alpha_2^{(3)}(4)\mid\frac{3\cos^2\theta - 1}{2}\mathbb{E}^2\,. \tag{3.6}$$

A comparison between the two models is plotted in Fig. 3.5. Thus the differential shift of the two hyperfine components F=4 and F=3 turns out to be the crucial test for the two models. This will be discussed in the chapter dedicated to experimental results.

Another interesting consequence of the quadratic Stark effect is the splitting

$$\Delta\nu_{(F,M)\to(F,M-1)} - \Delta\nu_{(F,M-1)\to(F,M-2)} = \frac{3}{28}\mid\alpha_2^{(3)}\mid\frac{3\cos^2\theta - 1}{2}\mathbb{E}^2$$

of single magnetic resonances within a given hyperfine level (see Section 2.4.4). This is plotted in Fig. 3.6 for $\theta = 0$ and $\theta = \pi/2$. One has to note here that since the absolute value of the tensor polarizability does not depend on F, the splitting has the same magnitude in the two hyperfine levels F=4 and F=3. The Stark effect thus produces a set of equally spaced peaks in both the levels F=4 and F=3.
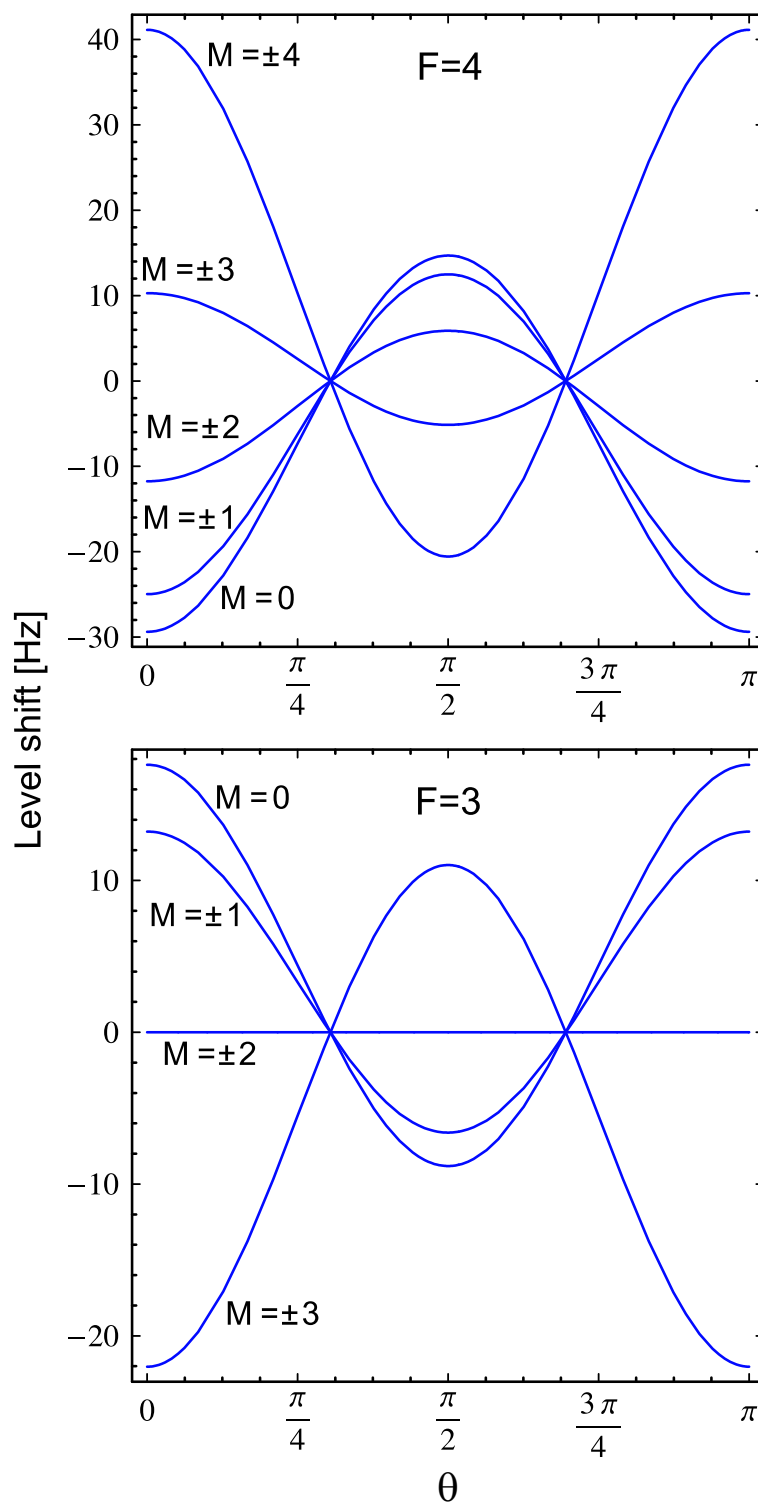
Figure 3.3: Quadratic Stark shift of the magnetic sub-levels of the ground state of Cs as a function of the orientation of the electric field with respect to the quantization axis z. The field is $50\,kV/cm$.
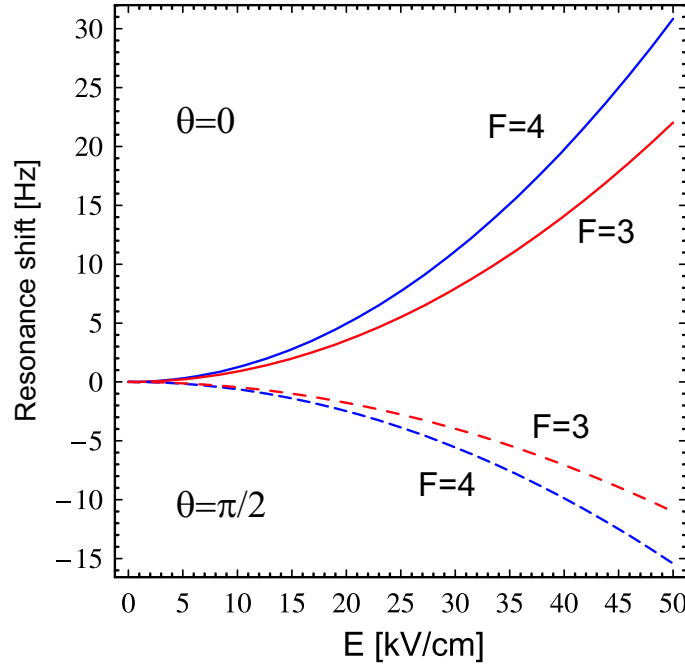
Figure 3.4: Quadratic Stark shift of the magnetic resonances $\mid F = 4, M = 4 > \rightarrow \mid F = 4, M = 3 >$ (in blue) and $\mid F = 3, M = 3 > \rightarrow \mid F = 3, M = 2 >$ (in red) as a function of the applied electric field. The solid lines refer to the configuration $\theta = 0$ while the dotted lines refer to $\theta = \pi/2$.
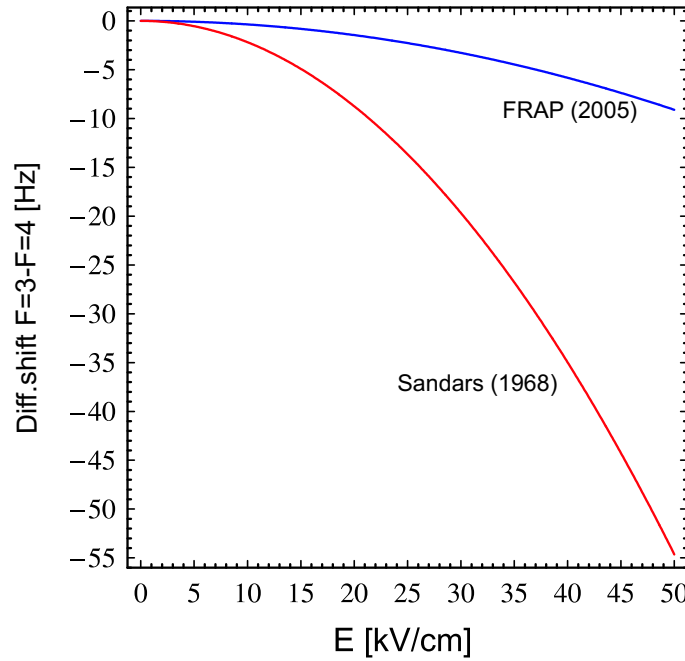


Figure 3.5: Differential shift $\Delta\nu_{(3,3)\rightarrow(3,2)} - \Delta\nu_{(4,4)\rightarrow(4,3)}$ according to our model (blue) and to Sandars' model (red).
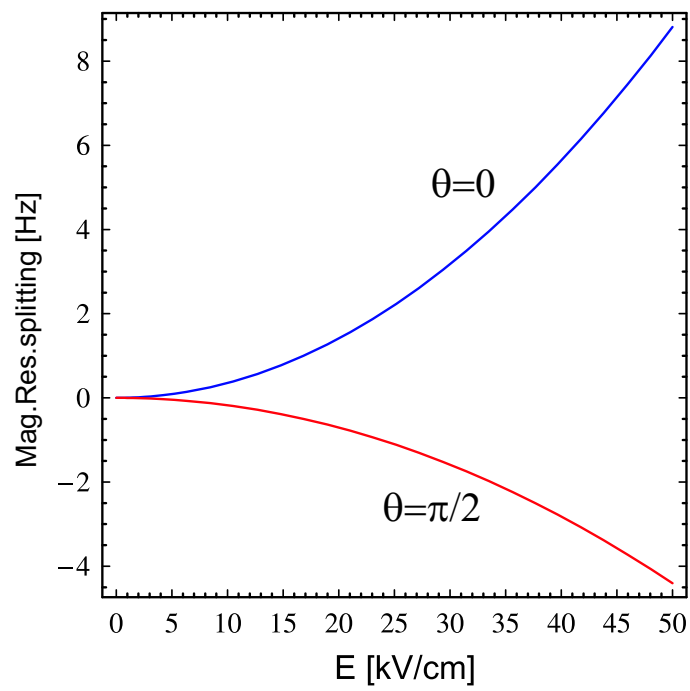
Figure 3.6: Quadratic Stark splitting of single magnetic resonances within a given hyperfine level. The splitting is the same for F=4 and F=3.

## 3.2 The quadratic Stark shift of the hyperfine clock transition

We recall from Section 2.4.5 that the Stark shift of the hyperfine clock transition frequency

$$\Delta\nu_{00} = |\, 6S_{1/2}, F = 4, M = 0 > \leftrightarrow |\, 6S_{1/2}, F = 3, M = 0 >$$

can be expressed in the form [2]

$$\Delta\nu_{00} = -\frac{1}{2}\left[\frac{16}{7}\alpha_0^{(3)}(4) - \frac{8}{7}\alpha_2^{(3)}(4)\frac{3\cos^2(\theta) - 1}{2}\right]\mathbb{E}^2\,. \tag{3.7}$$

The equation above is dominated by the third order scalar polarizability $\alpha_0^{(3)}$, which represents the contributions of the Fermi-contact interaction and of the scalar part of the magnetic dipole-dipole interaction, but it also has a small contribution, on the order of 1%, from the tensor part of the third order interaction [3].

The inclusion in the third order perturbation expansion of the off-diagonal contributions due to states $nS_{1/2}$, $nP_{1/2,3/2}$ and $nD_{3/2}$ with $n = 6$–18, as discussed in the previous chapter for the tensor polarizability, leads to the following result

$$\alpha_0^{(3)}(F = 4) = 1.81(1)\,\frac{Hz}{(kV/cm)^2}\,, \tag{3.8}$$

and

$$\alpha_0^{(3)}(F = 3) = -\frac{9}{7}\alpha_0^{(3)}(F = 4) = -2.33(1)\,\frac{Hz}{(kV/cm)^2}\,. \tag{3.9}$$

From Eq. 3.7 we obtain for the clock transition frequency

$$\Delta\nu_{00} = \left(-2.071 - 0.021\frac{3\cos^2(\theta) - 1}{2}\right)\mathbb{E}^2\left[\frac{Hz}{(kV/cm)^2}\right]\,, \tag{3.10}$$

where we have used our calculated value of the tensor polarizability (Eq. 2.137). This result yields

$$\Delta\nu_{00} = -2.09(1)\,\mathbb{E}^2\,\frac{Hz}{(kV/cm)^2}\quad\text{for}\ \theta = 0\,, \tag{3.11}$$

and

$$\Delta\nu_{00} = -2.06(1)\,\mathbb{E}^2\,\frac{Hz}{(kV/cm)^2}\quad\text{for}\ \theta = \frac{\pi}{2}\,. \tag{3.12}$$

This last value is in very good agreement with the very recent experimental result of Godone and collaborators [61] [point (g) in Fig. 3.7]

$$\Delta\nu_{00} = (-2.05 \pm 0.04)\mathbb{E}^2\,\frac{Hz}{(kV/cm)^2}\,,$$

---

[2]We have already observed in Section 2.4.5 that the coefficient of the tensor part of the effect, which is 8/7 in our case, has to be replaced by 2/7 if one assumes $\alpha_2(4) = \alpha_2(3)$ as prescribed by Sandars' model. This difference affects $\Delta\nu_{00}$ at a level which is only slightly below the present precision of primary atomic clocks. The next generation of Cs clocks will probably be sensitive to this correction.

[3]In other words, the contribution of the term $3M^2 - F(F + 1)$ evaluated for M=0.

obtained in the configuration $\theta = \pi/2$ and with the calculation of Micalizio et al. [92] [point (f) in Fig. 3.7].

As we discussed already in the previous chapter concerning the tensor polarizability $\alpha_2^{(3)}$, our theoretical estimations are affected by an uncertainty which is mainly due to the uncertainty of the calculated hyperfine and reduced dipole matrix elements. In Section 2.7.2 we have discussed the precision of our result and we have estimated an uncertainty of about 7% for the final value of the tensor polarizability. The situation is rather different and particularly interesting in the case of the clock frequency shift. As shown in Table 2.9, 99% of this effect is produced by 2 different types of hyperfine matrix elements only, i.e., the diagonal hyperfine interaction in the $6S_{1/2}$ ground state and the off-diagonal hyperfine interaction between the ground state and higher $nS$-states. Moreover, we found that 91% of the total effect (calculated for $n = 6\text{--}18$) is due only to these 2 families of matrix elements evaluated for $n = 6, 7$. In this case all the contributing hyperfine and electric dipole matrix elements can be traced back, directly or indirectly, to experimental quantities. The diagonal hyperfine matrix elements are proportional to the measured hyperfine splittings, while the off-diagonal hyperfine matrix elements between $S$ states of different principal quantum numbers $n$ can be expressed in terms of the geometrical averages of the hyperfine splittings of the coupled states. Dzuba et al. have shown [89] that this relation holds at a level of $10^{-3}$. Experimental values of the electric dipole matrix elements $< nS_{1/2} \parallel d \parallel mP_j >$ $(n, m = 6, 7)$ can be found in the literature [72–74] with relative errors on the order of $10^{-3}$. This gives us a high level of confidence in our value of the clock shift rate, for which we estimate an uncertainty in the sub-% range, represented in Fig. 3.7 by a horizontal band.

The effect of a static external electric field (static Stark effect) on the ground state hyperfine transition is of special interest for the atomic clock community, as it is strictly related to the so-called black body radiation (BBR) shift of the clock transition (dynamic Stark effect). The interaction of the atoms with the BBR field is one of the leading systematic shifts of the cesium clock frequency and it was shown [93] that the dynamic BBR shift can be parametrized in terms of the static Stark shift which is investigated here.

   At present, there are two conflicting experimental groups of results concerning the static Stark shift of the hyperfine transition in Cs. The most precise value of the first group was obtained by A.Clairon and collaborators at the Observatoire de Paris (France) in 1998 [60] [point (e) in Fig. 3.7] while the second group is represented by the recent result of Godone and collaborators at the Istituto Elettrotecnico Nazionale Galileo Ferraris (Torino, Italy) [61] (point (g) in Fig. 3.7). The difference between the results obtained by those two groups is 53 times the experimental uncertainty of the French result. At present the correction factor for the BBR shift commonly used by the atomic clock community is based on the precise experimental value of the Paris group [60] [point (e)], while our theoretical result seems to support the Italian measurement [61] [point (g)] in this open debate.

   We have to observe that the clock transition shift was calculated also by Feichtner et al. [65] [point (b)] in an approximation using hydrogenic wave functions and neglecting spin-orbit interactions, as already discussed in Section 2.5.7. Under these assumptions the scalar polarizability $\alpha_0^{(2)}$ can be factored out of their final result. Using a recent precision measurement of $\alpha_0^{(2)}$ [81] we have rescaled [point (b') in Fig. 3.7] the value of [65], which then becomes consistent with the present result.

   We believe that the problem of the large gap between the two families of experimental and theoretical results sketched in Fig. 3.7 deserves more attention due to its relevance in
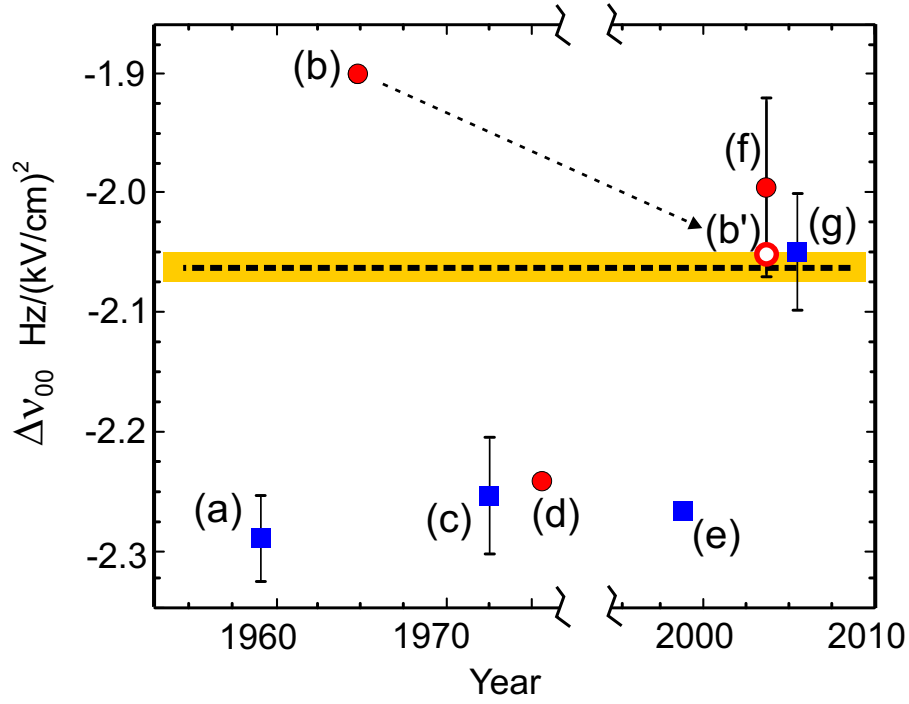
Figure 3.7: The static Stark shift of the clock transition frequency. The squares represent experimental values of Haun et al. [56](a), Mowat [59](c), Simon et al. [60](e), and Godone et al. [61](g). The dots represent theoretical values of Feichtner et al. [65](b), Lee et al. [94](d), and Micalizio et al. [92](f). The circle (b') represents the rescaled value of (b) as explained in the text. The error bar of point (e) is smaller than the symbol size. The dotted horizontal line is the result of the present work including uncertainty (shaded band).

the control of systematics effects in atomic clocks. Following this consideration, at present we are planning a novel refined measurement of the clock transition shift in an atomic beam experiment which will hopefully be started in the near future. We believe that new experimental data will help to shine more light onto this still unresolved important problem.

## 3.3 Summary

The quadratic Stark effect in the ground state $6S_{1/2}$ of cesium is represented graphically in Fig. 3.8 for a field of 20 kV/cm. We discuss briefly the figure.

In *first order*, the hyperfine interaction leads to the hyperfine splitting $\nu_{00}$ =9.192 GHz between the levels $F = I \pm J$. The contribution of the Stark interaction vanishes since the Stark operator cannot couple states with the same parity and in absence of magnetic fields the Zeeman sub-levels are degenerate.

In *second order*, the Stark interaction leads to a global scalar shift of the ground state. The second order effect does not depend on the quantum numbers F and $M_F$ and therefore the hyperfine and Zeeman sub-structures of the ground state are not affected by the interaction. The second order effect is parameterized in terms of the second order scalar polarizability $\alpha_0^{(2)}$. The estimation given in Eq. 2.47 yields a shift of the ground state of 20 MHZ.

In *third order*, the combination of the Stark interaction and of the hyperfine interaction leads to a scalar effect and a tensor effect. The scalar effect consists in an F-dependent contribution to the scalar polarizability which is responsible for the shift of the hyperfine clock transition frequency $\Delta\nu_{00}$. The scalar part of the third order perturbation is parameterized in terms of the third order scalar polarizability $\alpha_0^{(3)}$. The tensor effect depends on both the quantum numbers F and $M_F$. It gives a small additional contribution to the shift of the clock transition frequency $\Delta\nu_{00}$ and removes the degeneracy of the Zeeman sub-levels. The tensor part of the third order interaction is proportional to $3M^2 - F(F+1)$ and to the tensor polarizability $\alpha_2^{(3)}$. With our estimations of $\alpha_0^{(3)}$ and $\alpha_2^{(3)}$, given in Eqs. 3.8 and 2.137 respectively, and in a field of 20 kV/cm, the hyperfine transition frequency is reduced by 836 Hz while the splitting of the magnetic sub-levels can vary from 0.8 Hz to 5.6 Hz depending on the magnetic quantum number $M_F$.
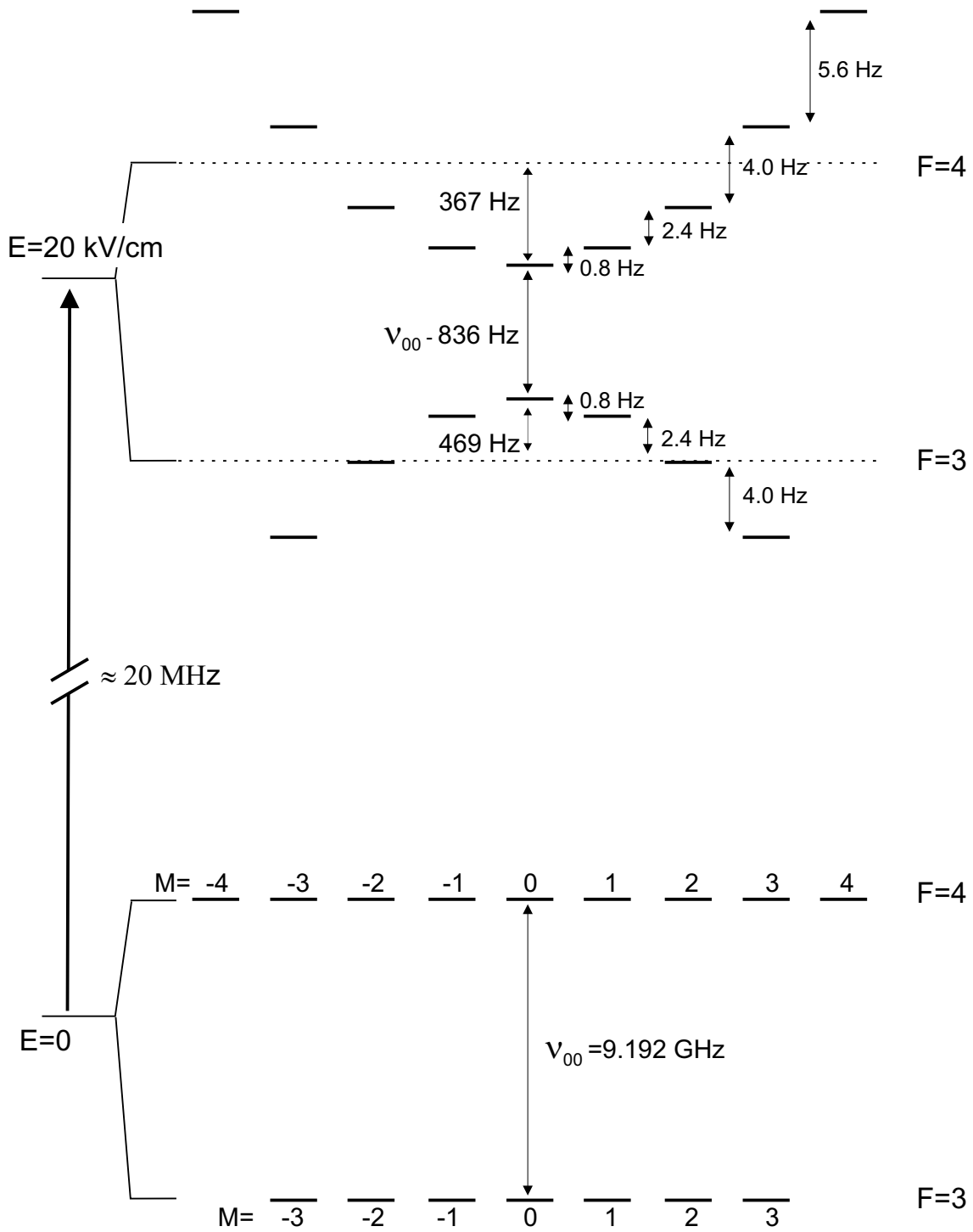
Figure 3.8: Résumé of the calculated Stark shifts of the Zeeman levels in the hyperfine structure of the cesium ground state. We assume an electric field of 20 kV/cm. Note that the details of this figure are not drawn to scale.

# Chapter 4

# The Optically Detected Magnetic Resonance

## 4.1 Introduction

In this chapter we describe the basic principles of the technique used in our experiments on Cs atoms embedded in solid $^4He$, i.e., the optically detected magnetic resonance (ODMR).

Magnetic resonance consists essentially in changing the orientation of the macroscopic magnetization associated with the spin polarization of the atomic sample by exposing it to a combination of static and oscillating magnetic fields. A high degree of spin polarization is thus the essential prerequisite for the occurrence and sensitive detection of magnetic resonance experiments.

In 1949 Kastler and Brossel [95] demonstrated that relevant population differences between the Zeeman sub-levels of the ground state can be created by irradiating a vapor of paramagnetic atoms with circularly polarized resonance light [1]. This process, known as optical pumping, is a very efficient method to create an orientation of the atomic spins and thus to produce a macroscopic magnetization. This technique cannot be applied to atoms isolated in conventional (Ne, Ar, Kr, Xe) rare gas solids because the spin polarization of the atoms is rapidly destroyed by the interaction with the crystal fields. In solid He, however, owing to its softness and compressibility, both a consequence of the quantum nature of this solid, the atoms reside in spherical bubbles in a diamagnetic and perfectly isotropic environment [2] and a very high degree of spin polarization can be achieved by optical pumping of embedded alkali atoms as first demonstrated by Weis et al. [17].

The optical pumping process changes the optical properties of the sample. The atoms irradiated with circularly polarized resonant light are transferred to a so-called *dark state* (the $| F = 4, M_F = 4 >$ state in the case of cesium) and the sample becomes transparent for the incoming laser beam. The decrease of fluorescence is then a direct measure of the efficiency of the optical pumping process. The contrast of the fluorescence

$$K = \frac{\mathcal{F}(t = 0) - \mathcal{F}(\infty)}{\mathcal{F}(t = 0)} \, , \qquad (4.1)$$

defines the relative change of the fluorescence rate $\mathcal{F}$ due to optical pumping. Typical

---

[1] A.Kastler was honored by the 1966 Nobel Prize in Physics for this discovery.

[2] As we explained in Chapter 1 this is only true in the bcc phase of solid $^4He$; the atoms are strongly perturbed in the anisotropic hcp phase as was first demonstrated by Kanorski et al. [23].

contrasts of 50% were observed in experiments on cesium atoms in solid helium [17].

When the atomic sample is exposed to a static magnetic field $\vec{B}_0$ the degeneracy of the Zeeman sub-levels is removed (Zeeman effect). In a classical picture the spin polarization precesses about the axis defined by the static magnetic field at the Larmor frequency $\omega_L = \frac{g\mu_B}{\hbar} B_0$.

The simultaneous interaction with an oscillating radio-frequency field $\vec{B}_1$, with frequency $\omega_{RF}$, induces magnetic dipole transitions between Zeeman sub-levels thus changing the orientation and/or the magnitude of the spin polarization of the atomic sample.

This change of polarization is most effective when the radio-frequency $\omega_{RF}$ matches the Larmor frequency $\omega_L$ associated with the static field $B_0$. The transitions induced by $B_1$ depopulate the dark state thus changing again the optical properties of the sample which is no longer transparent for the resonant radiation. The consequent increase of fluorescence can then be detected optically by scanning the radio-frequency $\omega_{RF}$ in the vicinity of the Larmor frequency $\omega_L$.

In conventional electron spin resonance (ESR) the polarization of the sample is obtained thermally and the detection of the magnetic resonance is performed by using pick-up coils. This traditional method can be successfully applied to typical samples characterized by atomic densities of $\approx 10^{20} - 10^{22}$ atoms/cm$^3$ but cannot be used in our experiment in which the density of atoms in the helium matrix is $\approx 10^8 - 10^9$ atoms/cm$^3$. On the contrary, the optical-rf double resonance technique with optical detection briefly described above guarantees both a very efficient preparation of the sample and an extremely sensitive detection thus enabling the investigation of low density samples.

## 4.2 Optical pumping

### 4.2.1 Creation of spin polarization

The basic idea of optical pumping is to transfer angular momentum from resonant circularly polarized light to the irradiated atomic sample to generate a non-thermal population distribution in the Zeeman sub-structure of the ground state, thus creating a spin polarization. This technique is illustrated in Fig. 4.1 for the D1 transition ($\mid 6S_{1/2} > \rightarrow \mid 6P_{1/2} >$) of cesium in solid helium.

Each photon of the resonant circularly polarized ($\sigma_+$) laser beam carries an angular momentum of $+\hbar$. When an atom absorbs a photon its angular momentum is thus increased by a quantum $+\hbar$. In other words, the resonant $\sigma_+-$polarized light induces transitions

$$\mid 6S_{1/2}, F, M > \rightarrow \mid 6P_{1/2}, f, M + 1 >,$$

and the magnetic quantum number of the irradiated atoms is thus increased by one unit at each absorption of a light photon.

The hyperfine structure of both the ground and excited states are not optically resolved in solid helium owing to the broadened excitation line ($\Delta\lambda \approx 10$ nm). For the same reason the optical transition is not saturated by applying typical light intensities $\leq 1$ mW. Under these conditions stimulated emission can be neglected and we can assume that the excited state relaxes back to the ground state only via spontaneous emission.

Under continuous optical excitation the ground-state levels with $M < 4$ are depopulated and all the atoms are finally transferred into the so-called dark state, i.e., the Zeeman level with the highest magnetic quantum number $\mid F = 4, M = 4 >$. This state does not
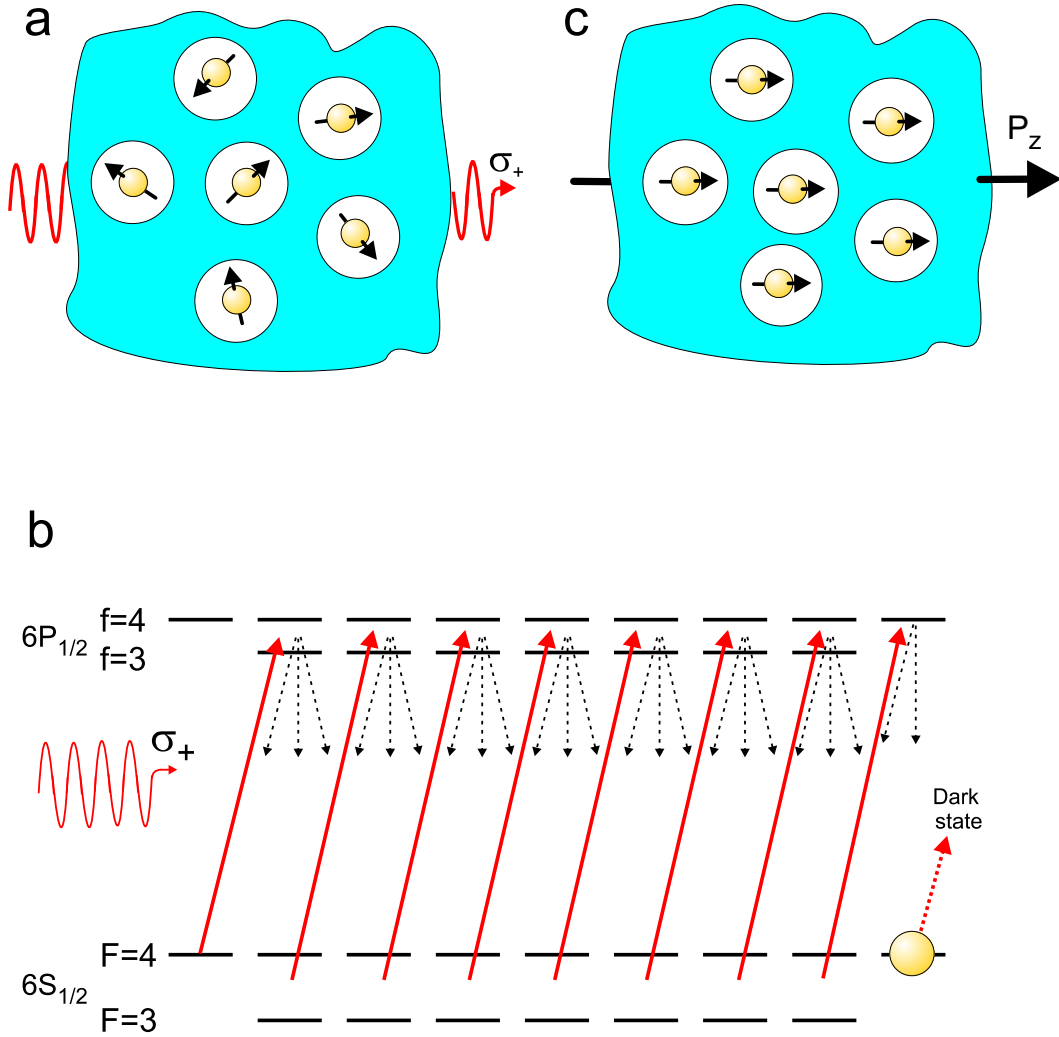
Figure 4.1: The optical pumping process in the solid He matrix. **(a)** The atomic sample is initially unpolarized, i.e., the atomic spins are uncorrelated and randomly oriented. This corresponds to equal populations $p_{F,M}$ of the Zeeman sub-levels of the ground state. We irradiate the atoms with $\sigma_+-$polarized light. **(b)** The resonant light induces $\Delta M = 1$ transitions represented by the solid lines. The excited state then relaxes via spontaneous emission back to the ground state through the allowed ($\Delta M = 0, \pm 1$) decay channels represented by the dashed lines. On average the populations are thus transferred to levels with higher magnetic quantum numbers M and finally all atoms end up in the *dark state* $| 4, 4 >$. Note that the hyperfine splitting in both the ground and the excited states cannot be resolved optically in solid helium owing to the broadened excitation line ($\Delta \lambda \approx 10$ nm). **(c)** The sample is polarized and the orientation of the atomic spins leads to a macroscopic spin polarization $P_z =< F_z >= \frac{1}{F} \sum_{M=-F}^{F} M_F p_{F,M}$.

couple to the resonant $\sigma_+$ light any more and the atomic sample becomes transparent for the laser beam with a corresponding decrease of the fluorescence intensity. The final orientation of the atomic spins leads to an ensemble spin polarization as sketched in Fig. 4.1.

The longitudinal polarization of an atomic ensemble with total angular momentum F is defined as the expectation value of the component $F_z$

$$P_z(F) \equiv\; < F_z > = \frac{1}{F} \sum_{M=-F}^{F} M_F p_{F,M} \, , \qquad (4.2)$$

where $p_{F,M}$ is the population of the Zeeman level $\mid F, M >$. This property of the spin polarized sample is then related to the fluorescence rate by [19]

$$\mathcal{F} = \mathcal{F}_{unpol} \left( 1 - \frac{1}{4}(P_z(4) - P_z(3)) \right) = \mathcal{F}_{unpol} \left( 1 - 2 < J_z > \right) \, , \qquad (4.3)$$

where $\mathcal{F}_{unpol}$ is the fluorescence rate of the unpolarized sample $(< J_z > = 0)$ and where the last equality can be proved by using well-known properties of the matrix elements of $J_z$ and $F_z$ (see for instance [86]). The fact that $\mathcal{F}$ does not depend on the quantum number F reflects the property that the hyperfine structure is not optically resolved in solid helium.

We can distinguish two different optical pumping mechanism, i.e., *repopulation pumping* and *depopulation pumping*. Basically, in repopulation pumping the spin-polarization is preserved in the excited state while in depopulation pumping the polarization in the excited state is destroyed by the coupling to the crystal (or by collisions in a high density vapor) and the populations are redistributed among the hyperfine and Zeeman sub-levels. In solid helium, owing to the spherical symmetry of the atomic bubble and to the diamagnetic character of the matrix, the atomic spins are not perturbed by crystalline fields and the dominant pumping mechanism turns out to be of the repopulation pumping type as first demonstrated by Lang et al. [19]. In this work it was also demonstrated that repopulation pumping is a more efficient mechanism than depopulation pumping for the creation of ground-state spin polarization.

### 4.2.2 The rate equations

A $\sigma^+-$polarized light beam of total intensity $I_0$, which propagates in a generic direction defined by the vector $\vec{k}$, can be decomposed into a sum of $\sigma^+$, $\sigma^-$ and $\pi$ eigenmodes with respect to the quantization axis $\hat{z}$. The intensities $I_{q=\pm1,0}$ associated with each polarization state can be written as

$$I_q = I_0 \chi_q \, , \qquad (4.4)$$

where

$$\chi_{+1} = \cos^4 \frac{\theta}{2} \, ,$$
$$\chi_0 = \frac{1}{2} \sin^2 \theta \, ,$$
$$\chi_{-1} = \sin^4 \frac{\theta}{2} \, , \qquad (4.5)$$

where $\theta$ is the angle between the propagation vector $\vec{k}$ and the quantization axis.

The steady-state polarization $P_z$ created by the optical pumping process depends essentially on 2 parameters:

- the pumping rate $\gamma_p$, which depends in general on the intensity, on the polarization, on the propagation direction and on the beam profile of the pumping light,

- the longitudinal relaxation rate $\gamma_1$ of the ground state which tends to make the populations $p_{F,M_F}$ evolve towards their thermal equilibrium characterized by $p_{F,M_F} = 1/16$.

Under the assumption $\gamma_p \ll \Gamma$, where $\Gamma$ is the relaxation rate of the excited state, the stimulated emission can be neglected. The circularly polarized light then couples only to the populations and we do not need to include sub-level coherences in the description of the optical pumping process, which then reduces to finding the solutions of a system of incoherent rate equations. Moreover, on the time scale of the ground-state evolution ($\approx 10^3 Hz$) we can neglect the very fast relaxation processes of the excited state $6P_{1/2}$ ($\approx 10^8 Hz$) and proceed to the so-called adiabatic elimination of the excited state variables [19]. In conclusion, the rate equations describing the time evolution of the atomic ensemble under optical pumping can be simplified to a system of 16 equations which involve only the ground state populations $p_{F,M}$. In the approximation of pure repopulation pumping one can write [19]

$$\dot{p}_{F,M} = -\gamma_p \sum_q \sum_f \chi_q R_{F,M,f,M+q} p_{F,M} +$$

$$+ \gamma_p (2j+1) \sum_q \sum_{F',M'} \sum_f \chi_q R_{F',M',f,M'+q} R_{f,M'+q,F,M} p_{F',M'} - \gamma_1 (p_{F,M} - \frac{1}{16}), \quad (4.6)$$

where

$$R_{F,M,f,m} = (2F+1)(2f+1) \begin{pmatrix} f & 1 & F \\ -m & m-M & M \end{pmatrix}^2 \begin{Bmatrix} 1/2 & f & I \\ F & 1/2 & 1 \end{Bmatrix}^2, \quad (4.7)$$

and the optical pumping rate $\gamma_p$ is defined as

$$\gamma_p = \frac{1}{\gamma_{hom}} \frac{E^2}{\hbar^2} \, |< 6P_{1/2} \parallel d \parallel 6S_{1/2} >|^2, \quad (4.8)$$

where $\gamma_{hom}$ is the homogeneous optical linewidth and $E^2$ is the intensity of the light field.

Note that this system of equations describe the evolution of the populations, and thus the build-up of the polarization, along the quantization axis $\hat{z}$. The orientation of the light beam is taken into account via the components $\chi_q$.

In Fig. 4.2 we show as an example the equilibroum population differences created by the optical pumping process for a normalized pumping rate $\gamma_p/\gamma_1 = 100$ and by assuming that the propagation direction of the light coincides with the quantization axis. We further assume that the light is 100% circularly polarized.
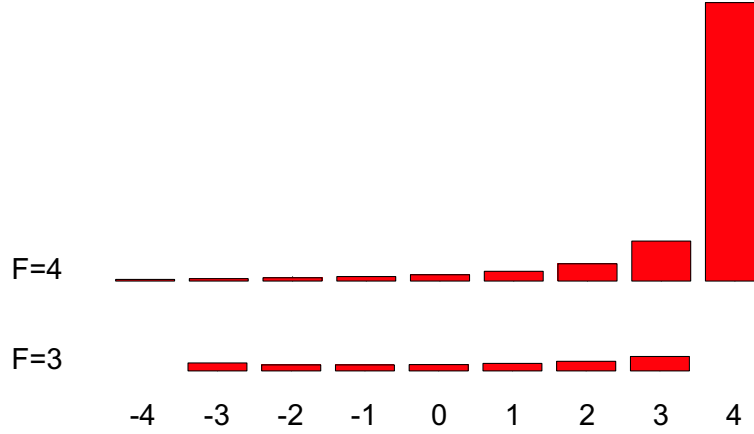
Figure 4.2: Steady state population distribution in the ground state of cesium after optical pumping with $\gamma_p/\gamma_1 = 100$ and by assuming that the propagation direction of the light coincides with the quantization axis.

## 4.3 Optical-RF double resonance

In the previous section we saw how an atomic ensemble can be spin polarized by the absorption of circularly polarized light. We discuss now in a classical picture the effect of the combination of static and oscillating magnetic fields on the magnetic moment associated with the spin polarization of the atomic ensemble.

### 4.3.1 The rotating wave approximation and the effective field

Let $\vec{B}_0$ be a static magnetic field and

$$\vec{B}_{rf}(t) = \vec{B}'_1 \cos \omega_{rf} t \tag{4.9}$$

an oscillating magnetic field perpendicular to the direction defined by $\vec{B}_0$. For the sake of simplicity we assume $\vec{B}_0 \parallel \hat{e}_z$ and $\vec{B}'_1 \parallel \hat{e}_x$. One can see the oscillating field as the sum of two rotating components with opposite sense of rotation

$$B'_1 \cos(\omega_{rf} t)\, \hat{e}_x = B_1 e^{i\omega_{rf} t} \hat{e}_+ + B_1 e^{i\omega_{rf} t} \hat{e}_- \,, \tag{4.10}$$

where $\hat{e}_\pm \equiv \hat{e}_x \pm i\hat{e}_y$ [3] and where $B'_1 = 2B_1$. The dynamic of the system is more conveniently discussed in a reference frame $\hat{e}'_{i=x,y,z}$ that rotates about $\hat{e}_z$ at the angular velocity $\omega_{rf}$. In this rotating frame one of the components of the oscillating field appears to be static $(B_1 \hat{e}'_x)$ while the other rotates at the double angular velocity $-2\omega_{rf}$. In the so-called rotating wave approximation (RWA) this fast latter component is neglected owing to its small effect on the atomic spins [4].

In the rotating frame an additional fictitious field $\vec{B}_f = -(\omega_{rf}/\omega_L)\vec{B}_0$ appears [5]. The equations of motion of an atomic magnetic moment in the rotating frame are then identical

---

[3] For the sake of simplicity we ignore the normalization of $\hat{e}_\pm$.

[4] The effect of the fast component is a small shift of the resonance frequency known as Bloch-Siegert shift, which is on the order of $(B'_1)^2/16B_0^2$ [96]

[5] It's a consequence of a classical mechanics theorem known as Larmor's theorem.

to the equations in the laboratory frame when the total field $\vec{B}_0 + \vec{B}_{rf}(t)$ is replaced by the effective field

$$\vec{B}_{eff} = \vec{B}_0 + \vec{B}_f + \vec{B}_1 = (B_0 - \frac{\omega_{rf}}{\omega_L} B_0)\hat{e}_z' + B_1 \hat{e}_x' \,. \qquad (4.11)$$

The magnetic moment thus precesses around the total effective field at the so-called *effective Rabi frequency*

$$\Omega_{eff} = \sqrt{(\omega_L - \omega_{rf})^2 + \Omega_R^2} \,, \qquad (4.12)$$

where $\Omega_R = \frac{g\mu_B}{\hbar} B_1$ is the Rabi frequency of the system [6].

### 4.3.2 The Bloch equations

The atomic sample under investigation is characterized by a *polarization vector* $\vec{P} = <\vec{F}>$, where $\vec{F}$ is the atomic spin, and by a *macroscopic magnetization* $\vec{M} = <\vec{\mu}>$, where $\vec{\mu}$ is the magnetic moment associated with the spin $\vec{F}$. The well-known relation $\vec{\mu} = \gamma\vec{F}$, where $\gamma$ is the gyromagnetic ratio, leads to the following equalities

$$\vec{M} = <\vec{\mu}> = -\gamma <\vec{F}> = -\gamma\vec{P} \,. \qquad (4.13)$$

The dynamic of the angular momentum $\vec{F}$ (in the rotating frame) is governed by the torque exerted by the effective field $\vec{B}_{eff}$ on the magnetic moment $\vec{\mu}$. By using Ehrenfest's theorem, which states that the expectation values of quantum mechanical operators obey classical equations of motion, one obtains

$$\frac{d\vec{F}}{dt} = \vec{\mu} \times \vec{B}_{eff} \,, \qquad (4.14)$$

$$\frac{d<\vec{F}>}{dt} = <\vec{\mu}> \times \vec{B}_{eff} \,, \qquad (4.15)$$

$$\frac{d\vec{P}}{dt} = \vec{M} \times \vec{B}_{eff} \,, \qquad (4.16)$$

$$\frac{d\vec{P}}{dt} = \vec{\Omega}_{eff} \times \vec{P} \,, \qquad (4.17)$$

where we have introduced the Rabi vector

$$\vec{\Omega}_{eff} = \gamma\vec{B}_{eff} = \begin{pmatrix} \Omega_R \\ 0 \\ \omega_L - \omega_{rf} \end{pmatrix} \,. \qquad (4.18)$$

After including the relaxation rates $\gamma_1$ and $\gamma_2$ for the longitudinal and transverse components, Eq. 4.17 yields the Bloch equations for the components $P_{x'}$, $P_{y'}$ and $P_{z'}$ of the polarization vector in the rotating frame

---

[6]The Rabi frequency is the precession frequency around the oscillating field $B_{rf}(t)$ that was formally brought to rest by the transformation into the rotating frame.
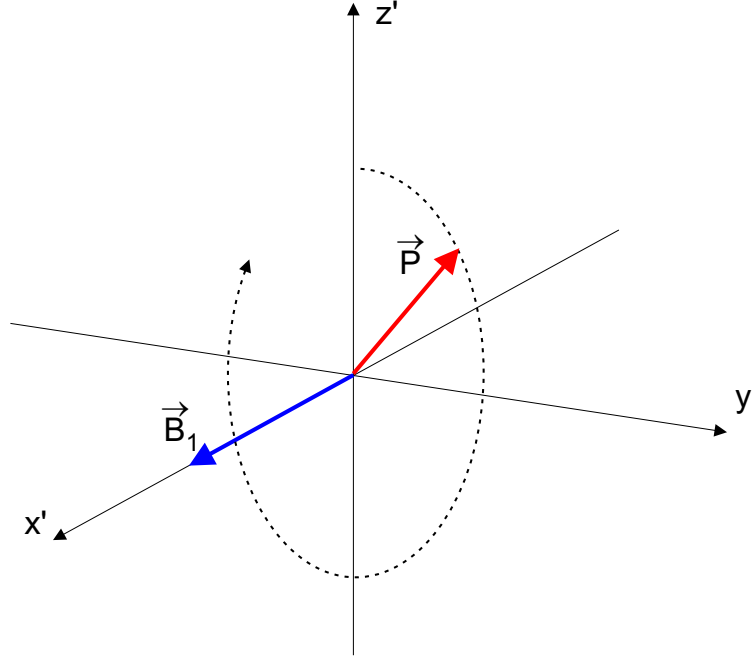
Figure 4.3: Motion of the polarization vector in the resonant case, in the rotating frame.

$$\frac{dP_{x'}}{dt} = \delta\omega P_{y'} - \gamma_2 P_{x'} \,, \tag{4.19}$$

$$\frac{dP_{y'}}{dt} = -\delta\omega P_{x'} - \Omega_R P_{z'} - \gamma_2 P_{y'} \,, \tag{4.20}$$

$$\frac{dP_{z'}}{dt} = \Omega_R P_{y'} - \gamma_1 (P_{z'} - P_{z'}^{eq}) \,, \tag{4.21}$$

where we have used $\delta\omega = \omega_L - \omega_{rf}$.

One can easily verify that in absence of relaxation processes, at resonance ($\delta\omega = 0$) and with the initial condition $\vec{P}(t = 0) = (0, 0, P_0)$, the Bloch equations yield a rotation (nutation) of the polarization vector $\vec{P}$ around $\vec{B}_1$ at the frequency $\Omega_R$

$$P_{x'}(t) = 0 \,, \tag{4.22}$$

$$P_{y'}(t) = P_0 \sin \Omega_R t \,, \tag{4.23}$$

$$P_{z'}(t) = P_0 \cos \Omega_R t \,. \tag{4.24}$$

The precession of $\vec{P}$ in the resonance case is represented graphically in Fig. 4.3 [7].

### 4.3.3 The steady state solution

The combination of relaxation and precession processes leads to an equilibrium state of the polarization vector. This steady state solution can be calculated analytically in the

---

[7]In the laboratory frame the tip of the polarization vector $\vec{P}$ describes a sphere with a fast precession at frequency $\omega_L$ about the z-axis and with a slow nutation at the frequency $\Omega_R$ between $P_z = +P_0$ and $P_z = -P_0$.

rotating frame from the Bloch equations 4.19, 4.20 and 4.21 by setting the left-hand sides equal to zero. One obtains

$$P_{x'} = P_0 \frac{\Omega_R \delta\omega}{\delta\omega^2 + \gamma_2^2(1+S)} \,, \tag{4.25}$$

$$P_{y'} = P_0 \frac{\Omega_R \gamma_2}{\delta\omega^2 + \gamma_2^2(1+S)} \,, \tag{4.26}$$

$$P_{z'} = P_0 \frac{\delta\omega^2 + \gamma_2^2}{\delta\omega^2 + \gamma_2^2(1+S)} \,, \tag{4.27}$$

where we have introduced the saturation parameter $S = \frac{\Omega_R^2}{\gamma_1 \gamma_2}$. S can also be written as $S = \frac{\gamma_{abs}}{\gamma_1}$, where $\gamma_{abs} = \frac{\Omega_R^2}{\gamma_2}$ is the rate at which photons are absorbed from the oscillating field.

The longitudinal component $P_z$ is directly related to the fluorescence rate and it is thus the quantity that we measure in a magnetic resonance experiment (see Eq. 4.3). It can be instructive to rewrite Eq. 4.27 in the form

$$P_{z'} = P_0 \left( 1 - \frac{S\gamma_2^2}{\delta\omega^2 + \gamma_2^2(1+S)} \right). \tag{4.28}$$

In the limit of weak rf-field, i.e., of $\Omega_R^2 \ll \gamma_1 \gamma_2$, the saturation parameter S in the denominator can be omitted and the steady state longitudinal polarization reads

$$P_{z'} = P_0 \left( 1 - \frac{S\gamma_2^2}{\delta\omega^2 + \gamma_2^2} \right). \tag{4.29}$$

Thus, when the rf-frequency of the oscillating field is scanned across the Larmor frequency $\omega_L$, the signal appears as an absorptive Lorentzian resonance centered at $\omega_{rf} = \omega_L$ and with a full width at half maximum (FWHM) of $2\gamma_2$. In the general case, one sees from Eq. 4.28 that the signal maintains its Lorentzian shape and that the resonance line is power-broadened by the rf-field. The FWHM turns out to be in this case $2\gamma_2\sqrt{1+S}$. Saturation occurs when $S \approx 1$, i.e., when $\Omega_R \approx \sqrt{\gamma_1 \gamma_2}$. In Fig. 4.4 one can see a typical magnetic resonance line obtained by detecting the fluorescence signal from cesium atoms implanted in a solid He matrix as a function of the tunable parameter $\omega_{rf}$.

In our typical experimental configuration, called $M_z$ geometry, the propagation direction $\vec{k}$ of the pumping light is parallel to the quantization axis, defined by the static magnetic field $B_0\hat{e}_z$. In this configuration there is only a static signal and the Larmor frequency is measured by detecting the fluorescence light during a sweep of the radio frequency $\omega_{rf}$ across $\omega_L$, as shown in Fig. 4.4.

Another geometry consists in orienting the light beam at 45° with respect to the quantization axis and in this case one speaks of $M_x$ geometry. In this configuration, the polarization rotates in the laboratory frame with $\omega_{rf}$ thus changing periodically its projection along $\vec{k}$. This leads to a modulation of the fluorescence signal which can be detected by means of a phase-locking technique. We will come back to this point in Chapter 6 and we will present an alternative way to describe the ODMR as a three-step process consisting in the preparation of a polarization state by optical pumping, the free evolution of the spins in the magnetic fields and the detection of the final spin state.
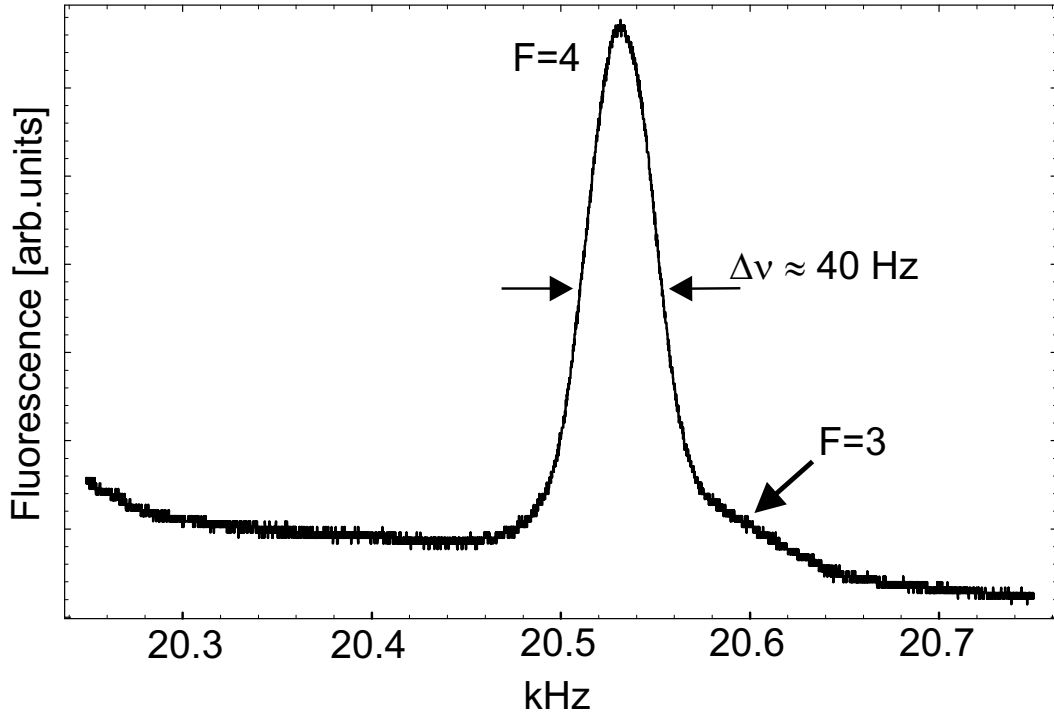
Figure 4.4: Typical ODMR signal from Cs atoms in the bcc phase of solid $^4$He. The data were recorded in a static magnetic field of $\approx 6\,\mu T$ and in a rf-field of $\approx 4\,nT$. One can observe that the width of the resonance is 3-4 times larger than the width of only 12 Hz measured in previous experiments [25]. The reason of this broadened line has to be ascribed to magnetic effects due to the electric field set-up inside the pressure cell where the interaction takes place. The slope of the background is due to a loss of atomic signal due to the recombination of Cs atoms into Cs clusters.

# Chapter 5

# The experimental set-up

Magneto-optical experiments at the very low temperature ($\approx 1.5\,K$) and at the very high pressure (in excess of 27 bar) needed for the solidification of helium, require an important experimental effort. Moreover, the study of the quadratic Stark effect which is addressed in this work requires the application of strong and highly uniform electric fields inside the doped crystal, thus increasing considerably the technical difficulties of the experiment.

The main features of the experimental set-up are described in details in the works of preceding PhD students [24, 25]. Here we will first give a general overview of the apparatus and we will then describe the main modifications that were made in the last two years to improve the performance of the set-up for electric field experiments.

## 5.1 The cryostat

Two section views of the cryostat are shown in Fig. 5.1 and 5.2. The helium crystal is grown in a cubic copper pressure cell (inner volume = 175 cm$^3$) which is immersed in a helium bath that can be filled up with 40 liters of liquid He. The helium bath is shielded against the thermal radiation of the surrounding environment by two layers of isolation vacuum and by an intermediate chamber of liquid nitrogen (which is refilled every 12 hours during an experimental run). Thermal radiation from the top flange is shielded by four gold-coated copper baffles (1 mm thickness).

When the cryostat is filled with liquid helium, the helium bath itself acts as a cryo-pump by freezing out residual gases in the isolation vacuum chambers, in which one achieves typical pressures of $\approx 10^{-7}$ mbar. The isolation vacuum is pumped by means of a turbo molecular pump (Pfeiffer, TMU 261) in series with a roots pump (Varian, SD-451).

The cryostat has windows in four lateral directions as well as on the top flange to give optical access to the inner part of the pressure cell, for the excitation and detection of the atoms (side windows), for the implantation of atoms and for the dissociation of clusters (top window). Five windows (4 side windows and a top window) are also flanged onto the body of the cell by a dedicated sealing technique [25].

An experiment typically requires the purchase of 80 liters of liquid He (from SL Gas, Lenzburg, Switzerland) at the price of 16 CHF/liter. The evaporation loss during the transfer of liquid helium from the He dewar to the cryostat is typically 10-20 liters of liquid helium.

The level of liquid helium in the He bath is controlled by means of a *level sensor*, which
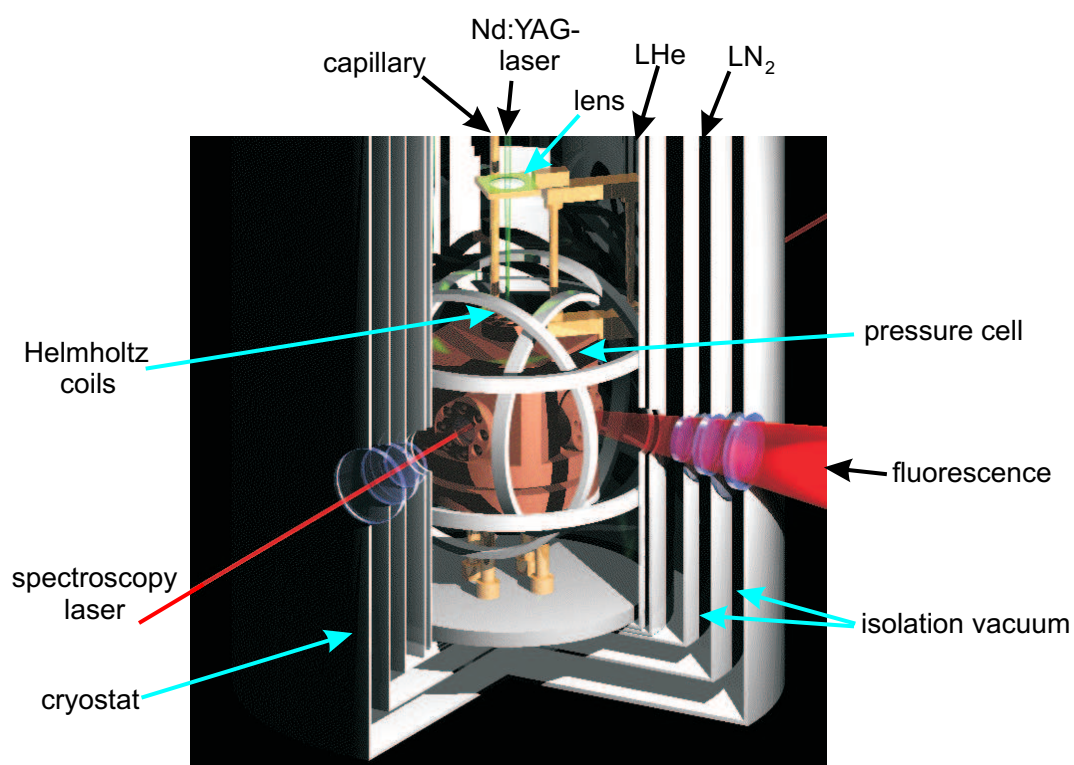
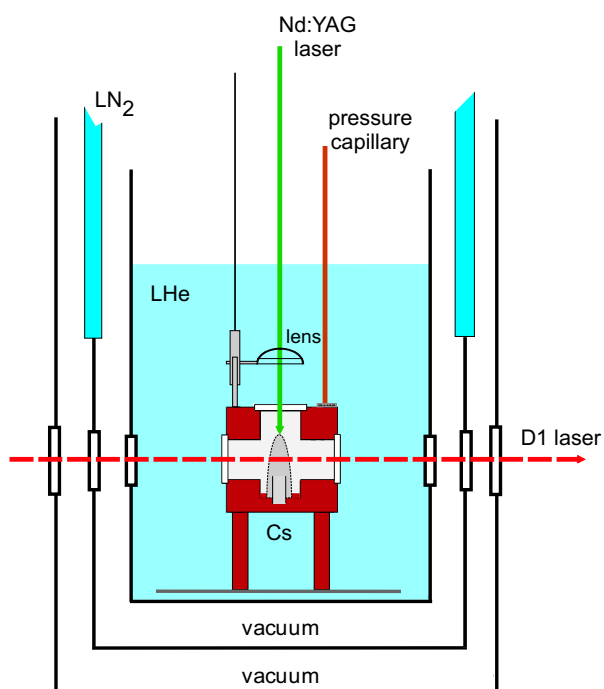Figure 5.1: Section through the cryostat.



Figure 5.2: Section through the cryostat and pressure cell.
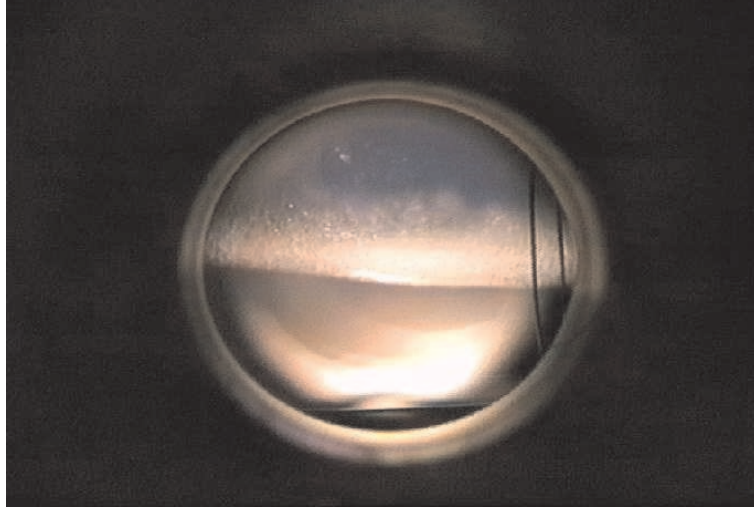
Figure 5.3: Growth of the He crystal by slow pressurization as seen from one of the side windows of the cryostat. The lower part is in the solid state, while the upper part is still liquid.

consists of a superconducting Ta wire immersed in the bath. The critical temperature $T_c$ of the sensor exceeds only slightly the boiling point of liquid helium and therefore only the part that is not immersed in the He bath contributes to its total resistance. A constant current of 170 mA is sent through the wire to prevent the part above the He surface to be cooled below its critical temperature. After the calibration of the device, the measurement of the resistance of the wire gives then the helium level in the bath.

When the He bath is filled with about 40 l of liquid helium we start pumping on its surface in order to cool it down to 1.5 K at a vapour pressure of about 2-3 mbar. The pumping of the bath is done by means of a rotary pump (TRIVAC, B-65-S) in series with a roots pump (Edwards, EH250). During the cooling process, which takes about 2 hours, we typically evaporate another 10-15 liters of liquid helium (about 30 % of the initial volume). The duration of the experiment is then about 48 hours. This time limitation depends mainly on the continuous pumping over the helium bath (which is needed to keep the temperature constant and low) and on the electrical and high-voltage cable feedthroughs, which represent the main heat leaks.

The pressure cell is mounted on an aluminium platform which is centered on the bottom of the cryostat. On top of the cell (Figs. 5.1,5.2), a height-adjustable lens (f=10 cm) enables us to focus the pulses of a frequency-doubled Nd:YAG laser into the Cs target (placed on the bottom of the pressure cell) during the implantation process. The cell is also connected via a capillary to an external reservoir of pressurized helium gas. When the final temperature of 1.5 K is reached, the crystal is grown by slowly increasing the pressure inside the cell via a needle valve (Fig. 5.3).

In order to control the crystalline phase (bcc or hcp) of the He matrix one has to control in a very precise way the pressure applied into the cell. Therefore He gas (nominal purity > 99.999 %) from a standard gas bottle (p=200 bar) is first transferred to a small
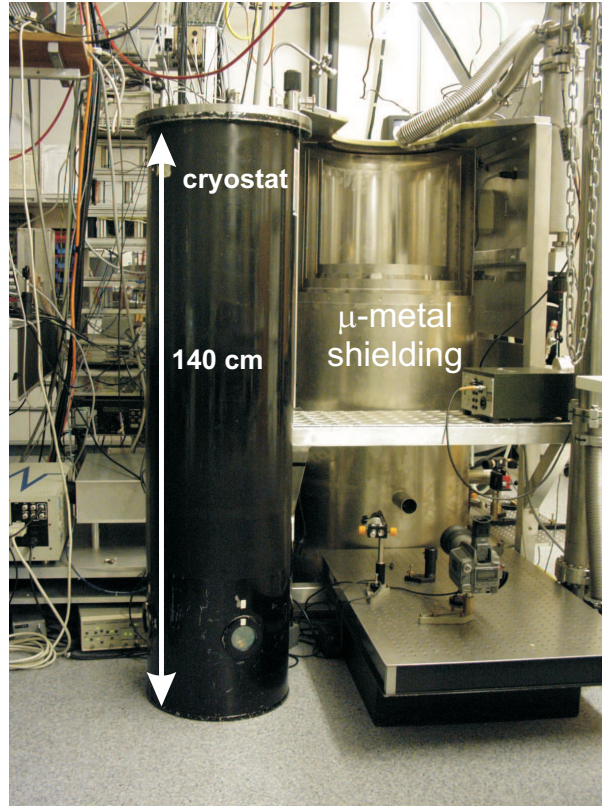
Figure 5.4: The cryostat and the $\mu$-metal shielding.

buffer reservoir (V = 1 liter) over a pressure-reducing valve. From here the helium can flow through a needle valve into a cold trap, consisting of several loops of copper tube immersed in a liquid nitrogen filled dewar, where condensable impurities in the He gas are removed. The copper tube is then connected through the capillary to the pressure cell.

The temperature has to be also controlled in a precise way. The helium bath is connected to the pumping line via a butterfly-valve whose position is controlled electronically. The temperature is actively regulated by changing the pumping rate over the helium bath using a feedback control of the valve. We use two temperature sensors (germanium resistors, Scientific Instruments) in the apparatus. The first one measures the temperature in the helium bath, while the other is placed directly inside the cell and is connected to an electrical feedthrough which is flanged onto the copper body.

On the same aluminium platform on which the cell is fixed, we also mount the superconducting (NbTi) Helmholtz coils that are used during the magnetic resonance experiment to produce the main static magnetic field. These coils are visible in Fig 5.1. A detailed description can be found in [25]. The coils to produce the oscillating RF-field are mounted inside the cell.

The cryostat is shielded from laboratory stray magnetic fields by an external three-layer $\mu$-metal shielding (Fig. 5.4).
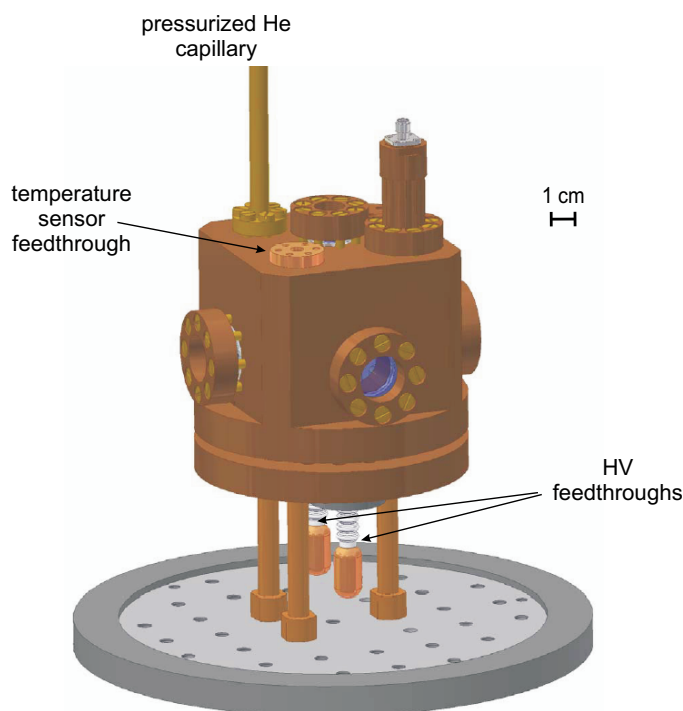
Figure 5.5: The pressure cell.

## 5.2 The pressure cell

The inside and outside of the pressure cell have been considerably modified over the last two years with respect to the description given in [24, 25]. The main modifications are related to the need for improving the performance of the set-up in high electric field experiments. The exterior of the pressure cell is shown in Fig.5.5.

The cell is a cube made of oxygen-free F30 copper. Its walls have a thickness of 17 mm and the inner volume (in which the crystal is grown) is about 175 cm$^3$. The optical access to the doped crystal is provided by 5 quartz windows ($\oslash = 25$ mm) mounted onto the main body of the cell, 4 on the sides of the cube (excitation and detection of the implanted atoms) and 1 on top of it (implantation and later cluster dissociation). The windows are sealed by using aluminium rings. Before each experiment, the cell is tested to hold a gas pressure of more than 50 bar at room temperature.

The main difference from the previous set-up consists in the presence of two HV feedthroughs mounted onto the bottom plate of the cell. In previous electric field experiments, only one of the electrodes inside the pressure cell was connected to the HV power supply while the other was held at ground potential [24, 25]. With the second HV feedthrough both the electrodes can be connected to two HV power supplies which enable the application of electric fields two times larger than in earlier experiments. The high voltage is brought to the HV feedthroughs by a HV-cable (Heinzinger HVC 65) through the top flange of the cryostat. At present we can apply electric fields up to 50 kV/cm. Electric breakdowns occur inside the cryostat, between a high voltage cable and the grounded pressure cell, at
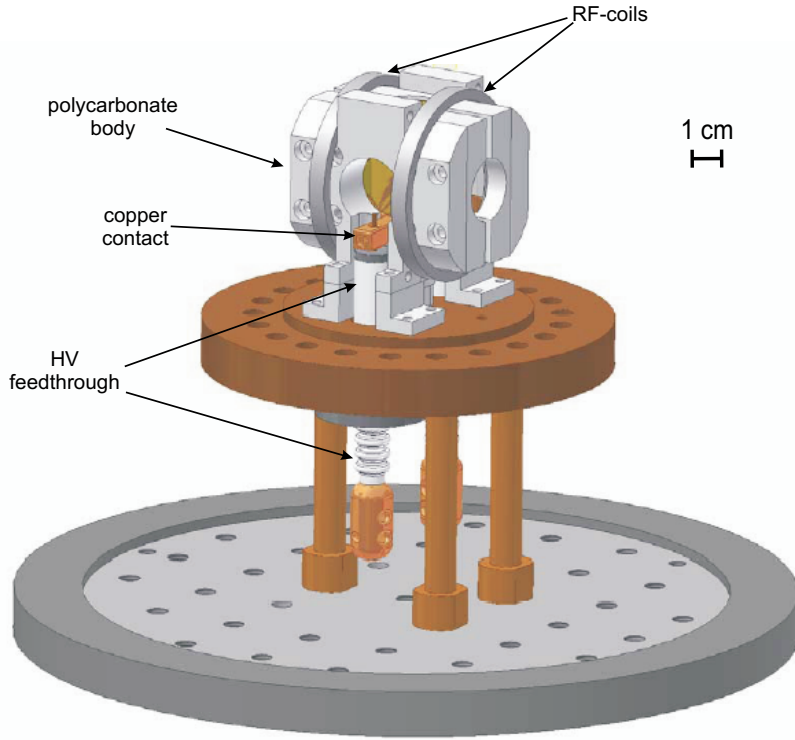
Figure 5.6: The inner part of the pressure cell.

voltages which are typically about 17 kV (which correspond to an electric filed strength in the cell of $\approx 50$ kV/cm).

In order to accommodate the second HV-feedthrough, the temperature sensor was removed from the bottom plate of the cell and mounted on the top part of the main body (see Fig. 5.5).

The inner part of the cell is shown in Fig. 5.6. Most of the inner volume is occupied by a polycarbonate body which holds the RF-coils for the magnetic resonance experiments as well as two transparent glass electrodes which are connected by a C-shaped copper ring to the HV feedthroughs (see Fig. 5.7).

The polycarbonate body is made of two independent identical parts. The absence of contacts between these two parts guarantees the minimization of surfaces along which electric breakdowns between the glass electrodes can take place. Each of these two components is then made of two sub-parts which are pressed together by PVC screws thus holding the glass electrode in the middle (see Fig. 5.8). The separation between the glass electrodes is 6 mm. This distance was chosen to create sufficiently high electric field strengths and to leave enough space for the implantation of atoms.

## 5.3 The HV supply and the HV feedthrough

The high voltage is generated by two HV power supplies (Heinzinger PNC 5 60000-1, Heinzinger PNC 60000-1) which can each provide up to 60 kV to the two HV feedthroughs
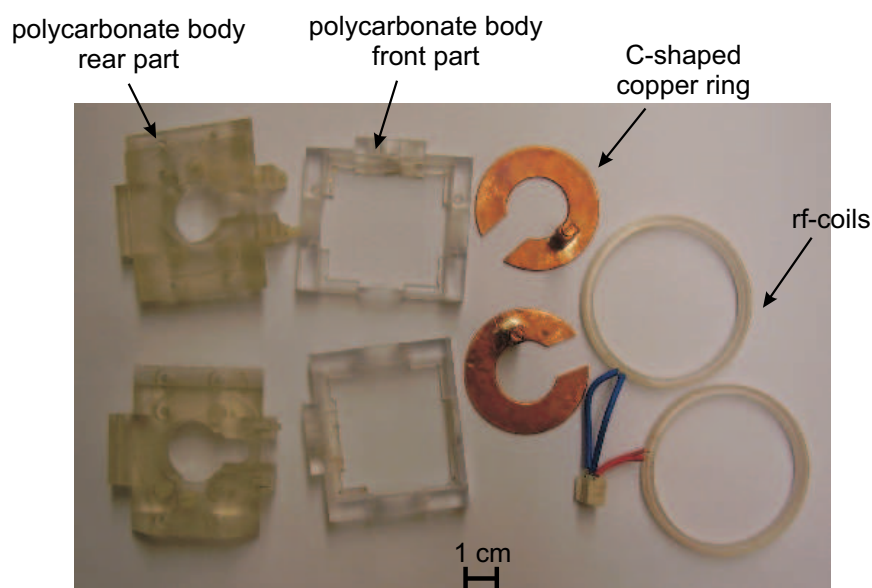
Figure 5.7: The polycarbonate body, the C-shaped copper rings and the rf-coils.

mounted onto the bottom plate of the pressure cell.

The HV feedthroughs were completely renewed after our first electric field experiments and they were specially manufactured for our application by Friatec AG (Germany). The HV feedthrough is shown in Fig. 5.9. The main change with respect to the old set-up consists in the fluted surface which was introduced to increase the breakdown voltage outside the pressure cell.

The feedthrough is made by a copper filament ($\oslash$ 1.5 mm) isolated by a special ceramic material (Frialit F99.7, $Al_2O_3$), fitted and sealed in a non-magnetic titanium flange. The flange is then sealed to the copper cell by aluminium rings in the same manner as the windows.

During the experiments we were limited by breakdowns which took place both inside and outside the cell. The maximum voltage applicable to each glass plate can vary in different experiments depending on the characteristics of the He crystal. The presence of charges in the solid matrix (mainly produced by the Nd:YAG laser pulses needed for the implantation and for the dissociation of clusters) constitutes the major limitation. We measured typical leakage currents between the electrodes of a few microampere. In general, we were never able to apply more than 20 kV to each feedthrough.

## 5.4 The glass electrodes

The glass electrodes used in our electric field experiments are described in [24, 25]. They consist of two quadratic high flatness glass plates (float glass) for standard industrial applications (side = 40 mm, thickness = 4 mm) coated on one side with a conductive tin
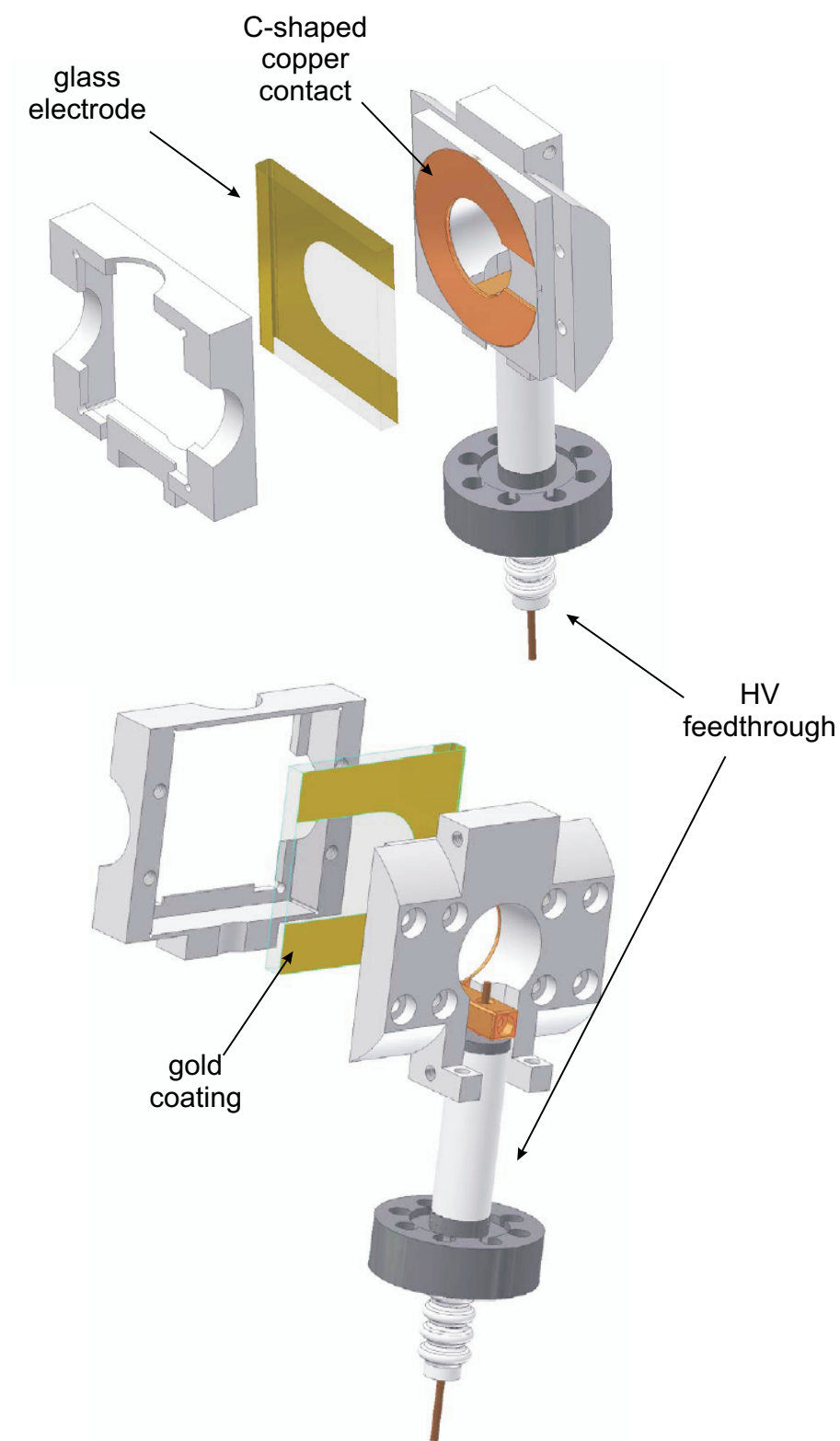
Figure 5.8: The polycarbonate body is made of two parts which are pressed together by PVC screws. The glass electrode is then held in the middle. The contact between the electrode and the HV feedthrough is provided by a C-shaped copper ring which is also held between the two components of the main polycarbonate body.
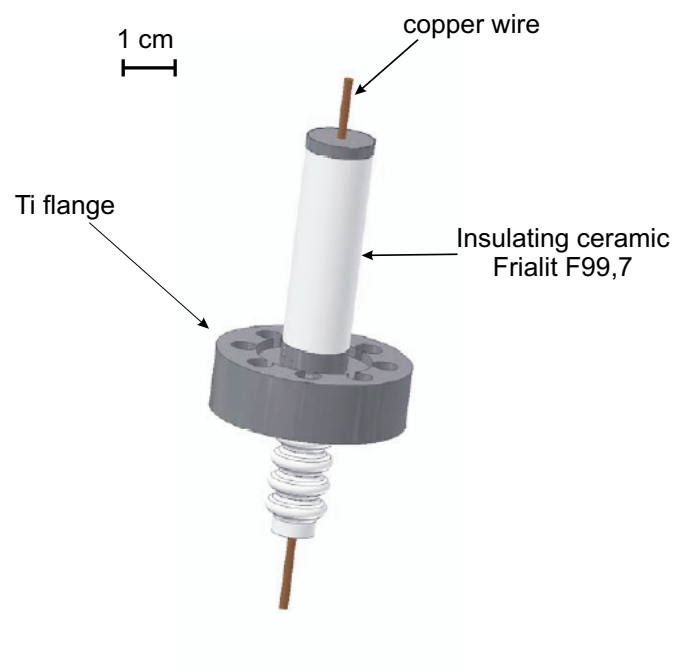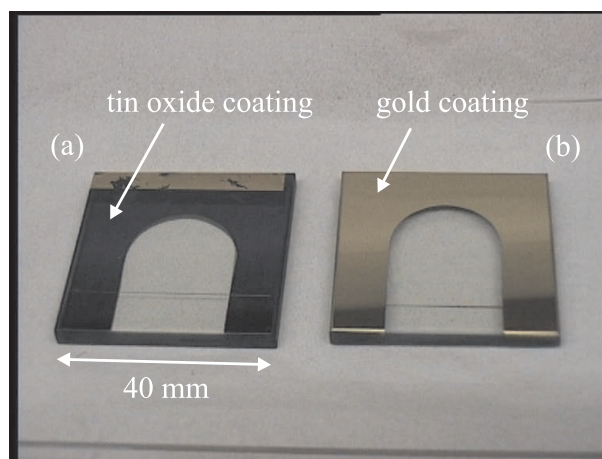
Figure 5.9: The HV feedthrough.



Figure 5.10: The glass electrodes.

polycarbonate          glass electrode
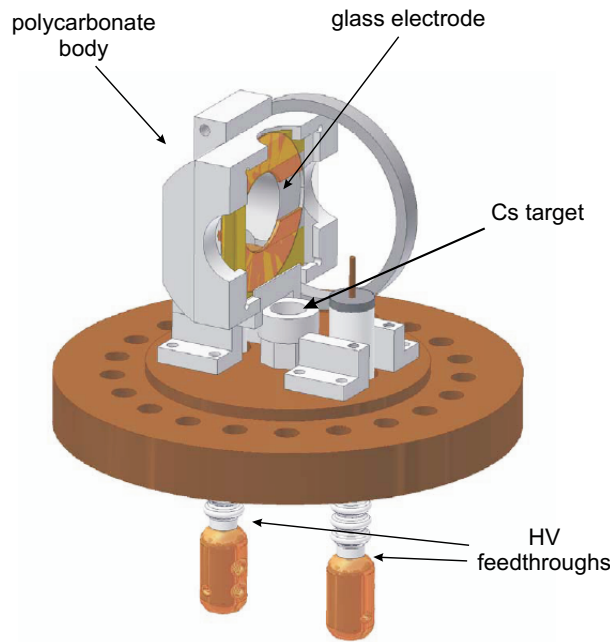body

Cs target

HV
feedthroughs

Figure 5.11: A section through the cell. One can see the cylinder that holds the Cs ampoule screwed to the bottom plate of the cell.

oxide layer. The non-conducting surface is then coated with gold [1] in order to establish an electrical contact between the front side and the rear part which is connected to the HV feedthrough. The glass electrodes are shown in Fig. 5.10.

## 5.5 The implantation

The Cs target, contained in a glass ampoule, is held by a hollow polycarbonate cylinder screwed to the bottom plate of the pressure cell (Fig. 5.11). Since alkali metals oxidize immediately in contact with air and react strongly with water or even with the humidity of the laboratory atmosphere, the positioning of the Cs target into the mount mentioned above has to be carried out in a neutral and dry environment, i.e., typically in a plastic glove-bag filled with argon.

Cesium atoms are implanted into the solid He matrix using the laser ablation technique [14, 15]. Pulses from a frequency-doubled Nd:YAG laser (Quanta-Ray, GCR-12 with frequency-doubling unit HG-2B, $\lambda$=532 nm, max.repetition rate 10 Hz) are sent into the cryostat through its top window and are then focused onto the Cs target by a height-adjustable lens mounted above the cell (see Figs. 5.1 and 5.2). The laser pulses used in the process have typical energies of 20 mJ/pulse with a repetition rate of 1 Hz and a pulse width of 10 ns.

The steps of the implantation process are shown in Fig. 5.12. The heat absorbed from the laser pulses melts the crystal above the Cs target and the material (atoms, clusters,

---

[1]The coating with gold is done in our laboratory, by using a vacuum coater (VACOTEC SA EDWARDS, AUTO 306 vacuum coater).
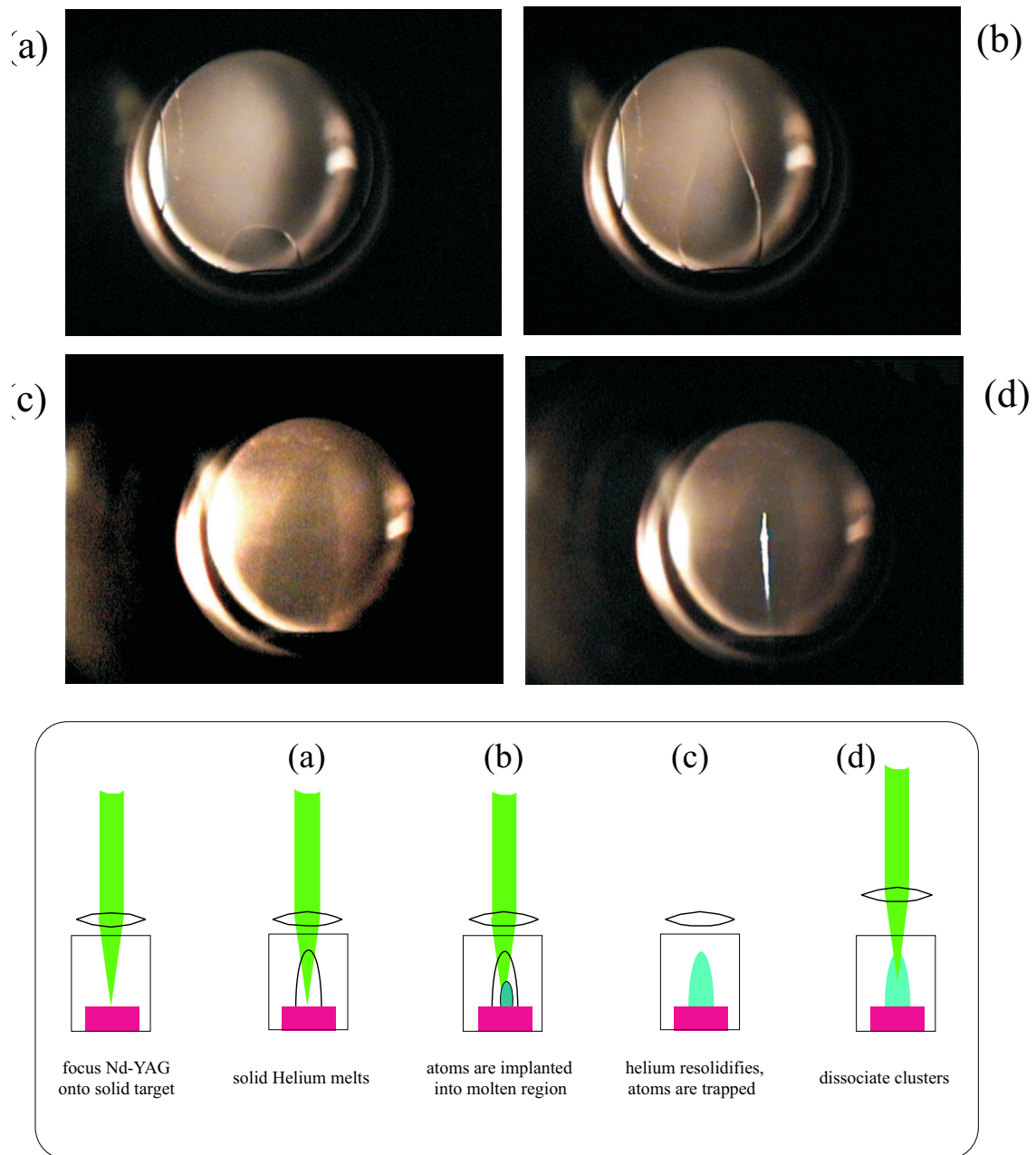
Figure 5.12: The implantation process. **(a)** and **(b)** Short pulses at $\lambda$=532 nm from a frequency-doubled Nd:YAG laser are focused onto the Cs target. The deposited heat melts the crystal and atoms can diffuse into the molten area. **(c)** Helium resolidifies leaving a column of implanted atoms and clusters. **(d)** In order to keep a constant fluorescence signal low-energy laser pulses are applied at a low repetition rate to dissociate molecules and clusters.

ions and charges) ablated from its surface can simultaneously diffuse into the liquefied helium volume. By progressively lifting the lens, the implanted material can diffuse up to the central region of the crystal and, after resolidification of the molten helium, the implanted particles become trapped in the He matrix. Clusters can then be dissociated by applying low-energy Nd:YAG pulses at a sufficiently low repetition rate (typically 0.04 Hz) thus keeping an average constant atomic density of $10^8$-$10^9$ cm$^{-3}$. The diffusion and recombination of atoms to form dimers and clusters is the main loss mechanism of the optical signal. These processes are investigated and described in detail in [22].

# Chapter 6

# Experimental results

## 6.1 Introduction

In this chapter we present results from magnetic resonance experiments in external electric fields. As discussed in Chapter 1 the main goal of these experiments was the measurement of the quadratic Stark effect in the ground state of cesium atoms embedded in a solid He matrix. Although a measurement of the tensor polarizability of the ground state of cesium had been carried out recently by our group in an all-optical atomic beam experiment [64], a new measurement of the Stark shift of the magnetic resonance transitions in the ground state of Cs atoms implanted in solid helium appeared to be necessary in the framework of an EDM experiment.

The first attempts to measure the quadratic Stark effect in solid helium were carried out by our group a few years ago, first at the University of Bonn, and later in Fribourg [24, 25]. The only conclusion that could be reached after these first experiments was that an effect of the electric field might be observed, but no quantitative results could be obtained because the quadratic effect was by far overridden by a strong linear contribution and the estimation of the tensor polarizability led to a value which was one order of magnitude smaller than expected from earlier measurements [1]. The considerable technical difficulties associated with the study of electric field effects in our cryogenic conditions made the measurement of the quadratic Stark effect a difficult experimental challenge. It was only after two years of work and test runs that we finally managed to measure unambiguously the tensor polarizability of the ground state of cesium atoms in the solid He matrix, with a very good agreement with measurements performed in more conventional experimental conditions [2].

This non-trivial experimental success then turned out to be even more exciting than what we expected. As we discussed in the Chapters 2 and 3, in parallel to our experimental efforts we developed a novel perturbative model to calculate the scalar and tensor polarizabilities of cesium atoms (and in general of any alkali atom). Among the exceptional

---

[1]The strong linear effect observed in the first experiments could be ascribed to a drift of the magnetic resonance line independent on the application of the electric field as observed for instance in [25]. The instability of the resonance frequency was one of the main problems we had to deal with during the last two years of activities with electric fields.

[2]We remark here that in the last two years several other research activities were carried out in parallel. Among the important scientific results obtained in our experiment we mention for instance the recent discovery of $Cs^*He_n$ exciplexes [30, 31].

results of this theoretical study, we realized the existence of a sign difference between our model and the "old" Sandars' theory [33]. We briefly recall this point. According to the historical model proposed in the 1960s by Sandars, the tensor polarizability in the ground state of cesium *does not* depend on the quantum number F. Conversely, in our model, the tensor polarizabilities of the two hyperfine levels F=3 and F=4 have *opposite signs*. This sign difference has a pronounced experimental signature when the differential shift of the resonances F=3 and F=4 is investigated as a function of the applied electric field. The experimental results that are shown in the following give a final answer to this open question, thus demonstrating that the sign error of Sandars' paper [33] has remained unnoticed for about 40 years.

We will first present the results obtained in the $M_z$ configuration, then the results obtained by running our set-up as a self oscillating magnetometer in the $M_x$ configuration. All the experimental results that follow are obtained in a geometry in which the electric field is parallel to the quantization axis, i.e., parallel to the main static magnetic field.

## 6.2 The quadratic Stark effect in the M $_z$ configuration

The top view of the experimental set-up is shown in Fig. 6.1. We use a diode laser at $\lambda$=852 nm, which corresponds to the D1 absorption line ($\mid 6S_{1/2} > \rightarrow \mid 6P_{1/2} >$) of cesium in the helium matrix [3]. The light power is controlled by a combination of a half-wave plate and a linear polarizer. The intensity of the laser beam is typically $\approx$1 mW. At higher intensities we observe a loss of the atomic signal owing to local melting of the crystal and consequent drift and recombination of the atoms. The incoming linearly polarized light is then turned into circularly polarized light by a quarter-wave plate. An additional $\lambda/2$ Fresnel Rhombus is needed to compensate for the stress-induced birefringence of the windows of both the cryostat and the cell. The orientation of this $\lambda/2$-element is determined by searching for a minimum in the fluorescence signal, which corresponds to the highest degree of spin polarization achievable by optical pumping. The atomic fluorescence signal ($\lambda \approx$885 nm in bcc) from the sample volume ($\approx$3 mm$^3$) is collimated by a lens in the cryostat and it is first detected by a CCD camera (Andor, DV420-OE, sensitive from the visible to 1050 nm) which is mounted on an imaging spectrograph (Oriel, MS257). The optical atomic fluorescence spectrum is used to optimize several parameters of the system as well as the alignment of various components.

A pivotable mirror then enables us to switch from the CCD-camera to a cooled avalanche photodiode (APD). An interference filter (FWHM of 9 nm) suppresses scattered laser light by several orders of magnitude. The signal from the APD is then read on a digital oscilloscope (Lecroy, 500MHz LC334A).

### 6.2.1 The tensor polarizability $\alpha_2^{(3)}(F = 4)$

The measurements were performed in the isotropic bcc phase of solid helium, at a temperature T=1.5 K and at a pressure p=26.9 bar, in a static magnetic field $B_0$=6$\mu$T. The rf-coils

---

[3]We recall that the absorption lines in the helium crystal are strongly blue-shifted owing to the interaction with the surrounding matrix. The D1 transition is thus excited at 850 nm, while the D2 transition is excited at 800 nm. The D1 emission line is then shifted to 878 nm when the crystal is in the hcp phase, and to 885 nm when it is in the bcc phase. The emission following D2 excitation is more complex [30, 31] and goes beyond the topic of this discussion.
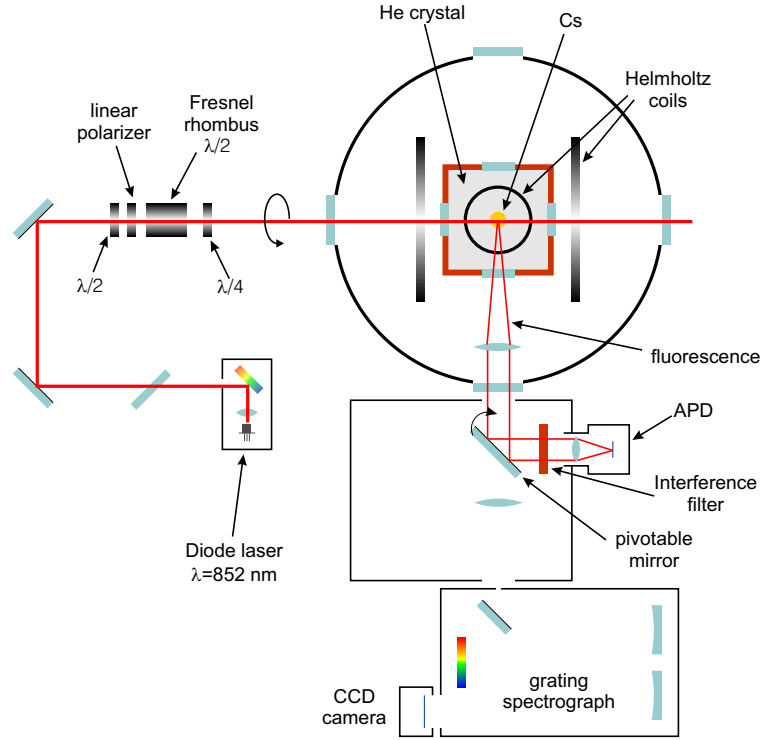
Figure 6.1: Top view of the set-up for magnetic resonance experiments in the $M_z$ configuration.

are driven by a function generator (SRS, DS345) and produce an oscillating magnetic field $B_{rf} \approx 4$ nT. The laser beam intensity was 1 mW.

The magnetic resonances were recorded by scanning the frequency of the rf-field across the Larmor frequency ($\approx 20.53$ kHz) which is determined by the choice of $B_0$. A measurement with electric field was always followed by a measurement in zero field, and for each measurement with electric field we switched the polarity of the field itself. The shift of the resonance under the effect of the electric field has to be thus understood as a shift with respect to the nearest (in time) zero-field measurement. In this way we minimize effects associated with the strong drift of the zero-field magnetic resonance (shown in Fig. 6.2), which is one of the main limitations to the sensitivity of our apparatus. In Fig 6.2 the zero-field resonance frequency exhibits a linear drift of 1.65 mHz/sec (corresponding to $\approx$ 0.5 pT/sec) over a measuring time of 45 minutes [4].

The drift of the magnetic resonance frequency was studied in the thesis of a former PhD student of our group [25]. In this work, the strong drift of the resonance was ascribed to a magnetic field gradient that was estimated to be on the order of 10 Hz/mm. The drift shown in Fig. 6.2 thus suggests a drifting velocity of the Cs atoms embedded in the He matrix of 0.1-0.2 $\mu$m/sec. We exclude a linear drift of system parameters such as pressure or temperature.

Beside this long-time scale drift, the behavior of the resonance frequency exhibits other more problematic features on shorter time scales. The Nd:YAG laser pulses, that are

---

[4]These values can change in different experiments. The behavior of the system depends strongly on the features of the crystal which are strictly related to some uncontrollable parameters of the implantation process.
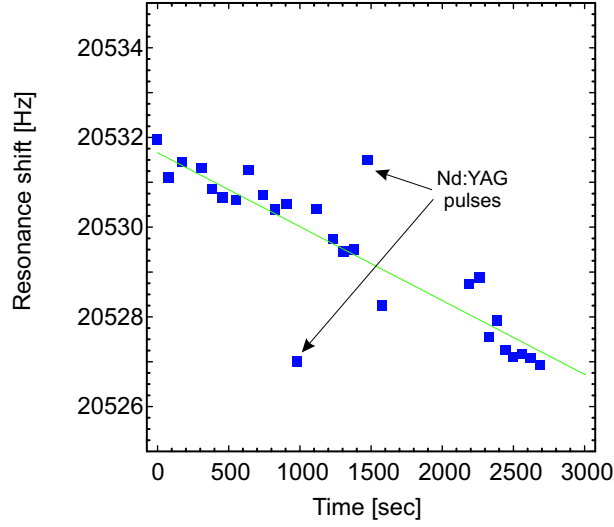
Figure 6.2: Drift of the magnetic resonance frequency without external electric fields over 45 minutes. The green solid line is a linear fit to the data: y=20531.7-0.00165x. The resultant linear shift thus corresponds to 1.65 mHz/sec. The Nd:YAG laser pulses sent into the crystal to dissociate clusters can occasionally induce a sudden strong drift of the atoms, which appear in our measurement as a sudden steep jump of the resonance frequency.
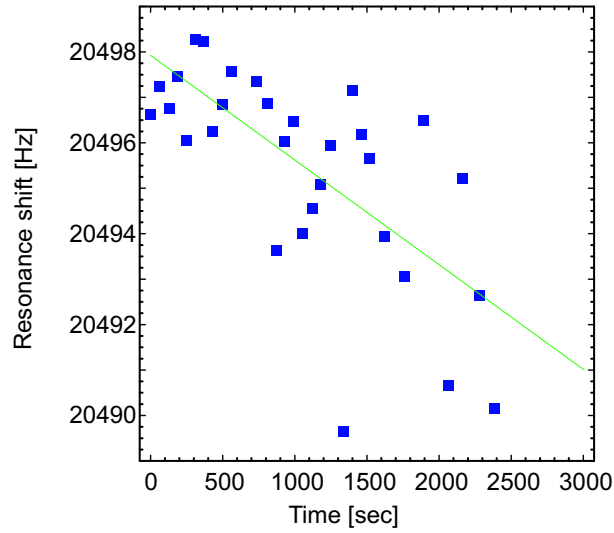


Figure 6.3: Drift of the magnetic resonance frequency without external electric fields over 45 minutes. The green solid line is a linear fit to the data: y=20497.9-0.00230x. The resultant linear shift thus corresponds to 2.30 mHz/sec. The instability of the resonance frequency is evident when compared to Fig. 6.2.
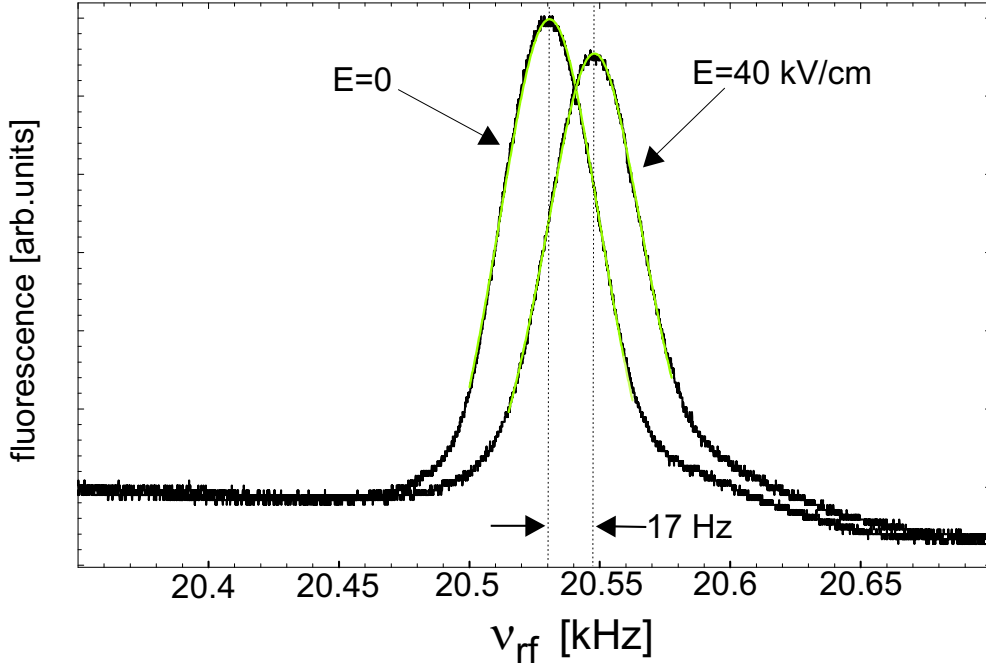
Figure 6.4: Frequency shift of the magnetic resonance line of Cs | 4, 4 >↔| 4, 3 > in an electric field of 40 kV/cm relative to the field-free resonance (E=0). The curves are fitted by Lorentzians $L(\nu) = \frac{a}{4(\nu-c)^2+w^2}$. The fit yields a FWHM of 60 Hz.

sent into the crystal every 30 seconds to dissociate clusters and to recover the optical fluorescence signal, can occasionally provoke a sudden strong drift of the atoms inside the volume interested by the experiment. These drifts appear in our magnetic resonance measurements as sudden steep jumps of the resonance frequency. This short-time scale instability of the zero-field resonance can strongly affect our estimation of the Stark shift. The importance of this effect strongly depends on the property of the crystal and it can thus change considerably in different experiments or even during the same experiment after different atomic implantations. The pressure in which the measurement takes place plays of course a relevant role. In Fig. 6.3 we show the behavior of the zero-field magnetic resonance frequency in the same experiment as Fig. 6.2 but after growing a new crystal and thus after a new implantation procedure. In this second case, the instability of the system strongly limited our sensitivity to the Stark shift of the resonance frequency.

Therefore we present our results by considering the set of data shown in Fig. 6.2. The shift of the magnetic resonance line of Cs detected in an electric field of 40 kV/cm is shown in Fig. 6.4. The different amplitudes of the two resonances is related to the variable density of atoms in the volume observed in the experiment. The curves are fitted by absorptive Lorentzian functions.

In Fig. 6.5 we plot the magnetic resonance frequency shift as a function of the applied electric field. Each measurement with electric field is compared to the averaged zero-field resonance frequency obtained by considering the preceding and the subsequent zero-field measurements [5]. The error bar is then obtained from the scattering of the zero-field points. One can note that the two large error bars in the figure correspond to the two "jumps"

---

[5]We recall that we always alternate measurements with electric field to measurements without field.
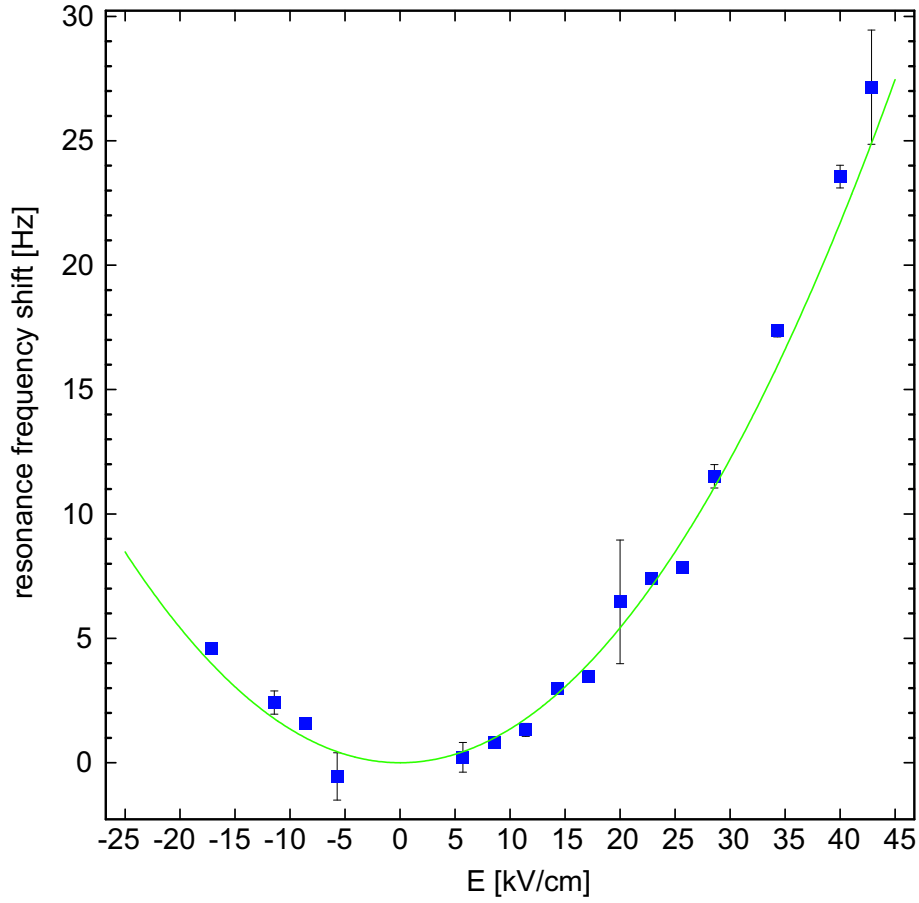
Figure 6.5: Shift of the magnetic resonance line as a function of the applied electric field. Higher fields in the negative direction were not reachable owing to technical problems with one of the HV power supplies.

observed in Fig. 6.2. We fit the data with the function $f(E) = \alpha E^2$ (solid line in the figure). The quadratic coefficient $\alpha$ yields our experimental value of the tensor polarizability

$$\alpha_2^{(3)}(F = 4) = (-3.51 \pm 0.2) \times 10^{-2} \frac{Hz}{(kV/cm)^2} \, . \tag{6.1}$$

This result is in good agreement with the experimental result obtained by our group in a recent atomic beam experiment [64]

$$\alpha_2^{(3)}(F = 4) = (-3.34 \pm 0.20) \times 10^{-2} \frac{Hz}{(kV/cm)^2} \, , \tag{6.2}$$

and with our theoretical calculation

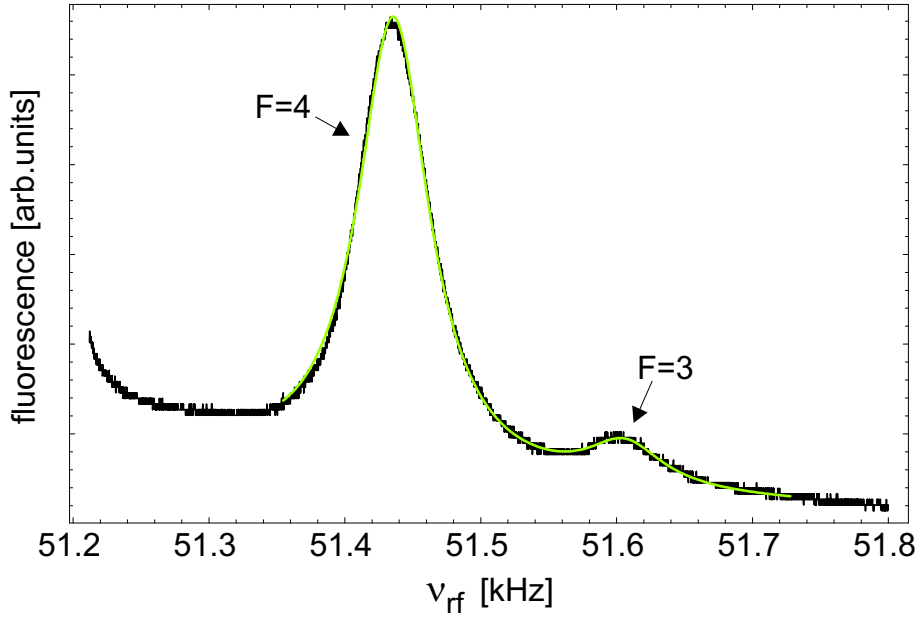$$\alpha_2^{(3)}(F = 4) = (-3.72 \pm 0.25) \times 10^{-2} \frac{Hz}{(kV/cm)^2} \, . \tag{6.3}$$

Figure 6.6: Magnetic resonances corresponding to the ground state levels F=4 and F=3. The magnetic field is of 14.7 $\mu$T and the separation between the two peaks is 162 Hz. The fit represented by the solid line is discussed in the text.

We also tried to fit the data with the function $g(E) = \alpha E^2 + \beta E^4$. The fitting procedure yielded a coefficient $\beta$ compatible with zero. Odd terms in E are not allowed by parity conservation.

## 6.2.2 The differential shift of the resonances F=4 and F=3

The experiment closely resembles the one described in the previous section. The measurements were performed at a temperature of 1.51 K and at a pressure of 27.1 bar, with a laser beam intensity of 1 mW and in a magnetic field $B_0 = 14.7\,\mu T$. The static magnetic field is larger than the one applied in the experiment described in the previous section. The reason for this change was to increase the separation between the resonances

$$| F = 4, M = 4 > \leftrightarrow | F = 4, M = 3 >    \text{and}    | F = 3, M = 3 > \leftrightarrow | F = 3, M = 2 > .$$

At 14.7 $\mu$T, the frequency splitting of the peaks F=3 and F=4 is 162 Hz as given by the Breit-Rabi formula. In Fig. 6.6 we show the magnetic resonances obtained by scanning the frequency of the rf-field across the Larmor frequencies of the two hyperfine components of the ground state of cesium.

The resonances are fitted with the function

$$F(\nu) = N_0 \left(1 + \frac{a_1}{4(\nu - c_1)^2 + w_1^2} + \frac{a_2}{4(\nu - c_2)^2 + w_2^2}\right) \left(e^{-\gamma_3(\nu - \nu_0)} + a_4 e^{-\gamma_4(\nu - \nu_0)}\right) ,$$

(6.4)

where $\nu_0$ is the starting frequency of the sweep. The combination of two exponentials enables us to fit the decaying background. The coefficients $\gamma_1$ and $\gamma_2$ typically differ
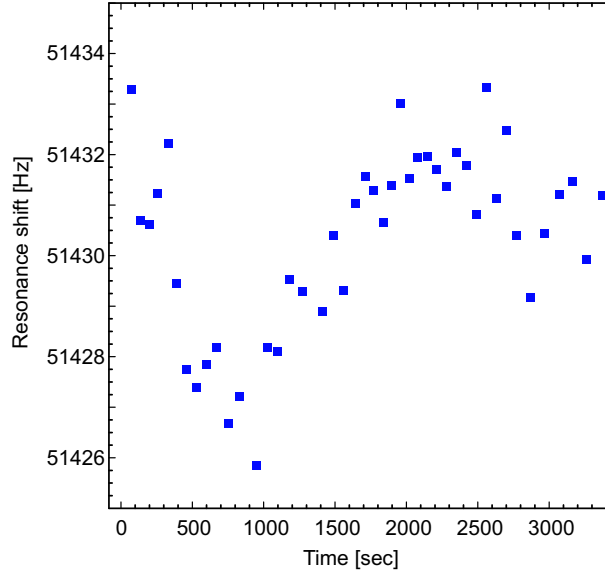
Figure 6.7: Drift of the magnetic resonance frequency without external electric fields over 1 hour.

by one order of magnitude and thus describe the superposition of a fast process (atom-cluster recombination) and a slow process (atom-atom recombination). The dynamics of the decaying background was studied in detail in [22].

The fitting procedure requires 2-3 minutes for each experimental curve on the computers of our laboratory. Therefore it takes about 2 hours to fit a complete set of data.

The evolution of the zero-electric-field resonance frequency over 1 hour is shown in Fig. 6.7. The instability of the system is in this case much more pronounced than in the case examined in the previous section. The error bars, which are determined by the scattering of consecutive zero-field points, are thus considerably larger.

We consider the differential shift of the resonances of the two hyperfine levels F=3 and F=4. We recall that the "old" theory proposed by Sandars in 1968 [33] predicts a differential shift

$$\Delta\nu_{(4,4)\to(4,3)} - \Delta\nu_{(3,3)\to(3,2)} = \frac{9}{14} \mid \alpha_2^{(3)}(4) \mid \mathbb{E}^2 \approx (2.18 \times 10^{-2})\mathbb{E}^2 \, \frac{Hz}{(kV/cm)^2} \,, \qquad (6.5)$$

whereas our novel theory predicts a shift

$$\Delta\nu_{(4,4)\to(4,3)} - \Delta\nu_{(3,3)\to(3,2)} = \frac{3}{28} \mid \alpha_2^{(3)}(4) \mid \mathbb{E}^2 \approx (0.36 \times 10^{-2})\mathbb{E}^2 \, \frac{Hz}{(kV/cm)^2} \,, \qquad (6.6)$$

where we have used our theoretical value (6.3) for the tensor polarizability. In Fig. 6.8 we plot the differential shift of the resonance frequencies in F=4 and F=3 as a function of the applied electric field. The experimental data are fitted by the function $k_1 E^2$. The fit yields the result

$$k_1 = (0.30 \pm 0.07) \times 10^{-2} \, \frac{Hz}{(kV/cm)^2} \,, \qquad (6.7)$$
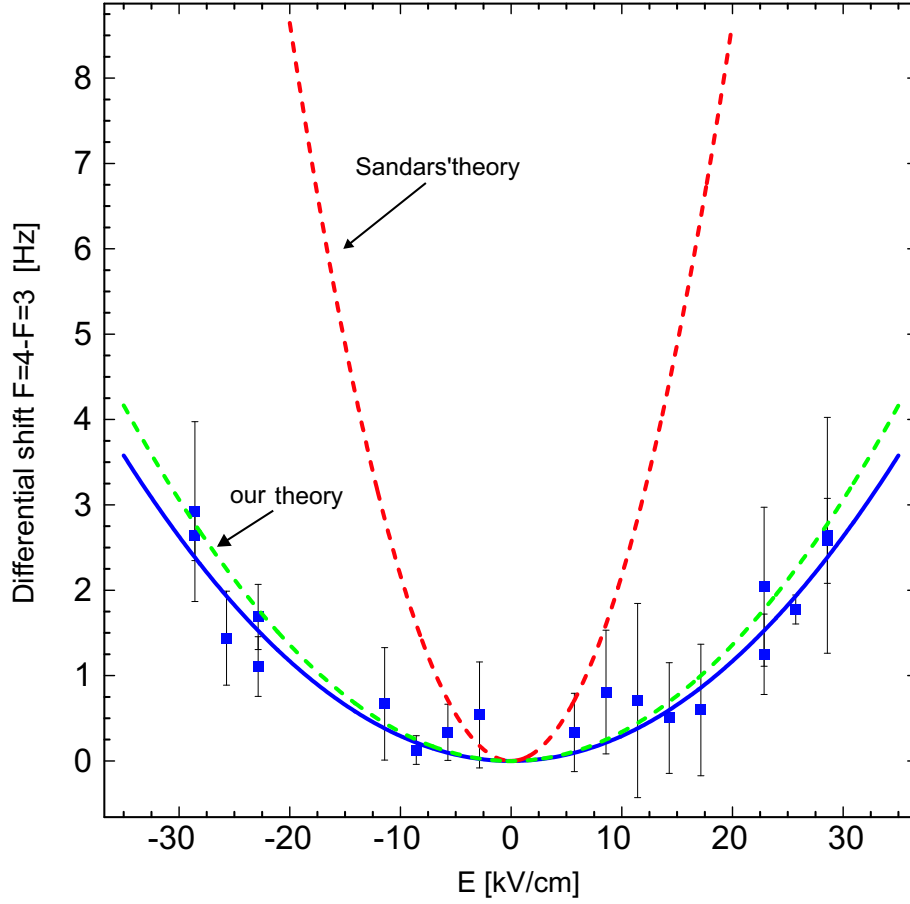
Figure 6.8: Differential shift $\Delta\nu_{(4,4)\to(4,3)} - \Delta\nu_{(3,3)\to(3,2)}$. The experimental data are fitted with the function $k_1 E^2$ (solid line). The dotted curves represent the theoretical predictions of Sandars' model and of our model.

in good agreement with our theoretical prediction (Eq. 6.6). This agreement can also be appreciated graphically in Fig. 6.8. On the other hand, the discrepancy between the experimental results and the prediction of Sandars'model is by far larger than the experimental uncertainty although the error bars in Fig. 6.8 are rather big. Therefore we feel confident enough to state that the sign of $\alpha_2^{(3)}(F)$ predicted by our model is the correct one.

As we did in the previous section, we tried to fit the data shown in Fig. 6.8 with the function $k_1 E^2 + k_2 E^4$. Also in this case the fit yielded a coefficient $k_2$ compatible with zero.
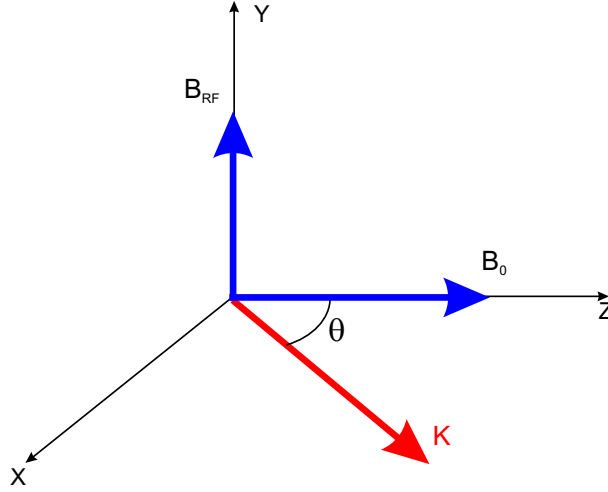
Figure 6.9: The $M_x$ geometry.

## 6.3 The quadratic Stark effect in the M $_x$ configuration

Our set-up can be operated as a self-oscillating phase-locked magnetometer in the so-called $M_x$ geometry [97]. In this configuration the laser beam (with propagation vector $\vec{k}$) is oriented at an angle of 45° with respect to the static magnetic field $\vec{B}_0$, which defines the quantization axis of the system (Fig. 6.9).

The spin polarization initially produced by optical pumping in the direction of $\vec{k}$ precesses around $\vec{B}_0$ thus changing periodically its projection along $\vec{k}$. This precession is driven by the rf-field $\vec{B}_{rf}$ and produces a modulation of the absorption coefficient of the atomic sample at the frequency $\omega_{rf}$. This modulation can be efficiently detected by measuring the fluorescence light with a lock-in detector. The phase between the oscillating rf-field and the system response exhibits a resonant dispersively-shaped enhancement when the rf-frequency matches the Larmor frequency $\omega_L$ associated with the static field $\vec{B}_0$. When the resonance condition $\delta\omega = \omega_L - \omega_{rf} = 0$ is fulfilled, one observes a maximum in the fluorescence modulation amplitude. This modulation is thus a direct measure of the Larmor frequency. The detected dispersive signal is fed back via a PID-amplifier to a voltage-controlled oscillator (VCO) which then drives the rf-coils. The rf-frequency is thus phase-locked to the Larmor frequency and the output of a frequency counter then provides a real-time monitoring of $\omega_L$.

The main motivation that led us to switch to the $M_x$ geometry is that with this real-time monitoring of the Larmor frequency we reduce considerably the systematic effects associated with the scattering of the zero-electric-field resonance frequency.

A top view of the experimental set-up is shown in Fig. 6.10. The polycarbonate body which is mounted inside the copper pressure cell was specially modified in order to accommodate two mirrors which enables us to have the laser beam oriented at 45° when it interacts with the atomic sample. Note that one can easily switch from the $M_z$ configuration to the $M_x$ configuration and viceversa by a mere translation of the laser beam (see Fig. 6.10) [6].

---

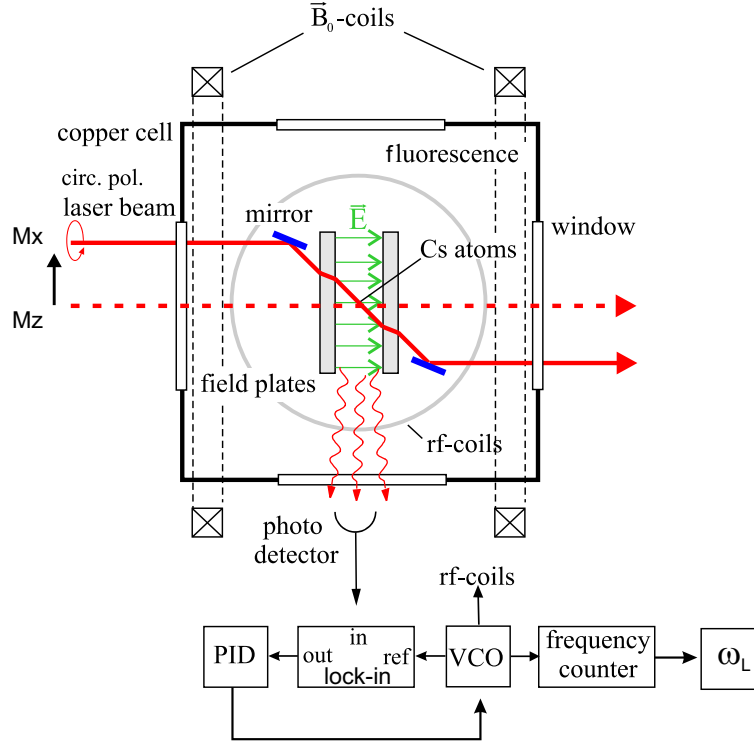[6]The set-up was designed by a preceding PhD student of our group [25].

Figure 6.10: Top view of the set-up for magnetic resonance experiments in the $M_x$ configuration.

## 6.3.1 The tensor polarizability $\alpha_2^{(3)}(F = 4)$

We performed our measurements in the bcc phase, with a temperature of 1.51 K, a pressure of 26.8 bar and in a field of 5.4 $\mu$T. The laser power was 1 mW.

The time evolution of the Larmor frequency before and after the application of an electric field of 43 kV/cm is shown in Fig. 6.11.

The shift of the resonance frequency measured with respect to the adjacent zero-field level is plotted as a function of the applied electric field in Fig. 6.12.

The experimental data are fitted with the function $f(E) = \alpha E^2$. As discussed in the previous section, the fitting procedure with $f(E) = \alpha E^2 + \beta E^4$ yields a coefficient $\beta$ compatible with zero and the fourth order term is thus neglected. The coefficient $\alpha$ yields

$$\alpha_2^{(3)}(4) = -(0.95 \pm 0.30) \times 10^{-2} Hz/(kV/cm)^2 \,. \tag{6.8}$$

This result is smaller than our theoretical calculation

$$\alpha_2^{(3)}(F = 4) = (-3.72 \pm 0.25) \times 10^{-2} \frac{Hz}{(kV/cm)^2} \,. \tag{6.9}$$

and than the experimental results obtained in solid helium in the $M_z$ configuration

$$\alpha_2^{(3)}(F = 4) = (-3.51 \pm 0.2) \times 10^{-2} \frac{Hz}{(kV/cm)^2} \,, \tag{6.10}$$

and in the atomic beam experiment
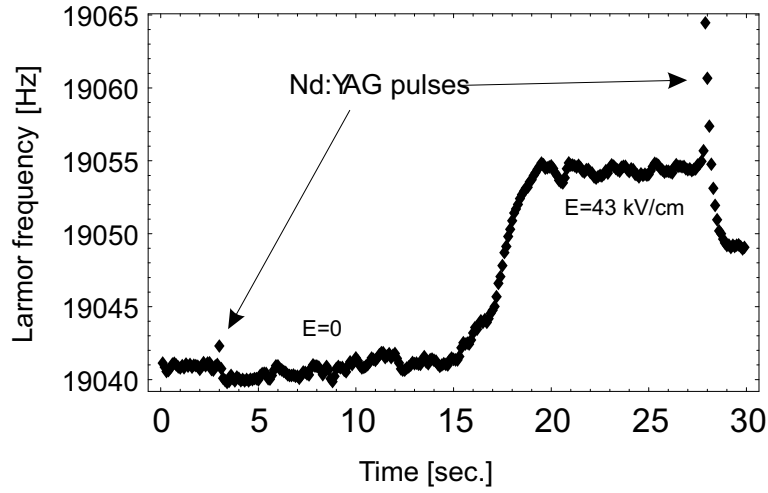
Figure 6.11: The output of the frequency counter shows the time evolution of the phase-locked radio-frequency. The HV is switched on at T=15 sec, and it takes $\approx 5$ seconds to build up an electric field of 43 kV/cm in the pressure cell. One can clearly observe a Stark shift of the Larmor frequency of $\approx 15 Hz$. The Nd:YAG pulses are applied every 25 seconds to dissociate clusters and recover the optical signal.



Figure 6.12: Stark shift of the magnetic resonance $\mid 4, 4 > \leftrightarrow \mid 4, 3 >$. The experimental data are fitted with the function $f(E) = \alpha E^2$ (solid line).

$$\alpha_2^{(3)}(F=4) = (-3.34 \pm 0.20) \times 10^{-2} \frac{Hz}{(kV/cm)^2} \, . \qquad (6.11)$$
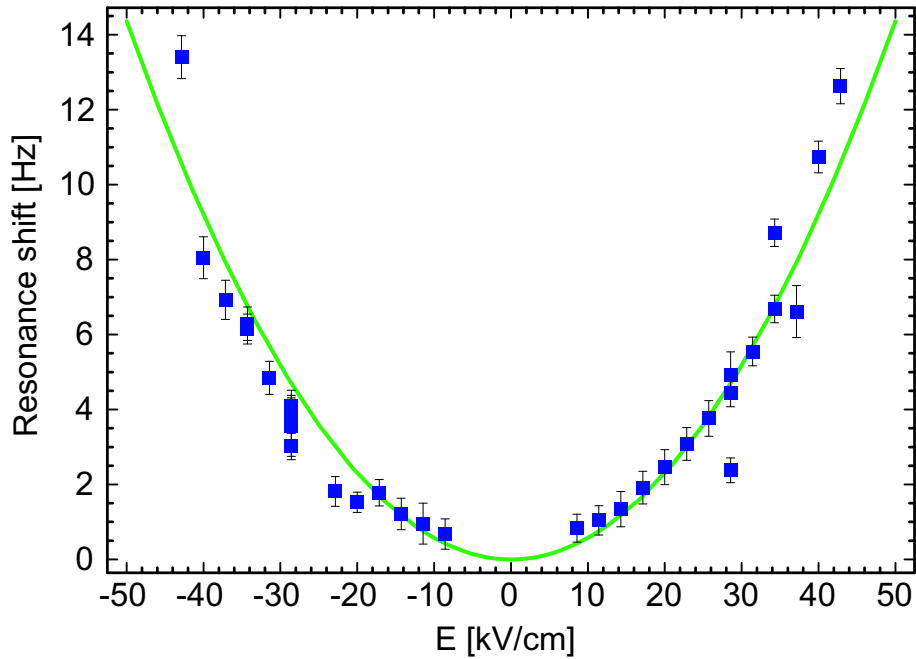
The discrepancy amounts to a factor $\approx 3.5$.

This feature of the new experimental result has to be ascribed to the specific geometry of the system. The estimation of the tensor polarizability given above (Eq. 6.8) is based on the assumption that the measured resonance is entirely due to the magnetic transition $\mid F = 4, M = 4 > \rightarrow \mid F = 4, M = 3 >$. We will show that this is a reasonable approximation in the Mz-configuration, but it turns out to be a misleading assumption when the laser beam is tilted and the pumping light creates a polarization at an angle $\theta$=45° with respect to the quantization axis. We introduce a *geometrical correction factor* by describing the phase-sensitive ODMR technique as a three-step process.

## 6.3.2 The ODMR as a three step process

The three steps are:

- *Optical pumping.* It consists in the preparation of the atomic spin polarization state. Optical pumping is discussed in Chapter 4. Here we will use the system of rate equations 4.6 to calculate the steady state population distribution which is created along the direction of $\vec{B}_0$.

- *Evolution under static and oscillating magnetic fields.* The coherent time evolution of the system under the effect of $\vec{B}_0$ and $\vec{B}_{rf}$ is described by the Liouville equation. Incoherent processes are taken into account by considering the relaxation towards the steady state populations calculated in the previous step and by introducing the longitudinal and transverse relaxation rates $\gamma_1$ and $\gamma_2$. We obtain a system of 25 rate equations for diagonal and off-diagonal elements of the density matrix $\rho$ (we consider only the hyperfine component F=4). We calculate the steady state solutions of these equations.

- *Detection.* We consider populations and coherences from the previous step, and we calculate the detected signal in the geometry of interest, with and without an external electric field. We will show that in the $M_x$ geometry, the simultaneous detection of several resonances ($4 \rightarrow 3, 3 \rightarrow 2, 2 \rightarrow 1$,etc.) strongly affects our estimation of the quadratic Stark shift. Thus we prove the need of a correction factor of geometrical nature, and we make an estimation of it.

We consider these three steps separately.

### 6.3.2.1 The optical pumping

We refer to Eqs. 4.6, 4.7 and 4.8 and we calculate the steady state population distribution in the ground state in a numerical way, i.e., for given values of the parameters $\gamma_1$, $\gamma_p$ and $\theta$ [7].

We first estimate the pumping rate $\gamma_p$ (see Eq. 4.8). The optical D1 transition in solid He has a typical width of $\approx$10 nm, or equivalently $\approx$4 THz.

The total intensity carried by the laser beam ($3 \times 3$ mm) is estimated to be

---

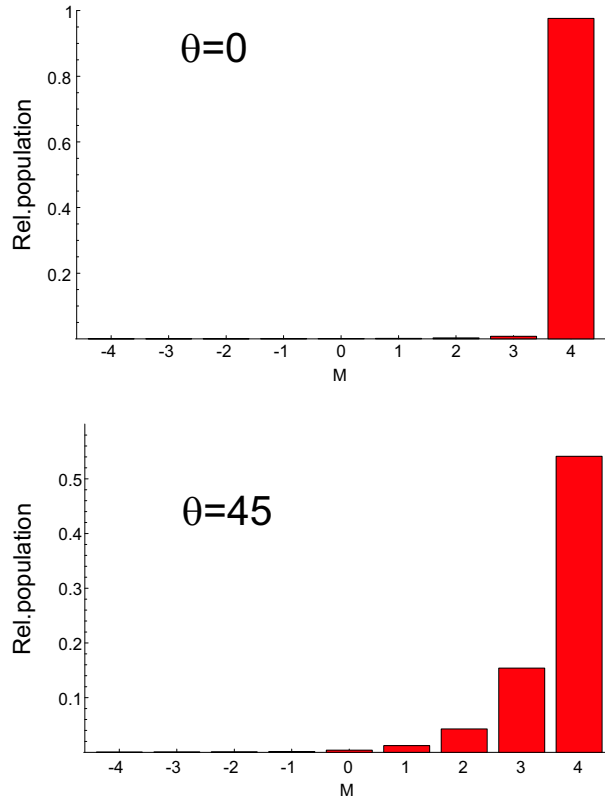[7]For the definition of these parameters one has to refer to Section 4.2

Figure 6.13: Steady state populations after optical pumping in the ground state level F=4, with $\theta = 0$ (left) and $\theta = 45$ (right). Note the different scales.

$$I_0 \approx \frac{1mW}{9mm^2} \approx 110\,W/m^2\,. \tag{6.12}$$

Therefore

$$E^2 = \frac{2I_0}{\varepsilon_0 c} \approx 5 \times 10^4\,V^2/m^2\,. \tag{6.13}$$

We use for the reduced dipole matrix element of the D1 transition the experimental value given by Rafac et al. [74]

$$< 6S_{1/2} \parallel er \parallel 6P_{1/2} >= -4.4978 a_0 e\,. \tag{6.14}$$

We obtain

$$\gamma_p \approx 2800\,s^{-1} \tag{6.15}$$

The experimental value reported in [19] is $\gamma_p \approx 2500\,s^{-1}$, in satisfactory agreement with our estimation. Finally, the longitudinal relaxation rate is $\gamma_1 = 1s^{-1}$ [17–19].

The steady state solutions $p^0_{n=-4,..,4}$ to Eq. 4.6 are shown in Fig. 6.13 for $\theta = 0$ (corresponding to the traditional $M_z$ configuration) and $\theta = \pi/4$ (corresponding to the $M_x$ configuration). The difference between the two population distributions is evident at first sight.

### 6.3.2.2 The evolution

The coherent time evolution of the system under the combination of a static and an oscillating magnetic field, $\vec{B}_0$ and $\vec{B}_{rf}$ respectively, is described by the Liouville equation for the density matrix $\hat{\rho} = \rho_{i,j}$ (i,j=-4,...,4)

$$\dot{\hat{\rho}} = -\frac{i}{\hbar}[\hat{H}(t), \hat{\rho}] = -\frac{i}{\hbar}[\hat{H}_0 + \hat{V}(t), \hat{\rho}], \quad (6.16)$$

where the Hamiltonian $\hat{H}(t)$ is defined as

$$\hat{H}(t) = -\mu\cdot(\vec{B}_0 + \vec{B}_{rf}) = -\mu\cdot(B_0\hat{e}_z + B_{rf}\cos(\omega_{rf}t)\hat{e}_x) = \omega_L\hat{F}_z - 2\Omega_R\hat{F}_x\cos(\omega_{rf}t) \equiv \hat{H}_0 + \hat{V}(t), \quad (6.17)$$

and

$$\omega_L = \frac{g\mu_b}{\hbar}B_0 \quad , \quad \Omega_R = -\frac{g\mu_b}{\hbar}\frac{B_{rf}}{2}, \quad (6.18)$$

are the Larmor and the Rabi frequencies respectively.

After applying the rotating wave approximation (RWA), the time dependance of the oscillating interaction disappears and we can rewrite the Liouville equation in the form

$$\dot{\hat{\rho}}_{RWA} = -\frac{i}{\hbar}[\hat{H}_0 + \hat{V}_{RWA}, \hat{\rho}_{RWA}], \quad (6.19)$$

where

$$\hat{H}_0 + \hat{V}_{RWA} = \omega_L\hat{F}_z - \Omega_R\hat{F}_x. \quad (6.20)$$

Hereafter we will neglect the subscripts RWA and assume that all the following calculations are done in the rotating frame.

If we consider only the hyperfine component F=4, and we introduce the longitudinal and transverse relaxation rates $\gamma_1$ and $\gamma_2$, we obtain 9 equations for the time evolution of the diagonal elements of the density matrix $\hat{\rho}$

$$\dot{\rho}_n = -iV_{n,n+1}(\rho_{n+1,n} - \rho_{n,n+1}) - iV_{n,n-1}(\rho_{n-1,n} - \rho_{n,n-1}) - \gamma_1(\rho_n - \rho_n^0), \quad (6.21)$$

where $n = -4, ..., 4$, $V_{n,m} = <n \mid V \mid m>$ and $\rho_{n=-4,..,4}^0$ are the steady state populations produced by the optical pumping.

For the off-diagonal matrix elements we have 8 additional equations

$$\dot{\rho}_{j,j-1} = -i\delta\rho_{j,j-1} - iV_{j,j-1}(\rho_{j-1} - \rho_j) - \gamma_2\rho_{j,j-1}, \quad (6.22)$$

where $j = -3, ..., 4$ and $\delta = \omega_L - \omega_{rf}$ is the detuning.

If we consider the 8 complex conjugates of Eq. 6.22 we obtain a total system of 25 differential equations. In order to calculate their steady state solutions we have to assign numerical values to the parameters $\gamma_1$, $\gamma_2$ and $\Omega_R$.

The relaxation rates for populations and coherences in solid He are known [17–19]. We assume $\gamma_1 = 1 \ s^{-1}$ and $\gamma_2 = 4 \ s^{-1}$.

The Rabi frequency can be estimated from its definition (Eq. 6.18)

$$\Omega_R \approx 2\pi \cdot 3.5 \cdot \frac{B_{rf}}{2} \quad [Hz/nT], \quad (6.23)$$

and with a typical rf-field of $\approx 4\ nT$ we have

$$\Omega_R \sim 44 \quad Hz\,. \tag{6.24}$$

For the time being we will assume for simplicity $\Omega_R = 50$ Hz, and we will discuss later how the results depend on the value of $\Omega_R$.

The steady state populations $\rho_n$ and the coherences $\rho_{j,j+1}$ (with their complex conjugates) are calculated and used in the third step.

### 6.3.2.3 The detection

This third step consists in the detection of the fluorescence signal associated with the coherence between adjacent magnetic sub-levels.

The problem of the detection of optical coherence signals between magnetic sub-levels in the ground state of alkali atoms is treated from an analytical point of view by Alexandrov et al. in [98]. According to the authors of this work, the general expression for the coherence signal of two ground state levels $M_1$ and $M_2$, observed in absorption of light with polarization $\mathbf{e}$, is:

$$S_{M_1 M_2} \propto \Re[\rho_{M_1,M_2} \sum_m < M_2 \mid (\mathbf{d} \cdot \mathbf{e})^+ \mid m > \xi(m) < m \mid (\mathbf{d} \cdot \mathbf{e}) \mid M_1 >]\,, \tag{6.25}$$

where $\xi(m)$ is the effective intensity of the light on the transitions $M_1, M_2 \leftrightarrow m$. In principle $\xi(m)$ is given by the convolution of the spectral profile of the absorption with the profile of the laser beam. In our special case, the absorption profile is broadened by about 5 orders of magnitude (from $\approx 30$ MHz to $\approx 4$ THz) due to the interaction of the atom with the surrounding helium matrix and the hyperfine structure is not resolved. We can therefore set $\xi(m)$ equal to a constant and neglect it in the equations that follow.

After some calculations, from Eq. 6.25 one obtains the following result

$$S_{M_1 M_2} \propto |< 1/2 \parallel d \parallel 1/2 >|^2 \times$$

$$\times \Re[\rho_{M_1,M_2} \sum_{f,m} \sum_{q_1,q_2} (2F+1)\sigma(q_1,q_2) C^{f,m}_{F,M_1,1,q_1} C^{f,m}_{F,M_2,1,q_2} \left\{ \begin{matrix} f & 1 & F \\ 1/2 & 7/2 & 1/2 \end{matrix} \right\}^2 ]\,, \tag{6.26}$$

where $C^{f,m}_{F,M,1,q}$ are Clebsch-Gordan coefficients and where $\sigma(q_1,q_2)$, with $q_1,q_2 = -1,0,1$, is the *light polarization matrix*, which has the form

$$\sigma = \begin{pmatrix} \sin^4 \frac{\theta}{2} & \frac{(1-\cos\theta)\sin\theta}{2\sqrt{2}} & \frac{\sin^2\theta}{4} \\[2mm] \frac{(1-\cos\theta)\sin\theta}{2\sqrt{2}} & \frac{\sin^2\theta}{2} & \frac{(1+\cos\theta)\sin\theta}{2\sqrt{2}} \\[2mm] \frac{\sin^2\theta}{4} & \frac{(1+\cos\theta)\sin\theta}{2\sqrt{2}} & \cos^4 \frac{\theta}{2} \end{pmatrix}\,, \tag{6.27}$$

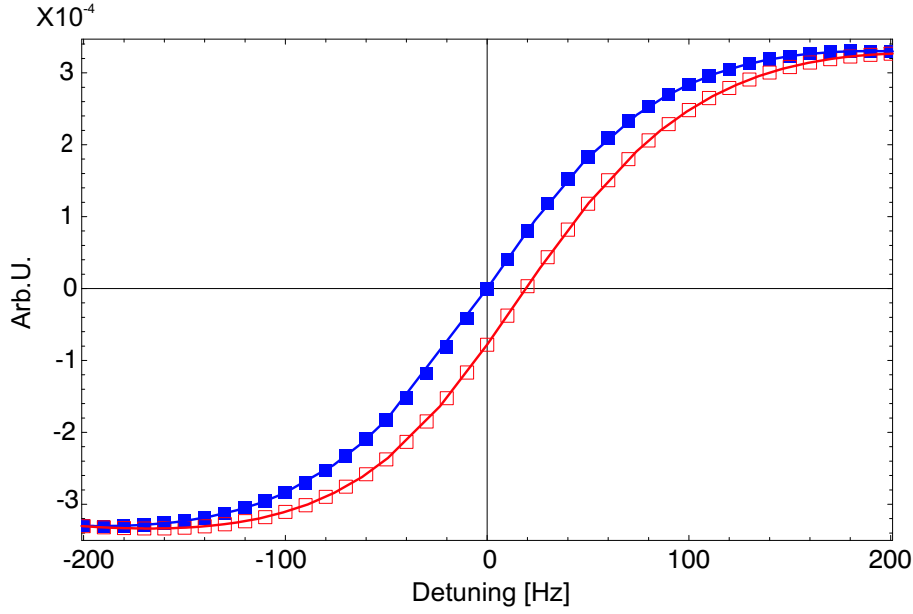under the assumption that the light beam is 100% circularly polarized.

Figure 6.14:  Calculated coherence signal produced by the single magnetic transition $\mid 4 > \rightarrow \mid 3 >$, without electric field (filled squares) and with $E = 40$ $kV/cm$ (empty squares). We have assumed $\alpha_2^{(3)} = -3.4 \times 10^{-2}$ $Hz/(kV/cm)^2$. The other parameters are: $\gamma_p = 2500$ $s^{-1}$, $\gamma_1 = 1$ $s^{-1}$, $\gamma_2 = 4$ $s^{-1}$ and $\Omega_R = 50$ $Hz$

It is straightforward to calculate with MATHEMATICA the coherence signal $S_{M_1,M_2}(\delta)$ relative to the magnetic transition $\mid M_1 > \rightarrow \mid M_2 >$.

In order to include the effect of the electric field, the detuning $\delta$ is re-defined as

$$\delta = \omega_L - \omega_{rf} + \frac{3}{56}(2M_1 - 1)\alpha_2^{(3)}\mathbb{E}^2 \, . \tag{6.28}$$

If we calculate $S(\delta)$ for different values of the detuning $\delta$, without changing the other parameters, we obtain a set of points in the plane $(S, \delta)$ which can be interpolated to visualize the signal that is detected in an experiment where the radio frequency $\omega_{rf}$ is scanned over a given range. In Fig. 6.14 we plot the calculated signal and its shift when a field of 40 $kV/cm$ is applied. We first consider only the signal produced by the single magnetic transition $\mid 4 > \rightarrow \mid 3 >$. This could be a good approximation in the case $\theta = 0$, where more than 90% of the population is transferred by the optical pumping to the level $M = 4$ (see Fig. 6.13).

The shift is estimated by considering the intersection of the interpolating function with the $\hat{x}$ axis. In the case shown in Fig.6.14, when only one magnetic transition is detected, the shift turns out to be 19.2 Hz.

The approximation that the detected signal is produced by a single magnetic resonance is no more valid for $\theta = \pi/4$ (see Fig. 6.13). In this case, the signal is given by the super-position of several resonances ($\mid 4 > \rightarrow \mid 3 >$, $\mid 3 > \rightarrow \mid 2 >$, etc.) of different amplitudes, as shown in Fig. 6.15.

Therefore, in order to calculate the total signal we use again Eq. 6.26 but we take the sum over all the resonances
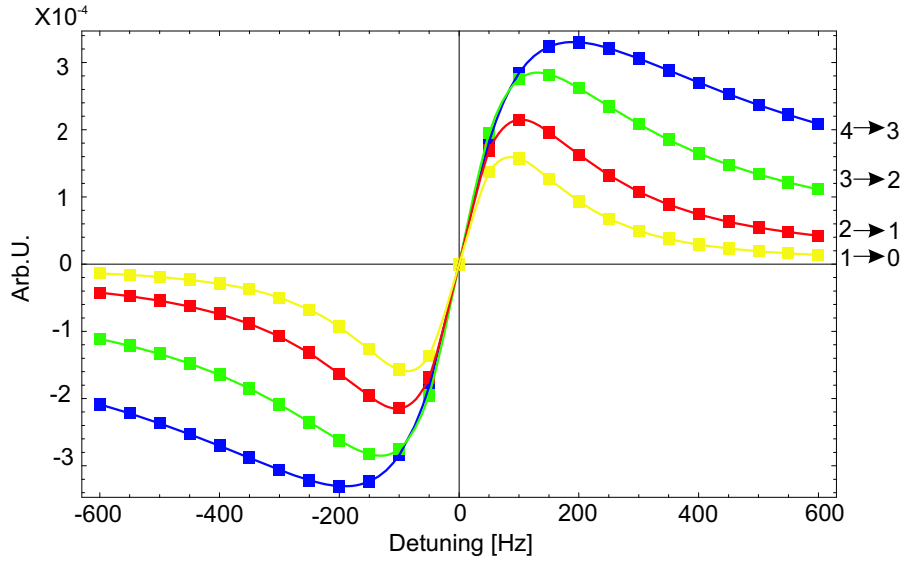
Figure 6.15: Calculated coherence signals produced by the first four magnetic transitions $\mid M >\rightarrow\mid M-1 >$ when $\theta = \pi/4$. There is no electric field. The other parameters are: $\gamma_p = 2500\ s^{-1}$, $\gamma_1 = 1\ s^{-1}$, $\gamma_2 = 4\ s^{-1}$ and $\Omega_R = 50\ Hz$
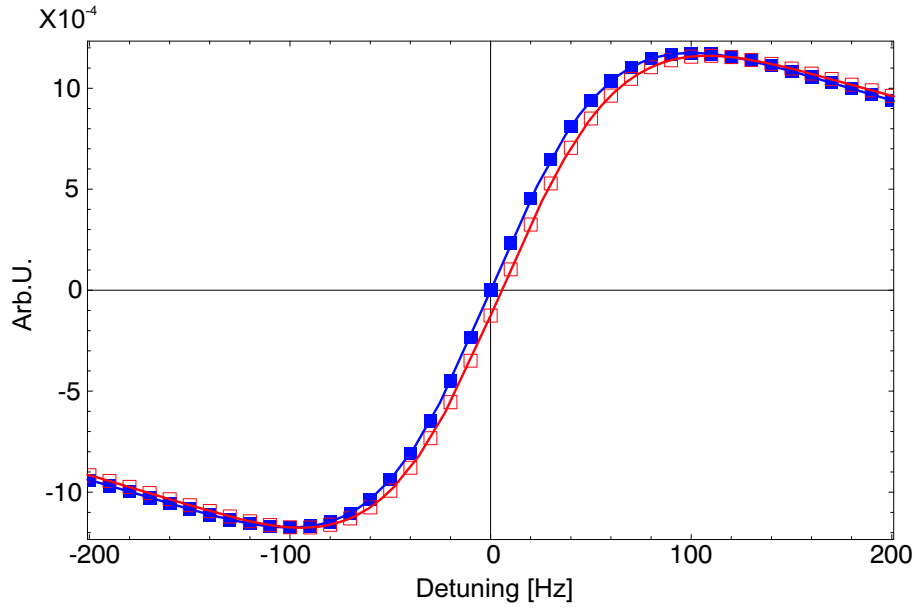


Figure 6.16: Calculated coherence signal produced at $\theta = \pi/4$ by the sum of all magnetic transitions $\mid M >\rightarrow\mid M-1 >$, M=4,...-3, without electric field (filled squares) and with $E = 40\ kV/cm$ (empty squares). We have assumed $\alpha_2^{(3)} = -3.4 \times 10^{-2}\ Hz/(kV/cm)^2$. The other parameters are the same as in Fig. 6.14. By comparing this result to the one reported in Fig. 6.14 it is evident that the co-existence of several magnetic transitions leads to an apparent reduction of the Stark shift.

$$S_{tot}(\delta) = \sum_M S_{M,M-1}(\delta) \tag{6.29}$$

When an electric field is applied, these single magnetic transitions are shifted by different amounts due to the $M^2$ dependence of the Stark interaction. As a consequence, the splitting of the resonances leads to a distortion of the signal and to a relevant reduction of the observed shift. This is clearly visible in Fig. 6.16. The shift is now reduced to 5.5 Hz, although we have used the same parameters that produced the result of Fig. 6.14 (especially we didn't change the value $\alpha_2 = -3.4 \times 10^{-2}~Hz/(kV/cm)^2$).

### 6.3.3 The geometrical correction factor

The distortion of the signal discussed above leads to under-estimate the tensor polarizability, if its value is extrapolated from the measured shift. Thus, the need of a correction factor is evident. In the case shown in Fig. 6.16 and in Fig. 6.14, this factor is

$$\varepsilon = \frac{19.2 Hz}{5.5 Hz} = 3.49\,. \tag{6.30}$$

Therefore our experimental result (Eq. 6.8) has to be corrected according to

$$\alpha_2^{(2)} = -(0.95 \pm 0.30) \cdot \varepsilon \cdot 10^{-2} Hz/(kV/cm)^2 = -(3.31 \pm 0.30) \cdot 10^{-2} Hz/(kV/cm)^2\,, \tag{6.31}$$

in excellent agreement with all previous experimental results and with our theoretical calculation.

There are two important remarks:

- Actually the estimation of the correction factor is affected by an error mainly due to the uncertainties of the numerical values of all the parameters used in the simulations. Although we do not consider it in Eq. 6.31, this error should be added to the experimental one.

- We run some simulations by changing the values of the parameters $\gamma_p$ and $\Omega_R$ and we estimate the corresponding correction factor $\varepsilon$. The result is shown in Fig. 6.17. A change of the Rabi frequency in the range from 30 Hz to 70 Hz leads to a change of the correction factor $\varepsilon$ of about 3%, while it seems to be only very weakly sensitive to changes of the pumping rate $\gamma_p$.
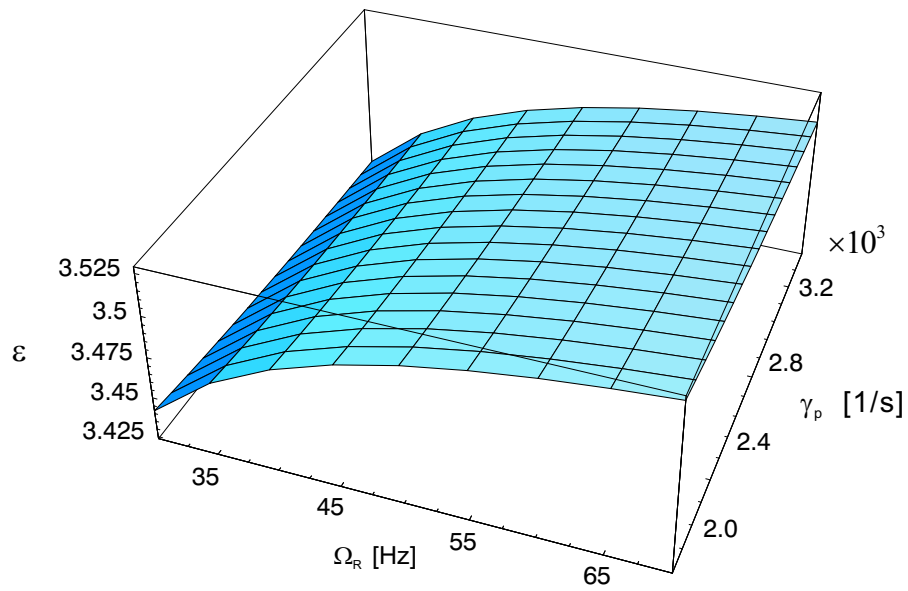
Figure 6.17: Correction factor $\varepsilon$ as a function of the parameters $\gamma_p$ and $\Omega_R$

# Chapter 7

# Conclusions

We conclude this work by coming back to the original motivation that some years ago triggered the investigation of electric field effects on doped solid helium matrices: the study of the applicability of paramagnetic atoms trapped in a helium crystal for a search for permanent atomic electric dipole moments (EDM).

Beside a number of relevant results, described in the previous chapters, we discovered systematic effects as well as technical difficulties which led us to conclude that our system is not a good candidate for a future EDM experiment. Here we give just a list of these effects.

One of the main limitations on the applicable electric field strength has a technical nature. An electric breakdown occurs inside the cryostat, between a high voltage cable and the grounded pressure cell, at voltages which are typically about 17 kV (equivalent electric filed strength in the cell ≈50 kV/cm). Moreover, at voltages above 15 kV the heat produced by the leakage current (approximately a few $\mu$A) in the cell becomes an issue. If the measurement takes longer than one minute, it results in the melting of the helium crystal and destruction of the sample. In the present experimental setup one measurement takes 20-30 seconds followed by another similar period without applied electric field, during which the heat is removed and a reference measurement performed. A significant increase in the applied electric field strength will reduce the time available for each single measurement.

The existing signal-to-noise ratio enables us to determine the magnetic resonance frequencies with an accuracy below 0.1 Hz. However the reproducibility of the measured value from one measurement to another is much poorer and limits the precision of the Stark shift measurements to $\approx$ 1 Hz. The analysis of experimental data shows that the resonance frequency is affected by a relatively slow drift on the time scale of hours, plus some sudden jumps that occur in between two consecutive measurements. These jumps have a magnitude on the order of 1 Hz and thus represent a major limitation on the accuracy of our Stark shift measurements.

In our experiment cesium atoms are implanted in the helium crystal by means of laser ablation. This is the most reliable technique for the doping of helium crystals with highly reactive species. However, the sample is indiscriminately doped with all products of the laser ablation process. Unfortunately, under these extreme conditions (low temperature and high pressure) the most part of ablated material appears in the form of clusters, rather than individual atoms. Accordingly to our estimations based on the transmission spectra of the sample, the total density of cesium atoms aggregated in clusters is on the order of $10^{17}$ cm$^{-3}$, whereas the density of lonely atoms is only $10^9$ cm$^{-3}$. This huge disproportion considerably affects the properties of the sample (for example, the absorption and scattering

of light), which are determined mostly by clusters rather than by the species of interest (atoms). Moreover, the diffusion of cesium atoms in the crystal allows cesium clusters to absorb the atoms distributed around them. The dissociation of the clusters, in order to maintain a reasonable atomic density, is produced by laser pulses (second harmonic of Nd:YAG laser) that are applied at time intervals of about 30 seconds. The drawbacks of this solution are: (i) the time of one measurement is limited by the interval between the two laser pulses; (ii) each recorded resonance lineshape is distorted because of the exponential decay of the atomic fluorescence after the laser pulse; (iii) a shock or even a partial melting produced by the laser pulse in the crystal redistributes the cesium atoms and, combined with the inhomogeneity of the static magnetic field, results in sudden shifts of the measured magnetic resonance frequency.

Not only neutral particles (cesium atoms, molecules and clusters) but also ions and electrons are produced by the laser ablation and they should thus be present in our sample. The presence of charged particles and their possible inhomogeneous distribution in the sample can significantly affect the electric field seen by the cesium atoms. Even in the absence of an external electric field, this effect may produce a Stark shift which is inhomogeneous across the sample and therefore it shows up as a broadening of the magnetic resonance peak. The laser pulses applied for the dissociation of the clusters may redistribute those charged particles in the crystal and further deteriorate the reproducibility of our Stark shift measurements.

Taking into account all effects mentioned above, one cannot expect an experiment using cesium atoms implanted in helium crystals to be competitive with other existing EDM experiments.


Independently on the search for the EDM, the study of the quadratic Stark effect has produced highly relevant results which are described in this work.

On the experimental side, after some years of significant efforts, the quadratic Stark effect in the Zeeman structure of the ground state of cesium atoms implanted in solid helium has been measured. The results are perfectly compatible with previous measurements performed in atomic beams.

From a theoretical point of view, the historical discrepancy between experiments and theoretical calculations, which existed since the 1960s, is now ruled out by our third order perturbation theory including off-diagonal hyperfine matrix elements. Moreover, our calculations have highlighted the existence of a sign error in the old theory of the quadratic Stark effect. It seems that over the last 40 years this sign problem was never remarked. We produced experimental evidence that the signs predicted by our model are the correct ones.

Our calculations led also to a prediction of the Stark shift of the hyperfine transition in the ground state of cesium. This is another extremely relevant result since it enters a very actual and open debate concerning the Stark shift of the clock transition. This is the main open question left by the experimental and theoretical studies described here. A possible answer could be found by realizing a new atomic beam experiment, which is now on our agenda for the near future.

# Appendix A

# The irreducible tensor formalism

The calculation of matrix elements in complex configurations can present considerable analytical difficulties. Some great notational and calculational simplifications of particular elegance are provided by the algebra of irreducible tensor operators, known as *Racah algebra*.

The methods of the Racah algebra present the big advantage of taking the rotational symmetries of the problem into account in a natural way and enable dynamical and geometrical factors in the equations of interest to be separated from each other.

An irreducible tensor operator of rank K is defined as a set of $2K+1$ components $T_Q^K$, with Q=-K,-K+1,...,K, that transform under rotations in the same way as the spherical harmonics $Y_{K,Q}$, i.e., as the eigenvalues $\mid K, Q >$ of an angular momentum operator $L_z$ of an orbital momentum state with $L = K$. Thus the operator components $T_Q^K$ defined in a reference system $XYZ$ can be related to the components $T_q^K$ defined in a rotated system $xyz$ by:

$$T_Q^K = \sum_q T_q^K D_{qQ}^K(\alpha\beta\gamma) \,, \tag{A.1}$$

where $\alpha$, $\beta$ and $\gamma$ are the Euler angles of the rotation, defined for instance as in [99], and where $D^K$ is the rotation matrix defined as

$$D_{qQ}^K(\alpha\beta\gamma) = e^{-iq\alpha} d_{qQ}^K(\beta) e^{-iQ\gamma} \,. \tag{A.2}$$

The *reduced rotation matrix* $d^K(\beta)$ describes by convention a rotation by an angle $\beta$ about the $y-$axis and can be defined as Eq.6.9 in [99].

Equivalently, an operator $T^K$ can be defined as an irreducible tensor if its components $T_Q^K$ satisfy the same commutation relations with the angular momentum operator J as the spherical harmonics $Y_{kq}$ do:

$$\left[J_\pm, T_Q^K\right] = \sqrt{(K \mp Q)(K \pm Q + 1)} T_{Q\pm1}^K \,,$$
$$\left[J_z, T_Q^K\right] = Q T_Q^K \,, \tag{A.3}$$

where $J_\pm = J_x \pm iJ_y$.

In general, any tensor operator $T^K$ that involves spatial coordinates $(r, \theta, \phi)$ and that does not act on spins can be decomposed into spherical harmonics and can thus be written as an irreducible tensor operator of the form

$$T_q^k = f(r) \cdot Y_{kq} \,, \tag{A.4}$$

where f(r) *does not* depend on $\theta$, $\phi$ and q.

A case of special interest is the case $k = 1$ Any vector operator $\mathbf{V}$ can be written in the form

$$\mathbf{V} = \begin{pmatrix} V_x \\ V_y \\ V_z \end{pmatrix} = \mid V \mid \begin{pmatrix} \sin\theta\cos\phi \\ \sin\theta\sin\phi \\ \cos\theta \end{pmatrix} \,, \tag{A.5}$$

where $\theta$ and $\phi$ are the polar and azimuthal angles respectively, defined as sketched in Fig. 2.1. We can define the spherical components $V_q$ of the operator $\mathbf{V}$ as

$$V_\pm = \mp\frac{1}{\sqrt{2}}(V_x \pm iV_y) \,,$$
$$V_0 = V_z \,. \tag{A.6}$$

and thus by using the relations A.5 in A.6 we can write

$$V_\pm = \mp\frac{\mid V \mid}{\sqrt{2}}\sin\theta e^{\pm i\phi} = \sqrt{\frac{4\pi}{3}}\mid V \mid Y_{1,\pm 1} = \mid V \mid C_{\pm 1}^1 \,,$$
$$V_0 = \mid V \mid \cos\theta = \sqrt{\frac{4\pi}{3}}\mid V \mid Y_{1,0} = \mid V \mid C_0^1 \,, \tag{A.7}$$

where

$$C_q^k(\theta,\phi) = \sqrt{\frac{4\pi}{2k+1}}Y_{kq}(\theta,\phi) \tag{A.8}$$

are the renormalized spherical harmonics. The important meaning of Eq. A.7 is that the spherical components of *any* vector operator $\mathbf{V}$ form an irreducible tensor operator or rank 1: $V_\pm = T_{\pm 1}^1$ and $V_0 = T_0^1$.

The electronic position operator $\mathbf{r}$ is an example of relevant interest in the frame of this work. This vector operator can be written as an irreducible tensor in the form

$$\mathbf{r}^1 = r\mathbf{C}^1 \,. \tag{A.9}$$

An angular momentum operator $J$ is another important example of a vector operator which satisfies the conditions A.3 and thus its spherical components $J_q$ form an irreducible tensor operator.

In the frame of the irreducible tensor formalism we are provided an extremely powerful method to expand matrix elements, known as the Wigenr-Eckart theorem:

$$< J,M \mid T_Q^K \mid J',M' > = (-1)^{J-M} \begin{pmatrix} J & K & J' \\ -M & Q & M' \end{pmatrix} < J \parallel T^K \parallel J' > \,. \tag{A.10}$$

The geometrical properties of the interaction are completely described by the 3j - symbol, which depends explicitly on the orientation of the coordinate system through M, M' and Q. On the other hand, the physical nature of the operator $T^K$ is contained entirely in the *reduced matrix element* $< J_1 \parallel T^K \parallel J_2 >$, which describes the purely dynamical part of the interaction and *does not* depend on M, M' and Q. Thus, if the quantization axis is changed by a rotation of the coordinate system, only the 3j - symbol will change while the reduced matrix element stays unchanged.

If the angular momentum J is obtained by coupling two angular momenta $J_1$ and $J_2$ and the tensor $T^K$ operates only in the space of $J_1$, the expression A.10 can be further reduced by uncoupling the angular momenta $J_1$ and $J_2$ and thus by rewriting the reduced matrix element as follows:

$$< \gamma J_1 J_2 J \parallel T^K \parallel \gamma' J_1' J_2' J' > = \delta_{J_2,J_2'} (-1)^{J_1+J_2+J'+K} \sqrt{(2J+1)(2J'+1)} \times$$

$$\times \left\{ \begin{array}{ccc} J_1 & J & J_2 \\ J' & J_1' & K \end{array} \right\} < \gamma J_1 \parallel T^K \parallel \gamma' J_1' > . \quad (A.11)$$

Of course a similar expression holds if the operator $T^K$ acts in the space of $J_2$:

$$< \gamma J_1 J_2 J \parallel T^K \parallel \gamma' J_1' J_2' J' > = \delta_{J_1,J_1'} (-1)^{J_1+J_2'+J+K} \sqrt{(2J+1)(2J'+1)} \times$$

$$\times \left\{ \begin{array}{ccc} J_2 & J & J_1 \\ J' & J_2' & K \end{array} \right\} < \gamma J_2 \parallel T^K \parallel \gamma' J_2' > . \quad (A.12)$$

Another case of special interest for this work is represented by the scalar product of two irreducible tensors:

$$T^K \cdot U^K = \sum_Q (-1)^Q T_{-Q}^K U_Q^K . \quad (A.13)$$

If the operators $T^K$ and $U^K$ act in two different spaces associated with the angular momenta $J_1$ and $J_2$ respectively, one can write (for a proof see [86, 100]):

$$< \gamma J_1 J_2 JM \mid T^K \cdot U^K \mid \gamma' J_1' J_2' J'M' > = \delta_{JM,J'M'} (-1)^{J_1'+J_2+J} \left\{ \begin{array}{ccc} J_1 & J_2 & J \\ J_2' & J_1' & K \end{array} \right\} \times$$

$$\times < J_1 \parallel T^K \parallel J_1' >< J_2 \parallel U^K \parallel J_2' > . \quad (A.14)$$

The interaction described by A.14 is thus diagonal in the coupled angular momentum quantum number J and in its projection M. This is for instance the case of the hyperfine interaction ($\propto J \cdot I$) which is always diagonal in F and $M_F$, and of the spin-orbit interaction ($\propto S \cdot L$), diagonal in J and $M_J$.

# Appendix B

# The reduced matrix elements

We give an explicit representation for the reduced matrix elements of the relevant operators used in this work. More details can be found in [86, 100].

We shall begin by considering the normalized spherical harmonics $C_q^k = \sqrt{\frac{4\pi}{2k+1}} Y_{kq}$. One can prove that

$$< L_1 \parallel C^k \parallel L_2 > = (-1)^{L_1} \sqrt{(2L_1 + 1)(2L_2 + 1)} \begin{pmatrix} L_1 & k & L_2 \\ 0 & 0 & 0 \end{pmatrix}. \qquad (B.1)$$

One can notice here that due to the presence of the parity conserving 3j-symbol, the reduced matrix element above is different from zero only if $L_1 + k + L_2$ is even.

Furthermore, from the symmetry properties of the 3-j symbol it follows that

$$< L_1 \parallel C^k \parallel L_2 > = (-1)^k < L_2 \parallel C^k \parallel L_1 > . \qquad (B.2)$$

As we already remarked in Appendix A the position operator $\mathbf{r}$ can be written as an irreducible tensor of rank 1 in the form: $\mathbf{r}^1 = r\mathbf{C}^1$. From B.1 and by using the algebraic expression corresponding to the 3-j symbol, it follows that

$$< n_1 L_1 \parallel r^1 \parallel n_2 L_2 > = < L_1 \parallel C^1 \parallel L_2 > \int_0^\infty \Psi(n_1 L_1) r \Psi(n_2 L_2) r^2 dr =$$

$$= (-1)^{L_1 + L_{max}} \sqrt{L_{max}} \int_0^\infty \Psi(n_1 L_1) r \Psi(n_2 L_2) r^2 dr =$$

$$= (-1)^{L_1 + L_{max}} \sqrt{L_{max}} \cdot R_{n_1 L_1, n_2 L_2} , \quad (B.3)$$

where $L_2 = L_1 \pm 1$, $L_{max} = Max[L_1, L_2]$ and $R_{n_1 L_1, n_2 L_2}$ is the so-called *radial integral*.

If we focus our attention on the specific case of Cs treated in this work, the reduced matrix elements of the position operator $\mathbf{r}$ have some interesting and useful properties. By applying the angular momenta decoupling rule A.11 and by taking B.3 into account, it is straightforward to prove that

$$< 6S_{1/2} \parallel r \parallel nP_{1/2} > = < nP_{1/2} \parallel r \parallel 6S_{1/2} > = -\sqrt{\frac{2}{3}} \cdot R_{6S,nP} \qquad (B.4)$$

$$< 6S_{1/2} \parallel r \parallel nP_{3/2} > = - < nP_{3/2} \parallel r \parallel 6S_{1/2} > = -\sqrt{\frac{4}{3}} \cdot R_{6S,nP} , \qquad (B.5)$$

and as a consequence

$$< 6S_{1/2} \parallel r \parallel nP_{3/2} > = \sqrt{2} < 6S_{1/2} \parallel r \parallel nP_{1/2} > \ . \tag{B.6}$$

Notice that here we are assuming that the radial integral $R_{n_1 L_1, n_2 L_2}$ does not depend on $J_1$ and $J_2$. Advanced theoretical methods based on relativistic many-body all-order perturbation calculations have been applied to Cs [69, 72] and led to a deviation from the general rule B.6 on the order of 1%. Such a deviation has been tested, e.g., in high precision lifetime experiments [101].

By applying the Wigner-Eckart theorem and the angular momenta decoupling rules to the matrix element of a generic component $r_q$ of the position operator, it is straightforward to verify another general rule

$$< L_1, J_1, F_1, M_1 \mid r_q \mid L_2, J_2, F_2, M_2 > = (-1)^{q \cdot} < L_2, J_2, F_2, M_2 \mid r_{-q} \mid L_1, J_1, F_1, M_1 > \ . \tag{B.7}$$

For a generic uncoupled angular momentum operator $J$ one can prove the following

$$< J_1 \parallel J \parallel J_2 > = \delta_{J_1, J_2} \sqrt{J_1(J_1 + 1)(2J_1 + 1)} \, , \tag{B.8}$$

which yields

$$< L \parallel L \parallel L > = \sqrt{L(L+1)(2L+1)} \, , \tag{B.9}$$

$$< S \parallel S \parallel S > = \sqrt{S(S+1)(2S+1)} = \sqrt{\frac{3}{2}} \, . \tag{B.10}$$

One has to notice here that in the case of coupled angular momenta like $\mathbf{J} = \mathbf{L} + \mathbf{S}$, by applying the decoupling rules of Appendix A one obtains

$$< J_1 \parallel J \parallel J_2 > = < J_1 \parallel L \parallel J_2 > + < J_1 \parallel S \parallel J_2 > =$$
$$= (-1)^{L+S+J_2+1} \sqrt{(2J_1 + 1)(2J_2 + 1)} \times$$
$$\times \left[ \begin{Bmatrix} L & J_1 & S \\ J_2 & L & 1 \end{Bmatrix} < L \parallel L \parallel L > + (-1)^{J_1 - J_2} \begin{Bmatrix} S & J_1 & L \\ J_2 & S & 1 \end{Bmatrix} < S \parallel S \parallel S > \right] \ . \tag{B.11}$$

The interaction is thus diagonal in L and S but not necessarily in J.

# Appendix C

# Cesium wave functions

## C.1 The Thomas-Fermi model

We used the Schrödinger equation with a statistical Thomas-Fermi model potential to calculate the relevant wave functions of the free cesium atom. In this statistical method one treats the electrostatic potential of the nucleus and the core electrons by treating the core electrons as a degenerate Fermi gas at temperature T=0 K. This is a good approximation when all the electrons are in their lowest possible energy state. Moreover the statistical approach is obviously valid only for systems with a large number of core electrons (54 in the case of cesium).

We will mention in this appendix just the main properties of this statistical approach. For more details one can refer to Norcross et al. [102] or Gombas [103].

The model first starts from two basic assumptions:

- the atomic potential has a spherical symmetry,

- the potential can be decomposed in small spherical shells, with volumes dV, in which the potential is assumed to be constant.

These assumptions are not good for regions close to the nucleus where the potential is characterized by steep changes and for regions far away from the nucleus where one can find only a few highly excited electrons and the statistical description does not apply any more. These are the main limits of the model.

The goal is now to calculate the potential in which the electrons are moving. One starts to fill the small spherical shells mentioned above with N electrons. The Pauli principle is respected by putting only two electrons, with opposite spins, in each elementary volume $h^3$ of the six dimensional phase space. The volume in phase space can then be written as

$$\frac{Nh^3}{2} = \frac{4\pi}{3} p_F^3 dV \; , \tag{C.1}$$

where $p_F$ is the electronic momentum. By writing the electron density as $\rho_e = N/dV$ one can write the relation between the maximal momentum and the density as

$$p_F = \sqrt[3]{\frac{h^3}{2} \frac{3}{4\pi} \rho_e} \; . \tag{C.2}$$

A bound electron in a spherical shell has a total energy of $\frac{p^2}{2m} - Ve$ which can not be higher than a maximal potential energy $V_0 e$. In a neutral atom this energy corresponds to the

ionization energy and hence $V_0 = 0$. From Eq. C.2 one can infer a relation between the electron density $\rho_e$ and the potential V. Then the Poisson equation

$$\Delta(V - V_0) = 4\pi e \rho_e \tag{C.3}$$

leads to the dimensionless Thomas-Fermi equation which can be expressed in spherical dimensionless coordinates as

$$\frac{d^2\chi(x)}{dx^2} = \frac{\chi^{\frac{2}{3}}(x)}{\sqrt{x}} \, , \tag{C.4}$$

where $\chi = \frac{r(V-V_0)}{Ze}$ and $x = \frac{2rZ^{\frac{1}{3}}}{a_0}(\frac{4}{3\pi})^{\frac{2}{3}}$. Z is the atomic number and $a_0$ is the Bohr radius. The solution of the Thomas-Fermi differential equation (C.4) leads to the self-consistent Thomas-Fermi atomic potential $V_{TF}$.

This is of course just a first approximation to the real potential. One problem for example is that the model predicts an infinite atomic radius. Several corrections are therefore included into this simple model.

## C.2 The Fermi-Amaldi corrrection

The Fermi-Amaldi correction excludes the electrostatic self-interaction of the electrons which was included in the simple Thomas-Fermi potential. Thus the valence electron in the S-state of an alkali atom will feel the potential generated by the electrons of the inner shells but not its own one.

## C.3 Core polarization potential

We take the polarization potential of the core into account. The valence electron of the alkali atom produces a field at the core and polarizes it. The dipole polarization potential can be modeled as[102]

$$V_{dip} = -\frac{\alpha_d}{2r^4}(1 - e^{-(\frac{r}{r_L})^6}) \, . \tag{C.5}$$

We include also the quadrupole polarization of the core which can be written[102] as

$$V_{quad} = -\frac{\alpha_q - 3\beta_q a_0}{2r^6}(1 - e^{-(\frac{r}{r_L})^{10}}) \, . \tag{C.6}$$

The parameter $r_L$ is a cut-off radius which depends on the angular momentum l and is assumed to be the same for the dipole and the quadrupole polarization. Values for the parameters $\alpha_d$, $\alpha_q$ and $\beta_q$ as well as more details about these approximations can be found in [102].

## C.4 Spin-orbit interaction potential

As a last correction we include in the model the spin-orbit interaction potential

$$V_{so} = \frac{\alpha^2}{2}\frac{1}{r}\frac{dV}{dr}\frac{1}{(1 + \frac{1}{4}\alpha^2 V)^2}\overrightarrow{L} \cdot \overrightarrow{S} \, , \tag{C.7}$$

where $V = V_{TF} + V_{dip} + V_{quad}$, and $\alpha$ is the fine structure constant. The term in brackets represents a relativistic correction.

## C.5 The Schrödinger equation

To calculate the wave functions of the free atom, the radial Schrödinger equation

$$\frac{d^2 u(r)}{dr^2} + \left( 2(E - V_{tot}) - \frac{l(l+1)}{r^2} \right) u(r) = 0 \tag{C.8}$$

was solved numerically with the total potential $V_{tot} = V_{TF} + V_{dip} + V_{quad} + V_{so}$. The radial part of the atomic wave function is then given by $R_{nlj} = u(r)/r$.

In Fig. C.1 we plot as an example the radial wave functions $u(r) = rR_{6S_{1/2}}(r)$ of an electron in the ground state of cesium and the radial wave functions $u(r) = rR_{6P_{1/2,3/2}}(r)$ of an electron in the first excited states $6P_{1/2,3/2}$.

A more detailed treatment of these calculations will be included in the Phd thesis of A.Hofer [104] who carried out most part of the calculations mentioned above.
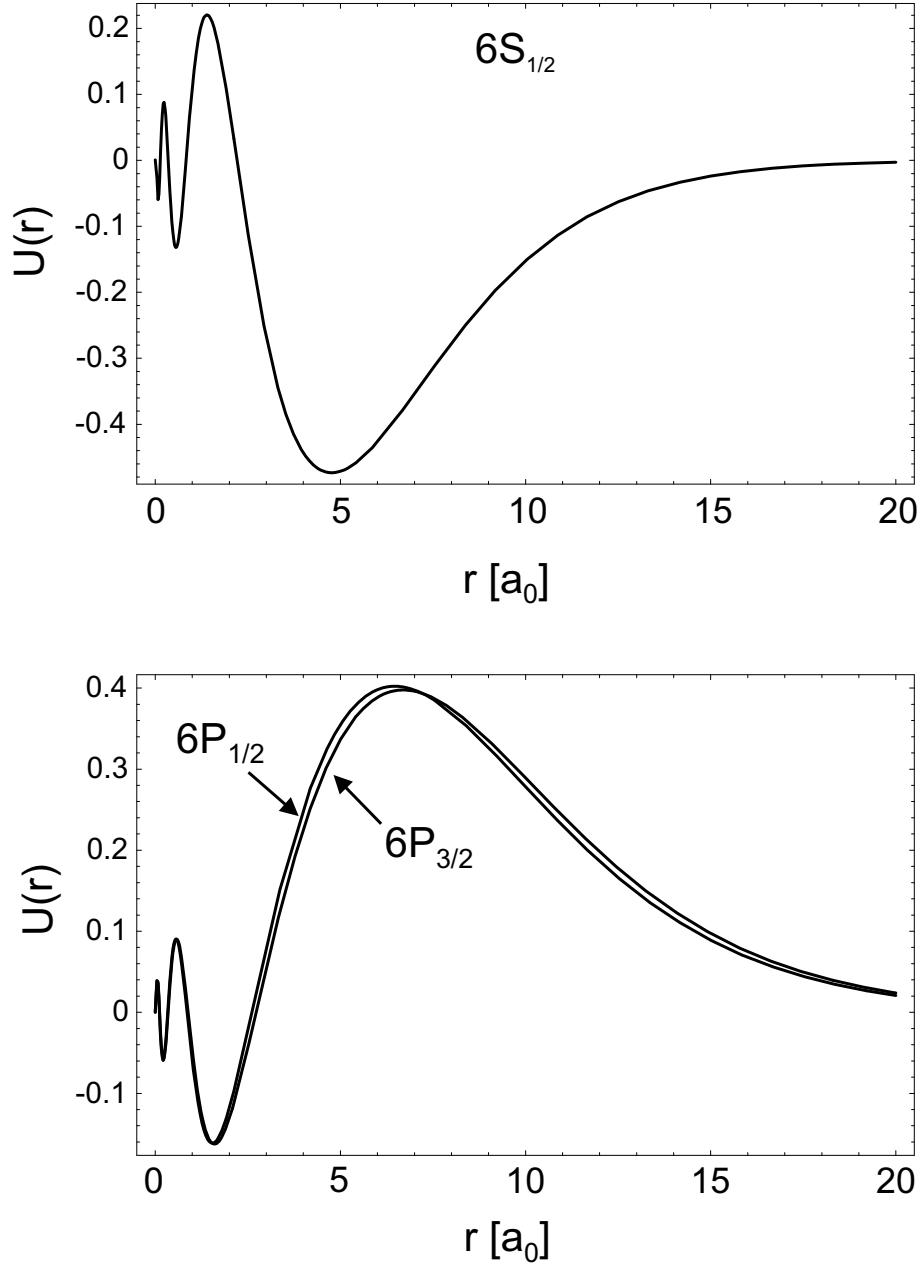
Figure C.1: Radial wave functions $u(r) = rR_{6S_{1/2}}(r)$ (top) and $u(r) = rR_{6P_{1/2,3/2}}(r)$ (bottom) of an electron in the ground state $6S_{1/2}$ and in the excited states $6P_{1/2,3/2}$ of a cesium atom. Note that the two wave functions for the P-states J=1/2 and J=3/2 are almost indistinguishable.

# References

[1] C.S.Wu, E.Ambler, R.W.Hayward, D.D.Hoppes, and R.P.Hudson. Experimental test of parity conservation in beta decay. *Phys.Rev.*, page 1413, 1957.

[2] R.Garwin, L.Lederman, and M.Weinrich. Obeservation of the failure of conservation of parity and charge conjugation in meson decays: the magnetic moment of the free muon. *Phys.Rev.*, page 1415, 1957.

[3] J.Friedman and V.L.Telegdi. Nuclear emulsion evidence for parity nonconservation in the decay chain $\pi^+ - \mu^+ - e^+$. *Phys.Rev.*, page 1681, 1957.

[4] J.H.Christenson, J.W.Cronin, V.L.Fitch, and R.Turlay. Evidence for the 2 $\pi$ decay of the $K_2^0$ meson. *Phys.Rev.Lett.*, 13(4):138, 1964.

[5] F.Abe et al. Measurement of the cp-violation parameter $sin(2\beta)$ in $B_d^0/\bar{B}_d^0 \rightarrow J/\psi K_S^0$ decays. *Phys.Rev.Lett.*, 81(25):5513, 1998.

[6] A.Angelopoulos et al. First direct observation of time reversal non-invariance in the neutral kaon system. *Phys.Lett.*, 444:43, 1998.

[7] P.G.H.Sandars. The electric dipole moment of the atom. *Phys.Lett.*, 14:194, 1965.

[8] J.J.Hudson, B.E.Sauer, M.R.Tarbutt, and E.A.Hinds. Measurement of the electron electric dipole moment using YbF molecules. *Phys.Rev.Lett.*, 89(2):023003–1, 2002.

[9] M.Arndt, S.I.Kanorsky, A.Weis, and T.W.Hänsch. Can paramagnetic atoms in superfluid helium be used to search for permanent electric dipole moments? *Phys.Lett.A*, 174:298, 1993.

[10] A.Weis, S.Kanorsky, S.Lang, and T.W.Hänsch. Can paramagnetic atoms trapped in solid $^4He$ be used to search for physics beyond the standard model? In *Lecture Notes in Physics*. Springer, 1997.

[11] A.Weis. Hunting the electron electric dipole moment. In *Electron theory and quantum electrodynamics: 100 years later*. Dowling, Plenum Press, 1997.

[12] S.Kanorski, M.Arndt, R.Dziewior, A.Weis, and T.W.Hänsch. Pressure shift and broadening of the resonance line of barium atoms in liquid helium. *Phys.Rev.B*, 50(9):6296, 1994.

[13] T.Kinoshita, Y.Takahashi, and T.Yabuzaki. Optical pumping and optical detection of the magnetic resonance of alkali-metal atoms in superfluid helium. *Phys.Rev.B*, 49(5):3648, 1994.

[14] S.Kanorski, M.Arndt, R.Dziewior, A.Weis, and T.W.Hänsch. Optical spectroscopy of atoms trapped in solid helium. *Phys.Rev.B*, 49(5):3645, 1994.

[15] M.Arndt, R.Dziewior, S.Kanorski, A.Weis, and T.W.Hänsch. Implantation and spectroscopy of metal atoms in solid helium. *Z.Phys.B*, 98:377, 1995.

[16] S.Kanorski, A.Weis, M.Arndt, R.Dzewior, and T.W.Hänsch. Pressure shift of atomic resonance lines in liquid and solid helium. *Z.Phys.B*, 98:371, 1995.

[17] A.Weis, S.Kanorski, M.Arndt, and T.W.Hänsch. Spin physics in solid helium: experimental results and applications. *Z.Phys.B*, 98:359, 1995.

[18] M.Arndt, S.Kanorski, A.Weis, and T.W.Hänsch. Long electronic spin relaxation times of Cs atoms in solid $^4He$. *Phys.Rev.Lett.*, 74(8):1359, 1995.

[19] S.Lang, S.Kanorski, T.Eichler, R.Müller-Siebert, T.W.Hänsch, and A.Weis. Optical pumping of cs atoms in solid $^4He$. *Phys.Rev.A*, 60(5):3867, 1999.

[20] S.Kanorski, S.Lang, S.Lücke, S.B.Ross, T.W.Hänsch, and A.Weis. Millihertz magnetic resonance spectroscopy of Cs atoms in body centered cubic $^4He$. *Phys.Rev.A*, 54(2):1010, 1996.

[21] S.Lang, S.Kanorski, M.Arndt, S.B.Ross, T.W.Hänsch, and A.Weis. The hyperfine structure of Cs atoms in the bcc phase of solid He. *Europhys.Lett.*, 30(4):233, 1995.

[22] S.Lang. *Optisch detektierte magnetresonanz an Cäsium atomen in festem $^4He$*. PhD thesis, Ludwig Maximilians Universität München, 1997.

[23] S.Kanorski, S.Lang, T.Eichler, K.Winkler, and A.Weis. Quadrupolar deformations of atomic bubbles in solid $^4$He. *Phys.Rev.Lett.*, 81(2):401, 1998.

[24] T.Eichler. *Magneto-optical spectroscopy of alkali atoms in helium crystals*. PhD thesis, University of Bonn, Germany, 2000.

[25] R.Müller-Siebert. *Optimierung und charakterisierung eines tieftemperatur spektrometers zur untersuchung von magneto und elektro optischen effekten an alkaliatomen in He kristallen*. PhD thesis, University of Fribourg, Switzerland, 2002.

[26] D.Nettels, R.Müller-Siebert, X.Huang, S.Ulzega, and A.Weis. Magnetic and electric properties of alkali atoms in solid helium. *Physica B*, 329:406, 2003.

[27] J.P.Toennies and A.F.Vilesov. Superfluid helium droplets: a unique cold nanomatrix for molecules and molecular complexes. *Angewandte chemie*, 43:2622–2648, 2004.

[28] D.Nettels, R.Müller-Siebert, S.Ulzega, and A.Weis. Multi-photon processes in the Zeeman structure of atomic Cs trapped in solid He. *Appl.Phys.B*, 77:563, 2003.

[29] D.Nettels, R.Müller-Siebert, and A.Weis. Relaxation mechanism of muti-quantum coherences in the Zeeman structure of atomic Cs trapped in solid He. *Appl.Phys.B*, 77:753, 2003.

[30] D.Nettels, A.Hofer, P.Moroshkin, R.Müller-Siebert, S.Ulzega, and A.Weis. Discovery of dumbbell shaped $Cs^*He_n$ exciplexes in solid he. *Phys.Rev.Lett.*, 94:063001–1, 2005.

[31] P.Moroshkin, A.Hofer, D.Nettels, S.Ulzega, and A.Weis. $Cs^*He_n$ exciplexes in solid $^4$He. *J.Chem.Phys.*, 123, 2006.

[32] S.A.Murthy, D.Krause, Z.L.Li, and L.R.Hunter. New limits on the electron electric dipole moment from Cs. *Phys.Rev.Lett.*, 63:965, 1989.

[33] P.G.H.Sandars. Differential polarizability in the ground state of the hydrogen atom. *Proc.Phys.Soc.*, 92:857, 1967.

[34] E.Whittle, D.A.Dows, and G.C.Pimentel. Matrix isolation method for the experimental study of unstable. *J.Chem.Phys.*, 22:1943, 1954.

[35] H.Coufal, E.Lüscher, H.Micklitz, and R.E.Norberg. *Rare gas solids*. Springer, 1984.

[36] I.R.Dunkin. *Matrix isolation techniques*. Oxford University Press, 1998.

[37] C.Pryor and F.Wilczek. "Artificial vacuum" for T-violation experiment. *Phys.Lett.*, B194:137, 1987.

[38] J.Wilks. *THe properties of liquid and solid helium*. Clarendon Press, Oxford, 1967.

[39] E.B.Osgood, V.J.Minkiewicz, T.A.Kitchens, and G.Shirane. Inelastic neutron scattering from bcc$^4$He. *Phys.Rev.A*, 5(3):1537, 1972.

[40] V.J.Minkiewicz, T.A.Kitchens, F.P.Lipschultz, R.Nathans, and G.Shirane. Phonon spectrum of hcp $^4$He. *Rev.Mod.Phys.*, 174(1):267, 1968.

[41] J.H.Vignos and H.A.Fairbank. New solid phase in solid helium. *Phys.Rev.Lett.*, 6:265, 1961.

[42] R.A.Aziz, A.R.Janzen, and M.R.Moldover. Ab initio calculations for helium: a standard for transport property measurements. *Phys.Rev.Lett.*, 74(9):1586, 1995.

[43] S.Kilic and T.Persi. Energy states of helium-4 dimer. *Croatica Chemica Acta*, 72(4):897, 1999.

[44] S.W.Van Sciver. *Helium cryogenics*. PLenum Press, New York, 1986.

[45] J.Jortner, W.R.Kestner, S.A.Rice, and M.H.Cohen. Study of the properties of an excess electron in liquid helium:the nature of the electron-helium interactions. *J.Chem.Phys.*, 43:2614, 1965.

[46] W.B.Fowler and D.L.Dexter. Electronic bubble states in liquid helium. *Phys.Rev.*, 176:377, 1968.

[47] A.Y.Parshin and S.V.Pereverzev. Spectroscopic study of excess electrons in liquid helium. *JETP*, 74:68, 1992.

[48] S.Kanorski and A.Weis. Atoms in nano-cavities. In *NATO Advanced Study Institute "Quantum optics of confined systems"*. Kluwer Academic Publishers, 1995.

[49] D.Nettels. *Optical magnetic resonance tomography and laser spectroscopy of cesium atoms trapped in solid helium*. PhD thesis, University of Fribourg, Switzerland, 2003.

[50] W.Bernreuther and M.Suzuki. The electric dipole moment of the electron. *Rev.Mod.Phys.*, 63:313, 1991.

[51] A.D.Sakharov. Violation of CP invariance, C asymmetry and baryon asymmetry of the universe. *JETP Lett.*, 5:24–27, 1967.

[52] M.Kobayashi and T.Maskawa. CP-violation in the renormalizable theory of weak interactions. *Prog.Theor.Phys.*, 49:652, 1973.

[53] S.M.Barr. A review of CP violations in atoms. *Int.J.Mod.Phys.*, A8:209, 1993.

[54] B.C.Regan, E.D.Commins, C.J.Schimdt, and D.DeMille. New limit on the electron electric dipole moment. *Phys.Rev.Lett.*, 88(7):071805, 2002.

[55] L.I.Schiff. Measurability of nuclear electric dipole moments. *Phys.Rev.*, 132(5):2194, 1963.

[56] R.D.Haun and J.R.Zacharias. Stark effect on Cesium-133 hyperfine structure. *Phys.Rev.*, 107(1):107, 1957.

[57] E.Lipworth and P.G.H.Sandars. Removal of Zeeman-level degeneracy in alkali atoms by an electric field. *Phys.Rev.Lett.*, 13(24):716, 1964.

[58] J.R.P.Angel and P.G.H.Sandars. The hyperfine structure Stark effect. I. Theory. *Proc.R.Soc.London, A*, 305(1480):125–138, 1968.

[59] J.R.Mowat. Stark effect in alakli-metal ground-state hyperfine structure. *Phys.Rev.A*, 5(3):1059, 1972.

[60] E.Simon, P.Laurent, and A.Clairon. Measurement of the Stark shift of the Cs hyperfine splitting in an atomic fountain. *Phys.Rev.A*, 57(1):436, 1998.

[61] A.Godone, D.Calonico, F.Levi, S.Micalizio, and C.Calosso. Stark-shift measurement of the $^2S_{1/2}$,F=3 $\rightarrow$ F=4 hyperfine transition of$^{133}$Cs. *Phys.Rev.A*, 71:063401–1, 2005.

[62] J.P.Carrico, A.Adler, M.R.Baker, S.Legowski, E.Lipworth, P.G.H.Sandars, T.S.Stein, and C.Weisskopf. Atomic beam resonance measurement of the differential polarizability between Zeeman substates in the ground state of the Cesium atom. *Phys.Rev.*, 170(1):64, 1968.

[63] H.Gould, E.Lipworth, and M.C.Weisskopf. Quadratic Stark shift between Zeeman substates in Cs$^{133}$, Rb$^{87}$, Rb$^{85}$, K$^{39}$ and Na$^{23}$. *Phys. Rev.*, 188(1):24–29, 1969.

[64] C.Ospelkaus, U.Rasbach, and A.Weis. Measurement of the forbidden tensor polarizability of Cs using an all-optical Ramsey resonance technique. *Phys.Rev.A*, 67:011402, 2003.

[65] J.D.Feichtner, M.E.Hoover, and M.Mizushima. Stark effect of the hyperfine structure of Cesium-133. *Phys.Rev.*, 137(3A):A702, 1965.

[66] V. A. Dzuba, V. V. Flambaum, P. G. Silvestrov, and O. P. Sushkov. Relativistic many-body calculations in atoms and parity violation in cesium. *J. Phys. B*, 18:597, 1985.

[67] W. R. Johnson, M. Idrees, and J. Sapirstein. Second-order energies and third order matrix elements of alkali metal atoms. *Phys. Rev. A*, 35(8):3218, 1987.

[68] V. A. Dzuba, V. V. Flambaum, A. Y. Kraftmakher, and O. P. Sushkov. Summation of higher orders of perturbation theory in the correlation correction to the hyperfine structure and to the amplitudes of e1-transitions in the Cs atom. *Phys. Lett. A*, 142(6,7):373, 1989.

[69] S. A. Blundell, W. R. Johnson, and J. Sapirstein. Relativistic all-order calculations of energies and matrix elements in cesium. *Phys. Rev. A*, 43(7):3407, 1991.

[70] S. A. Blundell, J. Sapirstein, and W. R. Johnson. High accuracy calculation of parity nonconservation in cesium and implications for particle physics. *Phys. Rev. D*, 45(5):1602, 1992.

[71] V. A. Dzuba, V. V. Flambaum, and O. P. Sushkov. Polarizabilities and parity nonconservation in the Cs atom and limits on the deviation from the standard electroweak model. *Phys. Rev. A*, 56(6):R4357, 1997.

[72] M. S. Safronova, W. R. Johnson, and A. Derevianko. Relativistic many-body calculations of energy levels, hyperfine constants, electric-dipole matrix elements, and static polarizabilities for alkali metal atoms. *Phys. Rev. A*, 60(6):4476, 1999.

[73] A. A. Vasilyev, I. M. Savukov, M. S. Safronova, and H. G. Berry. Measurement of the 6s-7p transition probabilities in atomic cesium and a revised value for the weak charge $Q_W$. *Phys. Rev. A*, 66:020101–1, 2002.

[74] R. J. Rafac, C. E. Tanner, A. E. Livingston, K. W. Kukla, H. G. Berry, and C. A. Kurtz. Precision lifetime measurements of the $6p^2P_{1/2,3/2}$ states in atomic cesium. *Phys. Rev. A*, 50(3):1976, 1994.

[75] R. J. Rafac, C. E. Tanner, A .E. Livingston, and H. G. Berry. Fast beam laser lifetime measurements of the cesium $6p^2P_{1/2,3/2}$ states. *Phys. Rev. A*, 60(5):3648, 1999.

[76] C.Cohen-Tannoudji. *Quantum Mechanics*, volume 2.

[77] H. L. Zhou and D. W. Norcross. Improved calculation of the quadratic Stark effect in the $6P_{3/2}$ state of Cs. *Phys. Rev. A*, 40(9):5048, 1989.

[78] M.Fabry. Theoretical and experimental determinations of cesium oscillator-strengths. *Journal of quantitative spectroscopy and radiative transfer*, 16(2):127, 1976.

[79] C.E.Moore. *Atomic energy levels*. National Standard Reference Data Series-National Bureau of Standards (US) 35. 1971.

[80] A. Derevianko and S. G. Porsev. Determination of lifetimes of $6p_j$ levels and ground state polarizability of Cs from the van der Waals coefficient $C_6$. *Phys. Rev. A*, 65:053403–1, 2002.

[81] J.M.Amini and H.Gould. High precision measurement of the static dipole polarizability of cesium. *Phys.Rev.Lett.*, 91(15):153001–1, 2003.

[82] E.Arimondo, M.Inguscio, and P.Violino. Experimental determinations of the hyperfine structure in the alkali atoms. *Rev.Mod.Phys.*, 49(1):31, 1977.

[83] R.J.Rafac and C.E.Tanner. Measurement of the $^{133}$Cs $6P_{1/2}$ state hyperfine structure. *Phys.Rev.A*, 56:1027, 1997.

[84] C.E.Tanner and C.Wieman. Precision measurement of the hyperfine structure of the $^{133}$Cs $6P_{3/2}$ state. *Phys.Rev.A*, 38:1616, 1988.

[85] S. Ulzega, A. Hofer, P. Moroshkin, and A. Weis. to be published.

[86] Sobelman. *Atomic spectra and radiative transitions*. Springer series on atoms and plasmas. Springer, 1992.

[87] S.L.Gilbert, R.N.Watts, and C.E.Wieman. Hyperfine structure measurement of the 7S state of cesium. *Phys.Rev.A*, 27:581, 1983.

[88] P.P.Herrmann, J.Hoffnagle, A.Pedroni, N.Schlumpf, and A.Weis. Doppler-free spectroscopy of the 8S state of cesium. *Opt.Comm.*, 56(1):22, 1985.

[89] V.A.Dzuba and V.V.Flambaum. Off-diagonal hyperfine interaction and parity nonconservation in cesium. *Phys.Rev.A*, 62:052101, 2000.

[90] V.V.Flambaum. private communication.

[91] V.Gerginov, A.Derevianko, and C.E.Tanner. Observation of the nuclear magnetic octupole moment of $^{133}$Cs. *Phys.Rev.Lett.*, 91(7):072501–1, 2003.

[92] S. Micalizio, A. Godone, D. Calonico, F. Levi, and L. Lorini. Black body radiation shift of the Cs hyperfine transition frequency. *Phys. Rev. A*, 69:053401, 2004.

[93] W. M. Itano, L. L. Lewis, and D. J. Wineland. Shift of $^2S_{1/2}$ hyperfine splittings due to blackbody radiation. *Phys. Rev. A*, 25(2), 1982.

[94] T.Lee, T.P.Das, and R.M.Sternheimer. Perturbation theory for the stark effect in the hyperfine structure of alkali metal atoms. *Phys.Rev.A*, 11(6):1784, 1975.

[95] J.Brossel and A.Kastler. La detection de la resonance magnetique des niveaux excites - l'effect de depolarisation des radiations de resonance optique et de fluorescence. *Comptes rendu hebdomadaires des seances de l'academie des sciences*, 229(23):1213–1215, 1949.

[96] F.Bloch and A.Siegert. Magnetic resonance for nonrotating fields. *Phys.Rev.*, 57(6):522, 1940.

[97] D.Nettels, R.Müller-Siebert, X.Huang, S.Ulzega, and A.Weis. Magnetic and electric properties of alkali atoms in solid helium. *PhysicaB*, 329-333:406–407, 2003.

[98] E.B.Alexandrov and D.A.Varshalovich. Polarization dependance of optical coherence signals between magnetic sublevels of alkali-atom ground-state hyperfine structure. *Optics and Spectroscopy*, 82(2):161–165, 1997.

[99] W.J.Thompson. *Angular momentum*. Wiley-Interscience, 1994.

[100] R.D.Cowan. *The theory of atomic structure and spectra*. University of California Press, 1981.

[101] R.J.Rafac and C.E.Tanner. Measurement of the ratio of the cesium D-line transition strengths. *Phys.Rev.A*, 58(2):1087, 1998.

[102] D.W.Norcross. Photoabsorption by cesium. *Phys.Rev.A*, 7(2):606, 1973.

[103] P.Gombas. *Atoms II*. Springer-Verlag Berlin-Gottingen-Heidelberg, 1956.

[104] A.Hofer. PhD thesis, University of Fribourg, Expected 2007.

# Acknowledgments

I would like to thank all the people who gave a contribution to the success of this work.

First of all, I would like to thank Prof.Dr.Antoine Weis for giving me the opportunity to join this group and enter the world of experimental research. This work would have never been completed without his constant incentive to achieve more and more ambitious goals. His passion for physics was for me a source of great motivation, and discussions with him a never-ending source of inspiration. I really owe him a lot.

I also would like to thank Prof.Dr.Jean-Claude Dousse and Prof.Dr. Majed Chergui for reading this manuscript and giving their precious suggestions.

In a complex experiment like ours, team working is an essential condition. Therefore I thank Peter Moroshkin and Adrian Hofer for the deep cooperation, the constant mutual help and obviously for all the funny nights spent in the lab. I specially wish Adrian good luck for his thesis.

I also thank all the colleagues who worked on the helium experiment with me during the past four years: Reinhard Müller-Siebert, Daniel Nettels and Huang Xueren. I owe most of what I know about the experiment to them.

I thank Paul Knowles for all his help. I learnt both physics and English with him. I thank all the other members of the group: Georg Bison, Hervé Sudan, Martin Rebetez, Nicole Haefliger. It's a pleasure to work with them.

I thank Prof.Dr.Andreas Züttel and all the assistants who worked with me in the Travaux Pratiques pour Débutants.

Among the people who have already left this group, a special thank goes to Stephan Gröger. He was both a special colleague and a friend. He was always present when I needed his help, for physics and for other things. I thank also Robert Wynands, Stephan Tandler, Anatoly Pazgalev, Mondher Gantri and José Lamas-Valverde.

L'aide reçue par l'atelier méchanique et l'atelier électronique de l'Institute de Physique a aussi grandement contribuée au succès de mon travail et je tiens beaucoup à remercier tous ceux qui travaillent dans ces ateliers. Je remercie aussi toutes les secrétaires et l'ensemble du personnel de l'Université.

Finally, but not in order of importance, a special thank goes to my family, all my friends and of course Magda.
Un grazie speciale alla mia famiglia, a tutti i miei amici e naturalmente a Magda.

# Curriculum vitae

**Personal information**

| | |
|---|---|
| Name | Simone ULZEGA |
| Address | Boulevard de Pérolles, 93 - 1700 Fribourg - Switzerland |
| | Via Roma, 21 - 20025 Legnano (MI) - Italy |
| Telephone number | +41 - (0)76 - 377 98 03 (CH) |
| | +39 - 347 - 721 98 03 (I) |
| E-mail | simone.ulzega@unifr.ch |
| | simoneulzega@gmail.com |
| Place/Date of birth | Milan (Italy)    October 28, 1973 |
| Nationality | Italian |
| Status | Bachelor |

## Education and professional experience

| | |
|---|---|
| 1987 – 1992 | High school (Liceo G.Galilei,Legnano(MI),Italy) |
| July 1992 | High school graduation: 58/60 (Maturità scientifica) |
| 1992 – 1998 | University of Milan, Faculty of Physics |
| Nov.1998 | Degree in Physics: 110/110 magna cum laude. |
| | Thesis title: *"Atomic collective effects in micromaser dynamics"*. Supervisor: Prof.F.Casagrande |
| Dec.1998 – Apr.1999 | Scholarship: *"Quantum optical systems dynamics: development of theoretical models and software for numerical applications"*, Physics Department, University of Milan (Italy). |
| May 2000 – Oct.2000 | Training course *"Internet technologies and systems"* at "Il Sole 24 Ore" (publisher and internet services provider), Milan, Italy. |
| Oct.2000 – Feb.2002 | Employee at Pirelli Cables and Systems - R&D New Telecom Businesses - Milan, Italy |
| | Role: Optical components designer |
| Mar.2002 – Mar.2006 | PhD student in the research group of Prof. Dr. A. Weis, Physics Department, University of Fribourg (Switzerland) |
| | PhD thesis title: *"Theoretical and experimental study of the Stark effect in the ground state of alkali atoms in helium crystals"*. |
| May 2003 – June 2003 | Graduate course (3ème cycle): *"Atomic physics tests of the Standard Model"*, by Prof. Dr. A. Weis. |
| Mar.2002 – Mar.2006 | Teaching assistant in the Beginner's Student Laboratory (*travaux pratiques pour débutants*), Physics Department, University of Fribourg. |
| 1993 – 2000 | Private tuition of physics and mathematics for high school and under-graduate students. |

## Publications

1. F. Casagrande, A. Lulli, and S. Ulzega. *Quantum-Trajectory approach to cavity quantum electrodynamics with up to three- atom collective effects*, Phys. Lett. A **255**:133, 1999.

2. F. Casagrande, A. Lulli, and S. Ulzega. *Collective effects and trapping states by a Quantum-Trajectory treatment of micromaser dynamics*, Phys. Rev. A **60**:1582, 1999.

3. D. Nettels, R. Müller-Siebert, X. Huang, S. Ulzega, and A. Weis. *Magnetic and electric properties of alkali atoms in solid helium*, Physica B, **329**:406, 2003.

4. D. Nettels, R. Müller-Siebert, S. Ulzega, and A. Weis. *Multi-photon processes in the Zeeman structure of atomic Cs trapped in solid helium*, Appl. Phys. B - Lasers and Optics, **77**(6-7):563–570, 2003.

5. D. Nettels, A. Hofer, P. Moroshkin, R. Müller-Siebert, S. Ulzega, and A. Weis. *Discovery of dumbbell-shaped $Cs^*He_n$ exciplexes in solid $^4He$*, Phys. Rev. Lett., **94**:063001–1, 2005.

6. P. Moroshkin, A. Hofer, D. Nettels, S. Ulzega, and A. Weis. *$Cs^*He_n$ exciplexes in solid $^4He$*, J. Chem. Phys., **124**:024511–1, 2006.

7. S. Ulzega, P. Moroshkin, A. Hofer, and A. Weis. *Observation of the quadratic Stark effect between Zeeman levels in the ground state of Cs atoms in solid $^4He$*, to be published.

8. S. Ulzega, P. Moroshkin, A. Hofer, and A. Weis. *Electric tensor polarizabilities and the black body shift of the clock transition in cesium*, to be published.

## Conferences

1. F. Casagrande, A. Lulli, and S. Ulzega. *Atomic collective effects and photon trapping states in micromaser dynamics*, INFM National Congress, Catania (Italy), 14/18 June 1999.

2. S. Ulzega, A. Lulli, and F. Casagrande. *Effetti collettivi atomici e stati di intrappolamento fotonici nel micromaser*, LXXXV National Congress SIF, Pavia (Italy), 20/24 settembre 1999.

3. D. Nettels, A. Hofer, P. Moroshkin, S. Ulzega, and A. Weis. *Atomic impurities in helium crystals - Formation of dumbbell-shaped $Cs^*He_n$ exciplexes*, Annual Meeting of the Swiss Physical Society (SPS), Neuchatel, March 2004.

4. P. Moroshkin, D. Nettels, A. Hofer, S. Ulzega, and A. Weis. *$Cs^*He_n$ exciplexes in solid $^4He$*, Conference on Laser Physics, Yerevan (Armenia), October 2004.

5. P. Moroshkin, D. Nettels, A. Hofer, S. Ulzega, and A. Weis. *Discovery of dumbbell-shaped $Cs^*He_n$ exciplexes in solid $^4He$*, Conference on Helium Clusters, Bad Honnef (Germany), March 2005.

6. P. Moroshkin, D. Nettels, A. Hofer, S. Ulzega, and A. Weis. *Laser induced formation and spectroscopy of $Cs^*He_n$ exciplexes in solid $^4He$*, ICONO, St.Petersburg, May 2005.

7. A. Hofer, D. Nettels, P. Moroshkin, S. Ulzega, and A. Weis. *Molecular impurities in solid helium - different formation paths of $Cs^*He_n$ exciplexes*, Annual Meeting of the Swiss Physical Society (SPS), Bern, July 2005.

8. S. Ulzega, A. Hofer, P. Moroshkin, and A. Weis. *Theoretical and experimental study of the quadratic Stark effect in the ground state of alkali atoms implanted in helium crystals*, Annual Meeting of the Swiss Physical Society (SPS), Bern, July 2005.

9. S. Ulzega, A. Hofer, P. Moroshkin, and A. Weis. *A new calculation of the static Stark shift of the cesium clock transition*, Conference on Precision Electromagnetic Measurements (CPEM), Torino, July 2006.
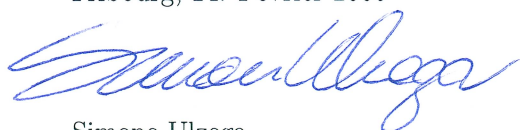
## Posters

1. D. Nettels, A. Hofer, P. Moroshkin, S. Ulzega, and A. Weis. *Observation of apple- and dumbbell-shaped $Cs^*He_n$ exciplexes in solid $^4He$*, ICAP, Rio de Janeiro, July 2004.

2. P. Moroshkin, A. Hofer, S. Ulzega, and A. Weis. *Spectroscopy of alkali dimers in solid $^4He$*, Annual Meeting of the Swiss Physical Society (SPS), Bern, July 2005.

3. A. Weis., P. Moroshkin, D. Nettels, A. Hofer, and S. Ulzega. *Observation of a $Cs^*He_2$ and discovery of a $Cs^*He_7$ exciplex in solid $^4He$*, $37^{th}$ Conference of the European Group for Atomic Systems (EGAS), Dublin, August 2005.

4. S. Ulzega, A. Hofer, P. Moroshkin, and A. Weis. *Electric tensor polarizabilities and the black body shift of the clock transition in cesium*, $20^{th}$ European Frequency and Time Forum (EFTF), Braunschweig (Germany), March 2006.

## Talks

1. S. Ulzega, A. Hofer, P. Moroshkin, and A. Weis, *Tiny electric field effects in magnetic resonance spectroscopy*, University of Fribourg - Department Day, December 2004.

2. S. Ulzega, A. Hofer, P. Moroshkin, and A. Weis, *Study of the Stark effect in the ground state of Cs atoms implanted in helium crystals*, Ecole Polytechnique Fédérale de Lausanne (EPFL), August 2005.

3. S. Ulzega, A. Hofer, P. Moroshkin, and A. Weis, *Study of the Stark effect in the ground state of Cs atoms implanted in helium crystals*, Istituto Elettrotecnico Nazionale G.Ferraris (IEN), Torino, January 2006.

Je certifie avoir effectué ce travail de manière autonome, sans l'aide de moyens non autorisés. Les sources utilisées sont répertoriées dans la bibliographie.

Fribourg, 14. Février 2006

Simone Ulzega